

Lecture Notes in Civil Engineering

Bibhu Prasad Swain
Uday Shanker Dixit *Editors*

Recent Advances in Civil Engineering

Select Proceedings of ICSTE 2023

 Springer

Lecture Notes in Civil Engineering

Volume 431

Series Editors

Marco di Prisco, Politecnico di Milano, Milano, Italy

Sheng-Hong Chen, School of Water Resources and Hydropower Engineering,
Wuhan University, Wuhan, China

Ioannis Vayas, Institute of Steel Structures, National Technical University of
Athens, Athens, Greece

Sanjay Kumar Shukla, School of Engineering, Edith Cowan University, Joondalup,
WA, Australia

Anuj Sharma, Iowa State University, Ames, IA, USA

Nagesh Kumar, Department of Civil Engineering, Indian Institute of Science
Bangalore, Bengaluru, Karnataka, India

Chien Ming Wang, School of Civil Engineering, The University of Queensland,
Brisbane, QLD, Australia

Lecture Notes in Civil Engineering (LNCE) publishes the latest developments in Civil Engineering—quickly, informally and in top quality. Though original research reported in proceedings and post-proceedings represents the core of LNCE, edited volumes of exceptionally high quality and interest may also be considered for publication. Volumes published in LNCE embrace all aspects and subfields of, as well as new challenges in, Civil Engineering. Topics in the series include:

- Construction and Structural Mechanics
- Building Materials
- Concrete, Steel and Timber Structures
- Geotechnical Engineering
- Earthquake Engineering
- Coastal Engineering
- Ocean and Offshore Engineering; Ships and Floating Structures
- Hydraulics, Hydrology and Water Resources Engineering
- Environmental Engineering and Sustainability
- Structural Health and Monitoring
- Surveying and Geographical Information Systems
- Indoor Environments
- Transportation and Traffic
- Risk Analysis
- Safety and Security

To submit a proposal or request further information, please contact the appropriate Springer Editor:

- Pierpaolo Riva at pierpaolo.riva@springer.com (Europe and Americas);
- Swati Meherishi at swati.meherishi@springer.com (Asia—except China, Australia, and New Zealand);
- Wayne Hu at wayne.hu@springer.com (China).

All books in the series now indexed by Scopus and EI Compendex database!

Bibhu Prasad Swain · Uday Shanker Dixit
Editors

Recent Advances in Civil Engineering

Select Proceedings of ICSTE 2023

 Springer

Editors

Bibhu Prasad Swain
Department of Physics
National Institute of Technology Manipur
Manipur, India

Uday Shanker Dixit
Department of Mechanical Engineering
IIT Guwahati
Guwahati, India

ISSN 2366-2557

ISSN 2366-2565 (electronic)

Lecture Notes in Civil Engineering

ISBN 978-981-99-4664-8

ISBN 978-981-99-4665-5 (eBook)

<https://doi.org/10.1007/978-981-99-4665-5>

© The Editor(s) (if applicable) and The Author(s), under exclusive license to Springer Nature Singapore Pte Ltd. 2024

This work is subject to copyright. All rights are solely and exclusively licensed by the Publisher, whether the whole or part of the material is concerned, specifically the rights of translation, reprinting, reuse of illustrations, recitation, broadcasting, reproduction on microfilms or in any other physical way, and transmission or information storage and retrieval, electronic adaptation, computer software, or by similar or dissimilar methodology now known or hereafter developed.

The use of general descriptive names, registered names, trademarks, service marks, etc. in this publication does not imply, even in the absence of a specific statement, that such names are exempt from the relevant protective laws and regulations and therefore free for general use.

The publisher, the authors, and the editors are safe to assume that the advice and information in this book are believed to be true and accurate at the date of publication. Neither the publisher nor the authors or the editors give a warranty, expressed or implied, with respect to the material contained herein or for any errors or omissions that may have been made. The publisher remains neutral with regard to jurisdictional claims in published maps and institutional affiliations.

This Springer imprint is published by the registered company Springer Nature Singapore Pte Ltd. The registered company address is: 152 Beach Road, #21-01/04 Gateway East, Singapore 189721, Singapore

Preface

“Recent Advances in Civil Engineering—Select Proceedings of ICSTE 2023” comprises a collection of research articles on Civil Engineering presented at the 1st International Conference on Sci/Tech and Engineering (ICSTE 23). Moreover, it is a matter of honor for NIT Manipur that Springer was associated with ICSTE 23 as a major publication partner for this event. The chapters of this book cover Civil Engineering topics of different approaches and techniques like the Soil and Water Assessment Tool (SWAT) Model, Geographic Information System (GIS) techniques and satellite data processing, bio-composite concrete, reinforced concrete buildings, geopolymer composites, analysis using finite element method, and metal additive manufacturing techniques.

Eminent speakers like Prof. Manoj Gupta, National University of Singapore, Singapore; Prof. Bharat Dahiya Thammasat University, Thailand; Prof. Surender Kumar, Ex. Prof. (BIT Mesra), India; Prof. Sawan Suman Sinha, IIT Delhi, India; Prof. Abhishek Dey, Indian Association for the Cultivation of Science, Kolkata, India; Prof. Bimlesh Kumar, IIT Guwahati, India, and Dr. Sanjeet Kumar Dwivedi, Green Hydrogen based Danish MNC, Denmark shared their knowledge and experience. The conference was attended and enriched by participants from numerous institutes such as IITs, NITs, NEHU, BIT, VIT, MIT Manipur, Manipur University, IEST Kolkata, and abroad; several speakers deliberated on their research works. In addition, the paper presentations were accompanied by six keynote addresses from leading academic and industrial researchers around the globe. Out of 268 papers, 138 papers were selected for publication in the ICSTE 23 Proceedings. The paper presentations took place on eight different tracks with parallel main sessions. On the ICSTE 23 platform, we got the opportunity to promote the national campaign ‘G20’ in 2023, which is being observed under the chairmanship of India.

The review committee has done an excellent job in reviewing articles and approving high-quality research articles to be published in the conference proceedings. The editors are thankful to all the faculty members and students of various committees for their dedication to making it a very successful conference. Thanks to

the editing and printing support staff of Springer for making the publication of this book possible. We sincerely hope that it will inspire researchers/scientists to explore the potential in the diverse upcoming research fields.

Manipur, India

Dr. Bibhu Prasad Swain
bpswain@nitmanipur.ac.in

Guwahati, India

Uday Shanker Dixit
uday@iitg.ac.in

Contents

Streamflow Assessment of Mountainous River Basin Using SWAT Model	1
Abhilash Gogineni and Madhusudana Rao Chintalacheruvu	
Slope Stability Analysis of Langdeibung Area Along Imphal-Jiribam National Highway (NH-37) Using Geoslope	11
Koko Karbia, Kakchingtabam Anil Sharma, Kosygin Leishangthem, Pukhrambam Jalajit Singh, Khwairakpam Selija, and Devasis Laishram	
Numerical Investigation of Circular and Square Hollow Steel Section Subjected to Torsion	21
Thounaojam Bidyaraj Singh, Khwairakpam Sachidananda, and Konjengbam Darunkumar Singh	
Carbon Pool Detection Through GIS Techniques and Satellite Data in a Semi Urban Region	29
Thiyam Tamphasana Devi and A. Abdulla Azaruden	
A Comparative Study Between Confined Masonry and Reinforced Concrete Buildings Performances	43
Angelica Chanu Chingakham, Angom Olivia Devi, Christina Sagolsem, Konthoujam Nungshithoi, Samjetsabam Chainey, and Sukumar Singh Ningthoukhongjam	
Influence of Normalization Techniques in CMIP Model Selection Using an MCDM Method MOORA	51
Gaurav Patel, Subhasish Das, and Rajib Das	
Numerical Simulation on the Hydrodynamics of Sedimentation Tank When Longitudinal Inclined Plates Are Employed	61
Kirpa Hirom and Thiyam Tamphasana Devi	

Behaviour of High Strength Steel Circular Hollow Section Subjected to Torsion—A Finite Element Study	71
Soibam Monika Devi, Sanasam Vipej Devi, and Tekcham Gishan Singh	
LULC Dynamics Study and Modeling of Urban Land Expansion Using CA-ANN	79
Srija Roy and Madhusudana Rao Chintalacheruvu	
Mapping of Suitable Areas for Mulberry Plantation Using GIS in Manipur	91
Deepali Gaikwad and Thiyam Tamphasana Devi	
Performance Appraisal of Ravi Shankar Sagar Project Using Comparative Indicators	101
Nikki Chanda, Madhusudana Rao Chintalacheruvu, Choudhary, and A. K.	
Sustainable Affordable Housing in Madhya Pradesh: Challenges and Opportunities	111
Vivek Garg and Bimal Chandra Roy	
Implementation of a Multiscale Method for Problems in Linear Elasticity	119
Devasis Laishram, Kosygin Leishangthem, Khwairakpam Selija, and Koko Karbia	
Evolution of Four Formulae Derived Over Five Decades to Predict Temporal Scour at Circular Pier	131
Buddhadev Nandi, Krishanu Sasmal, and Subhasish Das	
Improvement in Geometric Design of SH-18: A Case Study	141
Kundan Meshram and Dhananjay Pandya	
Comparison of Three Turbulence Models in Predicting the Particle Removal Efficiency of a Sedimentation Tank	151
Mk Raees and Thiyam Tamphasana Devi	
Response of Vertically Irregular Buildings to Tsunami	161
Mrityunjoy Naskar, Rana Roy, and Sunil Singh Mayengbam	
Integrated Modeling Approach for Developing Sustainable Buildings: A State of the Art	169
Shubham K. Verma, V. Gupta, S. Thappa, N. Gupta, A. Gupta, V. K. Dogra, Y. Anand, and S. Anand	
Investigation of Local Scour and Flow Field Around Bridge Pier with and Without Collar Through Numerical Simulation	181
Ningombam Bishwajit Singh and Thiyam Tamphasana Devi	

Significance of Effective CBR in the Design of Flexible Pavement	191
Khwairakpam Sachidanada, Polem Jesiada, and Naoroibam Bidyamani Chanu	
Rathong glacier's Line-Of-Sight (LOS) Velocity Measured Using the Modified Four-Pass DInSAR Technique	197
Devishri Kangjam, Rajkumar Kamaljit Singh, Khoisnam Nanaoba Singh, Jayaprasad Pallipad, Maganti Srinivasa Tarun, Deepak Putrevu, Arundhati Misra, and Mamata Maisnam	

About the Editors

Dr. Bibhu Prasad Swain is currently an associate professor at the Department of Physics, National Institute of Technology Manipur. He obtained his B.Sc. (Physics) from Utkal University, Bhubaneswar, M.Sc. (Physics) from the National Institute of Technology Rourkela, M.Tech. (Materials Science) from Barkatullah University, and Ph.D. from the Indian Institute of Technology, Bombay. His major areas of research interests include large bandgap Semiconductors, Mechanical Hard-Materials, Nanostructured Materials, Graphene-Based Supercapacitor, Photovoltaic Materials, Biocompatible Coating, and Modeling of Advanced MOSFET. He has published more than 150 papers in reputed international journals/conference proceedings and 4 edited books. Dr. Swain received the Brain Korea 21 Fellow and Japanese Society of Promotion of Science Postdoctoral Fellow from Materials Research, Seoul National University, and Government of Japan in the years 2007 and 2008. Currently, he is an editorial board member of the Nanoscience and Nanotechnology—Asia and a guest editor in “Materials” journals in MDPI publications.

Dr. Uday Shanker Dixit is currently a senior professor (HAG) at the Department of Mechanical Engineering, Indian Institute of Technology Guwahati. He obtained his B.Tech. (Mechanical Engineering) from the Indian Institute of Technology Roorkee, M.Tech. (Mechanical Engineering) from the Indian Institute of Technology Kanpur, and Ph.D. from the Mechanical Engineering, Indian Institute of Technology Kanpur. His major areas of research interest include Plasticity, Metal Forming, Laser-Based Manufacturing, and Finite Element Modeling and Optimization. He has published 146 papers in reputed journals and authored/edited 19 books. Prof. Dixit is an honorary fellow member of the Indian Welding Society and felicitated by the National Coordinator of NPTEL for getting larger number of viewers of his course on Engineering Mechanics. He was the director of CIT, Krokrajhar (2014–15), a BOG member of many institutes, and a guest editor for many special issues of reputed journals.

Streamflow Assessment of Mountainous River Basin Using SWAT Model



Abhilash Gogineni  and Madhusudana Rao Chintalacheruvu 

1 Introduction

Hydrologic models are valuable tools for planning and managing water resources in the river basin. These models are also helpful in understanding and simulating the hydrologic processes, assessing the effects of climatic and land use and land cover (LULC) changes, and investigating water quality in the river basin [1]. In recent research, hydrologic modeling has emerged as a critical achievement in watershed hydrological simulation with the development and incorporation of new tools like remote sensing (RS) and geographic information systems (GIS). The System Hydrologic European (SHE) model and the Soil and Water Assessment Tool (SWAT) model are a few such model applications widely used for hydrological modeling for river basin studies [2, 3].

Most rivers in the globe originate in high mountain regions, where snow and glaciers retain much water. In high snow and glacier catchments, melting water contributes more streamflow than rain [4, 5]. These rivers provide water for agricultural, industrial, and municipal applications. Recent figures show that over 50% of all disaster, losses are due to connected disasters, with over 70% of flood-related deaths attributed to mountain torrents [6]. Snowmelt floods are frequent, yet they represent severe environmental and economic risks.

Snowmelt hydrology is a crucial element in mountainous watersheds where melting snow is a significant source of stream flows. The simulation complexity leads to a perception that simulating snowmelt runoff in a mountainous area is challenging. Mountainous regions also frequently lack sufficient data, which increases computational simulation requirements [7, 8]. To represent the current complex mountainous

A. Gogineni · M. R. Chintalacheruvu (✉)
Department of Civil Engineering, National Institute of Technology Jamshedpur,
Jamshedpur 831014, India
e-mail: cmrao.civil@nitjsr.ac.in

environmental situation, calibration–validation and uncertainty analysis are necessary to effectively use the distributed hydrologic models [9]. Calibration is done by selecting model input parameters within acceptable ranges to signify the hydrological process accurately. Comparing the model outputs for a particular collection of observed data allows for evaluating this calibration [10]. Once calibrated, watershed models enable evaluation of the effects of environmental changes caused by management or natural processes in a method that is not attainable through field experiments and direct observation. Simulation analysis of situations, before they are implemented, can help reduce management uncertainty.

The two main approaches frequently employed in snowmelt runoff analysis are the temperature index and energy balance techniques. Whereas the energy balance method relies upon the quantity of energy input to the system, the temperature index strategy employs temperature as the primary driving element for snowmelt processes [11, 12]. The energy balance strategy is data-intensive and occasionally inappropriate owing to scarce data or unnecessary information, while the temperature index method is common, straightforward, and simple to utilize [13].

The Sutlej river basin contains many mountainous regions with complex topography. Temperatures rise dramatically in the spring, which causes an increase in flooding frequency. Elevation variations tremendously impact snow cover processes and melt in hilly basins. In watersheds with complex terrain and significant elevation variations, simulated accuracy has been proven to be improved by defining elevation zones within the model's subbasins [8]. The management of the water resources of the high mountain area needs to realize the connections between natural forests, snowpack, snowmelt, and streamflow production. Reliable modeling techniques are crucial for correctly reflecting the impacts of both the forest cover and the dynamics of snowmelt on runoff to calculate the streamflow hydrograph in these conditions. Temperature change is one of the most sensitive input characteristics to calculate snowmelt runoff in the high-altitude basin [14].

The primary snowfall-melting mechanism in SWAT was modified by adding snow accumulation, melting, areal snow coverage, and the ability to input snowfall and temperature as a proportion of elevation bands [8].

One of the more popular models is the SWAT, utilized in numerous nations worldwide [15, 16]. The physical foundation of the hydrological model SWAT is semi-distributed and continuous time. The SWAT model design and evolutionary methodology make it a good tool for examining how the management of rocky mountain forests affects the region's water supplies. However, the SWAT has not been explored much with rocky mountain river basins, which have significant elevation differences and are mainly covered with snowfall, technologies that have considered elevations to improve SWAT capacity to model snowmelt processes.

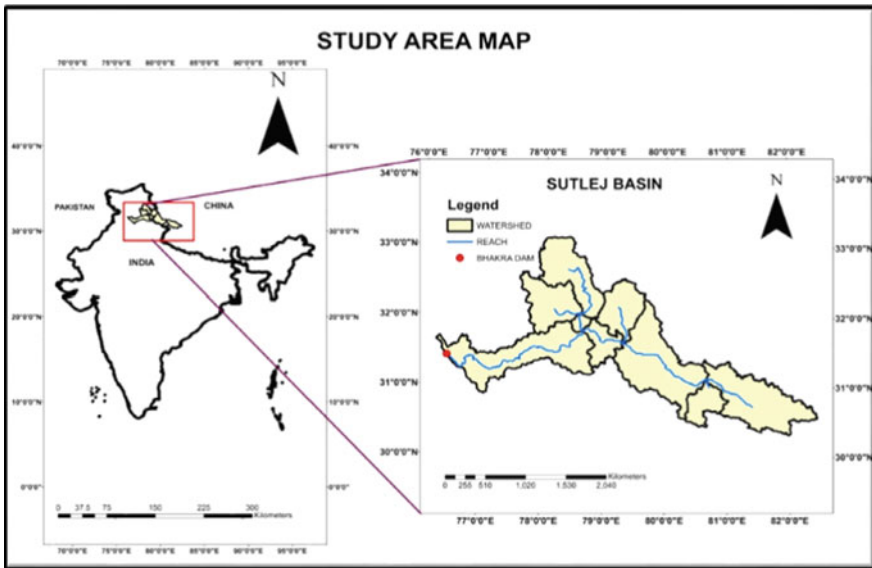


Fig. 1 Pictorial representation of the study area

2 Study Area

The present study is performed for the Sutlej River Basin, which receives its water from Manasorovar Lake, located on the southern flanks of Mount Kailash on the Tibetan Plateau at an altitude of more than 4500 m above sea level. Moreover, it covers several regions with varied topographic and climatic characteristics, including Punjab in northern India. In addition, runs through several regions of Pakistan [23, 24]. The area of the present study is 55,000 km². In addition, the Bhakra gauging station is considered an output gauging station to calibrate and validate the model (Fig. 1).

3 Methodology

3.1 Model Setup

This model was created to evaluate the effects on the water system in complex basins of long-term changes to the soil, Landover, and management practices. The flexible architecture of SWAT was created to employ easily accessible data to define a watershed's physical and climatic properties. In remote, ungagged basins where calibration is impossible, SWAT can estimate reasonable outcomes using physically-based

inputs. Because of the code's high computing efficiency makes continuous simulation over vast areas and lengthy timespan possible. The influence of management strategies can be assessed by simulating watershed processes over an extended period [10].

Digital Elevation Maps (DEM), land uses (LULC), soil maps, and details on meteorological data are the input data that the SWAT model requires. The watershed delineation was done using Shuttle radar topography mission (SRTM) data with a $30\text{ m} \times 30\text{ m}$ resolution. The Soil map taken from the FAO database with a $1 \times 1\text{ km}$ grid resolution and land use data from the NRSC/WRIS with a $1 \times 1\text{ km}$ grid resolution was used. The meteorological data such as Rainfall data, maximum and low-temperature data, relative humidity, and sunshine hours data over 35 years were collected from the CFSR database (1979–2013) with a warmup period of three years. The soil and water conservation service (SCS) curve number (CN) approach has been adapted to calculate stormwater runoff. For calculating evapotranspiration, the Penman–Monteith approach has been used in this model [17] (PET). The Muskingum routing technique approach determines channel routing [3]. Furthermore, the temperature index algorithm has been used to evaluate snowfall and snowmelt routine. The model has also been evaluated using two situations, one with elevation bands taken into account and the other without considering elevation bands in the model.

3.2 Sensitivity Analysis

In SUFI-2, the sequential and fitting approach based on the Bayesian framework is used to accomplish calibration and validation, respectively [18]. Observed data, model input, and model structure are just a few examples of the parameter uncertainty sources considered and described as uniform distributions in SUFI-2 [19]. Their *p-factor* and *r-factor* are indices used to evaluate the model's accuracy and uncertainty. The level of uncertainty is gauged using the *p-factor*, calculated via Latin hypercube sampling. The range of the *p-factor* is 0 to 100%, while the *r-factor* has an infinite range and should ideally be 1 and 0, respectively, whenever the model successfully reflects the observed data. An objective function is made, and the required termination rule is applied before doing an uncertainty analysis.

3.3 Objective Function

The present study KGE has been taken as the objective function to assess the degree to which actual and simulated streamflow was accurate. Since NSE uses the recorded mean as its baseline, it tends to overestimate model performance for solid seasonal parameters. To solve this problem between simulated and actual discharge, a new performance measure [20], KGE, based on the identical results of 3 significant

components those are bias ratio (α), linear correlation (γ), and variance (β).

$$KGE = 1 - \sqrt{(\gamma - 1) + (\alpha - 1) + (\beta - 1)^2} \quad (1)$$

where, $\alpha = \frac{\sigma_{sim}}{\sigma_{obs}}$, $\beta = \frac{X_{mean}^{sim}}{X_{mean}^{obs}}$

γ Is the coefficient of the linear regression between the simulated and observed value.

3.4 Performance Indicators

NSE: The normalized statistic difference between the residual variance and total variance of the observed and simulated data is how it is expressed [21]. Its values range from -1.0 , with 1 representing the model's optimal performance.

$$NS \text{ (Maximize)} = 1 - \frac{\sum_{i=1}^n (X_m - X_s)_i^2}{\sum_{i=1}^n (X_{m,i} - \bar{X}_s)^2} \quad (2)$$

where, X_m = observed discharge, X_s = simulated discharge.

R²: It is a statistic that expresses how closely calibrated data resembles the best-fit observed data. An improved model is indicated by a higher value ranging from 0 to 1 .

$$R^2 \text{ (Maximize)} = \frac{\text{Variance of the model}}{\text{Total variance}} = 1 - \frac{SS_{res}}{SS_{tot}} = \frac{S_{xy}^2}{S_{xy} * S_{yy}} \quad (3)$$

P-BIAS is the biased error percentage for both actual and simulated data. It is taken into account to be zero when choosing the most appropriate behavioral model. The performance of the model improves as the value decreases.

$$PBIAS \text{ (Minimize)} = \left[\frac{\sum_{i=1}^n (X_m - X_s)}{\sum_{i=1}^n X_m} * 100 \right] \quad (4)$$

where, X_m = observed discharge, X_s = simulated discharge.

4 Result and Discussion

The sensitivity analysis has been conducted using global sensitivity analysis, which explores the design space using a large set of samples. SWAT-CUP uses the values of *t-stat* and *p-value* to determine the relative importance of various parameters. High absolute values indicate greater sensitivity, whereas near zero indicates high significance levels. The most sensitive input parameters were identified using the global sensitivity technique has performed 1500 iterations using SUFI-2. Over 200 hydrological parameters are included in the SWAT model. However, not all of them are likely to impact the results significantly. It is required to determine the most sensitive input parameters to simulate the streamflow and the ranges within which they fall. 22 parameters were identified initially, and their initial ranges were chosen in this study. The streamflow simulations produced by the SUFI-2 were satisfactory, showing some uncertainty in the calibration and validation results. The ground-water and soil parameters GWQMN, SOL-K, and SOL-AWC are identified as the most sensitive parameters influencing model output results. Because the present study area lies in a snow-dominated mountainous region, moreover SWAT model has the limitation that the infiltration in frozen soil (snowpack and glacier) is neglected. In an actual situation, it does not exist. Table 1 shows the top 10 sensitive parameters with their sensitive ranking in *t-stat* and *p-value*.

The Himalayas mountain region of a river basin, i.e., the Sutlej river basin up to Bhakra, was modeled to determine how they would respond. Before applying elevation bands, the main problem was a persistent underestimation of both low and high flows during the calibration period.

Figure 2 shows that the simulated streamflows in the Sutlej river basin were still below observed streamflows. Furthermore, the correlation statistics were poor (KGE: 0.21 and NSE: 0.16). The underestimating issue was resolved using the elevation band approach [8]. An elevation band allows the model to consider their lapse rates according to elevation variance. The values of KGE and NSE for the calibration

Table 1 Sensitive ranking of SWAT parameters identified using SUFI-2

Parameters	Sensitivity rank	<i>t-stat</i>	<i>p-value</i>
R_GWQMN	1	-27.52	0.00
R-SOL-K	2	-26.51	0.00
R_SOL_AWC	3	-18.09	0.00
V-ALPHA_BF	4	-3.25	0.00
R_GW_REVAP	5	-2.88	0.00
R_CN ₂	6	-2.81	0.00
R_SUB_SMFMN	7	1.88	0.05
V_CH_K2	8	1.59	0.11
V_GW_DELAY	9	1.34	0.17
R_MSK_CO ₁	10	1.08	0.27

period after considering elevation bands are 0.91 and 0.81; moreover, validation values are between 0.87 and 0.75 and can be regarded as very good [22]. In addition, 82 and 71% of observed data lie within the uncertainty band. Figure 3 despite not accurately replicating the peaks and the recession limbs, the hydrograph shape could be replicated satisfactorily overall (Fig. 4). Figure 5 is a uniform distribution of points observed about the 1:1 line connecting the recorded and estimated monthly streamflow in the calibration and validation data scatter plot. Some data points were not in line but mostly lay on the line, which indicates the excellent correlation coefficient between observed and simulated streamflow. As a result, the SWAT model can be treated as a valuable tool for simulating the discharge hydrograph and many components of the water balance for a mountainous river basin (Fig. 6).

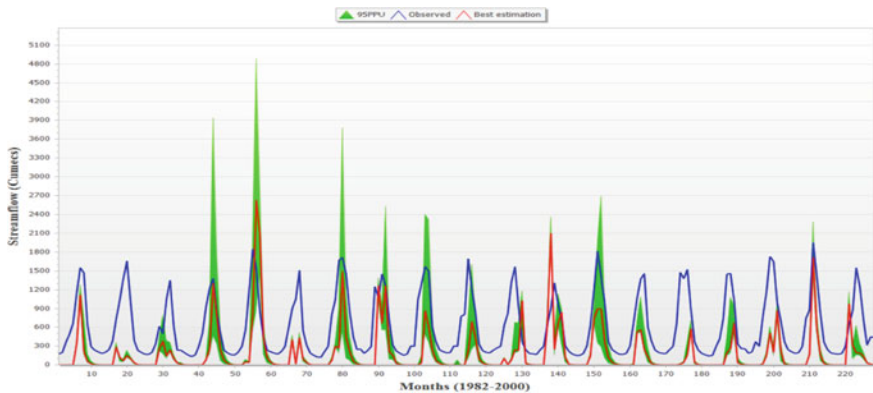


Fig. 2 95PPU plot of Sutelj river basin during calibration period (1982–2000) before implementing elevation bands with KGE as the objective function

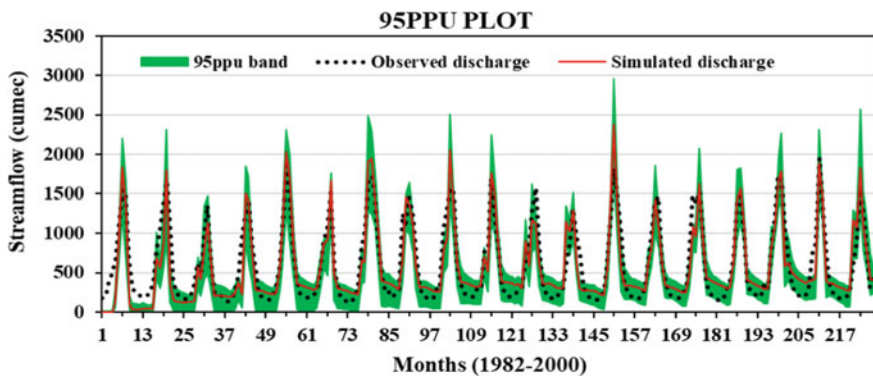


Fig. 3 95PPU plot of Sutelj river basin during calibration period after implementing elevation bands with KGE as the objective function

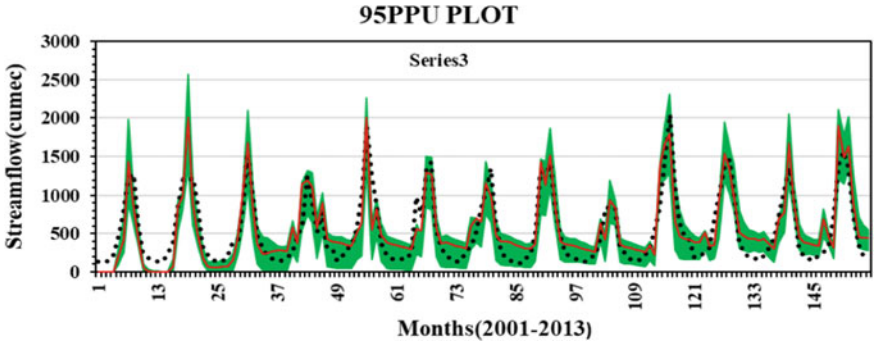


Fig. 4 95PPU plot of Sutlej river basin dung validation period after implementing elevation bands with KGE as the objective function

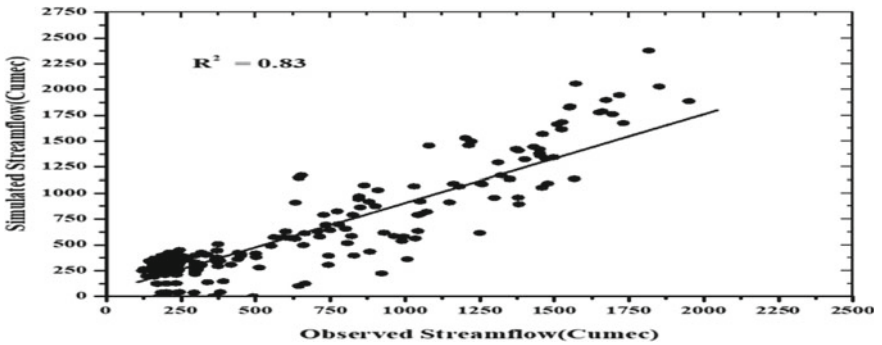


Fig. 5 Scatter plot between observed and simulated streamflow hydrographs during the calibration period after implementing elevation bands

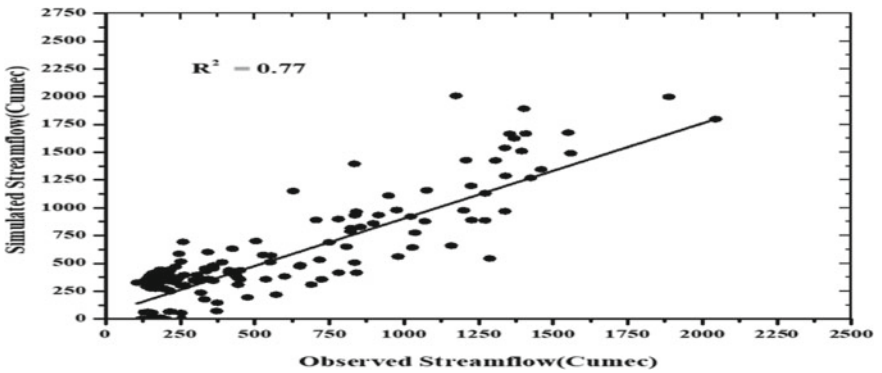


Fig. 6 Scatter plot between observed and simulated streamflow hydrographs during the validation period after implementing elevation bands

5 Summary and Conclusions

The semi-arid and mountainous watersheds in the Sutlej drainage basin, which are significantly influenced by snowmelt, are improved by the SUFI-2 technique employing KGE as the fitness function and combined with the SWAT model. Before implementing elevation bands to the model, the main problem was a persistent underestimating of low and high flows for the calibration period. Due to the SWAT model's failure to account for the impact of snow melt, the estimated streamflows in the Sutlej river basin were still below the observed streamflows. Additionally, the correlation statistics were poor. The systematic underestimating issue was resolved using the elevation band technique, and the outcomes were supported [8]. In NSE, the observed mean is utilized as a baseline and may lead to an overestimation of model performance for extremely seasonal variables. KGE was designed to address this issue. As a result, the KGE would be a better choice to employ as the objective function in a watershed where mountainous snowmelt predominates, such as the Sutlej watershed [25]. Despite producing good results, the present model does not adequately signify the infiltration and runoff processes related to snowmelt since it is predicted that infiltration does not occur in frozen soils. The model also performs poorly at times of base flow. By improving the components of the simulation that reflect groundwater discharge, snowmelt infiltration, and runoff in base flow, the performance of the model, as well as the actual representation of hydrologic processes in this and comparable mountain streams, has been greatly improved.

Further, a total of 35 years (1979 to 2013) of monthly streamflow data was collected from the Bhakra gauging station of the SRB and used for SWAT model calibration and validation. The results obtained with the elevation band use in the SWAT model proved better compared to the model without elevation band use. The model performance statistics, such as KGE, R^2 , *p-bias*, and *p-factor*, show 0.91, 0.83, 2.30, and 0.82, respectively, with the use of elevation band, and 0.21, 0.47, 0.85, and 0.01, respectively, for without the elevation band use in the model, signifies the SWAT model poorly performed without the use of elevation band or natural topography of the river basin. It confirms that the topography shows a significant effect on the streamflows of the mountainous river basins. Therefore, this work will undoubtedly help the researchers to make them aware of the limitations of the SWAT model use while applying it to the mountainous river basins.

References

1. Paul M, Impacts of land use and climate changes on hydrological processes in South Dakota Watersheds
2. Beven KJ, Warren ROSS, Zaoui JACQUES (1980) SHE: towards a methodology for physically-based distributed forecasting in hydrology. IAHS Publ 129:133–137
3. Arnold JG, Srinivasan R, Muttiah RS, Williams JR (1998) Large area hydrologic modeling and assessment part I: model development 1. JAWRA J Am Water Resour Assoc 34(1):73–89

4. Gascoïn S, Kinnard C, Ponce R, Lhermitte S, MacDonell S, Rabatel A (2011) Glacier contribution to streamflow in two headwaters of the Huasco River. *Dry Andes Chile Cryosphere* 5(4):1099–1113
5. Peltó MS (2015) Quantifying glacier runoff contribution to Nooksack River, WA in 2013–15. In: AGU fall meeting abstracts, vol. 2015. pp C33E-0862
6. Lian J, Gong H, Li X, Zhao W, Hu Z (2009) Design and development of flood/waterlogging disaster risk model based on Arcobjects. *J Geo-Inf Sci* 11:376–381
7. Hartman MD, Baron JS, Lammers RB, Cline DW, Band LE, Liston GE, Tague C (1999) Simulations of snow distribution and hydrology in a mountain basin. *Water Resour Res* 35(5):1587–1603
8. Fontaine TA, Cruickshank TS, Arnold JG, Hotchkiss RH (2002) Development of a snowfall–snowmelt routine for mountainous terrain for the soil water assessment tool (SWAT). *J Hydrol* 262(1–4):209–223
9. Abbaspour KC, Rouholahnejad E, Vaghefi S, Srinivasan R, Yang H, Kløve B (2015) A continental-scale hydrology and water quality model for Europe: Calibration and uncertainty of a high-resolution large-scale SWAT model. *J Hydrol* 524:733–752
10. Arnold JG, Fohrer N (2005) SWAT2000: current capabilities and research opportunities in applied watershed modelling. *Hydrol Process: Int J* 19(3):563–572
11. Tanasienko AA, Chumbaev AS (2008) Features of snowmelt runoff waters in the Cis-Salair region in an extremely snow-rich hydrological year. *Contemp Probl Ecol* 1(6):687–696
12. Neitsch SL, Arnold JG, Kiniry JR, Williams JR (2011) Soil and water assessment tool theoretical documentation version 2009. *Tex Water Resour Inst*
13. Hock R (2003) Temperature index melt modelling in mountain areas. *J Hydrol* 282(1–4):104–115
14. Tahir AA, Chevallier P, Arnaud Y, Neppel L, Ahmad B (2011) Modeling snowmelt-runoff under climate scenarios in the Hunza River basin, Karakoram Range, Northern Pakistan. *J Hydrol* 409(1–2):104–117
15. Gassman PW, Reyes MR, Arnold JG (2005) Review of peer-reviewed literature on the SWAT model. In: *Proceeding of the 3rd international SWAT Conference*. pp 13–15
16. Gassman PW, Reyes MR, Green CH, Arnold JG (2007) The soil and water assessment tool: historical development, applications, and future research directions. *Trans ASABE* 50(4):1211–1250
17. Monteith JL (1965) Evaporation and environment. In: *Symposia of the society for experimental biology*, vol 19. Cambridge University Press (CUP) Cambridge, pp 205–234
18. Khoi DN, Thom VT (2015) Parameter uncertainty analysis for simulating streamflow in a river catchment of Vietnam. *Glob Ecol Conserv* 4:538–548
19. Gupta HV, Kling H, Yilmaz KK (2009) Martinez GF decomposition of the mean squared error and NSE performance criteria: Implications for improving hydrological modelling. *J Hydrol* 377:80–91
20. Nash JE (1970) Sutcliffe JV river flow forecasting through conceptual models part I-A discussion of principles. *J Hydrol* 10:282–290
21. Moriasi DN, Arnold JG, Van Liew MW, Bingner RL, Harmel RD, Veith TL (2007) Model evaluation guidelines for systematic quantification of accuracy in watershed simulations. *Trans ASABE* 50(3):885–900
22. Singh P, Jain SK (2002) Snow and glacier melt in the Satluj River at Bhakra Dam in the western Himalayan region. *Hydrol Sci J* 47(1):93–106
23. Singh P, Jain SK (2003) Modelling of streamflow and its components for a large Himalayan basin with predominant snowmelt yields. *Hydrol Sci J* 48(2):257–276
24. Paul M, Negahban-Azar M (2018) Sensitivity and uncertainty analysis for streamflow prediction using multiple optimization algorithms and objective functions: San Joaquin Watershed, California Model. *Earth Syst Environ* 4:1509–1525

Slope Stability Analysis of Langdeibung Area Along Imphal-Jiribam National Highway (NH-37) Using Geoslope



Koko Karbia, Kakchingtabam Anil Sharma, Kosygin Leishangthem, Pukhrambam Jalajit Singh, Khwairakpam Selija, and Devasis Laishram

1 Introduction

Slope stability analysis is done to evaluate the equilibrium conditions and the safe design of a natural or man-made slope [1]. The slope of an inclined surface measures its resistance to failure by sliding or collapsing. Loss of lives and property may result from slope failure. Therefore, it is crucial to verify the stability of the suggested slopes. A safe and effective slope design is now achievable because of advancements in stability analysis and contemporary soil testing techniques. The various techniques for evaluating the stability of slopes and their limits should be thoroughly understood by the geotechnical engineer. The main objectives of slope stability analysis are finding weak spots, examining potential failure mechanisms, determining how sensitive a slope is to different triggers, building the finest slopes in terms of safety, dependability, and cost, and creating potential corrective procedures are the key goals of slope stability analysis [2]. Here the study is done on the finite slope analysis. The following are some common techniques for analysing finite slopes:

1. Morgenstern-Price method 2. Spencer Method 3. Bishop Method 4. Janbu Method 5. Ordinary Slices Method 6. Sarma Method.

The study area is done for a hill slope located at Langdeibung of Senapati District, Manipur, India. A portion of the slope in this location has developed a crown, which is a warning indication of a potential landslide. This is because of the slope's angle, the soil's characteristics, and the lack of vegetation in that particular area. Geoslope software is used to do slope stability analyses using Morgenstern Price's limit equilibrium method. Modern limit equilibrium tools like GeoSlope help manage complexity

K. Karbia (✉) · K. A. Sharma · K. Leishangthem (✉) · P. J. Singh · K. Selija · D. Laishram
Department of Civil Engineering, Manipur Technical University, Imphal 795001, India
e-mail: kokokarbia123@gmail.com

K. Leishangthem
e-mail: kosygin_1@mtu.ac.in

in analyses. Today, it is possible to handle complex stratigraphy, pore-water pressure conditions that are wildly inconsistent, a variety of linear and nonlinear shear strength models, virtually any slip surface shape, concentrated stresses, and structural reinforcement. In addition, limit equilibrium formulations based on the method of slices are increasingly being used to analyse the stability of structures such as tie-back walls, slopes reinforced with nails or fabric, and even the sliding stability of structures subjected to significant horizontal loading, such as that caused by ice flows. We aim to investigate the slope stability analysis using Morgenstern Price's method with the help of Geoslope software to find out the critical factor of safety.

1.1 Study Area

The study area is located along NH-39 in Langdeibung, Senapati district, Manipur. Rocky, steep terrain characterises the entire area. The hill ranges generally follow an NNE-SSW pattern, though this can occasionally switch to N-S or NE-SW. The main features in the area are hill ranges and river valleys. A large portion of the land is covered by structural and denudational hills that are aligned parallel to sub-parallel. The region experiences a mild, humid subtropical monsoon climate, with annual rainfall ranging from 671 to 1454 mm and temperatures ranging from 3 to 34 °C.

1.2 Geological Setting

A sequence of the Disang and Barail group of rocks and Quarternary alluvium make up the research region, which is situated in the northernmost section of the arcuate Arakan Yoma-Chin highlands. Disangs are tectonically deformed, dark grey, splintery shales intercalated with siltstones and fine-grained sandstones. Barails underlying Disangs are made up of huge to thick, strongly jointed sandstone strata that are frequently interbedded with shales. Individual sandstone strata range in thickness from 60 cm to more than a metre, whereas shale beds are between 1 and 2.5 cm thick [3]. The frequency and quantity of the arenaceous material are noticeably increasing in the direction of the north. A series of alluvium that is representative of quaternary deposits are characterised by the predominance of silty and clayey material and, occasionally, sandy to pebbly in texture. In Table 1, each unit's litho-character and simplified stratigraphic succession are shown.

Table 1 Stratigraphic succession of the study area [4]

Litho unit	Age	Description
Alluvium	Quaternary-holocene to pleistocene	Clay, silt, sand, pebble and boulder deposits
<i>Unconformity</i>		
Barails	Oligocene to upper eocene	Massive to thickly bedded sandstone. Alternations of shale and sandstone. Flyash sediments of turbidite character
<i>Gradational contact</i>		
Disangs	Eocene to upper cretaceous	Dark grey to black, splintery and earthy coloured shales, siltstones and sandstones showing occasionally rythmite characters
<i>Unconformity</i>		
Basement complex: Unseen		

2 Methodology

The methodology followed for the analysis of the stability of slope is:

- a. Marking the project site (Langdeibung) using polygon tool from Google Earth Pro.
- b. To extract DEM data for the project site from Global Mapper using the mark area of the site from Google Earth Pro.
- c. To generate elevation profile graph in QGIS using extracted DEM data from Global Mapper.
- d. Transferring the elevation profile data to GeoStudio.5. Creation of the elevation slope of the project site in GeoStudio.
- e. Analysis of Factor of Safety in GeoStudio.

The project is classified into two parts, the first part falls under the extraction of DEM format from Global Mapper using the marked area of Google Earth's polygon tool along with the preparation of data from the DEM in QGIS and the second part is the analysis of slope stability from the data prepared in QGIS using GeoStudio. The use of Google Earth and Global Mapper is to ease the extraction of elevation data for the project.

Google Earth is primarily used to mark the project location since it is simpler to mark the specific area as shown in Fig. 2. Transferring the KMZ file for the marked area to Global Mapper. The necessary DEM file for Global Mapper can be simply extracted using the online sources tool. The indicated area's KMZ file from Google Earth can be utilised as a reference layer.

Two types of DEM data are available worldwide in Global Mapper:

1. SRTM Worldwide Elevation Data (1-arc-second Resolution, SRTM Plus V3)
2. ASTER GDEM v2 Worldwide Elevation Data (1 arc-second Resolution)

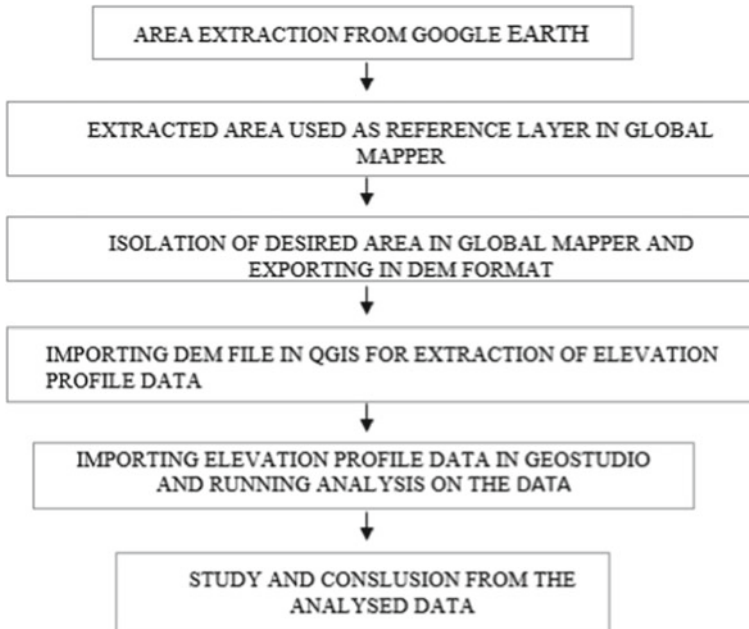


Fig. 1 Flow chart for the project

In Global Mapper, the SRTM Worldwide Elevation Data is used as a map model for elevation as shown in Fig. 3. Using the KMZ file as reference layer, the SRTM data for the project site can be extracted. The SRTM data available worldwide in Global Mapper is 1-arc-second resolution, which means that the size of the pixel in making the elevation data is 30 m. It is to be noted that the smaller the resolution (say 5, 10 m), the more accurate the data and vice versa. The flowchart for the project is shown in Fig. 1 (Fig. 2).

3 Results

The DEM data of the chosen layer from Global Mapper, displayed in Fig. 3, is imported into QGIS, where a 10 m contour is created as indicated by the blue line in Fig. 4. Drawing a profile elevation in the west-to-east direction produces elevation profile data in the form of elevation-distance in an excel spreadsheet. To determine the factor of safety, the data is sent to GeoStudio for a slope stability analysis.

Geostudio is used to import the elevation profile data exported from QGIS for additional analysis. A piece of software called Geostudio is used to examine the stability of various 1D, 2D, and 3D geometries and structures. In order to handle complex analyses of slope stability, pore-water pressure, earthquake, wind load and



Fig. 2 Marked area for the project site

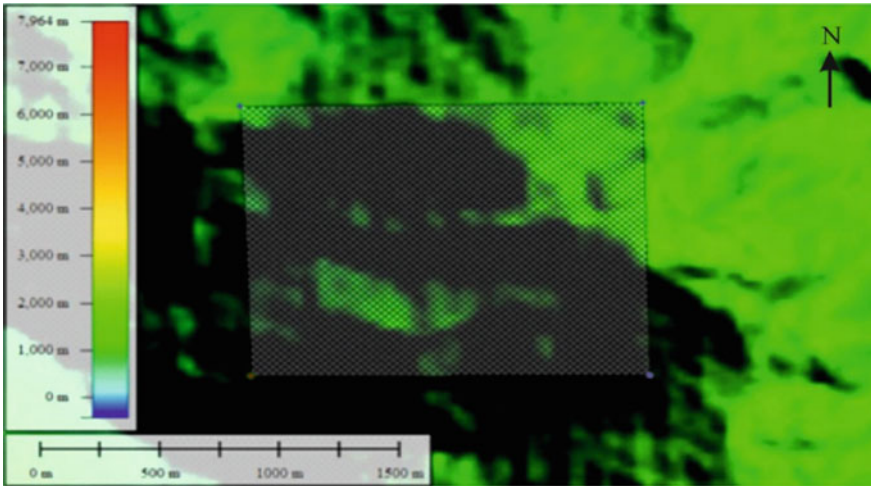


Fig. 3 Marked area of the project site along with elevation data

direction, etc., Geostudio is a limit equilibrium software. The objective of the slope stability analysis is to determine whether the area is stable or not. This is done by finding out the FOS for the area. The stability analysis for these finite slopes includes methods such as the Morgenstern-Price method, Bishop method, Spencer method, Janbu method, Ordinary Slices method, and Sarma method where the Morgenstern-Price method is used as a method of analysis for this project. A portion of the elevation profile data extracted from QGIS is shown in Fig. 4.

The line created to generate the data as illustrated in Table 2 is used to determine the distance and elevation for the elevation profile data. For ease of analysis, the

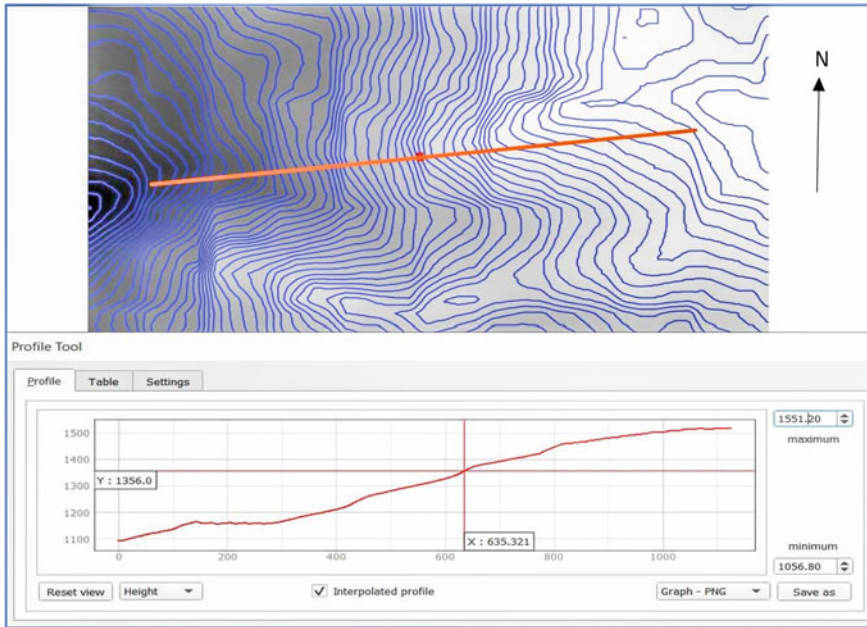


Fig. 4 Extraction of elevation profile graph in QGIS

elevation from mean sea level is ignored and the lowest elevation for the data is equalised from 0. The profile section generated from GeoStudio w.r.t. the distance and elevation data, is shown in Fig. 5.

The shape and size of the hill from Fig. 5 is obtained by plotting the actual value of the data and not a scaled down value.

As the hill's elevation changes from highest to lowest in a left-to-right direction in Fig. 6, the slip surface for the analysis is taken from left to right. A slip surface is one where there is a chance that the ground or other debris will fail. The number of important slip surfaces is assumed as one, and the entry and exit type slip surface is chosen. Where the factor of safety is lowest is where the crucial slip surface will appear.

The soil found in the area consists of shale, sandstone, alluvial, etc. Specific gravity of the area is around 2.36, and the natural water content of the area is 9.08%. The unit weight of the soil is 23.6 kN/m^3 with 7 kN/m^3 (kPa) as the cohesive stress and the angle of internal friction (ϕ) as 29° . The bed rock begins around 2 m below the topsoil. Figure 7 displays the topsoil and bedrock materials along with their corresponding colours. Since the thickness of the topsoil is so much thinner than the thickness of the bedrock, it will be difficult to see the colour of the topsoil in a cross section of the hill slope.

The slope after analysis is shown in Fig. 8, with the most important portion of the slope highlighted in red and coloured green. The slope's critical factor of safety is discovered to be 1.026, which is just a little bit above the permissible level.

Table 2 Data showing distance and its corresponding elevation (altogether there are 126 points taken)

Distance (m)	0	8	15	23	32	44	57	66	75	84	95	105	116	129	144	159	175	189	205	219	227	235	241
Elevation (m)	451	451	449	449	447	445	444	443	441	439	438	437	435	433	433	431	429	427	425	425	423	421	420

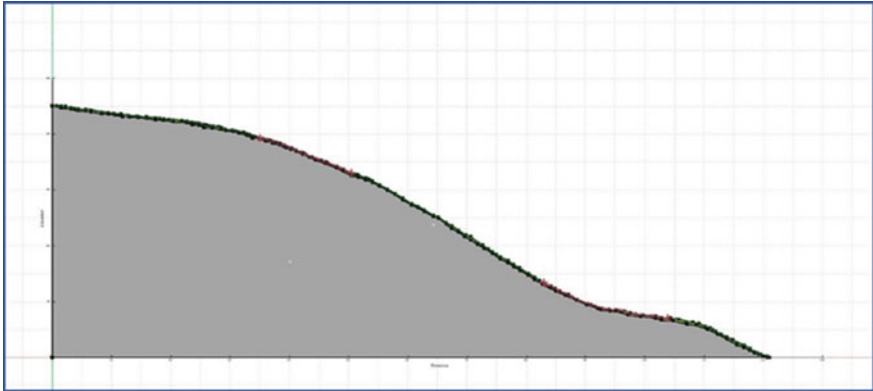


Fig. 5 Generated slope from the elevation profile data in GeoStudio

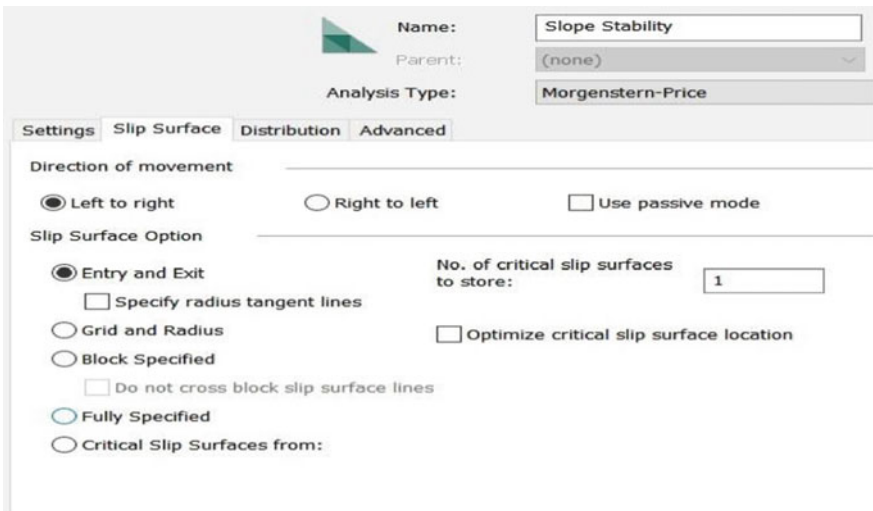


Fig. 6 Image showing analysis type along with options for slip surface

The comparison between the data from the elevation profile graph, where the area of the crucial factor of safety is surrounded by a black colour eclipse, and the Google Earth image, where the critical factor of safety is located, is shown in Fig. 9. Through it, the NH-53 passes. The area looks to be developing a crown, which is a warning sign for a potential landslide, according to the Google Earth image. Additionally, the soil doesn't appear to have any vegetation to hold it down.

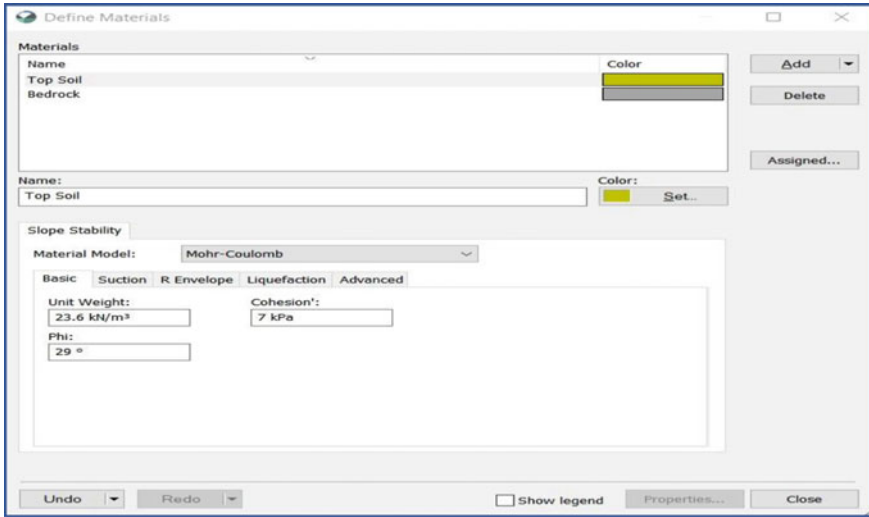


Fig. 7 Image showing defining of materials for the hill slope

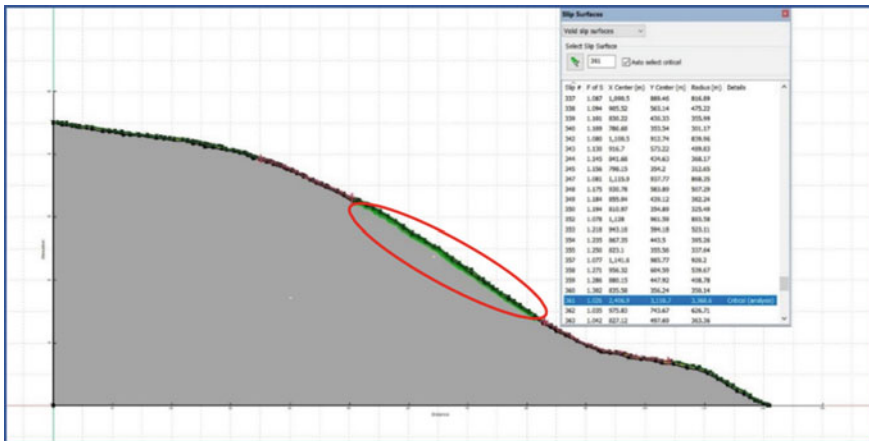


Fig. 8 Image showing the location of the area for the critical factor of safety

As per the analysis, the critical factor of safety is found to be 1.026. This value is above the most critical factor of safety which is 1. The area will be stable as long as there is no external disturbance such as excessive rainfall, earthquake, vibration from heavy loaded vehicles etc.

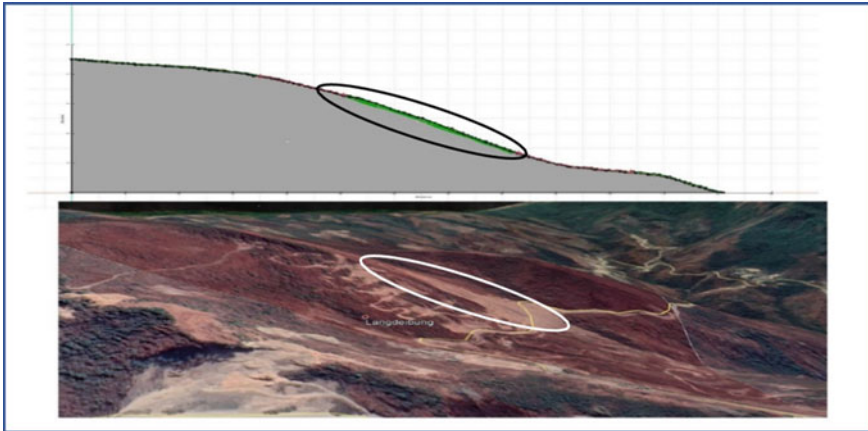


Fig. 9 Image showing comparison between hill slope in GeoStudio and image from Google Earth

4 Conclusion

The analysis for factors of safety and data extraction was carried out as a part of our project. The study for this project helps us in better understanding the knowledge about landslide and also in the field of remote sensing. The accuracy of DEM and profile elevation data can be improved if the high-quality DEM data is available to the public or the data is purchased from the government or performing drone surveying at the site. This study helps us to understand the difficulties faced when acquiring data through the process of remote sensing.

The stability of a slope can be increased by the following methods:

1. Slope flattening
2. By constructing proper drainage
3. Densification by vibrofloatation or terra probe
4. Grouting and injection of cement concrete mixture
5. Constructing sheet piles and retaining walls.

References

1. Digvijay PS, Guruprasad C, Rupa NB, Pooja RK (2017) An overview on methods for slope stability analysis. *Int J Eng Res Technol (IJERT)* 6:528–535. ISSN: 2278-0181
2. Talha N, Dahale PP, Mehta AA, Hiwase PD (2020) Slope stability analysis by geoslope 10(1):71–75
3. Devi D, Kushwaha RAS (2011) Landslide hazard zonation along NH-39 from Kangpokpi to Mao, Manipur, India. *Int J Econ Environ Geol* 2(1):30–35
4. Soibam I (1998) Structural and tectonic analysis of manipur with special reference to evolution of the imphal valley. PhD thesis, Manipur University (Unpublished)

Numerical Investigation of Circular and Square Hollow Steel Section Subjected to Torsion



Thounaojam Bidyaraj Singh, Khwairakpam Sachidananda, and Konjengbam Darunkumar Singh

1 Introduction

Carbon steel started to have an impact on the construction industry in the late nineteenth century when it became a widely used building material. Architects and engineers prefer hollow steel members in construction over open sections due to their high torsional rigidity, low drag coefficient, aesthetic appeal, interior space, etc. [1]. Closed hollow steel sections such as square, rectangle, circular etc. are fundamentally better than open sections at resisting torsional loads [2]. Ridley Ellis [3], Devi et al. [4] and Han et al. [5] conducted studies on rectangular, square hollow steel sections subjected to torsional load. Han et al. [5], Beck and Kiyomiya [6] carried out investigation on circular hollow steel section with pure torsion. As per the author's knowledge, a comparative study between circular and square steel hollow sections still has not been carried out. The aim of the study is to investigate the comparison between torsional behavior of circular and square steel hollow members based on the sections having the same perimeter, thickness and length. The finite element software ABAQUS [7] has been used for the study regarding numerical analysis of the hollow members subjected to torsion. The impact of varying thickness on the ultimate torsional load resisting capacity and the rotation angle at the failure of the sections were investigated using FEA modeling.

T. B. Singh (✉) · K. Sachidananda
Department of Civil Engineering, National Institute of Technology Manipur, Imphal, India
e-mail: bidyaraj@nitmanipur.ac.in

K. D. Singh
Department of Civil Engineering, Indian Institute of Technology Guwahati, Guwahati, India

2 Finite Element Modeling Procedure

2.1 General

Numerical parametric investigation on circular and square hollow steel members has been performed using finite element software ABAQUS [7] by keeping the perimeter (P) and length (L) of the members constant and varying the thickness (t). The members are subjected to torsion. A reliable experimental result from literature [3] has been used to validate the finite element models. Once the model gets validated, parametric investigation is carried out with the use of material properties of steel from literature [3]. The following sections present the details of the FE study.

2.2 Geometry and Boundary Condition

For the purpose of validating both square and circular hollow section members, FE models were generated using the cross sectional dimension of square member from those presented by Ridley-Ellis [3]. Typical cross sections are as shown in Fig. 1. In order to apply boundary conditions, the endpoints of the finite element models have been coupled to two reference points by utilizing the “kinematic coupling” feature of ABAQUS [7]. The member was kept fixed at one end (denoted as RP-1) while the other end was solely restrained against translation and rotation along lateral axes (RP-2). Using the displacement control approach, twisting force was applied at the centroid of the model through RP-2 at a constant rate of 9.68×10^{-4} rad/sec. Similar boundary conditions are frequently used in the literature under torsional investigation [8, 9].

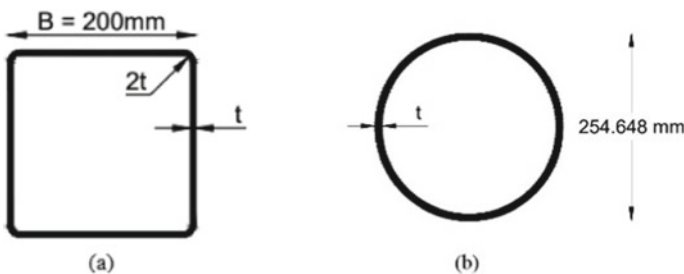


Fig. 1 Typical cross section of **a** Square member **b** Circular member

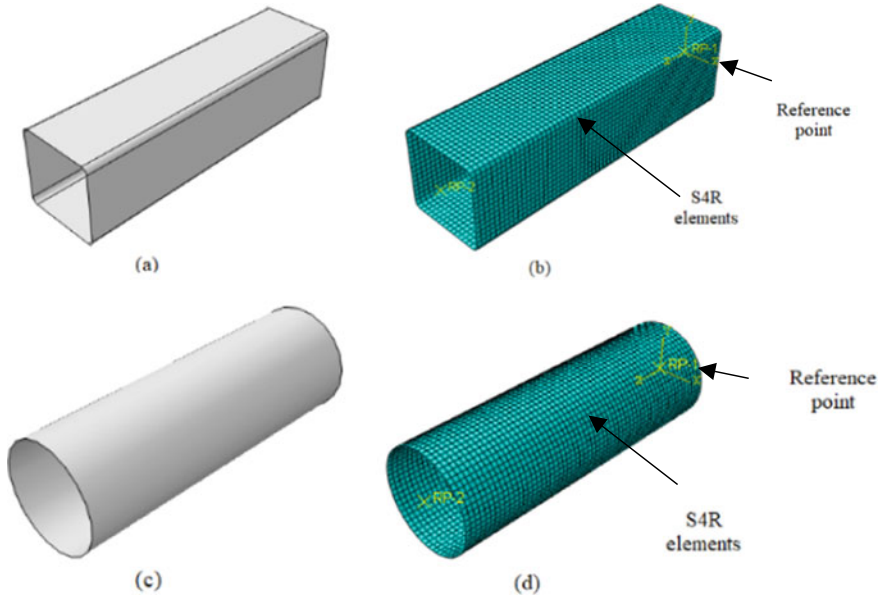


Fig. 2 Typical Finite element **a** SHS geometry, **b** SHS Finite element mesh, **c** CHS geometry, **d** CHS Finite element mesh

2.3 Finite Element Mesh

The models have been discretized using the shell element S4R [7] with reduced integration which is four noded. Each node has six degrees of freedom (3 rotations and 3 translations). It is generally reported in the literature that the S4R element can analyze both thin and thick hollow steel sections with a variety of cross sections, including square [10, 11], elliptical [12, 13] etc. As per the outcomes of the mesh convergence, the models utilized mesh sizes within the range ~12–15 mm, generating a total number of S4R elements in the range ~3000–4500 (Fig. 2).

2.4 Material Property

The FE models used the properties of steel reported in Ridley-Ellis [3]. The resulting stress strain values were transformed into true stress (σ_{true}) and true plastic strain (ϵ_{true}^{pl}) for use in Abaqus [7] using Eqs. (1) and (2).

$$\sigma_{true} = \sigma_{eng}(1 + \epsilon_{eng}) \tag{1}$$

$$\epsilon_{true}^{pl} = \ln(1 + \epsilon_{eng}) - (\sigma_{true}/E_0) \tag{2}$$

where σ_{engg} = engineering stress, ϵ_{engg} = engineering strain, E_0 = Initial young's modulus.

2.5 Geometric Imperfection, Analysis and Validation

In the beginning, eigen value buckling study was performed to derive buckling mode shapes which were utilized to incorporate geometric imperfections in the finite element models. *STEP Static, general solver which is available in ABAQUS [7] has been utilized to carry out nonlinear analysis. Using varied values of local geometric imperfection, notably $t/10$, $t/50$, and $t/100$, it was checked how the torsional performance of the finite element models was affected by the geometric imperfection. As per the analysis, $t/100$ has been chosen for validation of the numerical models since the varied imperfection amplitude values did not significantly affect the overall response. The T - θ curve obtained from the numerical model is in close agreement with that of literature [3], as can be shown in Fig. 3. Given the close similarity between the FE and experimental result, the current numerical modeling approach may be used to precisely predict cold formed hollow steel sections under torsional loading. Thus the validated finite element modeling procedures have been used for additional parametric investigation.

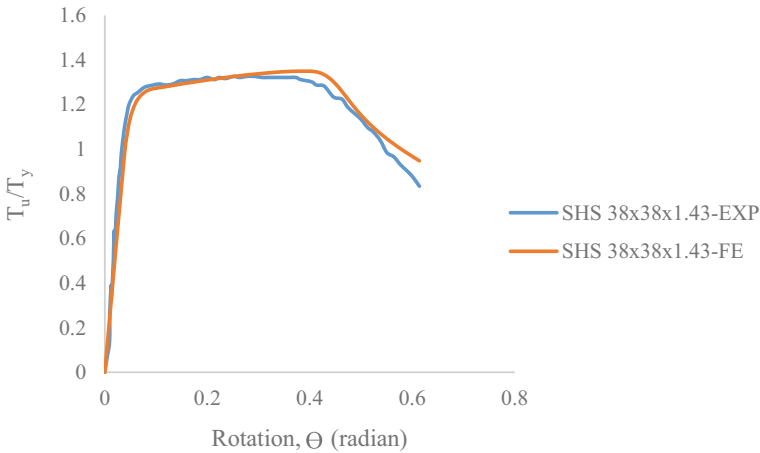


Fig. 3 Validation of finite element model with experimental result of Ridley Ellis [3]

3 Parametric Study

In order to study the comparison between square and circular hollow sections, members having same perimeter were considered. In accordance with IS 4923 [14], steel square section with width $B = 200$ mm and a diameter based external rounded corner equal to $2t$ were adopted (see Fig. 1). Circular hollow section with diameter = 254.648 mm were considered. All FE model member lengths (L) were kept constant at three times the diameter of the circular hollow section. Thickness of the models was altered within 2–13 mm in order to accommodate considerable variation in slenderness.

4 Results and Interpretation

To analyze the comparative behavior of circular and square hollow steel sections, slender and stocky sections of both members were taken into consideration. The cross sections were classified as per Eurocode 3 [15]. Based on the numerical analysis carried out, few results have been highlighted as can be seen in Figs. 4, 5 and 6. With reference to Fig. 4 it can be interpreted that the circular section is better at resisting the torsional force than the square section as it has higher torsional capacity and higher rotation angle at failure. From Figs. 5 and 6, it can be referred that with increase in thickness of the section, the corresponding torsional capacity and rotation angle at failure also increases gradually for both circular and square hollow steel members.

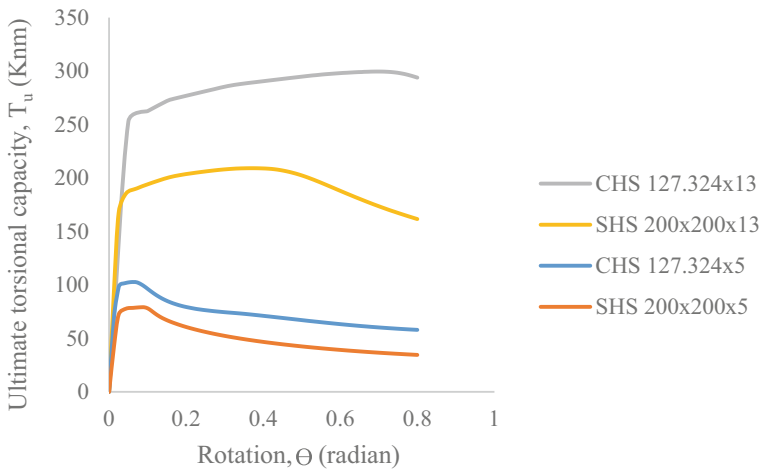


Fig. 4 $T_u-\theta$ response of circular and square hollow steel section under torsion

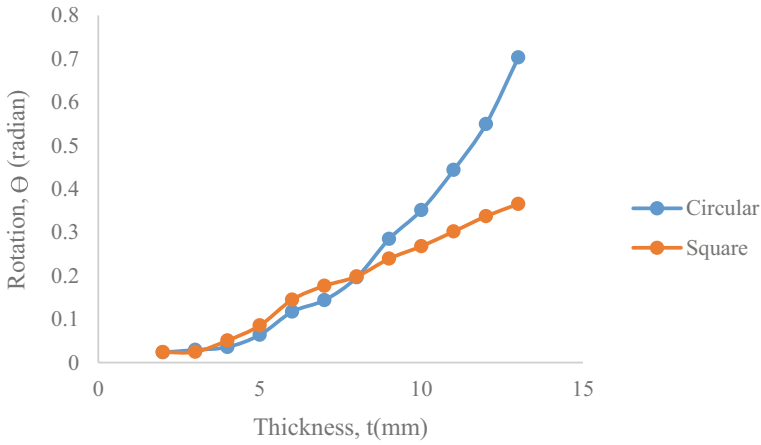


Fig. 5 θ -t response of circular and square hollow steel section under torsion

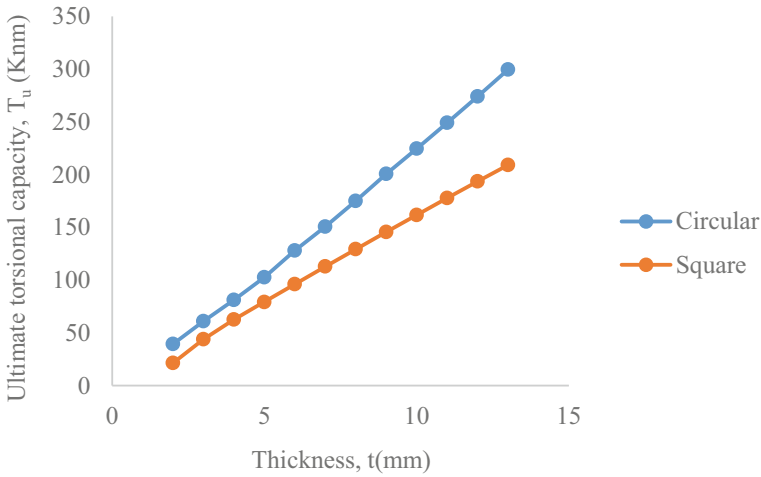


Fig. 6 T_u -t response of circular and square hollow steel section under torsion

5 Conclusion

A parametric study to analyze the ultimate torsional load resisting capacity of circular and square hollow members has been carried out by varying the thickness while keeping the perimeter and length of the members as constant by use of finite element analysis. According to the study, the following conclusions have been made:

- a. The circular hollow steel section has higher ultimate torsional resisting capacity as compared to square hollow steel section.

- b. With increase in thickness of the member, the stocky sections have higher resistance to torsion than that of slender section for both circular and square cross sections.
- c. As the thickness keeps on increasing from very slender to stocky section, the percentage increase in torsional resistance of circular to square section keeps on increasing.

References

1. Wardenier GJ, Packer J, Zhao JA, van der Vegte XL (2010) Hollow sections in structural applications
2. Ridley Ellis DJ, Owen JS, Davies G (2003) Torsional behaviour of rectangular hollow sections. *J Constr Steel Res* 59:641–663
3. Ridley Ellis D (2000) Rectangular hollow sections with circular web openings fundamental behaviour in torsion, bending and shear. PhD thesis University of Nottingham
4. Devi SV, Singh TG, Singh KD (2019) Cold-formed steel square hollow members with circular perforations subjected to torsion. *J Constr Steel Res* 162:105730
5. Han LH, Yao GH, Tao Z (2007) Performance of concrete filled thin walled steel tubes under pure torsion. *Thin Walled Struct* 45(1):24–36
6. Beck J, Kiyomiya O (2003) Fundamental pure torsional properties of concrete filled circular steel tubes. *Doboku Gakkai Ronbunshu* 60:285–296
7. Abaqus (2009) Abaqus/standard user's manual volumes I-III and ABAQUS CAE manual, version 6.9-EF1 dassault systems Corp, Providence, USA
8. Aisyah Mohd Zaifuddin S, Chen DH, Ushijima K (2017) Estimation of maximum torsional moment for multicorner tubes. *Thin-Walled Struct* 112:66–77
9. Shen K, Wan S, Mo YL, Song A, Li X (2018) Behavior of single-box multi-cell box-girders with corrugated steel webs under pure torsion. Part I: experimental and numerical studies. *Thin-Walled Struct* 129:542–557
10. Theofanous M, Gardner L (2009) Testing and numerical modelling of lean duplex stainless steel hollow section columns. *Eng Struct* 31:3047–3058
11. Patton ML, Singh KD (2012) Numerical modeling of lean duplex stainless steel hollow columns of square, L-, T-, and + - shaped sections under pure axial compression. *Thin-Walled Struct* 53:1–8
12. Silvestre N (2008) Buckling behaviour of elliptical cylindrical shells and tubes under compression. *Int J Solids Struct* 45:4427–4447
13. Silvestre N, Gardner L (2011) Elastic local post-buckling of elliptical tubes. *J Constr Steel Res* 67(3):281–292
14. IS 4923 (1997) Hollow steel sections for structural use—specification. Bureau of Indian Standards
15. EN 1993-1-5 (2005) Eurocode 3: design of steel structures—Part 1–5: plated structural elements. Eur Comm Stand Bruss

Carbon Pool Detection Through GIS Techniques and Satellite Data in a Semi Urban Region



Thiyam Tamphasana Devi and A. Abdulla Azaruden

1 Introduction

Carbon which is an important element required by all the living things on earth is stored in different places and in different forms. Thus, the amount of carbon stored in a system is known as “Carbon Stock” of Carbon Pool”. Carbon sequestration is a phenomenon for the storage of CO₂ or other forms of carbon to mitigate global warming. There are major carbon pools i.e., ocean, soil, atmosphere, and forests. In forest ecosystem carbon is stored as aboveground biomass (leaves, trunks, limbs), belowground biomass (roots), deadwood, litter (fallen leaves, stems), and soils. For mitigation of climate change and global warming, sustainable management of carbon pools is important [1–3]. Various human activities like afforestation and soil degradation constantly cause reductions in carbon stock and its sequestration. Thus, several researchers studied carbon stock and its sequestration through forest [4, 5] and soils [6, 7]. Ray et al. [8] did a study on estimation of carbon stock and sequestration at the mangrove forest of Sundarbans in the Bay of Bengal, India. They observed that carbon stock is lower in the tropical mangrove forest than in the terrestrial tropical forest and their annual increase exhibits faster turnover than the tropical forest. Feng et al. [9] studied soil carbon stock and its sequestration in China. They conclude that accumulation of soil carbon stock will not necessarily increase the amount of decomposition in warm climate; however, it will increase the productivity of crop land and its ecosystem functions. The integrated approach of GIS (Geographical Information System) techniques with satellite data is highly potential to generate reliable information on natural ground surface data i.e., land surface temperature, LULC (landcover/landuse), NDVI (normalized difference vegetation index). Using this generated information carbon stock [10] and its sequestration [11] can be calculated and is used for its sustainable management [12–14]. Bordoloi et al. [14] conducted a study to model

T. T. Devi (✉) · A. A. Azaruden
Department of Civil Engineering, National Institute of Technology, Manipur 795004, India
e-mail: thiyam85@gmail.com

the carbon stock and its sequestration using integrated approach of GIS techniques with satellite data in North Eastern part of India. They have shown that the use of different optical satellite derived vegetation index i.e., NDVI, SAVI (soil adjusted vegetation index), ARVI (atmospherically resistant vegetation index), and empirical modeling approach in the study is effective. In this present study, estimation of carbon stock and its sequestration is conducted in Imphal west district of Manipur state using integrated approach of GIS techniques with satellite data and open source tool InVEST model v3.5.0 (Integrated Valuation of Ecosystem Services and Trade-offs) for different types of LULC (landuse/landcover).

2 Study Area

The location of study area (Imphal West district) is provided in Fig. 1. The area of the district measured 558 Km² and it lies at a latitude of 24.30–25.00N and longitude of 93.45–94.15E. Imphal West has the highest population of 2,21,422 among the other district of the state Manipur. And most of the time, it enjoys the comfortable weather.

3 Data and Tools

The data used with its source of collection and extraction is provided in Table 1. Soil map prepared by National Bureau of Soil Survey & Land Use Planning (NBSS & LUP) on 1:500,000 scale was used for extraction of physical and chemical properties of soil viz. soil depth, soil texture, soil drainage, and soil erosion. Default carbon value is prepared by Intergovernmental panel for climate change based upon that holding capacity in different pools like Above ground biomass, Below ground biomass, Soil carbon, Dead wood, and Harvest wood products. LULC is generated from Landsat 5 TM and Landsat 8 OLI for the years 1996 and 2016 respectively by maximum likelihood supervised classification with the help of ArcGIS[®] software.

The elevation, slope and aspect map for the study area were generated from SRTM-DEM (shuttle radar topography mission—digital elevation model) (30 m resolution). Prediction of future LULC for the year 2026 was achieved through GeoSOS-FLUS (geographical simulation and optimization system—future land use simulation) which consists of two main parts as ANN-based (artificial neural networks) probability-of occurrence estimation module; and self-adaptive inertia and competition mechanism CA (cellular automata) module. In this study, ANN-based probability of occurrence estimation module was adopted. The input parameter used is aspect, elevation, slope, euclidian distance to Road, euclidian distance to settlement, and existing LULC (historical) map. Aspect and Slope for the district are obtained from DEM imagery which is taken from SRTM satellite. GeoSOS- FLUS software consists of two main parts. By using LULC and the default carbon value map carbon stock and carbon sequestration map were obtained.

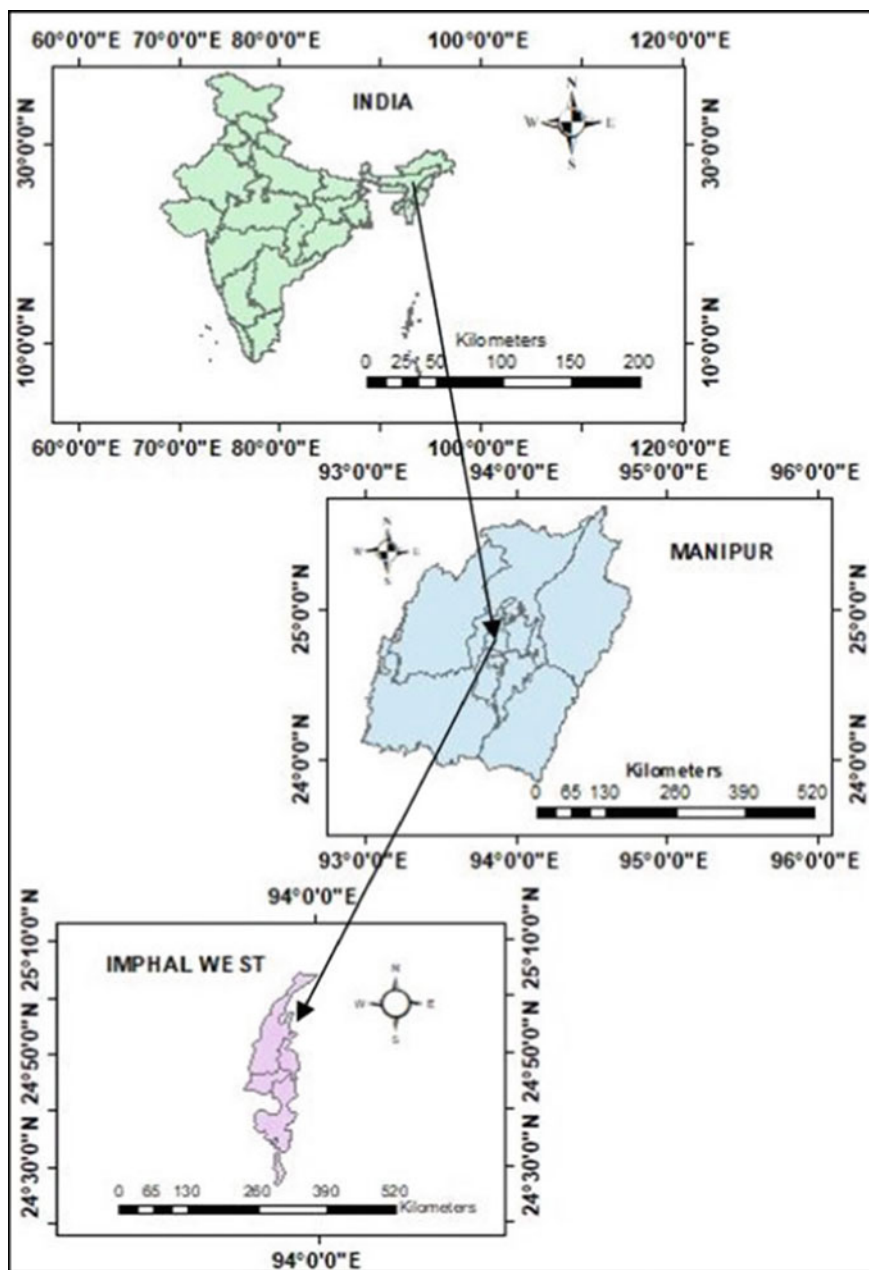


Fig. 1 Study area

Table 1 Data used in the study

Sl. no.	Data	Source	Generated data type
1	Soil map	NBSSLUP, Nagpur	Soil type
2	Landsat 8 OLI (Dated 17/01/2016), Landsat 5 TM (Dated 11/02/1996)	USGS	Land surface temperature and LULC
3	STRM-DEM (30 m resolution)	USGS	Slope and Aspect
4	Geological map	Geological Survey of India (GSI)	
5	Default carbon value	Intergovernmental panel for climate change (IPCC)	Default carbon value for different LULC

4 Equations

4.1 Land Surface Temperature

It is calculated as:

$$\text{Land surface temperature} = \frac{\text{Brightness temperature}}{\left[1 + \left(\frac{0.00115 \times \text{Brightness temperature}}{0.4388}\right) \times \ln(\text{land surface temperature})\right]} \quad (1)$$

$$\text{Brightness temperature} = \frac{Y_2}{\ln\left[\left(\frac{Y_1}{\text{TOA}}\right) + 1\right]} - 273.15 \quad (2)$$

where, Y_1 & Y_2 are the thermal conversion constant and TOA is the Top of Atmospheric spectral radiance and is calculated as:

$$\text{TOA} = X_L \times P_{\text{cal}} + R_L \quad (3)$$

where, X_L is the band-specific multiplicative rescaling factor, P_{cal} corresponds to band 10, R_L is the band-specific additive rescaling factor.

Then, land surface emissivity is calculated as:

$$\text{Land surface emissivity} = 0.004 \times \text{Proportion to vegetation} + 0.986 \quad (4)$$

Proportion of vegetation is calculated as:

$$\text{Proportion of vegetation} = \left(\frac{\text{NDVI} - \text{NDVI}_s}{\text{NDVI}_v - \text{NDVI}_s}\right)^2 \quad (5)$$

$$\text{NDVI is given as: } \text{NDVI} = \frac{(\text{NIR} - \text{RED})}{(\text{NIR} + \text{RED})}. \quad (6)$$

4.2 Accuracy Assessment for LULC

Accuracy of the classified feature is measured by the overall accuracy (OA) and Kappa coefficient (K) and is calculated as:

$$\text{OA} = \left(\frac{\text{Summation of all Total number Correctly Classified Samples}}{\text{Total Numbers of Samples}} \right) \times 100\% \quad (7)$$

$$\text{K} = \frac{(\text{Observed Accuracy} - \text{Chance Agreement})}{(1 - \text{Chance Agreement})} \quad (8)$$

If $\text{K} < 0.4$ poor, $0.4 < \text{K} < 0.75$ good, $\text{K} > 0.75$ excellent.

4.3 Carbon Stock and Sequestration Model

The default values of carbon values (Intergovernmental panel for climate change, IPPC) for different carbon pools are provided in Table 2 for different LULC types.

The carbon stock $\text{CS}_{x(i,j)}$ in a grid cell (i, j) is estimated as:

$$\text{CS}_{x(i,j)} = A \left[\begin{array}{l} (\text{CS_above})\text{CS}_{x(i,j)} + (\text{CS_below})\text{CS}_{x(i,j)} \\ + (\text{CS_soil})\text{CS}_{x(i,j)} + (\text{CS_dead})\text{CS}_{x(i,j)} \end{array} \right] \quad (9)$$

where, A is the area of the cell; C_above, C_below, C_soil, and C_dead are the above ground carbon, below ground carbon density, soil organic carbon density, and dead organic matter carbon stock. Total carbon stock (CS) and its sequestration (SS) are

Table 2 Default carbon value (IPPC)

Classes	C_above (Mg/ha)	C_below (Mg/ha)	C_soil (Mg/ha)	C_dead (Mg/ha)
Dense forest	140	70	35	12
Sparse forest	65	40	25	6
Crop land	23	35	30	5
Scrub/grass	30	30	30	13
Built-up	4	5	15	1
Water bodies	0	0	0	0

then estimated as:

$$CS = \sum_{x=1}^n CS_{x(i,j)} \tag{10}$$

$$SS = CS^{p_2} - CS^{p_1} \tag{11}$$

where, C^{p_2} and C^{p_1} are the carbon stocks of p_2 and p_1 year respectively.

5 Results and Discussion

5.1 NDVI

It is noted (Fig. 2) that in the year 1996 to year 2016, there is a change in vegetation which shows a decrease in the vegetation cover during the last decade and its responses to climatic parameters. In the year 1996, the vegetation dynamics ranges from -0.1561 to 0.6521 and the density is decreasing in the year 2016 ranging from -0.3636 to 0.6418 . It shows due to climatic parameter change vegetation dynamics also respond.

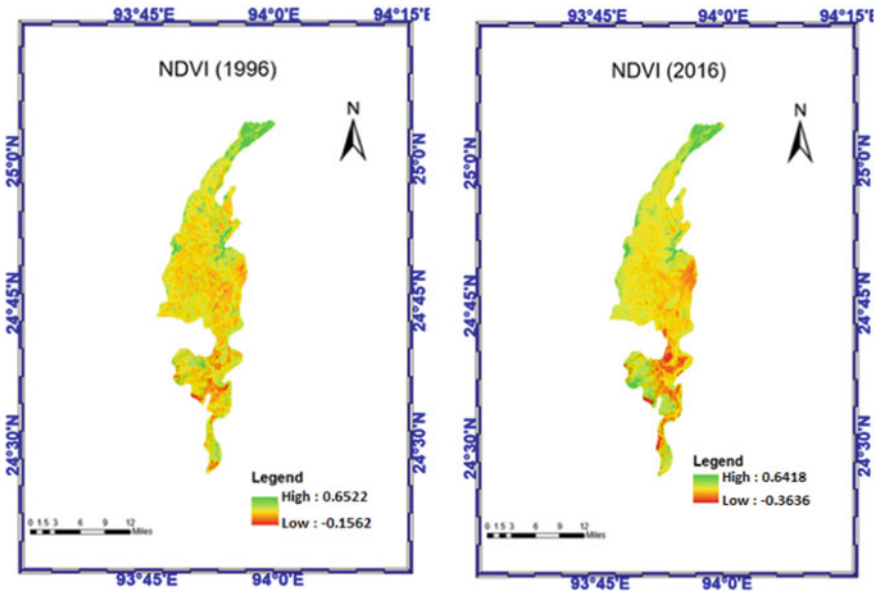


Fig. 2 NDVI of Imphal west district in year 1996 (left) and 2016 (right)

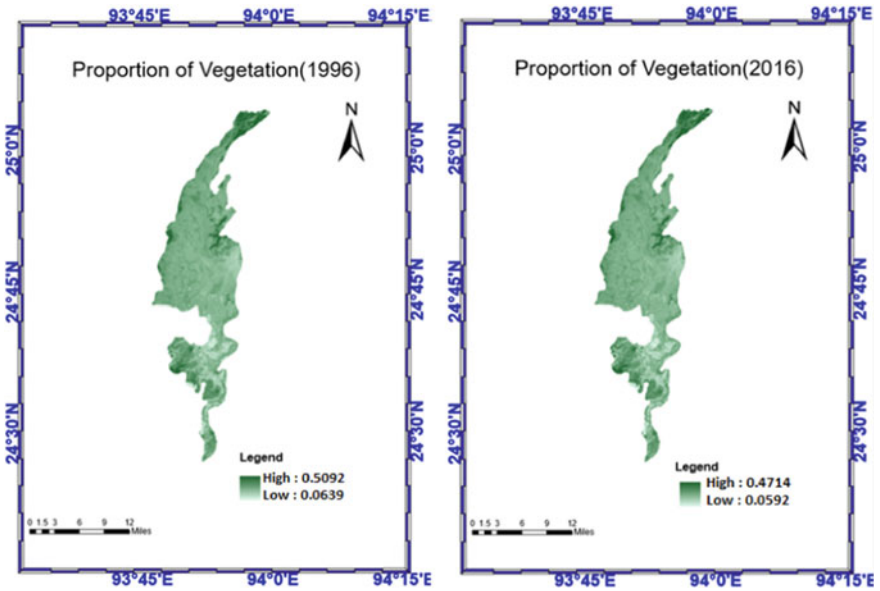


Fig. 3 Proportion of vegetation in the years 1996 (left) and 2016 (right)

5.2 Proportion of Vegetation

In the year 1996 to year 2016 there is a change in vegetation and it decreases in the vegetation cover during the last decade and its responses to climatic parameters (Fig. 3). In the year 1996 the proportion of vegetation ranges from 0.0639 to 0.5091 and the proportion is decreasing in the year 2016 ranging from 0.05919 to 0.4714. This will affect surface emissivity. This enormous variation will affect the carbon holding capacity of the vegetation and it lead the chance to global warming and climate change.

5.3 Land Surface Emissivity

Figure 4 shows the difference in emissivity during the year 1996 (Fig. 4 left) and year 2016 (Fig. 4 right).

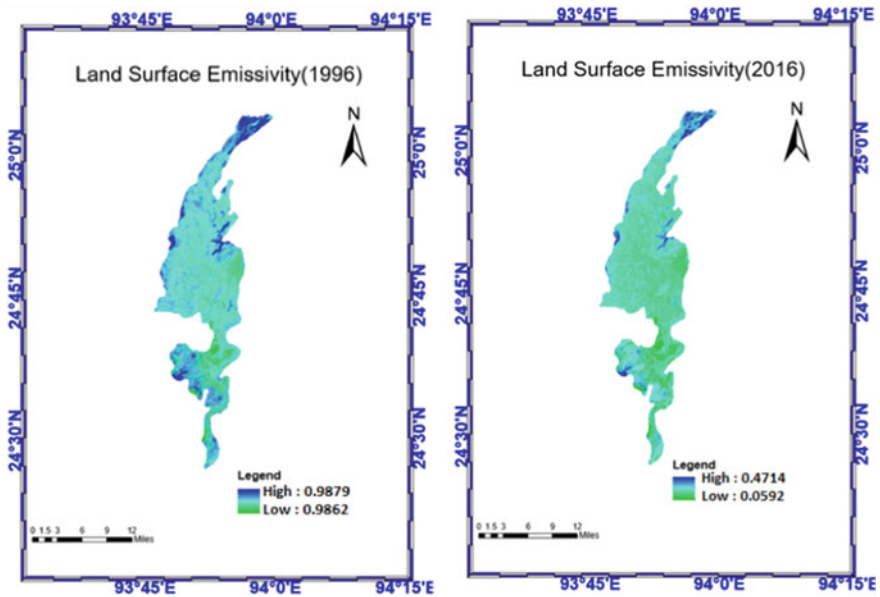


Fig. 4 Land surface emissivity in the years 1996 (left) and 2016 (right)

5.4 Land Surface Temperature

Land surface temperature for the year 1996 and year 2016 is shown in Fig. 5. Here, it shows that the temperature variation depends on the vegetation dynamics. The LST is high in urban places with 20.4 °C and low at forest areas with 9.93 °C in the year 1996 and 22.1 and 10.7 °C in the year 2016 respectively.

5.5 LULC

LULC for the years 1996 and 2016 are shown in Fig. 6 and is classified as dense forest, sparse forest, scrub/grass, crop land, built-up, and water bodies. The predicted LULC for the year 2026 is shown in Fig. 6 (bottom). In the accuracy assessment, the overall accuracy is obtained as $(41 + 40 + 39 + 47 + 28 + 33)/282 * 100 = 79.25\%$ and the corresponding Kappa coefficient as 0.78 which is in the acceptable range.

The distribution of LULC (Km²) is compared for the years 1996, 2016 and 2026 and is shown in Table 3. It is evident that in the study region crop land (26–35%) and built area (17–30%) are highest and lowest by dense forest from the year 1996–2026. Built-up area increased to 12.9% and crop land decreases at 8.7% from 1996 to 2026 in the study region.

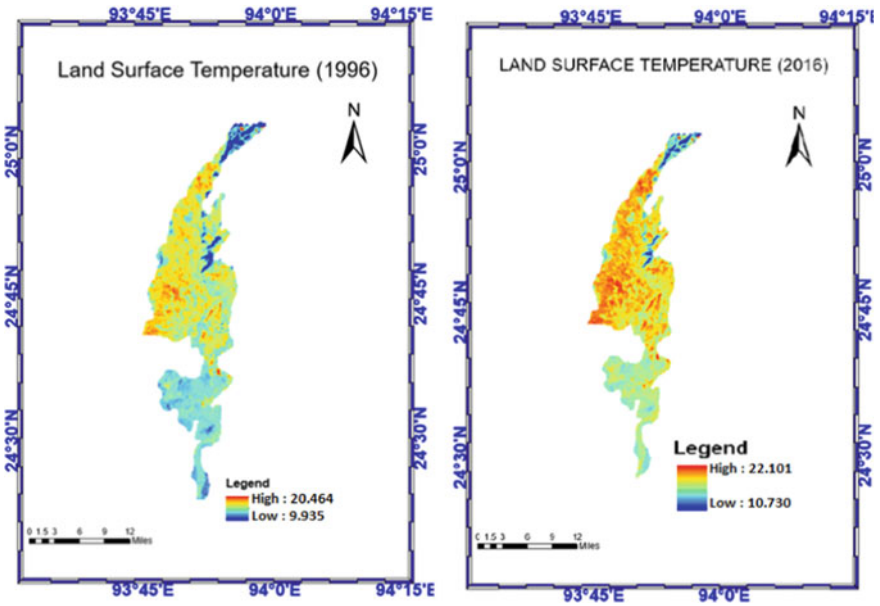


Fig. 5 Land surface temperature in the years 1996 (left) and 2016 (right)

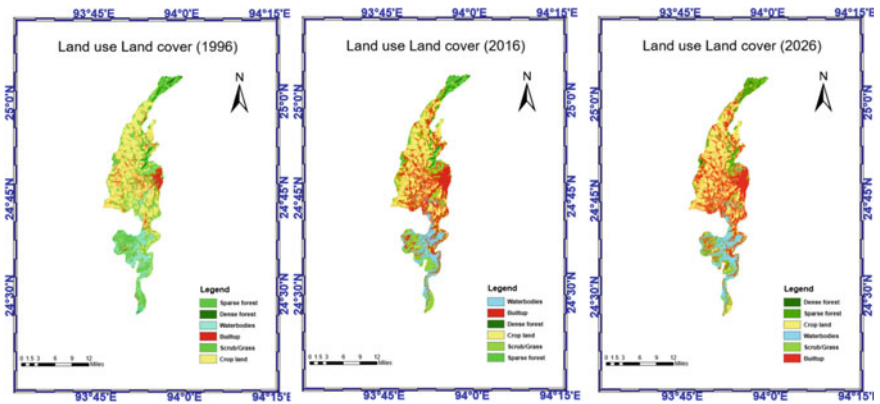


Fig. 6 LULC for 1996 (left), 2016 (right) and 2026 (bottom)

5.6 Estimated Carbon Stock and Sequestration

The amount of carbon stocks of the years 1996 (Fig. 7 left), 2016 (Fig. 7 right) and 2026 (Fig. 7 bottom). It ranges from 0 to maximum 26.6 mg of C for the year 1996 and 23.13 mg of C for the year 2016 and 21.27 mg of C for the year 2026 respectively.

Table 3 Distribution of LULC in 1996, 2016 and 2026

LULC types	1996		2016		2026 (future)		Total change (%)	
	Km ²	%	Km ²	%	Km ²	%	1996–2016	1996–2026
Dense forest	20.3	3.6	19.7	3.5	17.9	3.2	-0.1	-0.4
Sparse forest	40.0	7.2	36.6	6.6	38.2	6.8	-0.6	-0.4
Crop land	194.9	34.9	165.5	29.7	146.4	26.2	-5.3	-8.7
Scrub/Grass	136.2	24.4	112.9	20.2	116.1	20.8	-4.2	-3.6
Built-up	96.5	17.3	152.3	27.2	168.3	30.2	+9.9	+12.9
Water bodies	70.0	12.5	72.0	12.8	71.1	12.8	+0.3	+0.2

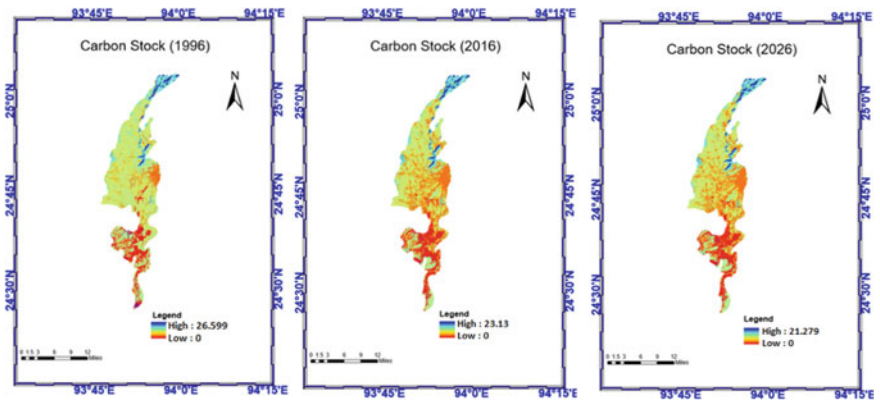
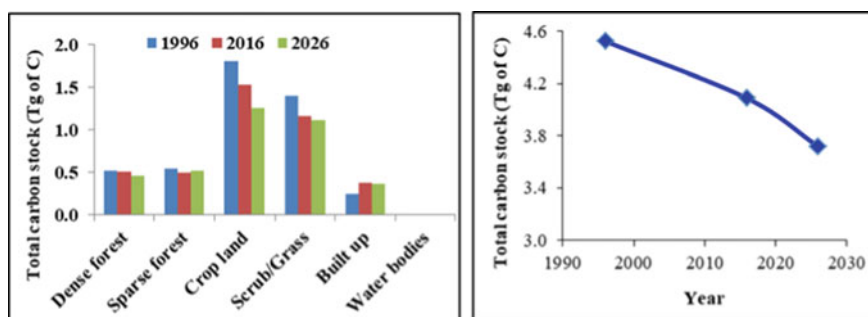


Fig. 7 Estimated carbon stock for 1996 (left), 2016 (right) and 2026 (bottom)

Table 4 representing the amount of carbon stock for each class for different years. As shown in Table 4 for the year 1996 carbon stock has been calculated as dense forest (11.55%), sparse forest (12.04%), crop land (40.07%), scrub/grass (31.01%), built-up (5.33%), and water bodies (0%). For the year 2016 it is as dense forest (12.4%), sparse forest (12.19%), crop land (37.65%), scrub/grass (28.44%), built-up (9.32%), and water bodies (0%) while the total of carbon stock is 4086645 Mg of C. In 2026 and percentage of carbon stock is as dense forest (12.36%), sparse forest (13.97%), crop land (33.95%), scrub/grass (30.01%), built-up (9.71%), and water bodies (0%) and the total is 3717033 Mg of C. Carbon stocking capacity is changing due to different parameters and Fig. 8 (right) shows comparison carbon stock value in different period while Fig. 7 (right) shows the decreasing trend from 1996 to 2026 (19.72%). Predicted carbon sequestration for the year 2026 is presented in Fig. 9. The southern part of the district has greater potential carbon sequestration than the northern part; however, this region as a whole has low carbon sequestration capacity (range 0 to -1.850).

Table 4 Estimated total carbon stock (Tg of C) for different LULC of 1996, 2016 and 2026

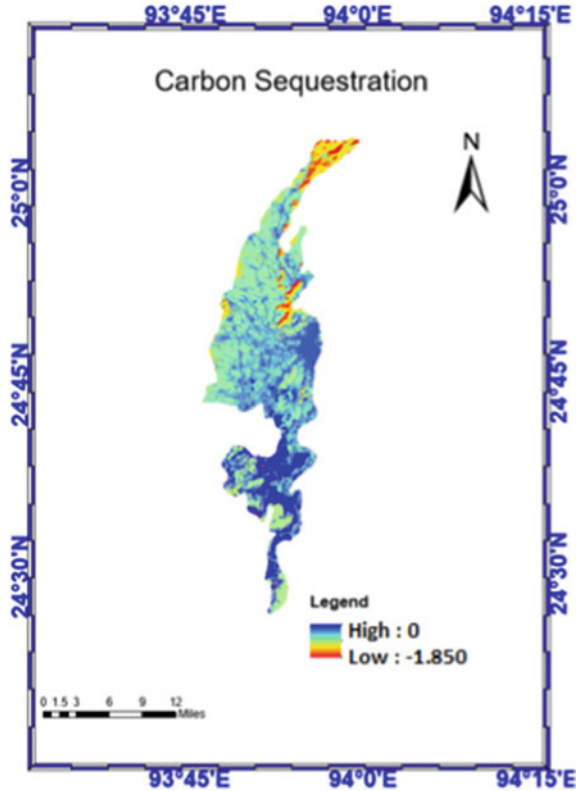
LULC types	Carbon value (Mg/hect)	1996		2016		2026	
		Tg of C	%	Tg of C	%	Tg of C	%
Dense forest	257	0.522	11.6	0.506	12.4	0.460	12.4
Sparse forest	136	0.544	12.0	0.498	12.2	0.519	14.0
Crop land	93	1.813	40.1	1.539	37.7	1.262	33.9
Scrub/grass	103	1.403	31.0	1.62	28.4	1.116	30.0
Built-up	25	0.241	5.3	0.381	9.3	0.361	9.7
Water bodies	0	0.000	0.0	0.000	0.0	0.000	0.0
Total		4.523	100	4.087	100	3.717	100

**Fig. 8** Comparison of carbon stock value (Tg) for different years (left) and changes in carbon stock from 1996 to 2026 (right)

6 Conclusions

The study region has poor potential for carbon stock as well as its sequestration as this region is rapidly urbanizing (built-up area increases at 13% approximately from 1996 to 2026). Thus, the amount of carbon stock is decreasing at 19.72% from 1996 to 2026. As forest area have an enormous change in carbon holding capacity, conservation or afforestation of forest area will help in maintaining the carbon stock in the region.

Fig. 9 Predicted carbon sequestration for the year 2026



References

1. Meena A, Bidalia A, Hanief M, Dinakaran J, Rao KS (2019) Assessment of above- and below-ground carbon pools in a semi-arid forest ecosystem of Delhi, India. *Ecol Process* 8:8. <https://doi.org/10.1186/s13717-019-0163-y>
2. Schulze ED, Sierra CA, Egenolf V, Woerdehoff R, Irslinger R, Baldamus C, Stupak I, Spellmann H (2020) The climate change mitigation effect of bioenergy from sustainably managed forests in Central Europe. *GCB Bioenergy* 12:186–197. <https://doi.org/10.1111/gcbb.12672>
3. Hou D (2021) Sustainable soil management and climate change mitigation. *Soil Use Manage* 37(2):220–223. <https://doi.org/10.1111/sum.12718>
4. Ramachandran A, Jayakumar S, Haroon RM, Bhaskaran A, Arockiasamy DI (2007) Carbon sequestration: estimation of carbon stock in natural forests using geospatial technology in the Eastern Ghats of Tamil Nadu, India. *Curr Sci* 92(3):323–331
5. Xiang S, Wang Y, Deng H, Yang C, Wang Z, Gao M (2022) Response and multi-scenario prediction of carbon storage to land use/cover change in the main urban area of Chongqing, China *Ecol Indic* 142:109205. <https://doi.org/10.1016/j.ecolind.2022.109205>
6. Martín JAR, Fuentes JA, Gonzalo J, Gil C, Miras JJR, Grau JMC, Boluda R (2016) Assessment of the soil organic carbon stock in Spain. *Geoderma* 264(A):117–125. <https://doi.org/10.1016/j.geoderma.2015.10.010>

7. Lan Z, Zhao Y, Zhang J, Jiao R, Khan MN, Sial TA, Si B (2021) Long-term vegetation restoration increases deep soil carbon storage in the Northern Loess Plateau. *Sci Rep* 11:13758. <https://doi.org/10.1038/s41598-021-93157-0>
8. Ray R, Mandal SK, González AG, Pokrovsky OS, Jana TK (2021) Storage and recycling of major and trace element in mangroves. *Sci Total Environ* 780:146379. <https://doi.org/10.1016/j.scitotenv.2021.146379>
9. Feng ZJ, Kun C, Xing PG, Smith P, Qing LL, Hui ZX, Wei ZJ, Jun HX, Ling DY (2011) Perspectives on studies on soil carbon stocks and the carbon sequestration potential of China. *Chinese Sci. Bull.* 56:3748–3758. <https://doi.org/10.1007/s11434-011-4693-7>
10. Roelofse C, Alves TM, Gafeira J, Omosanya K (2019) An integrated geological and GIS-based method to assess caprock risk in mature basins proposed for carbon capture and storage. *Int J Greenh Gas Control* 80:103–122. <https://doi.org/10.1016/j.ijggc.2018.11.007>
11. Li J, Wang Y (2019) Carbon sequestration service flow in the Guanzhong-Tianshui economic region of China: How it flows, what drives it, and where could be optimized? *Ecol Indic* 96:548–558. <https://doi.org/10.1016/j.ecolind.2018.09.040>
12. Sharma DP, Singh M (2010) Assessing the carbon sequestration potential of subtropical pine forest in North-western Himalayas—a GIS approach. *J Indian Soc Remote Sens* 38:247–253. <https://doi.org/10.1007/s12524-010-0031-9>
13. Xu X, Xu P, Zhu J, Li H, Xiong Z (2022) Bamboo construction materials: carbon storage and potential to reduce associated CO₂ emissions. *Sci Total Environ* 814:15269725. <https://doi.org/10.1016/j.scitotenv.2021.152697>
14. Bordoloi R, Das B, Tripathi OP, Sahoo UK, Nath AJ, Deb S, Das DJ, Gupta A, Devi NB, Charturvedi SS, Tiwari BK, Paul A, Tajo L (2022) Satellite based integrated approaches to modelling spatial carbon stock and carbon sequestration potential of different land uses of Northeast India. *Environ Sustain Indic* 13:100166. <https://doi.org/10.1016/j.indic.2021.100166>

A Comparative Study Between Confined Masonry and Reinforced Concrete Buildings Performances



Angelica Chanu Chingakham, Angom Olivia Devi, Christina Sagolsem, Konthoujam Nungshithoi, Samjetsabam Chainey, and Sukumar Singh Ningthoukhongjam

1 Introduction

Confined Masonry (CM) construction is a seismic-resistant construction technique where the walls are confined with horizontal and vertical ties to ensure stability and safety during seismic loading. Whereas Reinforced Concrete (RC) frame structure is a connected frame of members which are firmly connected by rigid joints. CM structures are appearing as an accepted building construction technique in many earthquake-prone countries including India. And moreover, CM structures become economically feasible and seismic resistant for low-rise buildings. Therefore, research works have been carried out to seek detailed information for CM structures. Rangwani et al. [1] conducted a comparative analysis of CM shear walls using Wide Column Model (WCM) approach and FEM macro-modeling approach. The results are obtained in terms of roof displacements, stiffness values and internal forces. No differences in results have been observed using both approaches. Pandey et al. [2] performed an investigation study on confined masonry for its seismic resistance and cost-effectiveness to compare with equivalent RC construction for low-rise residential buildings in Nepal using pushover analysis. The study showed that CM technology offers a better economic incentive in addition to enhanced performance in seismic loading pertinent to hazards defined by the current National Building Code (NBC) of Nepal. Sukarwa et al. [3] performed a numerical investigation of the behavior of confined masonry and its application for use as the main structure of multi-story buildings subjected to seismic loading. It was revealed that using shell elements for masonry walls, reinforced concrete beams, and tie-columns, the CM model mimics the load-deformation curve of tested specimens better than that

A. C. Chingakham (✉) · A. O. Devi · C. Sagolsem · K. Nungshithoi · S. Chainey · S. S. Ningthoukhongjam
Department of Civil Engineering, Manipur Institute of Technology, Imphal 795001, India
e-mail: changelica2018@gmail.com

using frame and shell elements in SAP2000. Arle Pratibha et al. [4] performed a comparative study between RC frame and CM constructions on different aspects like load resisting systems, foundation construction, etc. It has been found that for the seismic region, CM buildings give a better alternative for low-cost earthquake-resistant building construction. Chourasia et al. [7] discussed masonry construction in an Indian scenario and studied the performance of CM buildings on past earthquakes and their behavior under lateral cyclic loading. CM is found to be a promising technology that performs better under seismic loading and exhibits no significant damage. Also, the performance of CM buildings in India in comparison with unreinforced masonry (URM) and reinforced masonry (RM) in strength showed about 3.42 & 2.3 times improvement respectively. Ahmed et al. [9] analyzed the seismic functioning of CM brick buildings in earthquake-prone areas of Pakistan and other similar regions of the world. The results from this experimental study concluded that CBM building is sturdy against seismic loads because of the confining elements and is efficient in enhancing seismic performance. It has been observed from the above literature that CM structures are found to be economically feasible and seismic resistant when compared to their counterpart RC frame structures. Thus, in this paper, an attempt has been made to conduct a detailed comparative analysis between CM and RC structures along with their cost implications. Two similar buildings one as a CM structure and the other as an RC structure have been modeled SAP2000. Then the results have been compared in terms of storey drift, base shear and cost efficiency analysis.

2 Modeling

A five-room floor plan residential building of plan size $45' \times 42'$ has been drawn in AutoCAD for RCC and Equivalent Confined Masonry buildings respectively. The buildings are three storeys (G + 2) with 3.1 m storey height and with equal floor plan. The floor plans for RCC and CM structures are shown in Fig. 1a and b respectively.

2.1 Modeling of RC Frame Building Frame in SAP2000

Modeling of RC building is done using frame elements for columns, beams, equivalent strut, and shell element for slabs as shown in Fig. 2. The model is designed using IS 456: 2000, also the width of the equivalent strut for infill was designed using IS 1893 (Part 1): 2016, Clause 7.9. Dimensions considered for the design of G + 2 RCC building are listed in Tables 1 and 2.

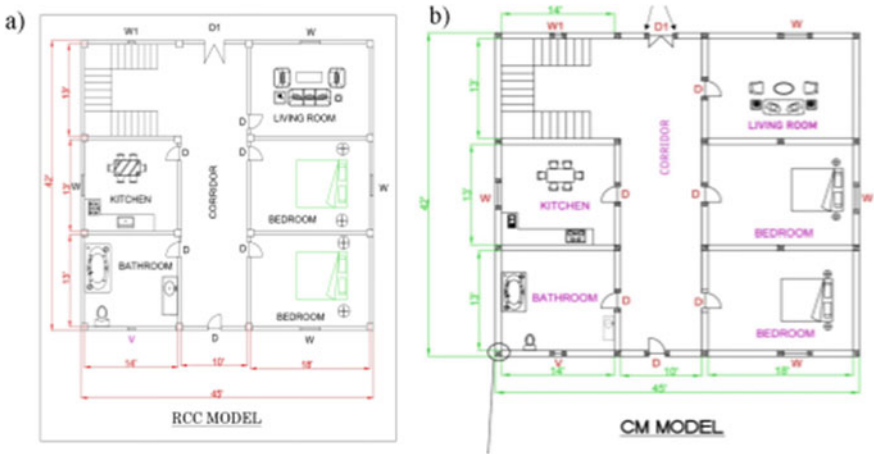


Fig. 1 a RC Framed Building and b Equivalent CM building plan

Fig. 2 RCC model in SAP2000 (using frame elements)

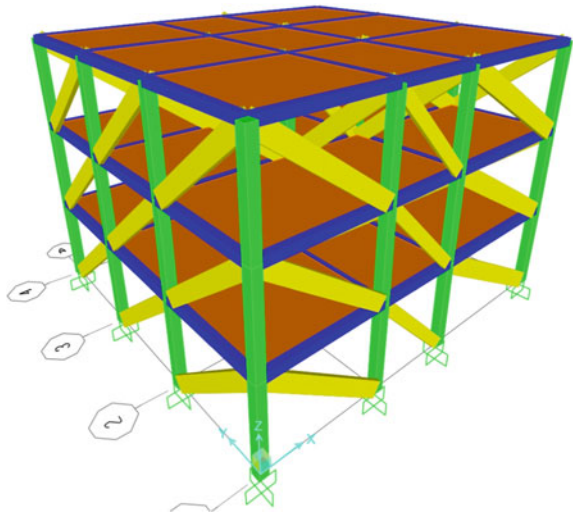


Table 1 Dimensions used to design the G + 2 RCC building

Specification	Value
Plan size	45ft × 42ft
No of floors	3
Floor height	3.1 m
Material	RCC
Thickness of slab	0.15 m
Column size	0.3 m × 0.3 m
Beam size	0.25 m × 0.25 m

Table 2 Dimensions of struts**

Length of wall	Length of equivalent strut (m)	Width of Equivalent strut (m)	Thickness of strut (m)
10ft wall	3.959	0.42	0.15
13ft wall	4.88	0.53	0.15
14ft wall	4.88	0.53	0.15
18ft wall	5.917	0.64	0.15

** Dimension of strut is designed according to IS 1893 (Part 1):2016, clause 7.9

2.2 Modeling of Confined Masonry in SAP2000

Modeling of the CM building has been done using Shell elements [3] (see Fig. 3) and designed in accordance to EERI, 2011 [23].

Dimensions considered for the design of G + 2 CM building are listed in Table 3.

2.2.1 Wall Density Index

The wall density index along Y-axis for the Ground floor, 1st floor and 2nd floor are 5.84% each and that along X-axis for the Ground floor, 1st floor and 2nd floor are 6.21, 6.44 and 6.44% respectively when all of them are greater than 5%, which

Fig. 3 CM model in SAP2000 (using shell elements)

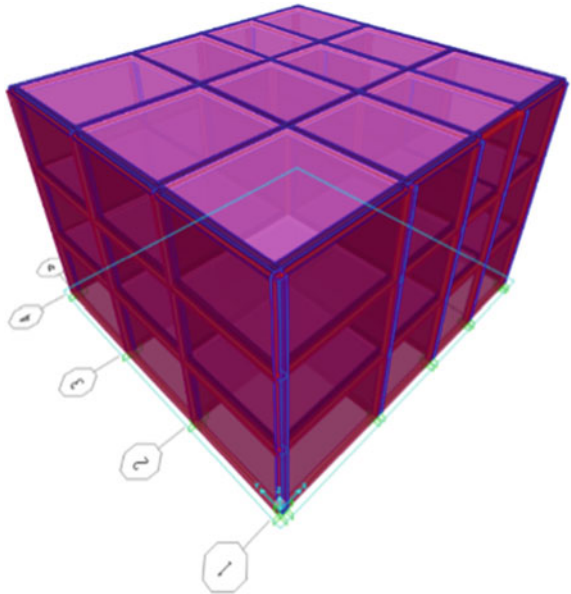


Table 3 Dimensions used to design the G + 2 CM building

Parameter	Value
Plan size	45ft × 42ft
Wall thickness	0.23 m
Tie column	(depth × width) (0.23 m × 0.2 m)
Tie beam	(depth × width) (0.23 m × 0.2 m)
Slab thickness	0.15 m

Table 4 Mechanical properties of CM building

Indian standard design	Value	Remark
Reinforcing bar	Min 10 mm dia	
Stirrup	6 mm dia	
Rebar	8 mm dia	
Modulus of elasticity of brick masonry, E (Mpa)	1,573,072.1	IS 1893, clause 7.9.2.1
Poisson, u	0.26	
Coefficient of thermal expansion, A,(°C ⁻¹)	4.5810 ⁻⁶	

is the minimum requirement according to [7] which states that wall density index should be at least 5% for the site of seismic Zone V for India.

3 Analysis of Results

Loading and load combination has been adopted as per IS: 875 (parts 1 and 2) [7, 8], IS 456 [6] and IS 1893 (Part 1) [9]. Equivalent static method is adopted for seismic analysis. The results are presented in terms of base shear, storey drift and cost analysis.

3.1 Base Shear and Storey Drift

It has been found that the base of RC structure is comparatively low (i.e., $V_b = 460.40211$ KN) as compared to that of CM structure (i.e., $V_b = 1098.575$ KN) as shown in Fig. 4. The reason for less base shear in case of RC and high base shear in case of CM structures are due to less design horizontal seismic coefficient for RC and high design horizontal seismic coefficient for CM structures. Although base shear for CM structure is higher as compared to that of RC structure, however storey drift

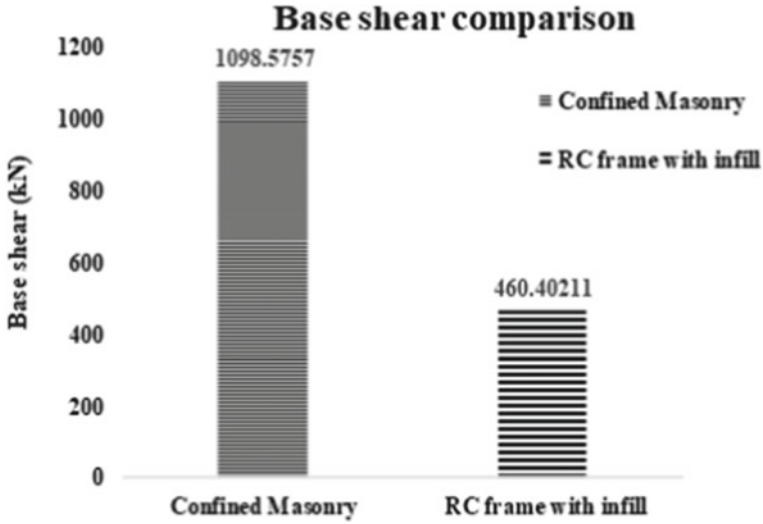


Fig. 4 Base shear comparison of Confined masonry and RC frame building with infill

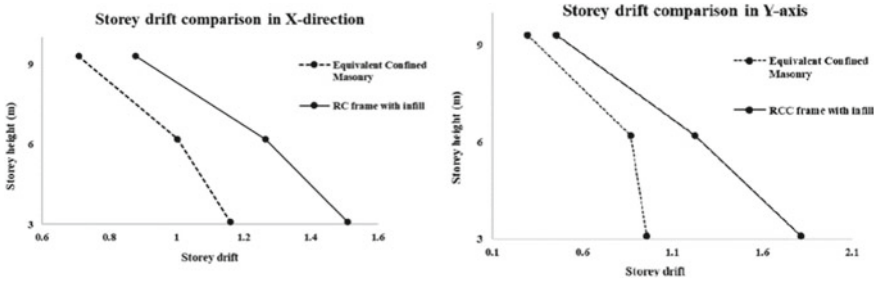


Fig. 5 Storey drift comparison of RC and CM structures along a X-direction and b Y-direction

of CM structure is found to be less than that of RC structures as shown in Fig. 5a and b.

3.2 Cost Estimation

Cost comparison has been conducted between RC and CM structures keeping concrete work, brick work and Steel reinforcement as differentiating factors [10]. It has been observed that CM structure cost 5.53% less as compared to RC structure as shown in Fig. 6. Thus, cost wise CM structure is more cost efficient than that of counterpart RC structure.

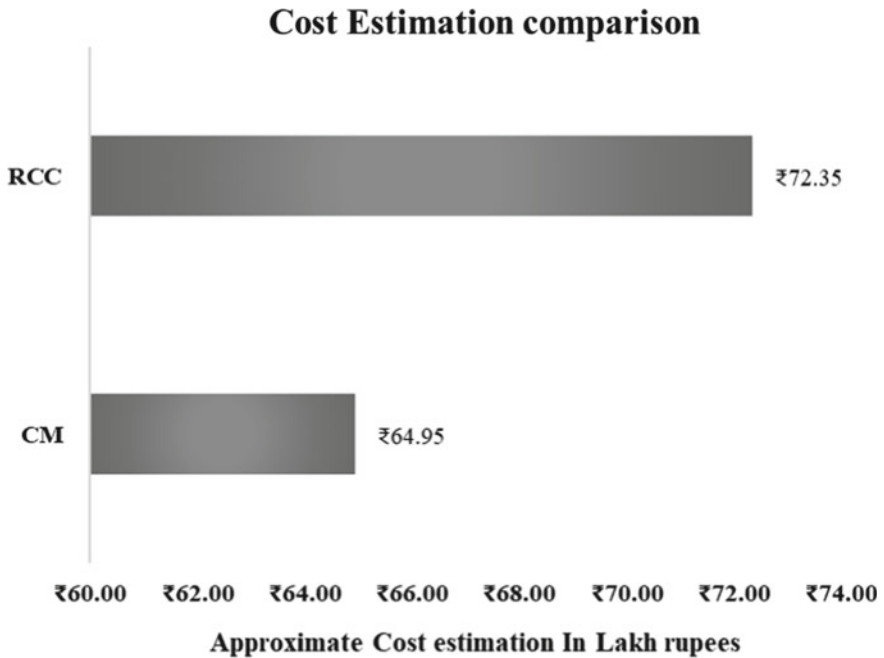


Fig. 6 Cost Estimation comparison of RC frame building with infill and equivalent Confined masonry building

4 Conclusion

In this paper, comparative study has been carried out between Confined Masonry (CM) and Reinforced Concrete (RC) building structures using SAP2000. Two similar building structures, one made of CM and the other made of RC have been modeled in SAP2000. CM building is modeled using shell elements and RC frame building is modeled using frame elements. The same loadings in the form of dead load, live load and seismic load have been applied to both the structures. It has been observed that confined masonry structure exhibits higher base shear and lower storey drift as compared to that of reinforced concrete structure. Further, it has also been observed that construction cost is less for confined masonry building than that of reinforced concrete building for the same building configuration.

In this paper, a comparative study has been conducted between Confined Masonry (CM) and Reinforced Concrete (RC) building structures of similar building geometry. CM building has been modeled using shell elements, whereas RC frame building has

been modeled by using frame elements. The same loadings have been applied to both the building structures. The following conclusions have been drawn from the analysis.

1. It has been observed that Confined Masonry (CM) structure exhibits higher base shear as compared to that of Reinforced Concrete (RC) building structures when subjected to same loading conditions.
2. Storey drift ratio of Confined Masonry (CM) structure has been found to be less as compared to that of Reinforced Concrete (RC) building structures for the same loadings.
3. It has also been found that Confined Masonry (CM) structure is more cost efficient as compared to that of Reinforced Concrete (RC) structure of same building configuration.

References

1. Rangwani K, Brzev S (2016) Seismic analysis of confined masonry shear walls using the wide column model. In *Applied Mechanics and Materials*, vol 857, pp 212–218. Trans Tech Publications Ltd
2. Pandey B, Ashish KC, Karna H, Motra G (2019) Application of confined masonry in lieu of RC construction in newly expanding urban area of Nepal
3. Sukrawa Made, Gede Pringgana, Putu Ayu Ratih Yustinaputri (2019) ing of confined masonry structure and its application for the design of multi-story building. *MATEC Web of Conferences*, vol. 276. EDP Sciences
4. Arle Pratibha R, Kubhar GJ, Shirsath MN (2019) Seismic analysis of confined masonry building and RCC building. *Int Res J Eng Technol* 6:7995–8005
5. Brzev S, Hart T (2017) Confined masonry network: An overview of guidelines and initiatives. In *Proceedings of the 16th World Conference on Earthquake Engineering*
6. IS 456:2000- Code of practice for design loads
7. IS 875 (parts 1) 1987- Code of practice for design loads (other than earthquake) for buildings and structures. (Dead loads)
8. IS 875 (parts 2) 1987- Code of practice for design loads (other than earthquake) for buildings and structures. (Imposed loads)
9. IS 1893 (part 1) : 2016 Criteria for Earthquake Resistant Design of Structures
10. Manipur Schedule of Rates 2022 Vol 1, (Building Works)

Influence of Normalization Techniques in CMIP Model Selection Using an MCDM Method MOORA



Gaurav Patel, Subhasish Das, and Rajib Das

1 Introduction

Researchers have been motivated to develop new techniques in response to the requirement for a variety of decision-making procedures for addressing various model selection difficulties. The use of multi-criteria decision-making (MCDM) methodologies has the potential to produce superior results. Finding a good model is critical for predicting forthcoming environmental difficulties. Global climate models (GCMs) are commonly used to forecast future climate. Various groups have created a significant number of GCMs. Climate datasets from many organizations are being used by the IPCC for climate impact assessments [1]. The Coupled Model Intercomparison Project Phase 6 (CMIP6) is commonly utilized for present and future climate analysis and projections. Despite substantial advancements in CMIP6, large uncertainty remains under a variety of climate circumstances. Many assumptions were made throughout the creation of GCMs due to a lack of accurate information on atmospheric events, leading to exaggerations or underestimations of climate change. This allows us to see where the climate models and observations diverge. Climate projection uncertainty can be decreased by using a proper collection of GCMs. The preliminary goal of any climate change impact research or climate modeling is to pick the best group of GCMs [2]. Typically, the ability of climate models to simulate past climate is utilized as the basis for selecting GCMs. The uncertainty in climate projections has a significant impact on impact estimation. A small adjustment in climate projection can drastically alter the return duration of hydrological disasters such as floods and droughts. As a result, selecting credible GCMs is regarded as one of the most successful methods of lowering uncertainty in climate change estimates. GCMs are typically chosen based on their capacity to recreate historical climates. To evaluate the performance measure of GCMs, time series of monthly or

G. Patel (✉) · S. Das · R. Das

School of Water Resources Engineering, Jadavpur University, Kolkata, West Bengal, India

e-mail: gauravp.wre.rs@jadavpuruniversity.in

annual observed and GCM simulated climate are typically compared. The typical method of selecting GCMs emphasizes their ability to replicate temporal variability in precipitation or temperature.

The biggest drawback of employing other performance indicators is that the timing info for the error positions is lost. As a result, any metric used to evaluate performance has advantages and disadvantages that are unique to it, and there is no single criterion for judging the quality of a model that has been established as standard across a wide range of contexts and purposes. To address these issues, MCDM methodologies were used to integrate the findings of different performance indicators into a single score. Because the aggregated results that are produced by the MCDM techniques are strongly dependent on the weights that are assigned to the numerous individual evaluation criteria, techniques for weightage division play a key role in the classification process. The reference gridded datasets that are employed and the interpolation techniques that correspond to them have a significant impact on the estimated values of the various performance metrics that are driven into the MCDM algorithms. There are various approaches for determining the efficacy of a classification problem, but because there haven't been many studies done on the effectiveness of normalization techniques for MCDM methods, it is still unclear how to select the most appropriate one. The process of normalization involves making adjustments to the values of the criterion so that they are approximately the same size. However, utilizing a variety of normalization approaches can result in a variety of solutions, which in turn can result in variations from the outcomes that were initially proposed.

In relation to the ranking of CMIP6 GCMs, the newly released CMIP6 model has only a limited amount of deployment in India. The selection of GCMs has been done using a variety of different methodologies. However, a good selection of normalizing approaches has not yet been explored in any of the relevant literature. The purpose of this study is to apply Multi-Objective Optimization based on Ratio Analysis (MOORA) MCDM with four different normalization techniques to determine which normalization technique is the most effective for particular this method that can be used to rank the CMIP6 GCMs utilizing the historical dataset to simulate precipitation. The goal of the research is to identify the finest normalization technique for particular this method. Finding the optimal normalization strategy can be of great assistance when selecting models, methods, and criteria for MCDM applications in a variety of fields.

2 Data Used and Methodology

The IMD Pune compiled daily gridded precipitation data from 1901 to 2020. With regard to precipitation, there is historical climatic data available with a grid precision of 0.25 degrees by 0.25 degrees [3]. These gridded datasets are widely used in India for climate-related studies and applications. This research makes use of downscaled datasets from the Coupled Model Inter-comparison Project, Phase 6 (CMIP6) that are made available by the NASA NEX-GDDP Program. The procedure known as

Table 1 Details of the 10 GCMs of the CMIP6

Model	Model name	Country origin	Resolution (km)	References
Mod-1	IITM ESM	India	250	Krishnan et al. [4]
Mod-2	CMCC CM2	Italy	100	Cherchi et al. [5]
Mod-3	CNRM ESM2-1	France	250	Séférian et al. [6]
Mod-4	INM CM4-8	Russia	100	Volodin et al. [7]
Mod-5	IPSL CM6A LR	France	250	Boucher et al. [8]
Mod-6	MIROC-6	Japan	250	Tatebe et al. [9]
Mod-7	MPI ESM1-2 h	Germany	100	Müller et al. [10]
Mod-8	MPI ESM1-2 LR	Germany	250	Mauritsen et al. [11]
Mod-9	NorESM2 LM	Norway	250	Seland et al. [12]
Mod-10	TaiESM 1	Taiwan	100	Wang et al. [13]

Bias Correction Spatial Disaggregation (BCSD) is utilized in its production. Table 1 presents the details along with a list of the 10 GCMs that are chosen based on the available data.

This study takes use of the historical CMIP6 GCMs as well as the IMD gridded precipitation of 64 years, from 1950 to 2014, to analyze various ranking and normalization procedures. The goal of this assessment is to determine the effectiveness of these strategies. Ten different performance criteria have been utilized in the process of assessing GCMs. These standards are determined by a combination of experience, trial and error, and effectiveness. In addition to that, the Shannon entropy approach is used for the weightage of different performance criteria to determine which is more important. In order to rank the concerned models, the MOORA technique is applied, along with four alternative types of normalization. It is proposed to use the normalization technique with the best performance, and using those strategies is how the ranking is established.

2.1 Indicators

Indicators are utilized in the process of comparing the GCMs' simulation of projected data with actual data. In this investigation, ten indicators (Table 2) are chosen after considering both their error rates and their overall productivity.

2.2 Weight Criteria Technique (Shannon Entropy)

There are several different approaches to choose from when figuring out weights. The entropy weight is the criterion that is employed for weighting in this study. It is

Table 2 Ten indicators selected to compare GCMs' simulation of projected data with actual data

Indicators	Abbreviations	Indicators	Abbreviations
Standard deviation	SD	Correlation coefficient	CC
Taylor skill score	TSS	Normalized root mean square error	NRMSE
Index agreement	IA	Kolmogorov–Smirnov test	KST
Skill score	SS	Nash–Sutcliffe efficiency	NSE
Percentage bias	PBIAS	Kling–Gupta efficiency	KGE

the procedure that is utilized most frequently for determining weights. It is necessary to take into account all of the parameters before assigning relative weight.

The entropy technique is established on a theory that takes both the amount of information that is now accessible as well as the significance of a criterion concerning that information. It does not take into account the preferences of the individual making the decision and instead uses the provided payoff matrix to determine the relative importance of the various criteria [14]. The following are the actions that need to be done to calculate the weightage of each indicator.

Step 1. Construct a payoff matrix and normalized it (Eq. 1)

$$N_{ij} = x_{ij} / \sum_{i=1}^m x_{ij}^2 \text{ for } i = 1, 2, \dots, m \text{ and } j = 1, 2, \dots, n \quad (1)$$

where i is the index for GCM, j is the index of the indicator, x_{ij} is the scale of the indicator j for GCM i , m is the total number of models and n represents the total number of indicators.

Step 2. Entropy and degree of diversification are calculated by using Eqs. 2 and 3,

$$E_j = - \sum_{i=1}^m N_{ij} \times \ln N_{ij} / \ln m \quad (2)$$

$$D_j = 1 - E_j \quad (3)$$

Step 3. Calculate the normalized weight matrix of indicators by Eq. 4,

$$w_j = D_j / \sum_{k=1}^n D_k \quad (4)$$

where E_j is entropy, D_j is the degree of diversification, w_j is the individual indicator's weightage.

2.3 MOORA MCDM

The MOORA technique begins with the creation of a decision criteria matrix, which compares the effectiveness of various options based on several distinct criteria (objectives). After that, a ratio matrix system is constructed, in which each parametric performance of a potential alternative on a particular attribute is equated to a denominator that serves as a representative for all of the potential alternatives concerning that attribute. In the context of multi-objective optimization methodology, the normalizing performances are increased in the event of maximization (for beneficial qualities), and they are decreased if minimization is the goal (for non-beneficial attributes) [15].

$$W_{ij} = w_j N_{ij} \quad (5)$$

$$y_i = \sum_{j=1}^h W_{ij} - \sum_{j=h+1}^n W_{ij} \quad (6)$$

where h is the number of parameters that aim to be maximized, $(n - h)$ is the number of parameters to be minimized, and y_i is the normalized value of i th alternative with respect to all the parameters.

2.4 Normalization Techniques

Normalization is a procedure to analyze various datasets on a similar comparable scale. Normalization is typically required when working with qualities that are measured on more than one scale. If normalization is not performed, the influence of a significant and equally important attribute that is measured on a smaller scale may be diminished because other attributes have values that are measured on a greater scale. Within the scope of this investigation, we have implemented a total of four distinct normalization strategies. Table 3 represents the different normalization techniques along with their formula.

2.5 Index Ranking (IR)

The IR describes the extent to which the rankings obtained from one normalization method are consistent with the results obtained from other methods. The consistency index is a metric that indicates how well one normalization procedure produces rankings that are comparable to those produced by other normalization procedures [16]. This comparison indicates how well one normalization procedure produces rankings that are comparable to those produced by other normalization procedures. They determined the IR for each method of normalization by counting the total number of

Table 3 Four different normalization techniques employed to analyze datasets

Normalization technique	Formula	Criteria
Linear: Max (N_1)	$N_{ij} = x_{ij} / x_{\max}$	Beneficial criteria
	$N_{ij} = x_{\min} / x_{ij}$	Non- beneficial criteria
Linear: Max- Min (N_2)	$N_{ij} = (x_{ij} - x_{\min}) / (x_{\max} - x_{\min})$	Beneficial criteria
	$N_{ij} = (x_{\max} - x_{ij}) / (x_{\max} - x_{\min})$	Non- beneficial criteria
Linear: Sum (N_3)	$N_{ij} = x_{ij} / \sum_{i=1}^m x_{ij}$	Beneficial criteria
	$N_{ij} = 1 - (x_{ij} / \sum_{i=1}^m x_{ij})$	Non- beneficial criteria
Vector (N_4)	$N_{ij} = x_{ij} / \sqrt{\sum_{i=1}^m x_{ij}^2}$	Beneficial criteria
	$N_{ij} = 1 - (x_{ij} / \sqrt{\sum_{i=1}^m x_{ij}^2})$	Non- beneficial criteria

instances in which these normalizations produce results that are comparable to one another or dissimilar to one another in the problem. This allowed them to determine how each normalization contributed to the overall solution. Because of this, they were able to discover which methods of normalization were more successful.

In the first phase, we determine the IR by counting the number of ways in which each of the normalizations that have been evaluated is the same and different from one another [16]. Because there are four distinct approaches to the process of normalization, we will start by defining the weight (WT) in the following way:

- if a ranking is similar with all approaches, then $WT_1 = 3/3 = 1$;
- if a ranking is similar to two of the three approaches, then $WT_2 = 2/3$;
- if a ranking is similar to one of the three approaches, then $WT_3 = 1/3$;
- if a ranking is not consistent, then $WT_4 = 0/3 = 0$.

and then the Index Ranking, for N_j , is calculated as in Eq. 7 [16].

$$IR_{N_1} = \frac{\left[(SR_{1234} \times WT_1) + (SR_{123} \times WT_2) + (SR_{124} \times WT_2) + (SR_{134} \times WT_2) \right] + (SR_{12} \times WT_3) + (SR_{13} \times WT_3) + (SR_{14} \times WT_3) + (DR_{1234} \times WT_4)}{CC} \quad (7)$$

where, IR_i : IR for normalization procedure ($i = N_1, N_2, N_3$ and N_4); CC : Number of complete cycles ($CC = 1$); SR_{1234} : Total number of similar ranking with N_1, N_2, N_3 and N_4 ; SR_{123} : Total number of similar ranking with N_1, N_2 and N_3 ; SR_{12} : Total number of similar rankings with N_1 and N_2 ; DR_{1234} : Total number of different ranking with N_1, N_2, N_3 and N_4 .

Table 4 Ranking of models using MOORA

Models	Normalization techniques				Models	Normalization techniques			
	N_1	N_2	N_3	N_4		N_1	N_2	N_3	N_4
Mod-1	8	1	10	10	Mod-6	2	5	3	2
Mod-2	3	4	4	3	Mod-7	6	8	7	7
Mod-3	7	9	6	6	Mod-8	1	2	1	1
Mod-4	9	7	8	8	Mod-9	10	6	9	9
Mod-5	4	3	5	4	Mod-10	5	10	2	5

3 Results and Discussion

Several metrics have been provided as a result of the research that may be utilized to evaluate the various normalization strategies that are utilized in MCDM procedures. During our investigation, we made use of the IR that was initially suggested in literature [16]. To identify which normalizing method led to the production of the best accurate rankings, we put the MOORA method and four distinct normalization methods through their paces.

3.1 Ranking of GCMs

The MOORA method is executed to calculate the ranking of ten GCMs. This is done for the variable of precipitation. The ranks of GCMs for precipitation, as determined by the MOORA methodology, are presented in Table 4. The findings of the ten GCMs, which are based on the four distinct normalization methods, each yield a different rating for the normalization method. The Mod-8 seems to be the most effective of all the other choices that are on the table, at least according to MOORA.

3.2 Index Ranking (IR)

The final findings for MOORA procedures based on IR suggest that N_4 has the greatest IR values, followed by N_3 , N_1 , and N_2 . Based on the results, it is simple to conclude that the vector normalizing technique is the most effective normalization technique for MOORA. The overall IR value is represented in Fig. 1 for each of the normalization procedures.

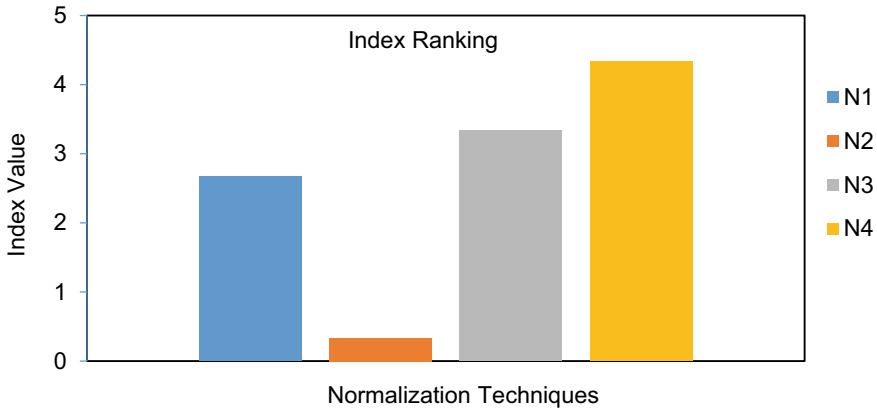


Fig. 1 Index ranking of normalizations

4 Conclusions

Because we need to obtain dimensionless units to calculate the final rating for each alternative, the process of decision-making cannot function without normalization playing a crucial role. Consequently, we cannot conduct one without the other. In this exploratory study, we demonstrated the effects of applying four distinct normalizing approaches that are common and well-known in their respective fields. In order to evaluate which normalizing approach is most suited for the MOORA method, we compared all four normalization strategies by utilizing a simple illustrative case. We are able to show that the vector normalization technique (N_4) is the one that works best for the MOORA. The outcome of various normalization strategies for MCDM approaches is similar to the findings of earlier research [16]. The procedure gave a ranking for the four standardization methods that are commonly used in order to offer decision-makers assistance in making better-informed judgments. When researchers and practitioners normalize their data in an MCDM application using the MCDM approach stated, they should keep these results in mind and consider them. Keeping these results in mind and considering them will help ensure accurate outcomes.



References

1. IPCC (2021) Summary for Policymakers. In: Climate Change 2021: The Physical Science Basis. Contribution of Working Group I to the Sixth Assessment Report of the Intergovernmental Panel on Climate Change. Masson-Delmotte V, Zhai P, Pirani A et al. (eds.). Cambridge University Press
2. Samadi SZ, Sagareswar G, Tajiki M (2010) Comparison of general circulation models: methodology for selecting the best GCM in Kermanshah Synoptic Station, Iran. *Int J Glob Warm* 2(4):347–365

3. Pai DS, Sridhar L, Rajeevan M et al. (2014) Development of a new high spatial resolution ($0.25^\circ \times 0.25^\circ$) long period (1901–2010) daily gridded rainfall data set over India and its comparison with existing data sets over the region. *Mausam* 65(1):1–18
4. Krishnan R, Swapna P, Vellore R et al. (2019) The IITM earth system model (ESM): development and future roadmap. In: D Randall, J Srinivasan, R Nanjundiah, P Mukhopadhyay (eds.) *Current trends in the representation of physical processes in weather and climate models*. Springer, Singapore, pp 183–195
5. Cherchi A, Fogli PG, Lovato T et al (2019) Global mean climate and main patterns of variability in the CMCC-CM2 coupled model. *J Adv Model Earth Syst* 11(1):185–209
6. S  f  rian R, Nabat P, Michou M et al (2019) Evaluation of CNRM earth system model, CNRM-ESM2-1: role of earth system processes in present-day and future climate. *J Adv Model Earth Syst* 11(12):4182–4227
7. Volodin E, Mortikov EV, Kostrykin SV et al (2018) Simulation of the modern climate using the INM-CM48 climate model. *Russ J Numer Anal Math Model* 33(6):367–374
8. Boucher O, Servonnat J, Albright AL et al. (2020) Presentation and evaluation of the IPSL-CM6A-LR climate model. *J Adv Model Earth Syst* 12(7):e2019MS002010
9. Tatebe H, Ogura T, Nitta T et al (2019) Description and basic evaluation of simulated mean state, internal variability, and climate sensitivity in MIROC6. *Geosci Model Dev* 12(7):2727–2765
10. M  ller WA, Jungclaus JH, Mauritsen T et al. (2018) A higher-resolution version of the max planck institute earth system model (MPI-ESM1.2-HR). *J Adv Model Earth Syst* 10:1383–1413
11. Mauritsen T, Bader J, Becker T et al. (2019) Developments in the MPI-M earth system model version 1.2 (MPI-ESM1.2) and Its response to increasing CO₂. *J Adv Model Earth Syst* 11(4):998–1038
12. Seland  , Bentsen M, Olivie D et al (2020) Overview of the Norwegian earth system model (NorESM2) and key climate response of CMIP6 DECK, historical, and scenario simulations. *Geosci Model Dev* 13(12):6165–6200
13. Wang YC, Hsu HH, Chen CA et al (2021) Performance of the Taiwan earth system model in simulating climate variability compared with observations and CMIP6 model simulations. *J Adv Model Earth Syst* 13(7):1–28
14. Pomerol JC, Romero SB (2000) Weighting methods and associated problems. In: *Multicriterion Decision in Management. International Series in Operations Research & Management Science*, vol 25, pp 75–104. Springer, Boston, MA
15. Brauers WKM (2013) Multi-objective seaport planning by MOORA decision making. *Ann Oper Res* 206(1):39–58
16. Chakraborty S, Yeh CH (2009) A simulation comparison of normalization procedures for TOPSIS. *International conference on computers & industrial engineering*. IEEE Press, France, pp 1815–1820

Numerical Simulation on the Hydrodynamics of Sedimentation Tank When Longitudinal Inclined Plates Are Employed



Kirpa Hirom  and Thiyam Tamphasana Devi 

1 Introduction

The settling of suspended particles through gravitational force occurs in a sedimentation tank and can be regarded as a crucial step for the treatment process of any water treatment system. The difference in density between the sediments and the water forces the sediments to follow a deviated path from that of the water streamlines towards the bottom and eventually settle out. Gravity is the main driving force of this process. Sedimentation tanks of various shapes and sizes are employed at multiple stages of both the potable water treatment (PWT) and wastewater treatment (WWT) plants [1].

There is a certain type of compact sediment settler usually deployed at industrial wastewater facilities (especially for mining and metal finishing industries) where there is no luxury of space for installation of large sedimentation tanks that take advantage of these factors—called lamella clarifier. However, in terms of versatility, ease of use, and large-scale water treatment, conventional sedimentation tanks dominate over lamella clarifiers. Taking cues from the lamella clarifier, many researchers have tried to reap its advantages by modifying existing geometries of conventional sedimentation tanks with inclined plates. The superiority of these modified sedimentation tanks retrofitted with inclined plates has been proven through many studies [3–6]. However, only lateral inclined plates are used in all of these studies and very few on longitudinal inclined plates. With 3-D numerical studies becoming a norm in the past few years, future studies on the optimisation of sedimentation tanks are expected to follow in a direction similar to this research area. Therefore, in this study, the effectiveness of longitudinal inclined plates in increasing the efficiency as well as

K. Hirom · T. T. Devi (✉)

Department of Civil Engineering, National Institute of Technology Manipur, Manipur 795004, India

e-mail: thiyam85@gmail.com

the improvement in the overall performance of the sedimentation tank is thoroughly investigated through 3-D numerical simulations.

2 Materials and Methods

2.1 Geometry and Meshing

The rectangular settling tank employed for this study has dimensions of 42.7 m * 11.5 m * 4.1 m (L * B * H) with the longitudinal inclined plates placed starting from 1 m away from the inlet baffle. A total of 25 longitudinal inclined plates of different surface areas are placed on each half of the sedimentation tank with an angle of 35° with respect to the horizontal and are 200 mm apart, as shown in Fig. 1. To support these inclined plates, three equally spaced support pillars are also installed right at the longitudinal centre line of the sedimentation tank, as shown in Fig. 2. This method of installing the inclined plates as two halves (rather than extending from one side wall to the other entirely, without any support pillars in the middle) was adopted to facilitate the movement of the settled particles onto the bed of the sedimentation tank for sludge removal. This would not have been possible if the inclined plates were placed from one side wall to the other since the inclination of the inclined plates will be very less and clogging can occur between the plates due to the settled particles. A gap of 500 mm is also maintained between the bottom end of the inclined plates and the bed of the sedimentation tank for the purpose of easier removal of these settled particles.

The geometry is divided into three regions—inlet, outlet, and mid-region—for a more efficient meshing, as shown in Fig. 3. Hybrid meshing is adopted for this study. The mid-region mainly comprises tetrahedron elements because of the addition

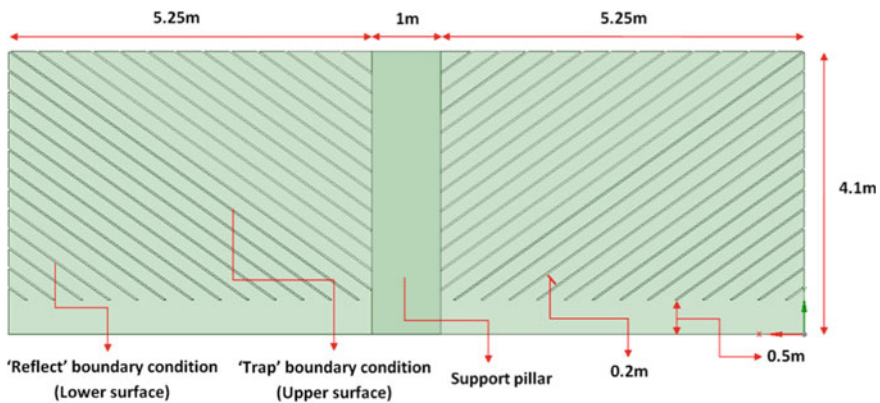


Fig. 1 Cross-sectional view of the new geometry at $z = 4.4$ m

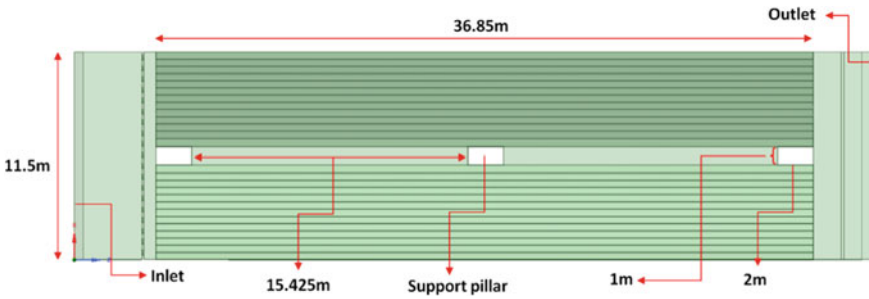


Fig. 2 Top-view of the new geometry

of inflation layers along the longitudinal inclined plates as well as the side walls and the bed of the sedimentation tank, to capture the boundary layer fluid flow more accurately. The inlet region and the outlet region mainly comprise the more economical and accurate hexahedron elements. The meshing of the geometries is performed using the Ansys meshing software.

The necessary grid-independence test was performed for this study by varying the ‘element size’ between 0.08 m and 0.5 m. The final selected value was 0.1 m since no significant change in solution was observed in further reducing the ‘element size’. A total of 10.44 million elements are present on the meshed geometry finally selected for simulation.

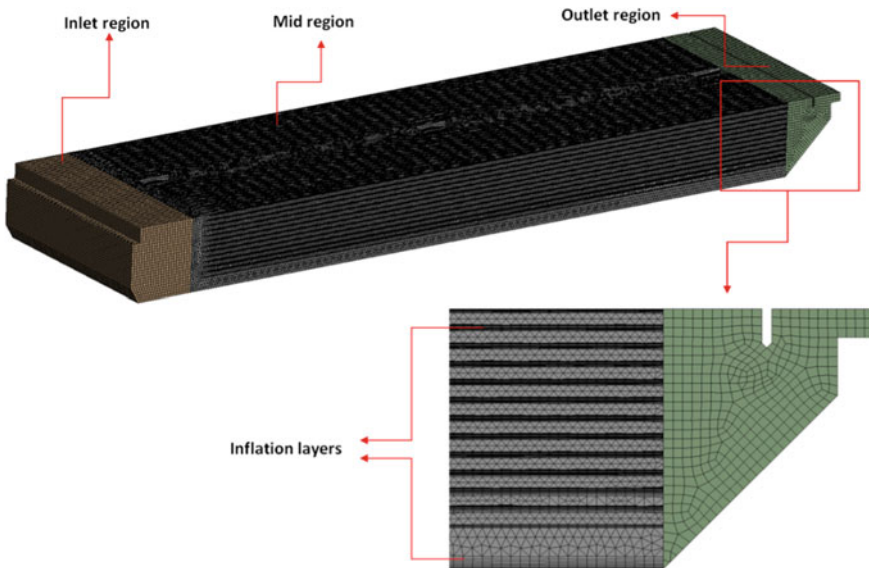


Fig. 3 The generated mesh for the modified geometry

2.2 Boundary Conditions

The inlet of the sedimentation tank is assigned as the ‘velocity-inlet’ boundary condition with 0.0281 m/s as the velocity magnitude. The primary phase (water), as well as the discrete phase (sediments), is discharged from the inlet surface at this velocity magnitude in the direction perpendicular to the specified inlet surface. As for the outlet, the ‘pressure-outlet’ boundary condition is assigned. ‘Symmetry’ boundary condition is assigned at the top of the sedimentation tank to model the zero-shear slip walls [8]. As for the inner surfaces of the sedimentation tank and the longitudinal inclined plates, the ‘stationary wall’ boundary condition is assigned with a ‘no-slip’ shear condition [9].

Additional boundary conditions specific to the DPM are required in order to decide the fate of the discrete particles when they come in contact with the boundary surfaces. The inlet and the outlet of the sedimentation tank are assigned the ‘escape’ boundary condition so as to allow free movement of the discrete particles through them. The bottom bed of the sedimentation tank and the upper surfaces of the longitudinal inclined plates (where sedimentation can take place) are assigned the ‘trap’ boundary condition. Any discrete particle that comes in contact with this boundary condition has its path terminated and its fate is reported as ‘trapped’ after the particle tracking process is completed. The ‘reflect’ boundary condition is assigned to the side walls of the sedimentation tank, the lower surfaces of the longitudinal inclined plates, and the inlet baffles. The discrete particles rebound off the surface when they come in contact with any surfaces with this boundary condition and continue on their path through the flow domain until it gets trapped or escaped.

2.3 Governing Equations

The governing equations are expressed as:

$$\frac{\partial u_i}{\partial x_i} = 0 \quad (1)$$

$$U_j \frac{\partial U_i}{\partial x_j} = -\frac{1}{\rho} \frac{\partial p}{\partial x_i} + \frac{\partial}{\partial x_j} \left(\nu \left(\frac{\partial U_i}{\partial x_j} + \frac{\partial U_j}{\partial x_i} \right) - \overline{u_i' u_j'} \right) \quad (2)$$

In the above equations, $u_i u_i$ is the instantaneous velocity along $x_i x_i$ direction; $U_i U_i$ and U_j are the mean velocity along x_i and x_j directions, respectively; ρ is the density fluid; p is the static pressure; and ν is the kinematic viscosity of the fluid. The term $\overline{u_i' u_j'}$ is solved using turbulence closure [10]. For this study, the $k - \omega$ SST (Shear Stress Transport) turbulence model is used since the geometries of our study comprise a good mixture of regions with near-wall region flows (when the

longitudinal inclined plates are present), and free surface flow region (in the absence of the longitudinal inclined plates).

The model used in this study calculates the path of each discrete particle injected using the resultant of all the associated forces on each particle. The resultant force is calculated by equating the inertia of the particle with that of the outside forces acting on the discrete particle, as shown in Eq. (3).

2.4 Particle Size Distribution

For WWT, the particle size distribution of Vahidifar et al. [7], which was obtained through the Particle Size Analyst (PSA) test is used. As for the PWT, the particle size distribution of Goula et al. [11], which was obtained using the Laser Diffraction Analyser.

2.5 Settling Efficiency Calculation

The settling efficiency for a particular particle class (E_i) and the total settling efficiency for a particular case (E_{total}) are calculated using Eqs. (3) and (4).

$$E_i = \left(\frac{n_{i, trapped}}{n_{total}} \right) \times 100\% \quad (3)$$

$$E_{total} = \sum_{i=1}^{13} \frac{E_i \times Mf_i}{100} \quad (4)$$

In Eqs. (3) and (4), $n_{i, trapped}$ is the number of particles reported as trapped for the i th particle class; n_{total} is the total number of particles tracked, i.e. 26,724; Mf_i is the mass fraction for the i th particle class.

2.6 Solution Procedure

As mentioned before, the fluid mechanics problem is decoupled and the steady-state flow characteristics of the primary phase (water) are calculated before the calculation of the path of the discrete particles (sediments) in the flow domain. This is accomplished by first obtaining a steady-state flow field of the primary phase and then the discrete particles are ejected from the inlet into the sedimentation tank using DPM. The fate of each of these ejected discrete particles is reported at the end of the particle tracking process and also their unique path can be traced in the post-processing. This process of particle tracking is done for each of the particle classes by taking the mean

particle size as their representative particle diameter. Finally, the settling efficiency (E_i) for each of the particle classes is calculated using Eq. (4), and then the total settling efficiency (E_{total}) for each of the 6 cases studied is calculated.

A converged solution is deemed to be obtained only when the mass flow rate imbalance between the inlet and outlet is less than 1% and the residuals of each of the variables fall below 10^{-4} . It takes approximately 10 h for these conditions to be fulfilled for a single simulation. All the simulations performed in this study are carried out in a workstation that has 24 cores and 64 GB of memory using the commercial CFD solver—ANSYS Fluent®.

For the particle tracking process, 26,724 discrete particles are injected from the inlet surface with the same velocity magnitude and direction as that of the primary phase. A test similar to the grid-independence test was also performed for the selection of the number of particles to strike a balance between total computational time and the accuracy of the result obtained.

3 Model Validation

The numerical model adopted for this study is validated by comparing the settling efficiencies obtained using our model (for the WWT particle size distribution data) with that of the counterpart experimental values of Vahidifar et al. [7] for identical flow conditions and geometry. As can be seen from Fig. 4, there is a good agreement between the two studies except for the values of some fine particle sizes. The discrepancy of the settling efficiency values in this particle size range may be due to some erroneous readings in the experimental readings of Vahidifar et al. [7] since the settling efficiency of larger particles is always higher than that of the finer particles in nature, which is not the case in the experimental values. The same discrepancy was also observed in their study when they compared the experimental values with results from their numerical simulations in their quest to find a better-suited turbulence model for their study.

4 Results and Discussions

The effectiveness of the longitudinal inclined plates can be investigated by comparing the settling efficiencies in Table 1. Huge improvement in the settling efficiencies is observed—24.87% and 15.60% increase in total settling efficiency for the WWT and PWT particle size distribution, respectively—due to the introduction of the longitudinal inclined plates in the settling region. Besides the total settling efficiency, the settling efficiency for each of the particle classes is higher for the modified tank compared to that of the original tank.

From Fig. 5, it is observed that there is excellent dissipation of the turbulence kinetic energy after the addition of longitudinal inclined plates. This decrease in

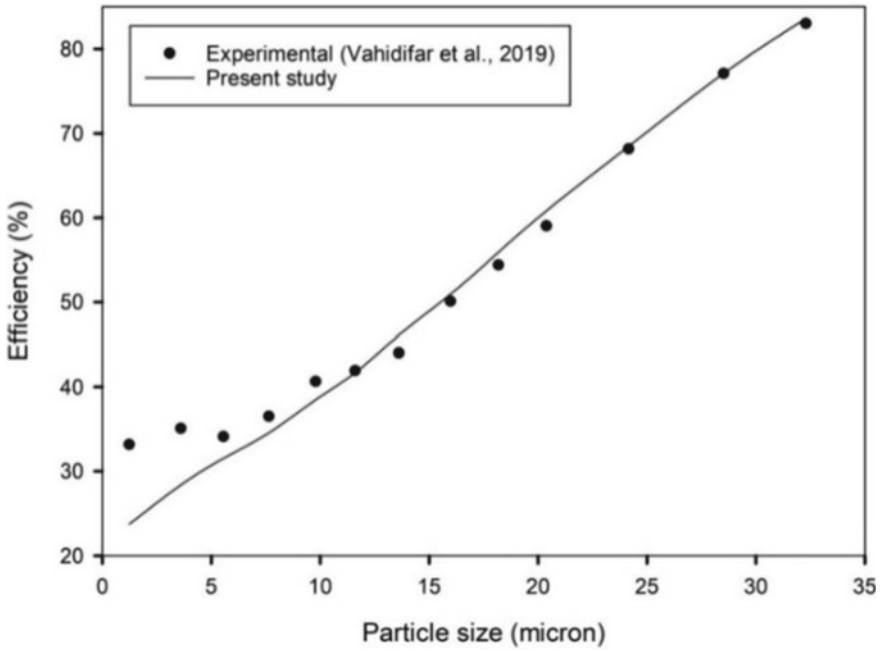


Fig. 4 Comparison plot of settling efficiencies obtained from this study with the counterpart experimental values of Vahidifar et al. [7]

Table 1 Calculated settling efficiencies for each of the particle classes

WWT			PWT		
Particle size (μm)	Original tank	Modified tank	Particle size (μm)	Original tank	Modified tank
1.232	33.16	50.47	20	26.69	50.90
3.6035	35.07	52.38	50	32.56	56.17
5.557	34.10	55.11	80	38.77	64.78
7.643	36.50	58.71	120	48.81	79.84
9.792	40.65	64.05	170	62.24	95.63
11.6045	41.93	68.70	200	69.64	98.96
13.6075	44.00	74.36	250	79.90	99.75
15.9815	50.08	81.64	350	92.17	99.74
18.188	54.39	87.89	450	95.84	99.75
20.385	59.03	93.14	550	96.43	99.88
24.1675	68.15	98.11	650	96.64	100.00
28.5265	77.10	99.42	750	97.30	100.00
32.3	83.01	99.81	850	97.41	100.00
Total efficiency	42.67	67.54	Total efficiency	79.15	94.75

turbulent kinetic energy allows the non-chaotic flow of sediments which results in easier sedimentation. Also, from Fig. 6, it is clear that the re-circulating currents have been eliminated besides slowing down the flow velocity, especially at the bottom part of the tank. This helps in eliminating any chances of re-suspension of settled particles.

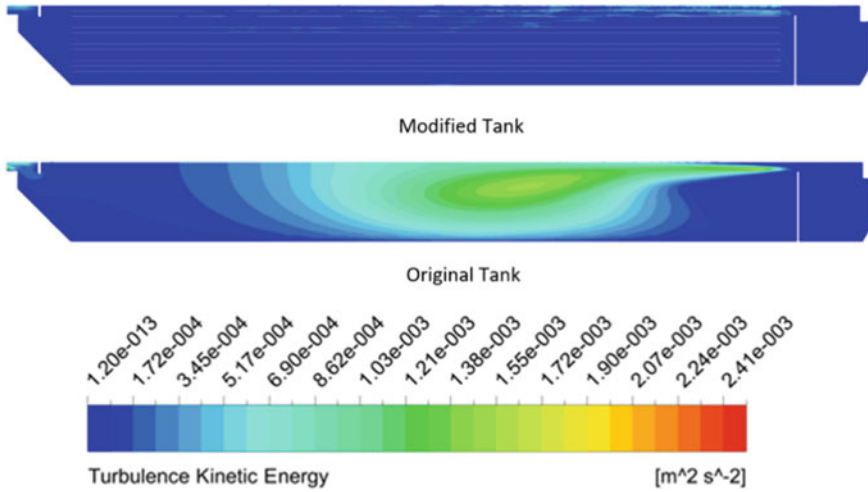


Fig. 5 Comparison of the contour of turbulence kinetic energy at the mid-width plane of one longitudinal half ($x = 2.875$ m)

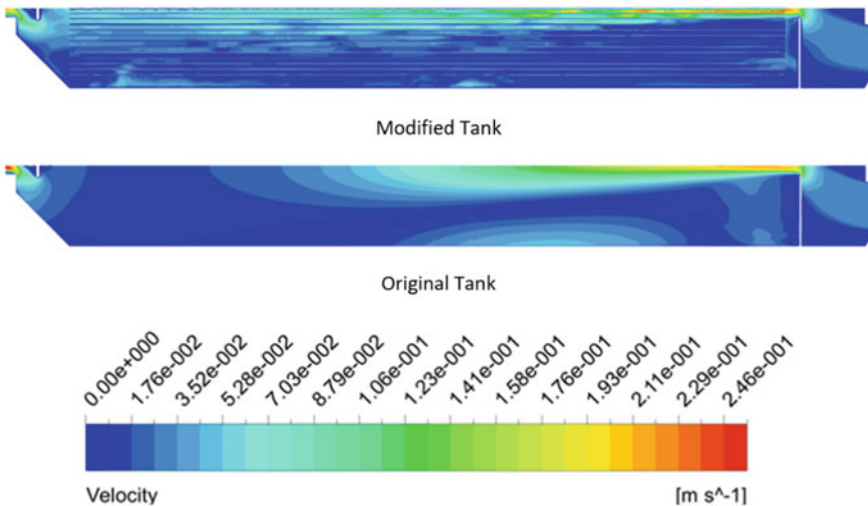


Fig. 6 Comparison of contour of velocity magnitude at mid-width plane of one longitudinal half ($x = 2.875$ m)

From these observations, it can be safely concluded that the longitudinal inclined plates are very much effective in increasing the settling efficiency and also the overall performance of the sedimentation tank by altering the hydrodynamics of the tank to suit the sedimentation process. Moreover, the longitudinal inclined plates also double up as additional settling beds and boost the settling capability of the tank.

5 Conclusion

The effectiveness of the longitudinal inclined plates in increasing the settling efficiency as well as the improvement in the overall performance of a rectangular sedimentation tank is thoroughly investigated through numerical simulations in this study. All the simulations in this study are done using a full-scale 3-D geometry to reduce errors. Experimentally obtained particle size distribution data of both the PWT and WWT are utilised in order to investigate any difference in results due to differences in the properties of the settling particles. The steady flow streamlines are obtained prior to the introduction of the settling particles using DPM and the efficiencies for each of the particle classes are calculated. Modifications are done to the existing sedimentation tank and compared with the original tank for improvements and any negative effects. Below are some of the key conclusions that can be drawn from the results obtained from this study.

- The introduction of longitudinal inclined plates helps in the dissipation of turbulent kinetic energy from the fluid flow and thereby improving the hydrodynamics of the sedimentation tank.
- The velocity of flow within the tank is also reduced greatly which aids in the sedimentation process.
- Adding the longitudinal inclined plates in the settling zone eliminates any chances of forming recirculation currents.

References

1. Al-Sammarraee M, Chan A, Salim SM, Mahabaleswar US (2009) Large-eddy simulations of particle sedimentation in a longitudinal sedimentation basin of a water treatment plant. Part I: Particle settling performance. *Chem Eng J* 152(2–3):307–314. doi: <https://doi.org/10.1016/j.cej.2009.04.062>
2. Boycott AE (1920) Sedimentation of blood corpuscles. *Nature* 104(2621):532. doi: <https://doi.org/10.1038/104532b0>
3. Takata K, Kurose R (2017) Influence of density flow on treated water turbidity in a sedimentation basin with inclined plate settler. *Water Sci Technol Water Supply* 17(4):1140–1148. <https://doi.org/10.2166/ws.2017.012>
4. Tarpagkou R, Pantokratoras A (2014) The influence of lamellar settler in sedimentation tanks for potable water treatment—A computational fluid dynamic study. *Powder Technol* 268:139–149. <https://doi.org/10.1016/j.powtec.2014.08.030>

5. Hirom K, Devi TT (2022) Determining the optimum position and size of lamella packet in an industrial wastewater sedimentation tank : a computational fluid dynamics study. *Water Air Soil Pollut* 233(261):1–16. <https://doi.org/10.1007/s11270-022-05742-2>
6. Nguyen TA, Dao NTM, Liu B, Terashima M, Yasui H (2019) Computational fluid dynamics study on attainable flow rate in a lamella settler by increasing inclined plates. *J Water Environ Technol* 17(2):76–88. <https://doi.org/10.2965/jwet.18-044>
7. Vahidifar S, Saffarian MR, Hajidavalloo E (2019) Numerical simulation of particle-laden flow in an industrial wastewater sedimentation tank. *Meccanica* 54(15):2367–2383. <https://doi.org/10.1007/s11012-019-01080-6>
8. Fluent A (2019) *Ansys fluent theory guide*. ANSYS Inc., USA, 15317:724–746
9. Gao H, Stenstrom MK (2019) Evaluating the effects of inlet geometry on the limiting flux of secondary settling tanks with CFD model and 1D Flux theory model. *J Environ Eng* 145(10):04019065. [https://doi.org/10.1061/\(ASCE\)EE.1943-7870.0001582](https://doi.org/10.1061/(ASCE)EE.1943-7870.0001582)
10. Tarpagkou R, Pantokratoras A (2013) CFD methodology for sedimentation tanks: the effect of secondary phase on fluid phase using DPM coupled calculations. *Appl Math Model* 37(5):3478–3494. <https://doi.org/10.1016/j.apm.2012.08.011>
11. Goula AM, Kostoglou M, Karapantsios TD, Zouboulis AI (2008) A CFD methodology for the design of sedimentation tanks in potable water treatment. Case study: The influence of a feed flow control baffle. *Chem Eng J* 140(1–3):110–121. doi: <https://doi.org/10.1016/j.cej.2007.09.022>

Behaviour of High Strength Steel Circular Hollow Section Subjected to Torsion—A Finite Element Study



Soibam Monika Devi, Sanasam Vipej Devi, and Tekcham Gishan Singh

1 Introduction

Increased research interest in high strength steels (HSS or high-performance steel) with strengths higher than 460 MPa has been observed in recent times due to their high strength-to-weight ratio compared to conventional low-strength steel. This enables the design of lighter and smaller structural members, reducing logistics and handling costs, and enabling the design of long-span bridges and high-rise buildings [1]. Among the family of hollow structural profiles, circular hollow sections (CHS) are preferred by structural engineers due to their high torsional and buckling resistance, as well as their attractive appearance. The use of HSS in CHS combines the advantages of both materials and structure, resulting in an efficient member for various structural applications [2]. Many researchers have conducted research on HSS, including experimental investigations on HSS with nominal strengths up to 1200 MPa for various tubular sections (SHS, RHS, and CHS) under compression [1–3]. The structural behaviour, material properties, and residual stresses have been examined. Experimental and numerical investigations on HSS members subjected to compression [4], bending, and combined loadings [5, 6] have also been conducted. Despite numerous studies on structural members subjected to torsion by various researchers, including the examination of steel CHS strengthened with Carbon Fibre Reinforced Polymer (CFRP) composites by Wu et al. [7], and the study of concrete-filled steel tubes under torsion by [8], and [9], the authors are not aware of any study on HSS subjected to pure torsion.

S. M. Devi · T. G. Singh (✉)

Department of Civil and Infrastructure Engineering, Indian Institute of Technology Jodhpur,
Jodhpur, Rajasthan 342030, India
e-mail: tekcham@iitj.ac.in

S. V. Devi

Department of Civil Engineering, National Institute of Technology Mizoram, Aizawl,
Mizoram 796012, India

Consequently, the objective of this study is to assess the structural behaviour of circular steel tubes made of HSS material when subjected to pure torsion. This paper presents an initial exploration that focuses on two grades of HSS, namely S700 and S900. A comprehensive examination is currently being carried out at the Department of Civil and Infrastructure Engineering, Indian Institute of Technology Jodhpur, India.

2 Finite Element Modelling

This paper utilizes the general-purpose FE software Abaqus [10] for numerical investigation. First, the finite element (FE) models were created and validated with test results from Beck and Kiyomiya [8] for carbon-steel CHS. Next, to focus on high strength steel, the accuracy of its material properties was checked. After validating both geometry and material modelling parameters, a parametric study was carried out. The key modelling parameters are explained in more detail in the subsequent sub-sections.

2.1 Geometry, Boundary Condition and Applied Load

The geometric dimensions, as presented in Table 1 and reported by Beck and Kiyomiya [8], were used for validation. The parameters D and t represent the section diameter and thickness respectively. The boundary conditions were implemented at two designated points located at the centroid of the cross-section at both ends. To distribute the applied torque evenly, the upper and lower edges were connected to the reference points using the kinematic coupling feature in Abaqus [10]. To impose a fixed-end condition at one end of the column, one of the reference points was restrained from all degrees of freedom (translations and rotations), while the other reference point was allowed to rotate about the longitudinal axis (all degrees of freedom were restrained except the longitudinal translation). A rotation about the longitudinal axis was applied at one end of the column to impose a pure torsion load.

Table 1 Dimensions and material parameters for validation

Steel grade	D (mm)	t (mm)	E (N/mm ²)	f_y (N/mm ²)	f_u (N/mm ²)
STK41	139.8	4	230,000	340.3	417.0

2.2 Material Property

The finite element models were validated using the material properties reported by Beck and Kiyomiya [8]. The generation of stress–strain curves was done using the revised two-stage Ramberg–Osgood model proposed by Gardner and Yun [11], which has been tailored to describe the behaviour of cold-formed steels. The stress–strain (f - ε) curves are presented in Eq. (1), as follows:

$$\varepsilon = \begin{cases} \frac{f}{E} + 0.002 \left(\frac{f}{E} \right)^n & \text{for } f \leq f_y \\ \frac{f-f_y}{E_{0.2}} + \left(\varepsilon_u - \varepsilon_{0.2} - \frac{f_u-f_y}{E_{0.2}} \right) \left(\frac{f-f_y}{f_u-f_y} \right)^m + \varepsilon_{0.2} & \text{for } f_y < f \leq f_u \end{cases} \quad (1)$$

$$E_{0.2} = \frac{E}{1 + 0.002n \frac{E}{f_y}}$$

where E , f_y , f_u , ε_u , $\varepsilon_{0.2}$, $E_{0.2}$, m and n are the Young's modulus, 0.2% proof stress, ultimate stress, strains corresponding to f_y and f_u , tangent modulus and strain hardening exponents respectively. The engineering stress strain has been converted into true stress σ_{true} and logarithmic plastic strain ε_{ln}^p , as defined by Eq. (2), which has been further employed in the FE models.

$$\begin{aligned} \sigma_{true} &= \sigma_{nom} (1 + \varepsilon_{nom}) \\ \varepsilon_{ln}^p &= \ln(1 + \varepsilon_{nom}) - \frac{\sigma_{true}}{E} \end{aligned} \quad (2)$$

where σ_{nom} and ε_{nom} are the engineering stress and strain respectively. Poisson's ratio of 0.3 has been considered for all FE models.

2.3 Element Type and Element Mesh

The FE models were discretized using shell elements due to their thin-walled nature. S4R four-noded doubly curved shell elements with reduced integration, featuring six degrees of freedom per node, were used. The six degrees of freedom include three translations and three rotations. A mesh size of $D_0/15$, as recommended by prior research [12], was applied to the FE model.

2.4 Geometric Imperfection and Residual Stress

The FE models were perturbed to account for imperfect geometry by superimposing the buckled mode shapes generated from Eigen-Value analysis [10]. The study analysed the impact of geometric imperfections with amplitudes of $t/100$, $t/50$, and $t/30$,

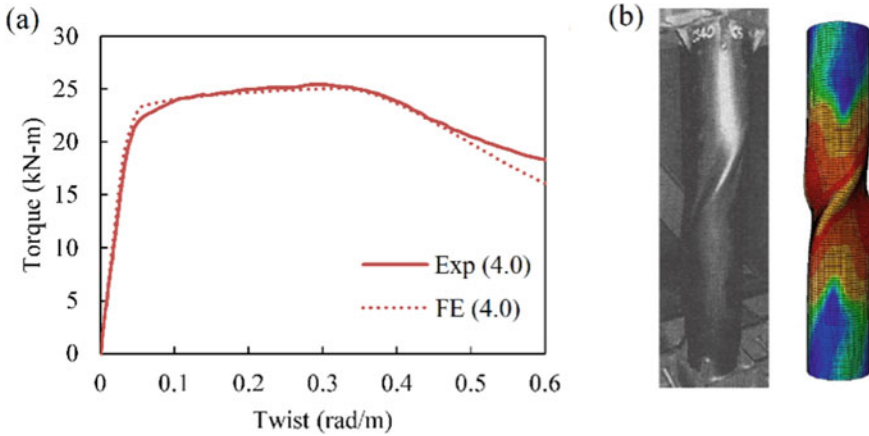


Fig. 1 Comparison of experimental and numerical results: **a** Torque versus twist curves, and **b** deformed shapes

scaled to the first Eigen buckling mode shape. The results showed that the capacity of the members was not significantly affected by the magnitude of the imperfections, except in the post-ultimate stage. The FE models did not account for global geometric imperfections, as the test members were short, or residual stress.

2.5 Validation of Finite Element Models

The numerical models developed using the above approach were verified using test results [8]. Figure 1a shows the comparison between the Torque (T)—twist (θ) curves generated from the FE models and the test results [8]. Figure 1b compares the deformed shapes. The FE models generally agree well with the test results, as seen in the figures. The FE models were created using the geometry and material properties reported by [12] and validated against the column capacity test results, as seen in Fig. 2, where good agreement was observed. Therefore, the modelling approach was used for further parametric study.

2.6 Parametric Study

The validated FE models were used in a parametric study. The material properties of HSS were taken from Ma et al. [12] for S700 and S900 steel and are summarized in Table 2. The outer diameter (D_0) was fixed at 150 mm and the thickness (t) was varied from 1.0 mm to 20 mm to cover a range of slenderness. The cross-section dimensions are summarized in Table 3. The length of the members was taken as

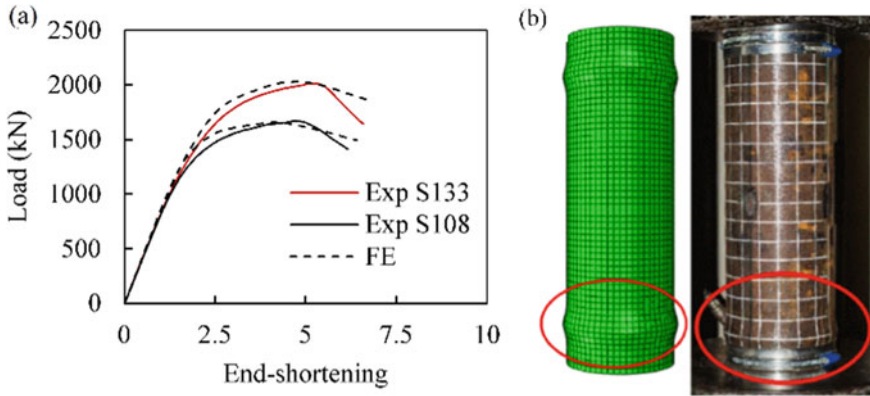


Fig. 2 Validation of FE modelling protocol for high strength steel: **a** Load versus end-shortening curves, and **b** deformed shapes

Table 2 Material parameters for parametric study

Steel grades	E (N/mm ²)	f_y (N/mm ²)	f_u (N/mm ²)	ϵ_u (%)
S700	214,000	772	816	4.6
S900	210,000	1054	1116	2.3

Table 3 Summary of cross-section dimensions of circular hollow section

Steel grades	D_0 (mm)	t (mm)
S700	150	1.0–20
S900	150	1.0–20

three times the outer diameter, following [12]. A stress–strain curve was generated using the material model proposed by Gardner and Yun [11] for cold-formed steel for the two grades of steel. A geometric imperfection in the form of the lowest buckling mode shape with a magnitude equal to $t/100$ was incorporated. Residual stresses were not considered as their effect is small and negligible [13, 14].

3 Analysis of Results

3.1 Deformed Shapes

The torque–rotation curves along with the corresponding deformed shapes of the slender and stocky members were presented in Figs. 3 and 4 for S700 and S900 steels. From the figures, it can be seen that slender sections for both S700 and S900, could not reach the yield load and strain-hardening characteristics. On the other hand,

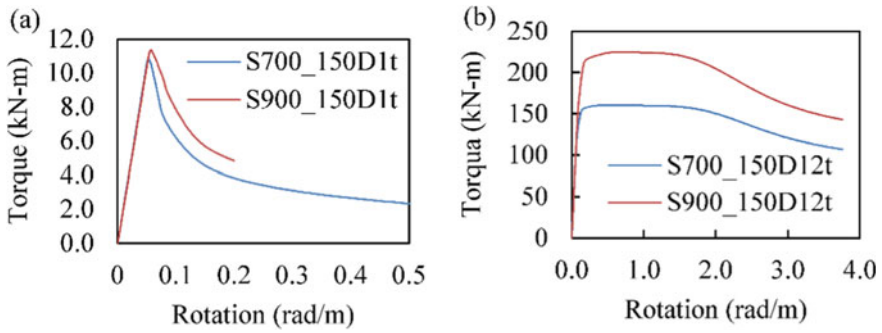


Fig. 3 Torque and rotation curves, a Slender sections, and b Stocky sections

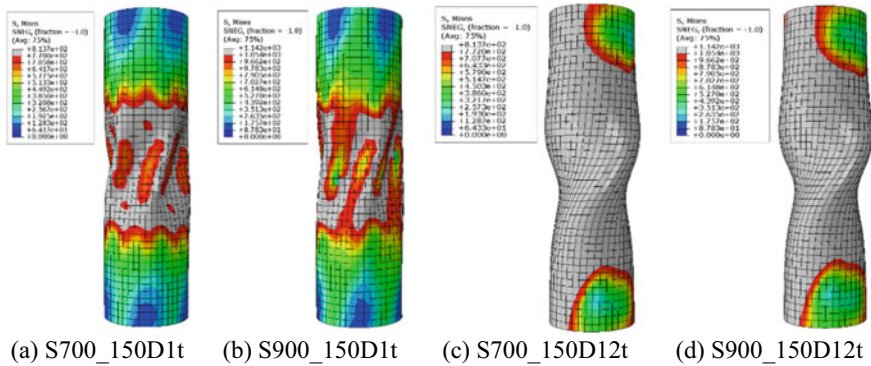


Fig. 4 Failure pattern of slender and stocky sections

clear strain-hardening characteristics can be achieved by stocky sections. In addition, slender sections are failed by local buckling, while material-yielding failure modes are observed for stocky sections, as can be seen from the Figs. 3 and 4.

3.2 Effects of Thickness

The variation of the torsional strength with respect to section thickness is presented in Fig. 5. It was observed that the torsional rigidity increases with an increase in cross-sectional thickness. A non-linear increase of $\sim +2100\%$ in torque resistance for S700, while a $\sim +2700\%$ for S900, is seen with the increase in thickness from $t = 1.0 - 20$ mm.

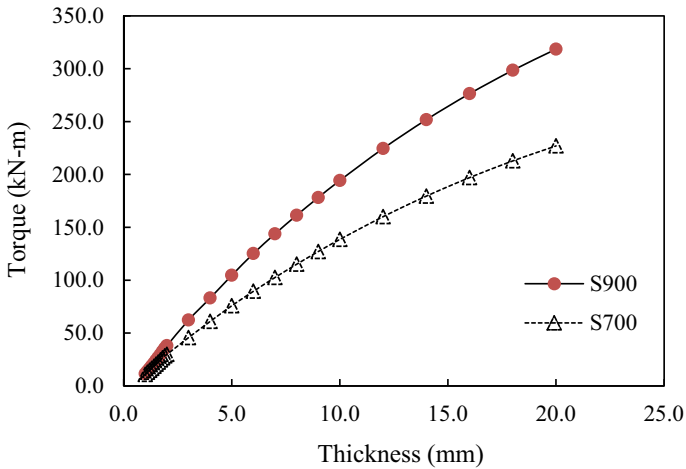


Fig. 5 Ultimate torque versus thickness comparison for S700 and S900

4 Conclusions

The present study aims to explore the torsion behaviour of circular hollow steel sections (CHS). The impact of varying thicknesses and steel grades on torsion behaviour was analysed through numerical investigation. The main conclusions of the study are:

1. Failure was observed to occur at the mid-height of the member, with the entire cross-sectional area contributing to torsional rigidity in the case of stocky sections.
2. Results indicate that torsional rigidity increases with increasing section thickness, with a non-linear increase of approximately $\sim 2100\%$ in torque resistance for S700 and $\sim 2700\%$ for S900 seen when thickness increases from 1.0 to 20 mm.

References

1. Hu YF, Xiao M, Chung KF, Ban H, Nethercot DA (2022) Experimental investigation into high strength S690 cold-formed circular hollow sections under compression. *J Constr Steel Res* 194:107306. <https://doi.org/10.1016/j.jcsr.2022.107306>
2. Ma J-L, Chan T-M, Young B (2016) Experimental investigation on stub-column behavior of cold-formed high-strength steel tubular sections. *J Struct Eng* 142:4015174. [https://doi.org/10.1061/\(asce\)st.1943-541x.0001456](https://doi.org/10.1061/(asce)st.1943-541x.0001456)
3. Kc A, Javidan F (2021) Circular hollow compression members of grade 1200 steel: experiments and design. *Aust J Struct Eng* 22:73–83. <https://doi.org/10.1080/13287982.2021.1889089>
4. Chen J, Chan T-M, Varma AH (2020) Stub column behavior of cold-formed high-strength steel circular hollow sections under compression. *J Struct Eng* 146:04020277. [https://doi.org/10.1061/\(asce\)st.1943-541x.0002828](https://doi.org/10.1061/(asce)st.1943-541x.0002828)

5. Pournara AE, Karamanos SA, Mecozzi E, Lucci A (2017) Structural resistance of high-strength steel CHS members. *J Constr Steel Res* 128:152–165. <https://doi.org/10.1016/j.jcsr.2016.08.003>
6. Meng X, Gardner L (2020) Cross-sectional behaviour of cold-formed high strength steel circular hollow sections. *Thin-Walled Struct.* 156:106822. <https://doi.org/10.1016/j.tws.2020.106822>
7. Wu C, He L, Ghafoori E, Zhao XL (2018) Torsional strengthening of steel circular hollow sections (CHS) using CFRP composites. *Eng Struct* 171:806–816. <https://doi.org/10.1016/j.engstruct.2018.06.014>
8. Beck J, Kiyomiya O (2003) Fundamental pure torsional properties of concrete filled circular steel tubes. *Doboku Gakkai Ronbunshu* 2003:285–296. https://doi.org/10.2208/jscej.2003.739_285
9. Le KB, Van Cao V, Cao HX (2021) Circular concrete filled thin-walled steel tubes under pure torsion: Experiments. *Thin-Walled Struct* 164:107874. <https://doi.org/10.1016/j.tws.2021.107874>
10. Dassault Systèmes, ABAQUS/Standard 2021 User's Manual, Provid. RI. (2021)
11. Gardner L, Yun X (2018) Description of stress-strain curves for cold-formed steels. *Constr Build Mater* 189:527–538. <https://doi.org/10.1016/j.conbuildmat.2018.08.195>
12. Ma J-L, Chan T-M, Young B (2018) Design of cold-formed high-strength steel tubular stub columns. *J Struct Eng* 144:4018063. [https://doi.org/10.1061/\(asce\)st.1943-541x.0002046](https://doi.org/10.1061/(asce)st.1943-541x.0002046)
13. Gardner L, Nethercot DA (2004) Numerical modeling of stainless steel structural components—a consistent approach. *J Struct Eng* 130:1586–1601. [https://doi.org/10.1061/\(asce\)0733-9445\(2004\)130:10\(1586\)](https://doi.org/10.1061/(asce)0733-9445(2004)130:10(1586))
14. Chen J, Zhu JY, Chan TM (2020) Experimental and numerical investigation on stub column behaviour of cold-formed octagonal hollow sections. *Eng Struct* 214:110669. <https://doi.org/10.1016/j.engstruct.2020.110669>

LULC Dynamics Study and Modeling of Urban Land Expansion Using CA-ANN



Srija Roy  and Madhusudana Rao Chintalacheruvu 

1 Introduction

Urbanization, which refers to the rapid growth in the proportion of the urban population, i.e., people moving to urban areas from rural areas, can cause deep-seated economic, environmental, and societal impacts and is one of the significant causes of concern in recent times. Urbanization results in unequal distribution of population and natural resources resulting in expansion of urban sprawl, deforestation, soil erosion, soil degradation, Etc. India, one of the fastest developing nations, is the second most populated country, with 1.21 billion people. About one-third of the modern Indian population is urban population, and the rate of urbanization is increasing rapidly at the rate of 34.47%, which is a rise of 4% since the last decade [1]. One of the most noticeable impacts of urbanization and population explosion combined with the advancement of science and technology is evident from the rapid change in Land Use Land Cover (LULC) over the decades [2], and this change in land use and land cover types has a significant effect on the change in ecology in the past few years and is a crucial driver of global change. Land use refers to the purpose for which the land is used, such as the Built-up area. Similarly, land cover indicates that area's surface or ground cover, for example, forest, water bodies, Etc. Mass destruction of forests to convert the land into agricultural and built-up areas cause major adversities in the form of loss of biodiversity, ecological imbalance, and increased radiation, which in turn impacts the climate and biosphere as a whole [3].

LULC change detection involves the identification of the differences in the state of a LULC class by observing it at different periods [4]. The satellite imageries enable accurate mapping of various land use categories, which are essential for monitoring change. Butt et al. [5] demonstrated the method of using Landsat 5 and SPOT 5

S. Roy · M. R. Chintalacheruvu (✉)
Department of Civil Engineering, National Institute of Technology Jamshedpur,
Jamshedpur 831014, India
e-mail: cmrao.civil@nitjsr.ac.in

images of Simly watershed, Pakistan, to perform change detection after performing supervised classification in ERDAS by the maximum likelihood classifier algorithm. Rapid land use and land cover shift from vegetation and waterbodies to settlement areas, agricultural and barren lands were observed. A comparative study between the tools of Maximum likelihood classification (MLC), support vector machine (SVM), and artificial neural network (ANN) identified ANN as the best tool amongst them for the classification of Landsat Imageries [6]. A significant rise in accuracy and decrement in long training time was observed using an ensemble of neural networks for LULC classification. AdaBoost.M1 algorithm, when applied to a sequence of three-layer feed-forward neural networks, performed LULC classification more accurately than MLC and SVM tools [7]. Chen [8] pointed out the spatial variations of the impacts of rapid urbanization and population explosion on LULC change in China. Although the urbanization rate is comparatively lower in China, the risk of rapid urbanization and its various impacts on waste disposal, food sagacity, soil pollution, Etc. It cannot be ignored. Patra et al. [9] performed Spatio-temporal change detection analysis of LULC due to urban growth in Howrah Municipality of West Bengal, India. Satellite images were used to perform the analysis. Hydrometeorological parameters such as rainfall, temperature, Etc., were also taken into account for the analysis of the impacts of the rapid rate of urbanization in the last two decades. The effect of urbanization on groundwater level was evident from the water level fluctuations in the northern, northwestern, and southwestern parts of the city. The artificial Neural Network based cellular automaton (ANN-CA) model exhibited further accurate results on implementing LULC changes for 2010 and prediction analysis for future years of 2040 and 2060 [10]. ANN-CA model could also successfully explain the correlation between the dependent variables of urbanization.

Kakinada is the sixth largest city of Andhra Pradesh, India. It was selected as one of the sites of implementation of the Smart Cities Mission launched by the Government of India (GOI) in 2015 to develop sustainable infrastructure and improve the quality of life (KSC. Corporation Ltd.) This is why there has been a rapid increase in the rate of urbanization in the last decade. This Study aims to analyze and quantify the rate of change of various land use and land cover categories with the help of CA-ANN Remote Sensing & GIS. It also attempted to establish the existing correlation between the explanatory variables of elevation, slope, population density, distance from roads, stream networks, and built-up areas on LULC change. Finally, an attempt has been made to predict the future LULC scenario of Kakinada for the year 2030 and 2040 based on the Cellular Automata-based Artificial Neural Network Model (CA-ANN).

Remote sensing (RS) and geographical information system (GIS) approaches coupled with ANN-based models can play a crucial role in conservation and decision support management systems, which could provide important information regarding ground-level management actions for prioritizing efforts and can further be utilized for checking the viability as well as quantification of these interventions to reduce rapid and unplanned spread of Urban sprawl.

2 Study Area

Kakinada City has a total area of 906.67 sq. Km and is one the important centers of trade and commerce on the eastern coast. This city is situated near the delta region of the Godavari River in the state of Andhra Pradesh and stretches from 16.42°N to 17.88° N and 82.43°E to 82.80°E. Kakinada has relatively low-lying land, with many parts of the city lying below sea level. Elevation varies from 0 m to 66 m above mean sea level. The average elevation of the area is about 10 m (Fig. 1).

The seaport of Kakinada used to act as a barrier island by protecting its harbor. However, the port has lost its erstwhile status due to incessant silting by the Godavari River and the requirement of constant dredging to maintain a uniform sea bed depth of 1.2 to 1.8 m [11]. Kakinada enjoys a Tropical climate with hot and humid conditions prevailing almost throughout the year. Kakinada receives rainfall from the southwest monsoon winds, and the average annual rainfall varies from 1000 mm to 3000 mm in this region. This region is very densely populated and is situated in the coastal region, which faces a lot of devastating cyclones. It is also planned to develop Kakinada as a smart city with all the facilities such as WIFI, properly planned infrastructure developed, smart solid-waste disposal, Etc., owing to which a lot of recent changes in urban management and LULC are taking place. Analyzing the trends of change will be significant in understanding the current scenario.

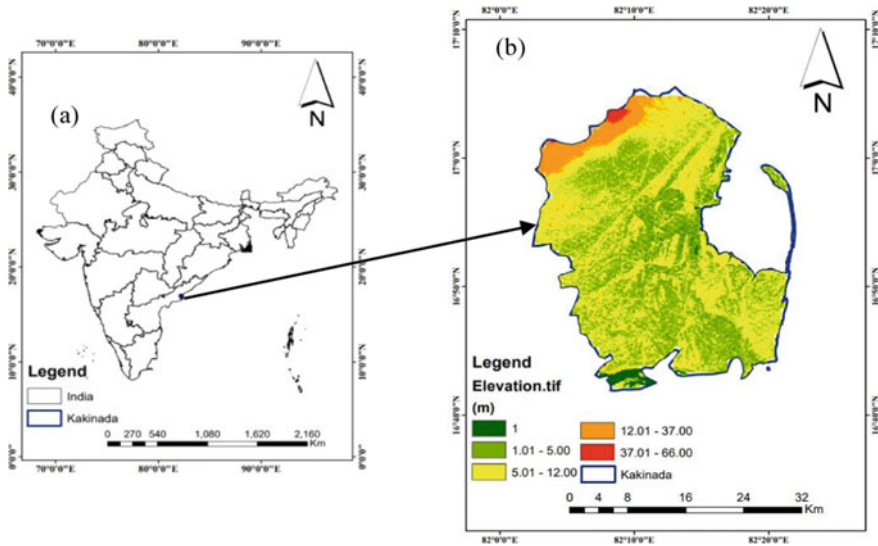


Fig. 1 Map of the study area under consideration. **a** Boundary map of India with Kakinada, **b** Kakinada district boundary

Table 1 Input data sets and their sources

Sl No	Datasets used	Source
1	Landsat5(08/12/1990); Path 141/Row 48, Resolution(m)-30	https://earthexplorer.usgs.gov/
2	Landsat7(08/12/2000); Path 141/Row 48, Resolution(m)-30	https://earthexplorer.usgs.gov/
3	Landsat5(04/12/2010); Path 141/Row 48, Resolution(m)-30	https://earthexplorer.usgs.gov/
4	Landsat8(21/11/2020); Path 141/Row 48, Resolution(m)-30	https://earthexplorer.usgs.gov/
5	SRTM DEM (30 m)	https://earthexplorer.usgs.gov/
6	Shapefile of India and Major Road layers	http://www.diva-gis.org/Data
7	Google Earth Images (1990, 2000, 2010 & 2020)	Google Earth
8	Gridded Population Density (2000, 2010 & 2020)	https://doi.org/10.7927/H49C6VHW [11]

3 Input Data

Landsat satellite data and DEM (30m), major roads, and FAO soil layers were downloaded for the study years of 1990, 2000 and 2010, and 2020. Google Earth Images of the respective years were further utilized for referencing and accuracy assessment. The datasets used in the Study and their sources are presented in Table 1.

4 Methodology

In order to perform land use and land cover classification of the selected study area, we applied an ensemble of RS and GIS-based CA-ANN models. These methods have the upper hand over the conventional methods of manual investigation of sites and validation from an authentic published survey of India (SOI) topographic maps. Landsat satellite images for 1990, 2000, 2010, and 2020 were downloaded and extracted for our study area. Radiometric correction and cloud removal of the satellite images were performed, followed by composite band creation and generation of False Colour Composite (FCC) in ArcMap 10.3. Digital Elevation Model(DEM) and population density layers for the years 2000,2010 and 2020 were downloaded from the Socio-economic data and applications center (SEDAC). Rectification and correction of the downloaded DEM were performed, followed by mosaicking. Sinks in the DEM were filled using the fill option of the hydrological toolbox. All the downloaded layers were resampled and reprojected to 30 m. The Projected Coordinate System (PCS), i.e., WGS 1984 UTM zone 44 N. LULC classification for all the years, was performed in ERDAS IMAGINE 2013 using the MLC algorithm. Accuracy assessment was

done by taking 300 random sample points for the generated LULC maps of 1990, 2000, 2010, and 2020. Change detection maps were generated to establish the trend of urbanization. Elevation and slope maps were generated using the surface toolbox of Arc toolbox in Arc Map 10.3. The stream network layer was extracted from them using the hydrology Toolbox of ArcMAP 10.3. Built-up areas and significant road layers were extracted for the study area, along with the creation of maps. Modules for land use change simulations (MOLUSCE) plugin was installed as a Python script in QGIS2.18.16. Wherein raster layers of 1990, 2000, 2010, and 2020 were used as input layers (i.e., initial and final state rasters, respectively) in the CA-ANN model based on which analysis and predictions were performed. The dependent variable, i.e., LULC change, was analyzed in correlation with the explanatory variables of elevation, slope, population density, and distance from major roads, streams, and settlement layers in the QGIS 2.18.16 using the CA-ANN model. Based on the LULC classification raster layers and the explanatory variable, the CA-based ANN model was trained by simulations of neural networks with thirteen iterations, a learning rate of 0.001, and a neighborhood of 6 pixels to produce prediction maps of LULC for the years 2030 and 2040. Validation of the projected layers was performed finally using kappa statistics.

5 Results and Discussions

The downloaded data was unzipped and were layer stacked in Arc GIS 10.3 software. The study area, i.e., the city of Kakinada, was extracted from the Landsat images over all the years. Pre-processing was done in QGIS to convert DN Numbers to surface reflectance using a semi-automatic plugin (SCP), [13]. A raster calculator in the map algebra toolbox of Arc Toolbox was used to perform the radiometric correction. The work has been carried out using the visual image interpretation technique at 1: 25,000 scales. ERDAS Imagine 2013, QGIS 2.18, and ArcGIS 10.3 software were used for image processing and mapping.

5.1 Classification of Satellite Images and Accuracy Assessment

Supervised image classification was performed for the years 1990, 2000, 2010, and 2020 in ERDAS Imagine 2013 by the Maximum Likelihood Classifier (MLC) classification algorithm. MLC is the most commonly used algorithm where the classification is done by identifying representative areas, called training zones. This method is based on the probability that a pixel belongs to a particular class. The basic theory assumes these probabilities are equal for all classes, and the input bands have normal

distributions. [13]. The LULC was classified into five major division's viz. agricultural land, built-up areas, vegetation, wetlands, and waterbodies, and is given below in Fig. 2. Following classification, accuracy assessment was performed for the classified images for all the years in ERDAS imagine 2013 to derive the accuracy of the information obtained from the data. Accuracy assessment was carried out by implementing the Kappa test and utilizing reference points from Google Earth. The Kappa test measures the extent of agreement between predefined producer ratings and user-assigned ratings and the kappa value varies between 0 and 1.

$$K = \frac{P(A) - P(E)}{1 - P(E)} \tag{1}$$

wherein P(A) is the number of times the k -raters agree, and P(E) is the number of times the k-raters are expected to agree only by chance [14, 15]. The obtained results of the accuracy assessment are given in Table 4.

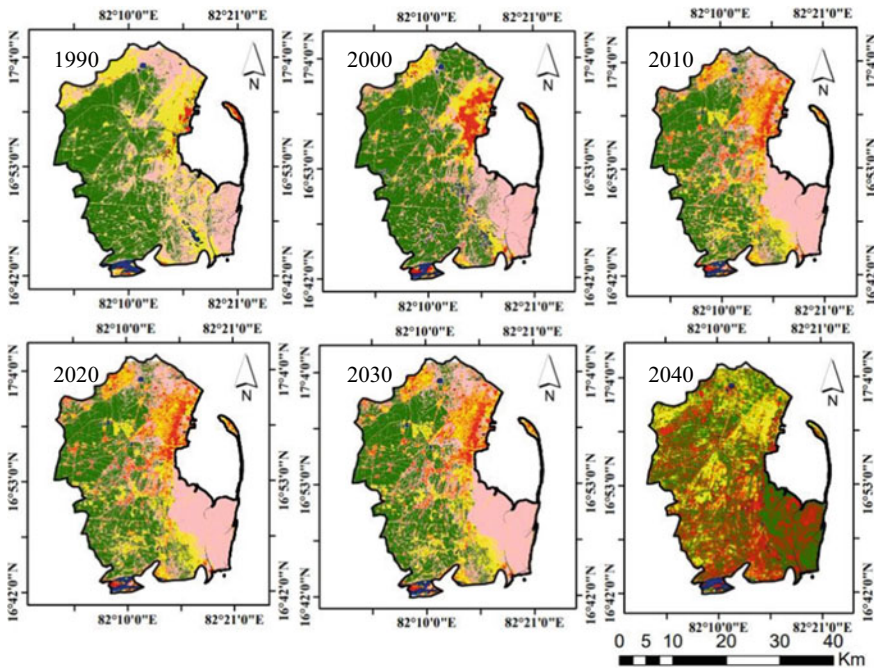


Fig. 2 Decadal Land use and Land Cover Classification Maps of Kakinada

Table 2 Cramer's Correlation Coefficients between explanatory variables (1990–2020)

Cramer's correlation	Elevation (30 m)	Population density (30 m)	Distance from roads (30 m)	Slope (30 m)	Distance from streams (30 m)	Distance from built-up areas (30 m)
Elevation (30 m)	–	0.16	0.61	0.06	0.22	0.11
Population density (30 m)		–	0.77	0.02	0.77	0.61
Distance from roads (30 m)			–	0.07	0.77	0.83
Slope (30 m)				–	0.07	0.05
Distance from streams (30 m)					–	0.65
Distance from built-up areas (30 m)						–

5.2 Explanatory Variables and Correlation Coefficient

For predicting future LULC scenarios, physiographic and socioeconomic parameters like elevation, slope, and distance from roads, settlement areas, and stream networks were considered along with the generation of the Cramer's correlation coefficient amongst each parameter (Table 2).

5.3 Cellular Automaton based Artificial-Neural-Network Model for Simulations and Prediction of Future LULC Scenarios

Land use and land cover change and simulations for future predictions of LULC change were performed using CA-ANN-based Modules for land use change evaluation (MOLUSCE) plugin of QGIS 2.18.16. This plugin involves the usage of classic Multilayer perceptron along with NumPy tanh sigmoid function [16], and the neural network layer consists of three layers, i.e., input, hidden, and output layers. The number of neurons and the number of hidden layers were initially set arbitrarily to train the model. After repeated simulations and model training, the number of iterations, as well as several hidden layers, was set to 7 by following [17] criteria of choosing $2n/3$ number of hidden layers, where n is the total number of spatial variables or attributes of each pixel. This criteria of choosing several hidden layers of a neural network produce accurate results while utilizing much less time for simulations. The transition probability was determined using multiple neural networks within the framework of the CA-ANN model. The Change map (Fig. 3) and the

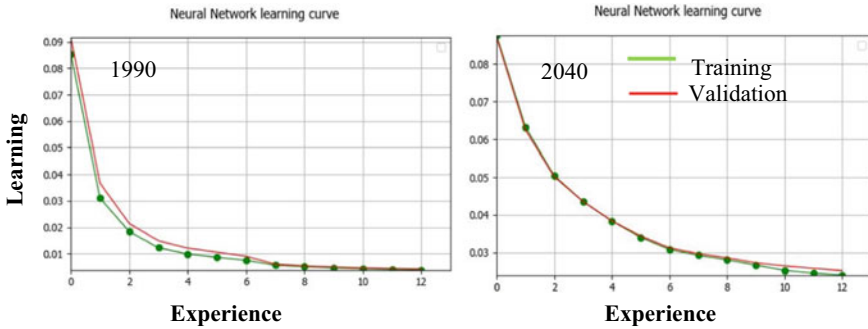


Fig. 3 Neural Network learning curve for 1990 and 2040 exhibiting learning versus experience relation

creation of projection maps were performed using a cellular automaton. Initially, the input raster layers, i.e., raster layers of the years 1990 and 2000 were given as inputs, followed by the raster layers of 2000, 2010 and 2010, and 2020 along with the explanatory variables of elevation, slope, distance from roads, streams, and settlement areas. Area analyzer error was removed by matching the geometries and LULC categories in the input layers. In the second step, the transition matrix of different LULC categories of each decadal change was produced. The Monte Carlo algorithm-based Cellular Automata approach is implemented to generate prediction maps of LULC for the years 2030 and 2040 (Fig. 2).

5.4 Simulations and Evaluation of Decadal Area Changes of LULC

The simulator module of the CA-ANN model performs LULC change evaluation. The predictor module takes into account the state of the initial and the factor rasters to depict the prevalent existing conditions as well as calculate the transition potentials of the factor rasters. The given neighborhood of the model was fixed to 6 pixels, and the transition potentials of every transition class were calculated. In order to perform simulations, the initial state rasters must be changed on the subsequent iterations, and the first simulated map must be used as the initial state raster to generate the results of the second iterations and so on.

Fig. 2 clearly depicts the rapid and immense expansion in the area occupied by the settlement areas from 1990 to 2040, along with the aerial changes in other LULC classes in the city of Kakinada. In Table 3, the decadal changes in the area of different LULC classes are quantified.

The simulator module of the CA-ANN model performs LULC change evaluation. The predictor module takes into account the state of the initial and the factor rasters to depict the prevalent existing conditions as well as calculate the transition potentials

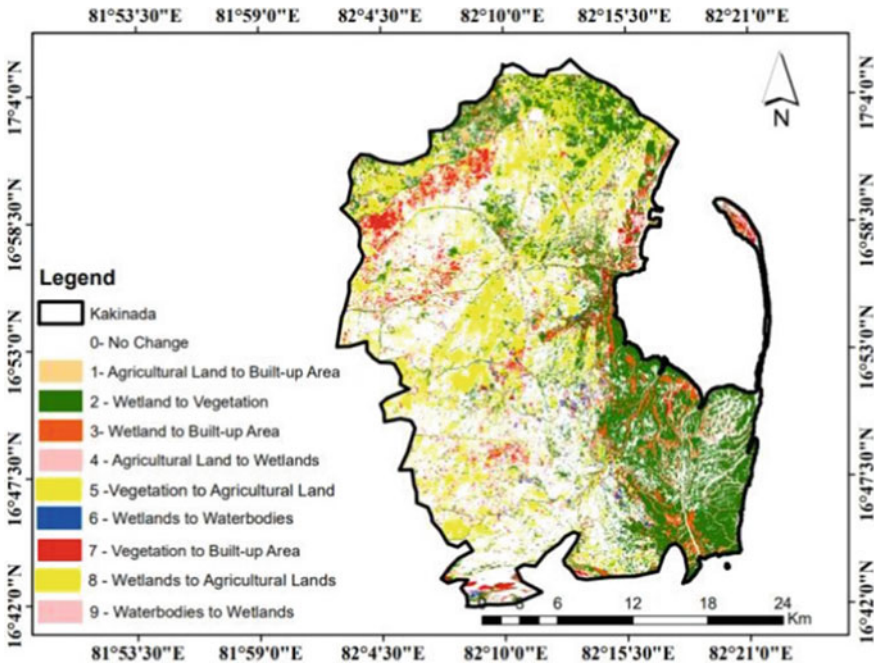


Fig. 4 LULC change map of the years 1990 and 2040

of the factor rasters. The given neighborhood of the model was fixed to 6 pixels, and the transition potentials of every transition class were calculated. In order to perform simulations, the initial state rasters must be changed on the subsequent iterations and the first simulated map must be used as the initial state raster to generate the results of the second iterations and so on.

Fig. 2 depicts the rapid and immense expansion in the area occupied by the settlement areas from 1990 to 2040 along with the aerial changes in other LULC classes in the city of Kakinada. In Table 3, the decadal changes in the area of different LULC classes are quantified.

5.5 Validation

The Kappa coefficient is used as the parameter for validation. Accuracy assessment was done for all the classified images of the year 1990, 2000, 2010, and 2020 and the prediction layers of 2040 (Table 2). Thus, after the model produced results of good kappa values, these layers were used as the initial state raster layer to generate a prediction map for the years 2030 and 2040 by the same CA-ANN model. The predicted map of 2040 provided sufficient accuracy, i.e., % of correctness and kappa values of 96.49 (kappa overall = 0.95), and the expansion of settlement areas is

Table 3 Decadal changes of LULC classes of the city of Kakinada (1990–2040)

LULC Class (1990–2040)	1990–2000		Change		2000–2010		Change		2010–2020		Change		1990–2040		Change	
	1990 (sq. Km)	2000 (sq. Km)	Area (sq. Km)	Δ (%)	2000 (sq. Km)	2010 (sq. Km)	Area (sq. Km)	Δ (%)	2010 (sq. Km)	2020 (sq. Km)	Area (sq. Km)	Δ (%)	1990 (sq. Km)	2040 (sq. Km)	Area (sq. Km)	Δ (%)
Agricultural lands	114.74	162.96	48.22	5.31	162.96	184.50	21.54	2.37	184.50	197.59	130.9	1.44	114.74	212.49	14.9	10.79
Built-up areas	60.15	90.24	30.09	3.31	90.24	134.28	44.04	4.85	134.28	188.98	54.7	6.03	60.15	223.52	163.37	18.02
Vegetation	408.59	298.49	-110.10	-12.14	298.49	233.06	-65.43	-7.21	233.06	287.96	54.9	6.05	408.59	293.55	5.59	-12.62
Wetlands	279.18	327.82	48.64	5.36	327.18	325.52	-1.66	-0.25	325.52	210.92	-11.4	-12.63	279.18	158.25	-52.67	-13.32
Waterbodies	44.13	27.28	-16.85	-1.85	27.28	29.43	2.12	0.23	29.43	21.18	8.22	-0.90	44.13	18.58	-2.6	-2.81

Table 4 Kappa statistics

YEAR	1990 (MLC)	2000 (MLC)	2010(MLC & ANN-CA respectively)	2020(MLC & ANN-CA respectively)	2040(ANN-CA)
% Correctness	93.80	92.00	93.39 & 96.71	93.42 & 96.77	96.494
Kappa(overall)	0.873	0.8502	0.862 & 0.956	0.865 & 0.958	0.9500

evident from the maps mentioned earlier, the city of Kakinada. Based on current trends, if urbanization of Kakinada happens at this rate, then the majority of the forest areas, i.e., vegetated lands and wetlands, will be converted into built-up and agricultural lands. Another notable observation from the prediction maps of 2040 is that the expansion of urban sprawl is happening along the lengths of the primary road layers and near the streams. Easy accessibility combined with a desire for a better quality of life is one of the major causes of Kakinada's rapid, unplanned urbanization.

6 Conclusions

This Study observed the rapid and unprecedented increment in the area occupied by built-up areas. The transition matrixes revealed that most vegetated wetlands are being converted into built-up and agricultural lands to mitigate the need for settlement and industrial expansion space. CA-ANN model provided results with sufficient accuracy after proper training of the ANN with historical data and explanatory variables. However, it should be noted here that no physical procedures, such as variations in temperature or rainfall, groundwater level, Etc., were considered to perform future predictions of changes in LULC. The prediction maps, though accurate, might vary from reality in the event of unprecedented catastrophes such as tsunamis, Amphan, Etc. Amongst the utilized explanatory variables, anthropogenic factors like population density and distance from roads and settlement areas were observed to be majorly impactful in urban expansion. Much population pressure and exploitation of natural resources in this region can lead to a significant cause of problems soon. Kakinada is expected to become a smart city. A lot of initiatives are already being implemented to address these issues of changing LULC and anthropogenic dynamics. However, being a low-lying coastal city, proper care must be taken for the disposal of solid waste management in and around the city, and the loss in the coastal wetland ecosystem must be mitigated by implementing sustainable growth and urbanization policies.

In this study, an analysis of LULC change in the city of Kakinada was performed. Also, in order to create an updated database and take preventive measures beforehand, predictions of LULC maps were created for the years 2030 and 2040. Thus, this study contributes to the efficient planning and management of land, forest, and water

resources by creating a database of information that can be considered before making decisions related to infrastructure planning and development.

References

1. Plecher H (2019) Global urbanization in India. Statista Report
2. Vitousek PK, Global Environmental Change: an introduction. *Ann Rev, Ecol System* 55(1):23:1–14
3. Riebsame WE, Meyer WB, Turner BL (1994) Modelling land-use and cover as part of global environmental change. *Clim Change* 28:45–64
4. Singh A (1989) Digital change detection techniques using remotely sensed data. *Int J Remote Sensing* 10(6):989–1003
5. Butt A, Shabbir R, Ahmed SS, Aziz N (2015) Land use change mapping and analysis using Remote Sensing and GIS: A case study of Simly watershed, Islamabad, Pakistan. *Egypt J Remote Sens Space Sci* 18(2):251–259
6. Srivastava PK, Han D, Rico-Raamirez MA, Bray M, Islam T (2012) Selection of classification techniques for land use/land cover change investigation. *Adv Space Res* 50:1250–1265
7. Canty MJ (2008) Boosting a fast neural network for supervised land cover classification. *Comput Geosci* 35:1280–1295
8. Chen J (2007) Rapid urbanization in China: A real challenge to soil protection and food security. *Catena* 69:1–15
9. Patra S, Sahoo S, Mishra P, Mahapatra SC (2018) Impacts of urbanization on land use/cover changes and its probable implications on local climate and groundwater level. *J Urban Manag* 7:70–84
10. Saputra MH, Lee HS (2002) Prediction of land use and land cover changes for North Sumatra, Indonesia, Using an Artificial-Neural-Network-Based Cellular Automaton. *Sustainability* 11:3024
11. Britannica T (2015) Editors of Encyclopedia. “Kakinada.” *Encyclopedia Britannica*, <https://www.britannica.com/place/Kakinada>
12. Centre for International Earth Science Information Network - CIESIN - Columbia University (2018) Gridded Population of the World, Version 4 (GPWv4): Population Density, Revision
13. Congedo, Luca. Semi-automatic classification plugin documentation., Release 4, no. 0.1 29. (2016):
14. Lillesand TM, Kiefer RW, Chipman JW (2008) Remote sensing and image interpretation. John Wiley & Sons Ltd. 6th edition (New York: John Wiley & Sons Ltd) (2008)
15. Gwet K (2002) Kappa statistic is not satisfactory for assessing the extent of agreement between raters. *Stat. Methods Inter-Rater Reliab*. *Int J Rem Sens* 23:2989–3008
16. Viera AJ, Garrett JM (2005) Understanding interobserver agreement: the kappa statistic. *Nat Libr Med*
17. NextGIS MOLUSCE-quick and convenient analysis of Landcover Changes. [https://nextgis.com/blog/molusce/\(2017\)](https://nextgis.com/blog/molusce/(2017)) (accessed 01 May 2019)
18. Li X, Chen G, Liu X, Liang X, Wang S, Chen Y, Pei F, Xu X (2017) A new global land-use and land-cover change product at a 1-km Resolution for 2010 to 2100 Based on Human-Environment Interactions. *Ann. Am. Assoc. Geogr.* (2017), 107, 1040–1059. (2014). doi:<https://doi.org/10.1088/0031-8949/2014/T163/014017>

Mapping of Suitable Areas for Mulberry Plantation Using GIS in Manipur



Deepali Gaikwad and Thiyam Tamphasana Devi

1 Introduction

Sericulture is a widely practiced agro-based industry in India and thus is the second largest producer of silk in the world. This sector contributes to the growth of economy in the country and helps to alleviate poverty. It can also provide various types of jobs, especially in rural areas with higher income as compared to other agricultural activities. Mulberry and castor (natural silkworm food plant) plantation help in preventing soil erosion in long term and such activity is eco-friendly. As mulberry and castor plants are perennial crops which have the property to maintain the ecosystem in the surrounding area due to its non-seasonal nature. Mulberry, Muga, Eri and Tasar are the types of silk widely grown in India [1] and becoming 2nd largest producer in the world.

Mulberry plantation prevents soil erosion and therefore study on soil erosion is encouraged. “Soil erosion is a serious problem arising from agricultural intensification, land degradation and other anthropogenic activities” [2–6]. Soil erosion not only lessens the productivity of agriculture, but also lowers the availability of water [7]. “The average amount of soil loss from natural erosion is around 0.1–1 t/ha/year; however, the soil loss becomes 10–1,000 times faster when erosion is exacerbated by human activities” [8]. Use of GIS (Geographic Information System) technology in agriculture and sericulture activities is highly beneficial and several studies conducted a mapping of site suitability for different crops and finding its management strategy with the help of satellite images and GIS tools [9–13].

D. Gaikwad

Department of Civil Engineering, Indian Institute of Technology, Ropar, Rupnagar,
Punjab 140001, India

T. T. Devi (✉)

Department of Civil Engineering, National Institute of Technology, Manipur, Langol 795004,
India

e-mail: thiyam85@gmail.com

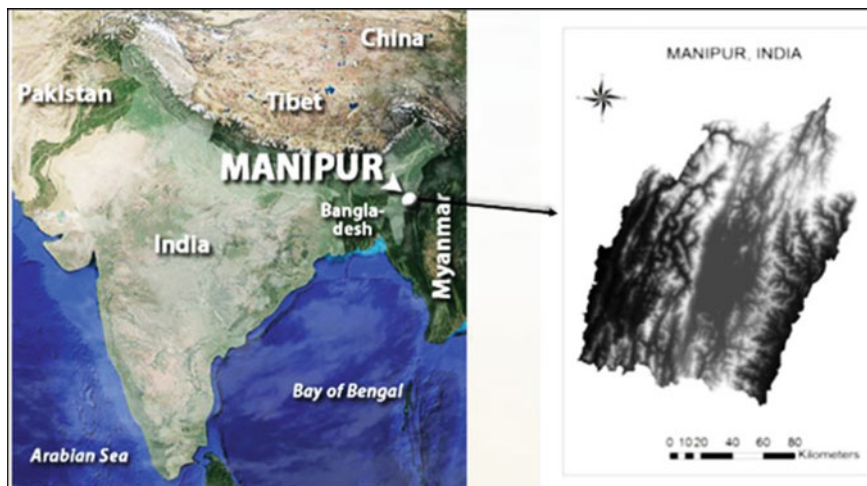


Fig. 1 Study area (Manipur)

In this study, mapping of a cultivable area or site suitability for mulberry plantation in Manipur state (north eastern part of India) is conducted using the soil loss model (Revised Universal Soil Loss Equation, RUSLE) with GIS techniques.

2 Study Area

The selected study area for this study is Manipur (north eastern state of India) which is shown in Fig. 1, having a total geographical area of around 22,437 km². Earlier, Manipur has 9 districts, i.e., Ukhrul, Chandel, Bishnupur, Thoubal, Imphal east, Imphal west, Churachandpur, Tamenglong and Senapati. Study area is 90% hilly terrain and remaining 10% is valley plain which is the central part of the state. Hilly part is covered by the red ferruginous soil and the central valley part is by alluvium soil. Climatic condition of the state is moderate and temperature range from few minus degrees in winter to a maximum of 37 °C in hottest summer. The annual average rainfall is in the range of 1200 mm to 1350 mm which is high as compared with other parts of India.

3 Materials and Methods

Different criteria (topographic and landscapes, soil characteristics and climatic parameters) were chosen for deciding the site suitability of the mulberry plantation. Overall methodology for mulberry cultivation is shown in Fig. 2.

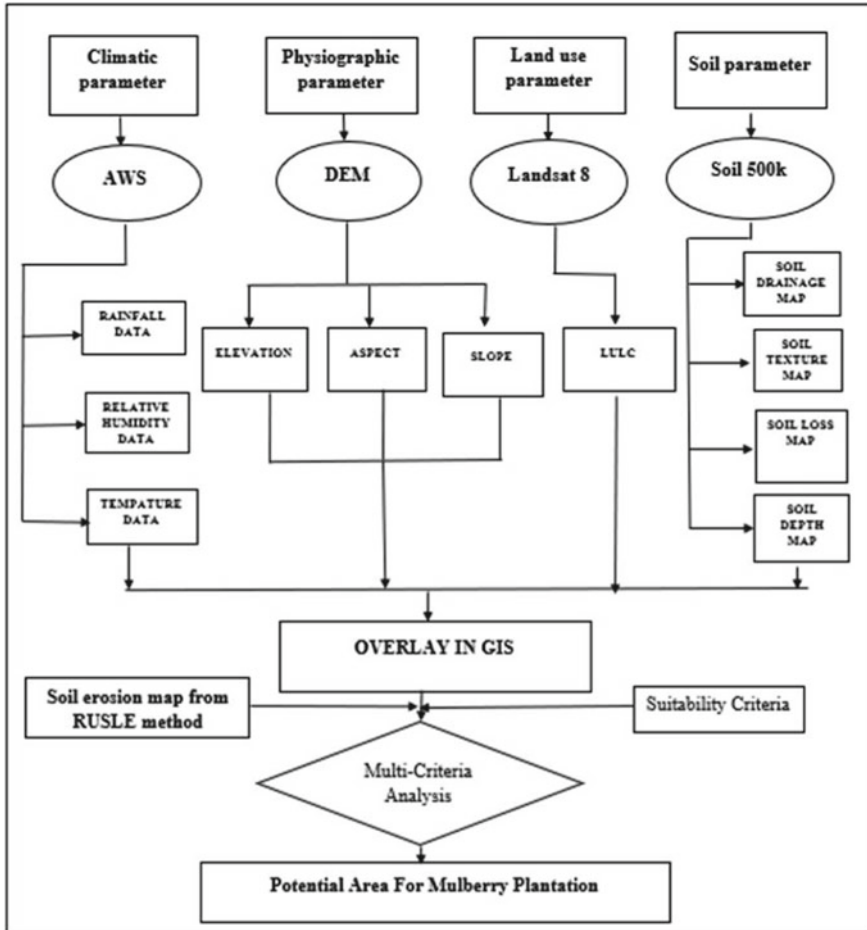


Fig. 2 Flowchart of methodology

The methodology of the RUSLE model adopted for this study is shown in Fig. 3. Assessment of suitability of land for sericulture has been done by different multi-thematic layers viz, climate conditions (temperature, rainfall and humidity), topographic conditions (slope and elevation), soil properties parameters (drainage, depth, erosion and texture) and cultivable land. For the climate condition AWS (automatic weather station) data were used for rainfall map and Land Surface Temperature map obtained by Landsat 8 satellite imagery.

Soil properties parameters were generated by the National Bureau of Soil Survey and Land Use Planning (NBSS-LUP) soil map on a 1:500,000 scale. Landsat 8 satellite imagery of year 2018 was used to compute cultivable land. Topographic maps were generated from Shuttle Radar Topography Mission—Digital Elevation Model (SRTM DEM, 30 m resolution). For quantitative assessment of soil erosion, soil

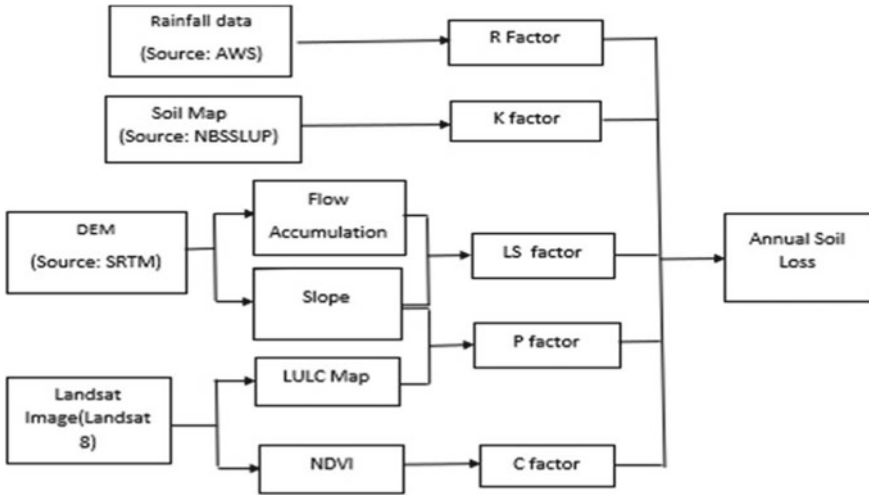


Fig. 3 Concept of RUSLE model

erodibility factor (K factor), rainfall erosivity factor (R factor), cover management factor (C factor), conservation practice factor (P factor) and slope length gradient (LS factor) were calculated by RUSLE [10, 12] model which can be written as:

$$A = R \times K \times L \times S \times C \times P \tag{1}$$

Here, A represents the annual average soil loss in tons/hectare/year. Land use/land cover was classified into six categories: forest, agriculture, wastelands, shifting cultivation, settlement (built-up) areas, and water bodies.

4 Results and Discussion

4.1 Results

From the landuse/landcover (LULC) analysis shown in Table 1, most of the area in the study location is covered with dense forest i.e. 17,122.74 km² (76.19%), settlement area is 1424.71 (6.64%) and water bodies area is 119.11 (0.53%) of total geographical area (TGA). The remaining area can be used for mulberry cultivation including agriculture, wasteland and shifting cultivation area, which is 3983.72 km² (16.96%).

Figure 4 shows the different forms of presenting soil textures like soil depth, soil drainage, soil erosion, soil texture; slope and land surface temperature map of the study area respectively. These factors are very important as it adversely affects

Table 1 LULC (2018)

LULC	Area (km ²)	% of TGA
Agriculture land	1250.95	5.57
Settlement area	1424.71	6.64
Forest	17,122.74	76.19
Shifting cultivation	22.47	0.1
Wastelands	253.654	11.29
Waterbody	119.11	0.53

the plantation. The soil textures in the study region are classified as very fine, fine and fine silty. Soil erosion is slight and moderate in 7.85% and 52.34% of the area respectively, which favors the plantation.

The major parts have very poor or excessive drainage which is not suitable for plantation. The depth is greater than 100 cm in 90.51% of the area, which is highly suitable. Slope varies from moderate (valley region) to very steep (hilly region). And

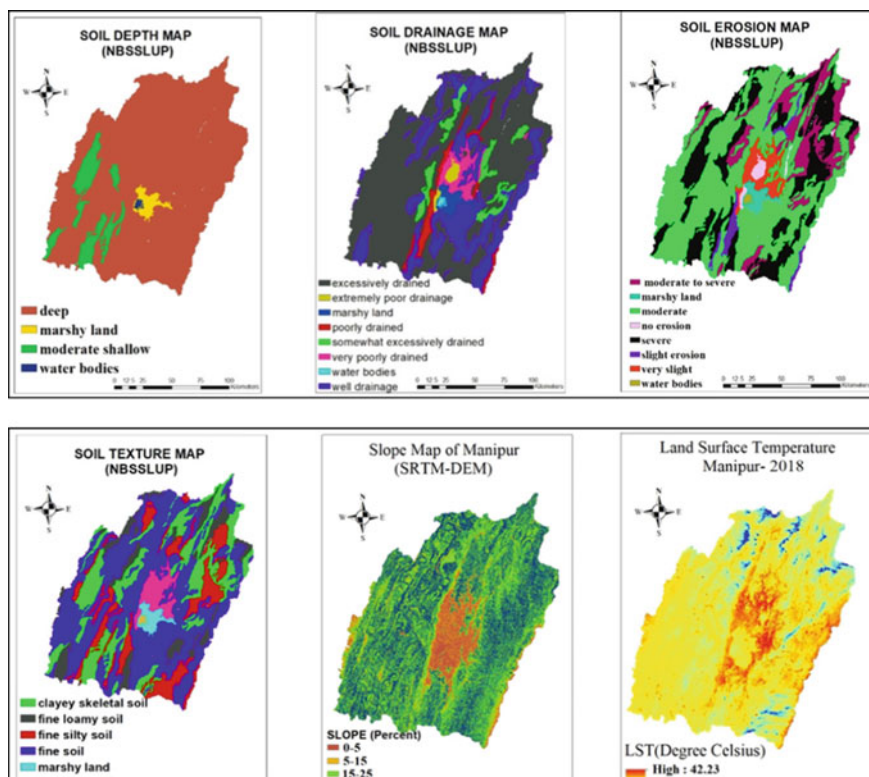


Fig. 4 Soil depth, soil drainage, soil erosion, soil texture, land surface temperature and slope of Manipur

from the land surface temperature map, it is also observed that temperature goes as much as high as around 42 °C and low as much as -7 °C but a majority of the study area is under moderate temperature (25 to 30 °C). It is understood that the temperature above 30 °C directly affects the health of the worm and the temperature below 20 °C worm becomes too weak and susceptible to disease. Study area comes in a heavy rainfall zone which can affect plantations adversely especially small plants.

Figure 5 shows different parameters (C, K, LS, P and R factors) for the assessment of quantitative analysis of soil loss map and soil loss map computed by RUSLE method. Soil erodibility factor (K) depends on soil composition and represents susceptibility to erosion and rate and amount of runoff. Length and degree of slope are indicated by topographic factor (LS) and it is directly proportional to erosion by water. Cover management factor (C) mainly depends on land use or vegetation cover. Area with vegetation cover shows less erosion. Rainfall erosivity factor (R) represents the erosion potential caused by rainfall. Conservation practice factor (P) depends on a slope under cultivable area category [10, 12]. In Fig. 5, including dense forest it has been found that 19,958.87km² (i.e. 90.68%) are favorable for mulberry cultivation in Manipur out of which 8458.78km² (38.43%) were highly suitable, 6816.071km² (30.97%) moderately suitable and 4684.02km² (21.28%) marginally suitable, but 1622.79km² (7.37%) not suitable. Quantitative assessment of soil loss is done by RUSLE model [10, 12]. Soil loss is categorized from very slight to very severe erosion range, details shown in Table 2 and suitability class in Table 3. It has been noted that the cultivable area also includes dense forests in this study. Using the present approach, soil loss assessment and mulberry suitability analysis can be carried out for all the districts and are presented in Table 4.

Figures 6 and 7 show the Soil Erosion risk by RUSLE model and potential sites for mulberry plantation in Manipur (2018). Very slight to moderate soil loss risk is stable for mulberry cultivation, so the total suitable area is 21,654.29 km² (98.05%) where the area of soil loss risk under very slight is 18,807.54 km² followed by a slight range of 2025.19 km² and under moderate is 821.56 km² (Fig. 6). Thus the study area was not found soil erosion hazardous. Suitable areas for mulberry plantations are all three categories of highly, moderately and marginally suitable areas. District wise suitability of mulberry plantation is presented in Table 4. The highest suitable area in whole state is 4116.73 km² found in Ukhrul district followed by Tamenglong district i.e. 3899.4 km² and the lowest 237.84 km² in Imphal west, due to more urbanization. The percentage of suitable area in a total geographical area in the district is highest in Churachandpur district.

4.2 Discussion

The average soil loss rate was estimated as 40.519 t/ha/yr and the maximum value was found as 81.038 t/ha/yr. The predicted soil loss rate and its spatial distribution map can be informative in comprehensive and sustainable land management to mitigate

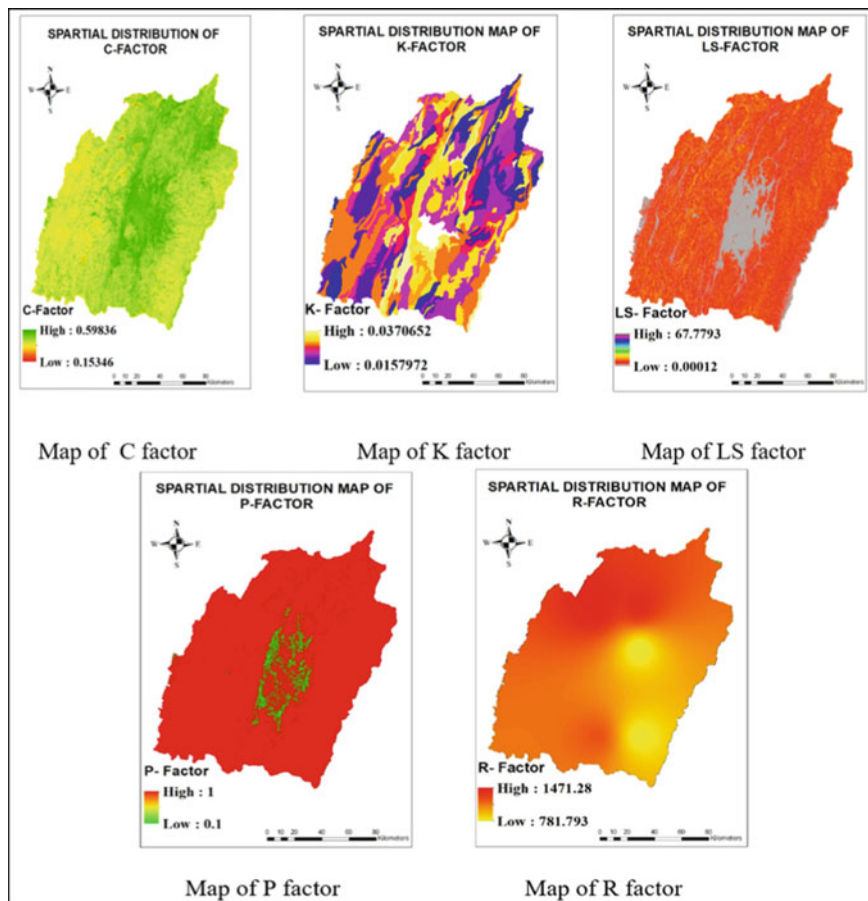


Fig. 5 Parameters assessment for quantitative analysis of soil loss map and soil loss map computed by RUSLE method

Table 2 Percentage of area of soil erosion risk in Manipur

Soil loss (t/ha/year)	Range	Area in km ²	Area in percentage
0–5	Very slight	18,807.54	85.16
5–10	Slight	2025.19	9.17
10–20	Moderate	821.56	3.72
20–40	Severe	46.38	0.21
40–80	Very severe	2.65	0.012

Table 3 Suitable areas for Mulberry cultivation in Manipur

Class	Area in km ²	Area in percentage
Highly suitable	8458.78	38.43
Moderately suitable	6861.07	30.97
Marginally suitable	4684.02	21.28
Not suitable	1622.79	7.37

Table 4 District wise area (km²) of mulberry plantation in Manipur

Districts	Total area (km ²)	Highly suitable (km ²)	Moderately suitable (km ²)	Marginally suitable (km ²)	Not suitable (km ²)	Total suitable area (km ²)
Ukhrul	4396.11	1083.37	1919.24	1114.11	279.38	4116.73
Chandel	1901.88	1056.06	141.40	609.40	95.023	1806.86
Bishnupur	265.12	81.367	36.99	64.26	82.51	182.614
Thoubal	477.97	163.87	93.89	114.94	105.27	372.7
Imphal east	558.76	202.56	87.057	129.16	139.97	418.785
Imphal west	437.56	42.68	26.74	168.42	199.72	237.84
Churachandpur	4834.81	1767.88	1963.06	862.61	241.26	4593.55
Tamenglong	3964.84	1557.92	1732.04	609.44	65.44	3899.4
Senapati	3398.08	829.03	1168.73	994.046	406.27	2991.81
Total	20,235.13	6784.77	7169.14	4666.38	1614.84	18,620.29

soil erosion hazards. GIS-based RUSLE methodology can be implemented to assess the spatial distribution of erosion risk zone in the study area.

This has been observed that both maps (prepared based on NBSS-LUP and RUSLE method) vary significantly, in soil loss map by NBSSLUP, moderate erosion risk has been observed in maximum percentage of areas in Manipur (i.e. 52.45%) whereas in soil loss by RUSLE model, very slight erosion risk observed maximum percentage of areas in Manipur i.e. 85.16%. However, severe erosion risk was observed minimum percentage of areas in Manipur i.e. 0.21% in soil loss by NBSS-LUP whereas very severe erosion risk was observed minimum percentage of areas in Manipur i.e. 0.012% in soil loss by RUSLE method.

This study has some limitations as RUSLE model use for long term soil loss evaluation but here only one year of losses has been computed. PH data and relative humidity have not been taken as a parameter for soil suitability assessment. And this study has not considered a future expansion of urbanization and development.

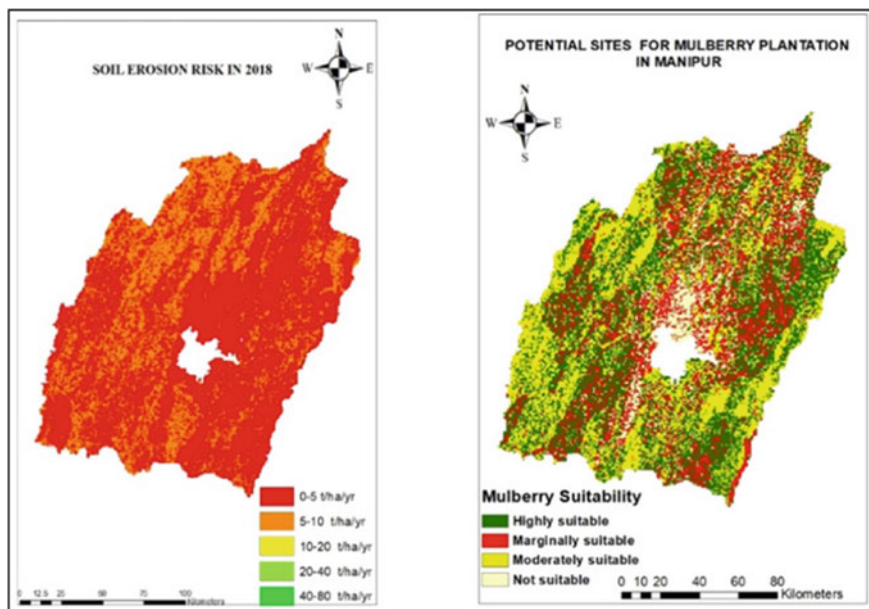


Fig. 6 Soil erosion risk by RUSLE model and potential sites for mulberry plantation in Manipur (2018) map

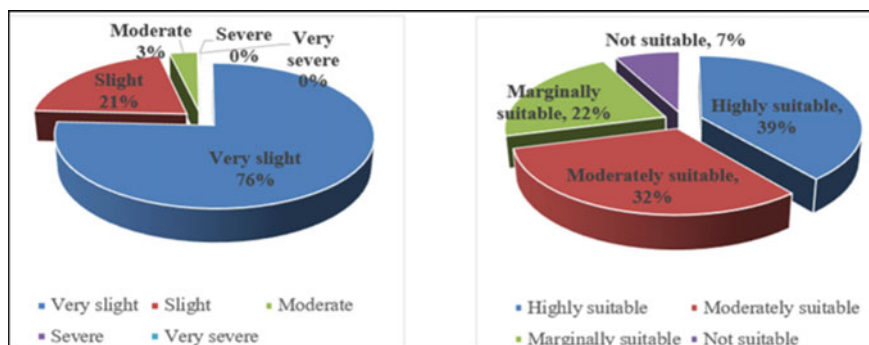


Fig. 7 Pie chart of soil erosion risk by RUSLE model and potential sites for mulberry plantation in Manipur (2018)

5 Conclusions

GIS and remote sensing techniques were utilized for mapping site suitability of mulberry cultivation in Manipur in the present study. By providing the removal or improvement of limiting parameters, the areas mapped under not suitable category can be turned into highly, moderately and marginally suitable areas, which increases

the area for mulberry plantation. Mulberry cultivation gives employment opportunities to the farmer throughout the year, which empowers socioeconomic activity for the farmers. Active support of concerned state government authorities can help to achieve this goal.

References

1. Sharma NK, Jeyaseelan AT, Ravish K (2012) Geospatial technology for sericulture development in Jharkhand: a pilot study, Jharkhand space applications center. *J. Rem. Sens. GIS.* 3(2):34–45
2. Xie Y, Lin J (2010) RUSLE model based quantitative evaluation on the soil erosion of Wen County of Gansu Province, China. In: 2010 18th International Conference on Geoinformatics, Beijing (2010) 1–6
3. Ganasri BP, Ramesh H (2016) Assessment of soil erosion by RUSLE model using remote sensing and GIS—A case study of Nethravathi Basin. *Geosci Front* 953–961. doi:<https://doi.org/10.1016/j.gsf.2015.10.007>
4. Gayen A, Saha S, Pourghasemi HR (2019) Soil erosion assessment using RUSLE model and its validation by FR probability model. *Geocarto Int* 35(15). doi: <https://doi.org/10.1080/10106049.2019.1581272>
5. Panditharatne DLD, Abeysingha NS, Nirmanee KGS, Mallawatantri A (2019) Application of Revised Universal Soil loss equation (Rusle) model to assess soil erosion in “Kalu Ganga” river basin in Sri Lanka. *Appl Environ Soil Sci* 1–15. doi: <https://doi.org/10.1155/2019/4037379>
6. Ghosal P, Bhattacharya SD (2020) A Review of RUSLE model. *J Indian Soc Remote Sens* 48(1):689–707. <https://doi.org/10.1007/s12524-019-01097-0>
7. Kouli M, Soupios P, Vallianatos F (2009) Soil erosion prediction using the revised universal soil loss equation (RUSLE) in a GIS framework, Chania, Northwestern Crete, Greece. *Environ Geol* 57:483–497. <https://doi.org/10.1007/s00254-008-1318-9>
8. Demirci A, Karaburun A (2012) Estimation of soil erosion using RUSLE in a GIS framework: a case study in the Buyukcekmece Lake watershed, northwest Turkey. *Environ Earth Sci* 903–913. doi: <https://doi.org/10.1007/s12665-011-1300-9>
9. Kalita P, Goswami C (2018) Identification of potential sites for Mulberry cultivation in West Garo Hills of Meghalaya using geospatial techniques. North Eastern Space Applications Centre (NESAC), Umiam
10. Kalita J, Deka B, Kalita DN (2018) Assessment of rice-based cropping systems for maximizing productivity and profitability in Kamrup district of Assam. *Int J Agric Sci* 10(18):7209–7211
11. Wischmeier WH, Smith DD (1978) Predicting rainfall erosion losses: a guide to conservation planning. *Agriculture Handbook* 282 USDA-ARS, USA
12. Handique BK, Das PT, Goswami J, Goswami C, Singh PS, Prabhaka CJ, Bajpeyi CM, Raju PLN (2016) Expansion of sericulture in India using geospatial tools and web technology. *Curr Sci* 111(8):1312–1318. <https://doi.org/10.18520/cs/v111/i8/1312-1318>
13. Patil BR, Singh KK, Pawar SE, Maarse L, Otte J (2011) A Living from Livestock Research Report, 2011, RR No: 09-03

Performance Appraisal of Ravi Shankar Sagar Project Using Comparative Indicators



Nikki Chanda , Madhusudana Rao Chintalacheruvu , Choudhary, and A. K. 

1 Introduction

The limited availability of water resources and increasing water demand in various sectors, such as food and energy, create a gap between demand and supply. The variations in inflow into the reservoir, meteorological conditions, lifestyle changes, and increasing population have contributed to new challenges and highlighted the necessity of strategic management of water resources. Water resource management is crucial for irrigation facilities. Due to the unfavorable monsoon in India, irrigation production and food harvest are primarily irrigation dependent on surface water reservoirs [1, 2]. Hence, performance monitoring of the reservoir is essential to satisfactorily meet the varying water demand in various areas such as agriculture, municipal, industrial, and hydropower generation. Performance assessment of reservoirs has gained prominence in recent years, making it essential to pursue new projects and enhance the effectiveness of current projects [3, 4].

Apart from performance assessment, periodic evaluation of reservoir operating policies is a must for optimum storage water utilization to resolve the complexities of the multipurpose reservoir system. An optimization algorithm cannot be universally applicable [5] as it depends on several factors such as inflows, physical characteristics, constraints, Etc. Therefore specific optimization technique is developed for a particular study area. It is well known that Linear Programming is frequently utilized as an optimization technique in water resources planning and management. The LP through LINGO was used and developed optimal operating policies to estimate actual deficits and reduced deficits of RSSP during 1981–2010 and measured performance based on vulnerability, reliability, and resilience [6].

N. Chanda · M. R. Chintalacheruvu (✉) · Choudhary · A. K.
Department of Civil Engineering, National Institute of Technology Jamshedpur,
Jamshedpur 831014, India
e-mail: cmrao.civil@nitjsr.ac.in

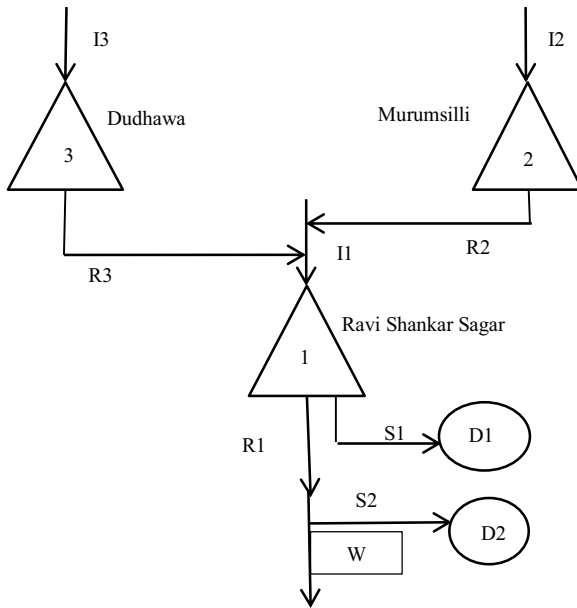
Particle Swarm Optimization (PSO) computational algorithm through MATLAB provided optimal operating policies for RSSP during 1965–1995 [7]. These studies are done in the RSSP, emphasizing the optimal operating policies developed by conventional approaches. Therefore, to be different from other studies, the present study is carried out to provide optimum operating policies using LP through Python 3.9 script and assessed eight selected comparative performance indicators, namely, (i) agricultural (standard gross value of production (SGVP)); (ii) water-use (relative water and irrigation supply); (iii) Physical (irrigation ratio), and (iv) Hydropower (relative power supply). Performance indicators evaluation to attain the strategic objectives and develop optimum reservoir operation are the need of the hour. This study helps improve reservoir operation's efficacy by maximizing the benefits and developing effective management and operational procedures to address complex challenges.

2 Study Area

Ravi Shankar Sagar is a multipurpose reservoir with geographical coordinates $20^{\circ}37'N$ and $81^{\circ}34'E$ built in 1978 by constructing Gangrel Dam (Fig. 1). It is one of the largest storage structures in the Mahanadi river basin, situated in Dhamtari district, Chhattisgarh. The other two reservoirs on the Mahanadi river basin, Murumsilli, and Dhudhawa are feeder reservoirs of RSSP. This reservoir meets various irrigation, municipal, industrial, and hydropower generation demands. The reservoir is 25 km long and 15 km wide and has a catchment area of 367,000 ha. The total installed hydropower capacity is 11.20 MW. The reservoir has a gross capacity of 910 Mcum and a dead storage capacity of 144 Mcum. The annual irrigation capacity of the project is 239000 ha, intended to irrigate 264,310 ha of the Cultural Command Area. The catchment area receives an average rainfall of 1288 mm. The irrigated area predominately consists of black clayey soil.

3 Methodology

A framework for performance evaluation of RSSP is proposed and applied for a case study. Performance assessment is measured using a set of selected indicators, which provide the level of performance related to irrigation and hydropower. The set of performance indicators given by many researchers is water use performance, agricultural performance, economic performance, and environmental performance on varied schemes like agricultural production, economic management, water-use management, physical, hydropower generation, environmental management, Etc. [8–10]. Among the above-mentioned indicators, eight indicators used



- | | | | |
|---------------|---------------------|------------------------|--------------------------------------|
| Reservoir : | Inflow in reservoir | Release from reservoir | Supply in Canals |
| 1 Ravishankar | I1 : Ravishankar | R1 : Ravishankar | S1 : Supply in Mahanadi Feeder Canal |
| 2 Dudhawa | I2 : Dudhawa | R2 : Dudhawa | S2 : Supply in Mahanadi Main Canal |
| 3 Murumsilli | I3 : Murumsilli | R3 : Murumsilli | |
| W : | | | Demands : |
| Rudri Weir | | | D1 : Mahanadi Feeder Canal |
| | | | D2 : Mahanadi Main Canal |

Fig.1 Schematic diagram of RSSP

in this study described underwater use performance, physical performance, agricultural performance, hydropower performance associated with agriculture outputs, and hydropower.

3.1 Physical Performance

Physical indicators relate to the loss or alteration of irrigable land in the catchment command area for various reasons. To estimate the physical performance, possession of irrigable land is calculated by the ratio of irrigated to irrigable land.

$$\text{Irrigation ratio} = \text{Irrigated land} / \text{Irrigable land.}$$

3.2 Agricultural Performance

Standardized Gross Value of Production (SGVP) provides an ease to estimate the irrigation system's performance without considering the type of crops grown; instead, it takes care of both local and international preferences. Equivalent yield is estimated to obtain SGVP, based on the local crop grown prices, compared to the primarily grown base crop [9].

$$SGVP = \left(\sum_{crop} A_i Y_i \frac{P_i}{P_b} \right) P_{district} \quad (1)$$

where A_i represents the land area cropped with crop i , Y_i represents the production of crop i , P_i represents the local rate of crop i , P_b represents the local rate of base crop, $P_{district}$ represents the rate of base crop traded.

Output/land cropped (Rs/ha) = SGVP/Irrigated cropped area.

Output/command area (Rs/ha) = SGVP/Command area.

Output/irrigation supply (Rs/m³) = SGVP/Irrigation supply.

Output/water consumed (Rs/m³) = SGVP/Volume of water consumed by ET

$$ET = ETo * kc \quad (2)$$

where ETo is reference evapotranspiration (mm) calculated using CROPWAT 8.0 tool [11], and kc is the crop coefficient for the main crops from FAO guidelines and adjusted for regional conditions. The volume of water consumed in cubic meters is calculated by multiplying each ET value by the cultivated area [10].

3.3 Water Use Performance

The two fundamental water use performance indicators widely applied to study the adequacy of water supply are relative water supply (RWS) as developed by [12] and relative irrigation supply (RIS) by [13]. RWS and RIS provide a relationship between supply and demand and show water scarcity and abundance conditions. RWS measures the capability of the irrigation system in comparison to the crop water demands. The value 1 shows that the supply and demand are exact, while values less than 1 indicate water scarcity, and values more than 1 indicate an oversupply of water. RIS is one of the exceptional performance indicators which shows the suitability of the supply system of irrigation water only in contrary to RWS, where rainfall is also included for agricultural production. The value of a ratio greater than 1 indicates over-irrigation; lower than one indicates under-irrigation, and 1 indicates the ideal irrigation condition [9]. However, $RIS < 1$ or > 1 does not show good or bad irrigation conditions, deficit condition may be an intended strategy, and over-irrigation may be required to leach salts or groundwater recharge approach [14–16].

$RWS = \text{Total water supply} / \text{Crop demand.}$

$RIS = \text{irrigation supply} / \text{Irrigation demand.}$

where total water supply = surface water diverted + net groundwater draft + rainfall.

Crop demand = potential crop evapotranspiration.

Irrigation supply = surface water diverted + net groundwater draft for irrigation.

Irrigation demand = crop evapotranspiration – effective rainfall.

3.4 *Hydropower Performance*

A hydropower reservoir releases water to produce electricity, and the power generated is the function of the hydraulic head and discharge. So, here both discharge and hydraulic head are kept constant. Power production is assumed to depend on the volume of water passing through the turbines and effective head only. The amount of power demanded and generated over time is expressed in kilowatt-hr. For the current study, the amount of volume water demanded and supplied in a month is considered to estimate the performance indicator. To compute the performance of the hydropower reservoir volume of water demanded and supplied to generate the demanded amount of electricity can be considered [17]. The region's electricity demand is 1961 kilowatt-hours/capita/month [18]. The water consumption factor for hydropower generation from multipurpose dams is estimated at 92.3 L/kWh [19]. Relative power supply = volume of water supplied / volume of water demanded.

4 Results and Discussion

4.1 *Irrigation Water Requirement (IWR)*

Figure 2a and b shows the annual IWR and ETo in the catchment area of Ravi Shankar Sagar reservoir in MCM from 1989 to 2018. The maximum IWR and ETo are observed in 2018–2019 and 2003–2004, respectively. The lowest IWR and ETo are observed during 1994. The CROPWAT 8.0 is used to determine the ETo and IWR of the crops in the study area. Climate data obtained from CLIMWAT 2.0, i.e., wind speed, lowest and highest air temperature, relative humidity, and sunshine duration, are supplied to the CROPWAT tool. The output parameters obtained are ETo in mm/period, Crop coefficient Kc, Effective rainfall in mm/period, and IWR in mm/period. The total command area in Ravi Shankar Sagar reservoir is 264310 ha. The major crops grown in this command area are Rice, Pulses, Maize, Wheat, and Sugarcane.



Fig. 2 **a** Annual IWR in the catchment area of Ravi Shankar Sagar reservoir in MCM from 1989 to 2018. **b** Annual ETo in the catchment area of Ravi Shankar Sagar reservoir in MCM from 1989 to 2018

4.2 Performance Indicators

The required data of production, cultivated area, and price rates of each crop for 2010–2011 are utilized to estimate productivity [20, 21]. The rates mentioned here are not for the current period. The details of crop area, yield, and price are shown in Table 1. Details of crop water and irrigation demand are mentioned in Table 2.

- i. Irrigation ratio = 0.90
- ii. SGVP/Land cropped (Rs/ha) = 1,55,375
- iii. SGVP/Command Area (Rs/ha) = 1,40,630
- iv. SGVP/Irrigation supply (Rs/m³) = 34

Table 1 Major crops yield and price rates

Major crops	Area (ha)	Yield (tones)	Yield (kg)	Productivity (kg per ha)	Price (Rs per kg)
Rice	46,764.820	229,143.6	229,143,600	4899.91	41.12
Pulses	2549.2	2039.36	2,039,360	800	114.85
Maize	274.6	214.19	214,190	780.01	37
Wheat	23,823.8	59,557.5	59,557,500	2499.91	35
Sugarcane	2774.6	16,800.20	16,800,200	6055	5.27

Table 2 Net crop water demand and net irrigation demand

Major crops	Area (ha)	Net crop water demand (mm per season)	Net irrigation demand (mm per season)	SGVP (Rs)
Rice	46,764.82	988.9	478	9,422,376,985
Maize	274.6	536.6	79.8	234,220,496
Sugarcane	2774.6	1298	408	7,925,057.6
Pulses	2549.2	440.5	170.5	2,084,507,455
Wheat	23,823.8	484.52	186.7	88,537,069.8

- v. SGVP/Water consumed (Rs/m³) = 26.5
- vi. RWS = 3.97
- vii. RIS = 0.80
- viii. Relative power supply = 0.32

4.3 Reservoir Operation

In the present methodology, the optimal operation policy is developed to evaluate the performance of RSSP. In this study, the water year begins in June and ends in May of the subsequent year. Monthly data of inflow in the reservoir has been collected from Dhamtari gauging station for 30 years (1989–2018). LP model is formulated following monthly time steps to evaluate the optimum releases from the RSSP that can be supplied for irrigation, industrial and drinking, and hydropower generation purposes. The cultivable command area under various canals of the RSSP is combined, and the conveyance factor is assumed to be 0.75. Since the model runs for monthly time steps, all the input values of drinking water demands, hydropower demands, industrial demands, irrigation demands, evaporation losses, and inflows are converted and supplied on a monthly scale to calculate the month-wise optimal water releases. Figure 3 shows the total demand, release, and deficit from (1989–2018). The beginning and end storage of the reservoir is also estimated through the model. The release of water is calculated according to the available water in the reservoir at the beginning of each month. The optimal operation policy is developed by using

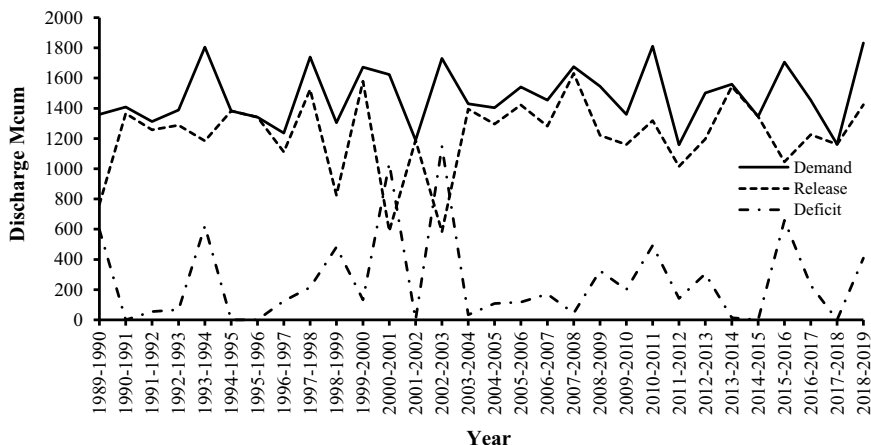


Fig. 3 Demand, release, and deficit for 30 years (1989–2018)

Python 3.9. The prime objective of this study is to maximize the total reservoir release considering domestic, industrial including hydropower, and agricultural aspects.

The objective function of the problem can be formulated as

$$Max = \sum_{i=1}^n Ri \tag{3}$$

Linear constraints

$$Ri \geq 0 \tag{4}$$

$$\eta(Ddi) \leq Ri \leq \eta(IrDi + InDi + Ddi) \tag{5}$$

$$0 \leq S \leq K \tag{6}$$

$$Si + 1 = Si + Ii - (IrDi + Ddi + InDi + Ei) \tag{7}$$

where, R = Release, S = Storage, K = Reservoir capacity, I = Inflow into the reservoir, n = Number of periods, Dd = Drinking water demand, IrD = Irrigation demand, InD = Industrial demand, E = Evaporation losses.

A total of 1080 decision variables for 360 months and 1800 constraint equations are applied to estimate the optimal release using the linear programming model for 30 years of monthly historical data.

5 Conclusions

Physical performance is one of the prime indicators of farmers' engagement in irrigation. The observed value of the irrigation ratio is equal to 0.9, showing that 90% of the irrigable area is under irrigation. Variation in the irrigation ratio depends on numerous factors: input charges, national agricultural policy, land ownership situation, poor farmer training, and insufficient water resources.

Agricultural performance indicators associate the monetary worth of the irrigation system inputs, land, and water with the final output of agricultural production, addressing the direct impact of operational inputs on crop production [9]. If the input factor of water is considered limited compared to land, output per unit of water becomes crucial. Similarly, output per unit of land becomes crucial if the land is considered a limiting factor in production. A few factors, like an increase in irrigated area size considerably, efficient irrigation scheduling, or change in crop patterns in the same scheme yearly, can improve the agriculture performance of the reservoir. The calculated value of water use performance indicators RWS and RIS are 3.97 and 0.80, respectively. The higher value of RWS may indicate the appropriate application of available water; a lower RWS would be less desirable. The value of RIS less than 1 shows a deficiency in irrigation supply. The lower value of hydropower performance (0.32) indicates the inadequacy of the reservoir to supply water for hydropower production as per the demand.

The linear programming monthly time step model shows that the reservoir fails to meet the total demands for 80 out of 360 months (1989–2018). The spill is observed in 46 out of 360 months in 30 years. An active and strict water management system to specify the amount of release of water for several purposes from storage at any given time as per demands, storage level, and any information about the likely inflow in the reservoir can improve the overall reservoir performance.

Final declaration. The performance of the Ravi Shankar Sagar reservoir to meet the designed demands highlights the situation of aging and deterioration. Reduction in the reservoir capacity due to sediment deposition in due course of time might be the reason for poor performance. To improve the performance significantly, adequate facilities to handle sediment are required. However, scheduled maintenance of the reservoir can improve performance. Some necessary measures should be taken for effective performance, like the availability of secondary storage structures or alternate water supply, which is maintained to store extra water without wastage and to be utilized as per requirement. Lining of canals to reduce losses in the canal and judicious use of water without causing wastage of irrigation water by releasing water when the crop is in need and not according to water availability could be the effective steps. Suitably changing the cropping pattern with less water-consuming crops in conjunction with better groundwater use plans to increase irrigation water supply during periods of water shortage could improve system performance.

References

1. Oza A (2007) Part I irrigation: achievements and challenges. *India Infrastruct Rep, Irrig Water Resour* 178–196
2. Rao CM, Kale RV (2013) Performance evaluation of Sri Ram Sagar irrigation project. *J Int Water Res Soc* 33:1–10
3. Gorantiwar SD, Smout IK (2005) Performance assessment of irrigation water management of heterogeneous irrigation schemes: a framework for evaluation. *Irrig Drain Syst* 19:1–36. <https://doi.org/10.1007/s10795-005-2970-9>
4. Lacombe G, Douangsavanh S, Baker J, Hoanh CT, Bartlett R, Jeuland M, Phongpachith C (2014) Are hydropower and irrigation development complements or substitutes? The example of the Nam Ngum River in the Mekong Basin. *Water Int* 39:649–670. <https://doi.org/10.1080/02508060.2014.956205>
5. Chauhan S, Shrivastava RK (2008) Optimal operation of a multipurpose reservoir using genetic algorithm. *J Indian Water Resour Soc* 28:9–17
6. Anusha N, Verma MK, Bajpai S (2017) Performance measures for Ravi Shankar Sagar reservoir using simulation-optimization models
7. Ananda Babu K, Shrivastava RK, Dikshit M (2015) Optimal operation policies for Ravishankar Sagar reservoir-A case study. *J Indian Water Resour Soc* 35
8. Bos MG, Nugteren J (1974) On irrigation efficiencies. In: International Institute for Land Reclamation and Improvement (ILRI) Publication, Wageningen, 19 (1974) Revised (1990)
9. Molden DJ, Sakthivadivel R, Perry CJ, De Fraiture C (1998) Indicators for comparing performance of irrigated agricultural systems 20
10. Şener M, Yüksel AN, Konukcu F (2007) Evaluation of Hayrabolu irrigation scheme in Turkey using comparative performance indicators. *Tekirdağ Ziraat Fakültesi Dergisi*
11. Joint FAO/WHO Codex Alimentarius Commission (1992) Codex alimentarius. Food Agric Org
12. Levine G (1982) Relative water supply: an explanatory, variable for irrigation systems. Ithaca, New York, USA, Cornell University, Technical Report No. 6
13. Pery CJ (1996) Quantification and measurement of a minimum set of indicators of the performance of irrigation systems. Colombo, Sri Lanka, IWMI
14. Ayers RS, Westcot DW (1985) Water quality for agriculture. Rome: Food and Agriculture Organization of the United Nations 29:174
15. Fereres E, Soriano MA (2007) Deficit irrigation for reducing agricultural water use. *J Exp Bot* 58:147–159. <https://doi.org/10.1093/jxb/erl165>
16. Letey J, Hoffman GJ, Hopmans JW, Grattan SR, Suarez D, Corwin DL, Amrhein C (2011) Evaluation of soil salinity leaching requirement guidelines. *Agric Water Manag* 98:502–506. <https://doi.org/10.1016/j.agwat.2010.08.009>
17. Jain SK (2009) Statistical performance indices for a hydropower reservoir. *Hydrol Res* 40:454–464. <https://doi.org/10.2166/nh.2009.072>
18. CEA Annual report, Central Authority of Electricity (2018–19)
19. Lee U, Han J, Elgowainy A, Wang M (2018) Regional water consumption for hydro and thermal electricity generation in the United States. *Appl Energy* 210:661–672. <https://doi.org/10.1016/j.apenergy.2017.05.025>
20. OECD-FAO Agricultural Outlook (2010)
21. States of agriculture in Chhattisgarh, agro- economic research centre for madhya pradesh and Chhattisgarh Jawaharlal Nehru Krishi Vishwa Vidyalaya, Jabalpur, (2014)

Sustainable Affordable Housing in Madhya Pradesh: Challenges and Opportunities



Vivek Garg and Bimal Chandra Roy

1 Introduction

The prosperity of urban growth and sustainability are ensured by one of the most significant economic sectors, housing improvement [1]. The built relationship between the environment and the building sector is prioritized highly in many countries' pursuit of sustainable development, which aims to improve the environmental, social, and economic elements. More than 40% of the energy produced is used by the building construction industry alone by humans, among other activities like manufacturing, agriculture, and transportation [2]. As a result, when it comes to building sustainably considered the building construction industry's solution to the problem of sustainable development [3]. Consequently, to construct sustainable housing successfully, it is important to hit the ideal balance between sustainable housing and client happiness [4].

This study aimed to evaluate residents' satisfaction with the affordable housing options provided by the Madhya Pradesh government utilizing the physical characteristics and traditional social elements of the dwelling, urban planning, and the social climate in the neighborhood, as well as their impact on people's lives based on general social and cultural happiness with housing. In both national and international contexts, the housing crisis is a major issue today. 3 billion people worldwide will lack homes and require affordable housing by 2030, according to the United Nations Habitat program. India is the second-largest country in the world by population, with 1.34 billion people, and the seventh-largest country in terms of land [5, 6]. Analysis of residential complexes' environmental, social, and economic sustainability can help establish specific design guidelines that new developments should adhere to in order to promote sustainability (Fig. 1).

V. Garg (✉) · B. C. Roy

Department of Architecture and Planning, Birla Institute of Technology, Mesra, Ranchi 835215, Jharkhand, India

e-mail: vivekgarg8193@gmail.com

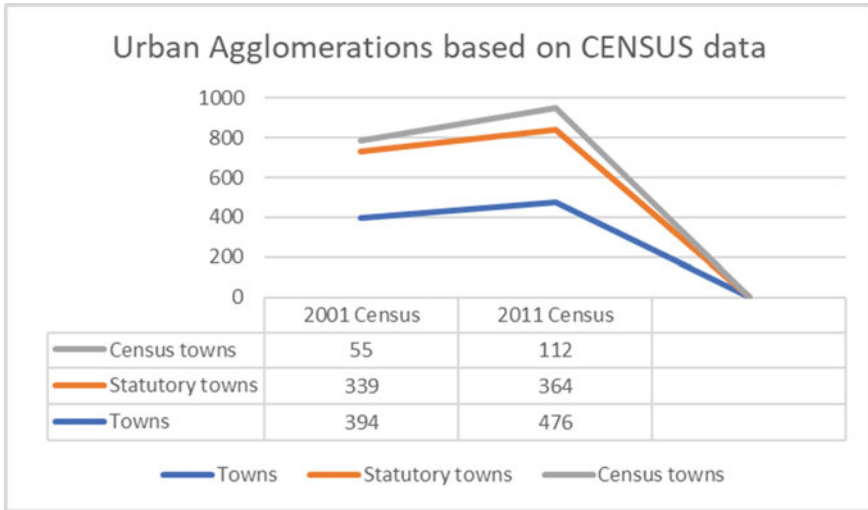


Fig. 1 Urban agglomerations based on CENSUS data of Madhya Pradesh

In Madhya Pradesh, 27.6% of the population resides in urban areas, according to the 2011 Census. In 2001, 26.5% of the population resided in urban areas. In 2011, there were 476 towns in the state as opposed to 394 in 2001. 33 of them have towns with a population of more than a thousand. Larger cities with populations of above 10 lakh people include Indore, Bhopal, Jabalpur, and Gwalior [7]. The following study has researched Madhya Pradesh’s current policies in terms of affordability, tenure, community participation, incentives, housing areas, type of development, etc. in order to make policy recommendations on how to provide underprivileged populations with adequate housing and shelter.

Policies and Laws at the State Level for Madhya Pradesh (Table 1) is one of the states that contributes the most to the number of people living in slums in India, out of all the states. Out of the 364 statutory towns in the state, slum zones have been located in 303. According to estimates, 28% of the people of Madhya Pradesh reside in slums [8, 9]. The majority of slum dwellers live in Jabalpur, where that number is about 45%. Slum dwellers make up 10.87 lakh families in Madhya Pradesh [10]. These are divided into three categories: habitable (38.41%), good [57.18%], and deteriorated (3.71%). The census also shows that 79.01% of slum households are self-sufficient, 17.24% are renters, and the remaining percentage reside in various types of housing. According to the number of rooms in these homes, 32.53% of households have one living room, 34.84% of households have two living rooms, and 31.17% of households have three or more living rooms [11]. The settlements may be reasonably well-built, according to all of this. In contrast to this, however, there are inadequate levels of basic utilities like water and sanitization [12].

Table 1 State level policies and acts of Madhya Pradesh [13–18]

S. no.	Name of the state level policies and acts	Year of enactment
1	The Madhya Pradesh Bhumi Vikas Rules	1984
2	The Madhya Pradesh Nagariya Kshetron Ke Bhumihin Vyakti Adhinyam	1984
3	Guidelines for Re-densification Projects	2005
4	State Housing and Habitat Policy	2007
5	Atal Ashray Yojana	2011
6	Redevelopment of Slums policy	2012
7	EWS and LIG Housing through PPP Policy	2014
8	Real Estate Policy for Madhya Pradesh	2019

1.1 Objectives of Study

To understand the current Sustainable affordable housing needs and shortage in India. Understand the framework supporting Sustainable affordable housing. To Study the Government's existing policy framework and Schemes for Affordable Housing. Factors influencing beneficiaries for availing affordable housing. To measure the beneficiary's satisfaction level related to housing provided under previous Government housing policy.

2 Need for Sustainable Affordable Urban Housing in Madhya Pradesh

An integrated strategy for sustainability is necessary in Madhya Pradesh to effectively address sustainability challenges in the context of the urban poor. The living conditions of the urban poor are marked by a high vulnerability. Essentially, sustainable social housing is a place where the poor have the chance and the desire to live beyond the short term, one that supports their socio-economic development and is considerate of the surrounding environment.

2.1 Initiatives to Promote Sustainable Affordable Housing

The National Urban Housing and Habitat Policy emphasizes the need to investigate various technological possibilities in order to achieve energy and cost efficiency in its "affordable housing" part. Unfortunately, operational policy documents like the JNNURM and RAY guidelines have not yet reflected these aims. According to BSUP, adopting environmentally friendly reforms is voluntary and is only limited to

adopting bye-laws requiring rainwater harvesting in all future buildings and establishing a framework for water discussion. The prior abilities are no longer sufficient to adopt sustainable practices due to the quick growth of sustainable technologies and activities [19].

2.2 Crucial Issues in the Sustainable Affordable Housing Sector

Here, the issue of sustainable housing is addressed. The integration of sustainability into the housing stock is challenging since many stakeholders may have conflicting interests [20]. In addition to the well-acknowledged economic dimension, understanding affordability in the context of sustainability broadens the scope of affordable housing to include social and environmental considerations [21]. The target population's home design must satisfy their income level without compromising the standards of suitable housing conditions for the delivery of cheap housing to continue to be sustainable [22]. The integration of sustainable and affordable housing calls on the knowledge of building professionals. Developers are unable to incorporate affordability and sustainability concepts in their project development due to the scarcity of professionals in the field [23].

2.3 Income Levels and Housing Affordability

The affordability of different income groups in response to income supports some nonlinear drift. Rent and other non-food necessities contribute significantly to the income of groups with lower incomes. As we progress toward greater income levels, these rising expenses won't rise as quickly. As a result of having more discretionary income, persons with higher income levels can afford to buy new homes. Profits are made by concentrating on low- to medium-cost dwellings, which continue to rule the market. Developers are hesitant to commit to something new because they are at ease with their business's marketability [24].

The fact that this disposable excess is still very sensitive to this small adjustment in spending should be taken into consideration. For instance, if housing costs rise by 15–20%, the amount of disposable income available to a LIG household (a person with a monthly salary of INR 10,000) drops from 35 to 30%. When rent increases from 15 to 20%, it can be seen that the surplus income decreases by a comparable amount—from 64 to 59%—for a person with a monthly payment of about INR 120,000 (Table 2).

Table 2 Housing affordability

Housing target group categories	Carpet area	EMI or rent	Maximum price
Economically weaker section (EWS)	21–27 m ²	Not exceeding 30–40% of gross monthly income	300,000
Lower income group (LIG)	28–60 m ² (LIG-A: 28–40 m ² and LIG-B 41–60 m ²)		600,000

Source Affordable Housing Partnership guidelines 2011 (Amended), Govt. of Partnership Guidelines 2011 (Amended), Govt. of India

3 Affordability

There is a consistent trend in income and affordability for various income categories. For lower to higher income categories, “disposable or excess income”⁸ is typically accounted for when buying a home. The higher income groups typically are not impacted by cost increases at the same rate; however, this is not always the case for the lower income groups. At lower income levels, disposable income is greatly reduced, but it increases at higher levels of income.

4 Structural Safety Aspect of the Buildings in Madhya Pradesh

Floods are the most frequent and dangerous of all the natural disasters that threaten the State of Madhya Pradesh. The state is therefore quite vulnerable to the risk of flooding. The next severe risk that the state is subject to is drought, which comes after floods. Based on data from the previous 30 years, it was determined that the state’s drought pattern is complex, occasionally affecting the entire state, other times a small number of regions, and still other times just a few districts. Another significant risk that applies to the state of Madhya Pradesh is earthquake. Significant areas of the state experience moderately high seismicity. A few incidents, particularly recent ones, set off the entire state. The earthquake is then treated very seriously here. However, according to the Vulnerability Atlas of India, 22 districts are classified as being in earthquake Zone II, while 28 districts are classified as being in Zone III. According to the 2007 Vulnerability Atlas of India [25], 56.3% of Madhya Pradesh’s houses (made of mud, stone, or unburned brick walls) are vulnerable to disaster impacts, which is significantly higher than the Indian average of 39%. This indicates that the state’s housing is 17% less safe than the rest of the country.

5 Case Study—Ground-Level Voice

The problems with housing in Madhya Pradesh's urban marginalized communities are the subject of this case study. The following study takes a bottom-up approach in order to accurately portray the reality and issues these communities are facing. The research for this chapter was conducted through site visits and conversations with more than 2 small and major groups in the Madhya Pradesh cities of Indore, Bhopal, and Jabalpur.

Bhuri Tekri Basti Indore—On a hillside that had previously been used for quarrying, the Bhuri Tekri settlement was founded more than 40 years ago. The in-situ growth of the PMAY program has had an impact on the community and, as some people assert, caused it to be “displaced.” Because they do not want to pay for the homes that have been built on their property, some people have yet to accept the homes that have been provided to them. There are 11 units in the Bhuri Tekri community's resettlement site, each of which has about 42 dwelling units. As a result, the resettlement has room for about 500 units.

Arjun Nagar—In-situ Redevelopment Bhopal—Almost 1200 homes make up the community of Arjun Nagar, which was developed over the course of the last 20–30 years. Diverse migrants who came to this area in search of work, primarily from Maharashtra and Bihar, helped to create the community. When the government decided to develop the nearby property, the town gained notoriety. Additionally, in 2012, eviction was a threat. Since then, the residents have abandoned their original plans for relocation and have chosen the BSUP in-situ redevelopment approach instead. The inhabitants list additional issues they encounter.

Resettlement Sites and Vijay Nagar Jabalpur—The resettlement colony close to Vijay Nagar was constructed as part of JNNURM's BSUP component, and it is situated in the city's southwestern outskirts. The resettlement site currently contains a variety of communities despite having been vacant for a long time. The older communities in Vijay Nagar among these numerous ones have had pattas in the previous ten to fifteen years.

6 Research Methodology

The research mostly draws on secondary data sources to answer the aforementioned questions. International journals, books, research papers, multimedia, and other online resources are used to compile pertinent data. Primarily exploratory in nature, the study. Divided into three sections, the study.

Part I is the majority of the study's literature is an existing Affordable housing framework that the government has embraced. It also offers definitions of Affordable housing and a thorough analysis of national strategies for affordable housing implemented in India. The study examines the demand- and supply-side restrictions that are influencing the implementation of HFA initiatives.

Part II is the study hypotheses that have been analyzed from stakeholder meetings and field trips. Interviews are conducted with the unique stakeholders from each representative group who are in charge of providing homes for everyone. To evaluate the potential efficacy of PMAY, a new HFA strategy, the tri approach to slum upgrading, providing public housing and redeveloping slums is advocated. The report introduces the three national housing policies: BSUP, RAY and NSDP, which support the three-pronged efforts started by the federal and state governments.

Part III Speculated that HFA be recommended by 2022. According to interviews and publications published by different institutions, these recommendations have been recommended by various stakeholders. The three government-proposed solutions were compared in order to determine which worked best in India while keeping in mind the need to resolve the housing scarcity problem as the ultimate aim.

7 Conclusion

Affordable housing problems are mostly caused by supply and demand limitations imposed by housing governance. Five assessing target-based criteria, openness, administrative homogeneity, sustainability, and efficacy are chosen to define the interpretation of the results. In Madhya Pradesh, there are three widely implemented housing improvement, rehabilitation, and public housing projects. There is a huge disparity between the approaches taken by housing programs and how they are implemented. Going forward, a sustainability approach should be used because it is determined that cheap housing does not now include it. To prioritize a sustainable solution for the affordable housing segment, the government must enact a policy. The building of Sustainable, affordably priced housing has become necessary due to India's cities' today's rapidly growing urbanization. It is challenging to achieve sustainability and affordable housing, and it can only be done via cooperation between people, the public and private sectors, government and policy-makers, and the three pillars of sustainability, namely social, economic, and environmental issues.

References

1. World Business Council for Sustainable Development (2009) Energy efficiency in buildings: transforming the market. Atar Roto Press SA, Switzerland
2. Hoffman AJ, Henn R (2008) Overcoming the social and psychological barriers to green building. *Organ Environ* 21(4):390–419
3. Rahman NA, Ab Manan NA, Saad NL, Abdullah K, Soffian NSM, Ahmad AL (2018) Public facilities guidelines calculator for sustainable housing development. *Inov Malays* 1(2):125–144
4. Chan AP, Adabre MA (2019) Bridging the gap between sustainable housing and affordable housing: the required critical success criteria (CSC). *Build Environ* 151:112–125
5. The Government of India (2011) Census
6. aiggpa.mp.gov.in

7. Population Division (2014) World urbanisation prospects: the 2014 revision. United Nations, Department of Economic and Social Affairs
8. <http://censusmp.nic.in/censusmp/All-PDF/3TrendsInUrbanization21.12.2011>
9. http://timesofindia.indiatimes.com/articleshow/27986846.cms?utm_source=contentofinterest&utm_medium=text&utm_campaign=cppst
10. <https://www.censusindia.gov.in/2011-Documents/Slum-26-09-13>
11. Bhopal has 1.03 lakh slum households, it's the second highest in rank after Indore, which has 4.8 lakh slum population. 27% of Bhopal population lives in slums. Indore has 5.90 lakh population in 1.14 lakh slum households, which is highest in MP. 27% of Indore population lives in slums (National Informatics Centre, Madhya Pradesh)
12. https://terraurban.files.wordpress.com/2014/01/indore_bhopal-study-report-april-2014
13. <http://www.mpmsme.gov.in/website/acts-&-rules>
14. Sustainable Development Solutions Network (SDSN) (2015) Multidimensional poverty index
15. Government of Madhya Pradesh (2007) M.P. housing and habitat policies
16. Census (2011) Trends in urbanization. Government of Madhya Pradesh
17. 2007 vulnerability atlas of India
18. Affordable housing in India—JLL
19. 39.86% have water source in their homes, 20.49% have water source in nearby area and the rest 39.65% of the household have to travel far off for water source. These figures might have changed after the urban schemes targeting sanitation
20. Abidin NZ (2010) Investigating the awareness and application of sustainable construction concept. *Hab Int* 34(4):421–426
21. Yang J, Yan Z (2015) Critical factors affecting the implementation of sustainable housing. *J Hous Built Environ* 30(2):275–292
22. Ezennia IS, Hoskara SO (2021) Assessing the subjective perception of urban households on the criteria representing sustainable housing affordability. 13:e00847
23. Ackley AU, Teeling C, Atamewan E (2018) Factors affecting the shortage and or provision of sustainable affordable housing in developing countries. *Sustain Archit Civ Eng* 22(1):27–38
24. Goh KC, Seow TW, Goh HH (2015) Challenges of implementing. *Sustainability Housing Industry*
25. Abidin NZ, Yusof, NA, Othmana A (2013) Enablers and challenges of a sustainable housing industry. *Constr Innov* 13(1):10–25

Implementation of a Multiscale Method for Problems in Linear Elasticity



Devasis Laishram, Kosygin Leishangthem, Khwairakpam Selija,
and Koko Karbia

1 Introduction

The aim of mathematical modelling varies based on the discipline one approaches it from. Physicists, for instance, create simulations at the atomistic level, which, in theory, could determine the entire macroscopic behaviour of a material, such as its thermal conductivity, deformation, fracture etc. Engineers, on the other hand, approach mathematical modelling with a pragmatic outlook, primarily concerned with predicting the behaviour of material vis-à-vis its intended engineering use.

Multiscale modelling is an approach which follows this general philosophy. A multiscale model takes into consideration the atomic or microscopic properties of a material, but does so with the aim of increasing its predictive accuracy, while at the same time making sure it is computationally cost effective. This paper focuses on multiscale PDEs known as *homogenization problems*, which deal with materials whose properties are represented by highly oscillating functions. Homogenization refers to the mathematical process of converting such problems into an averaged version to be modelled at the macroscopic level. It is a rich area of research, but falls short in terms of real-world application as homogenizing, or averaging, these highly oscillating material coefficients are a challenging task. The overarching goal of multiscale methods is to overcome this difficulty, thereby enabling its application to a much wider range of problems [8].

Model Problem. Let $\Omega \subset \mathbb{R}^N$, $N = 1, 2, 3$ denote a region with boundary $\partial\Omega$, where the Dirichlet boundary conditions are prescribed on $\Gamma_D \subset \partial\Omega$ and the Neumann boundary conditions on $\Gamma_N = \partial\Omega \setminus \Gamma_D$. If $\bar{\Omega}$ represents a linearly elastic material in static equilibrium when acted upon by body forces $\mathbf{f} \in L^2(\Omega)^N$ and surface traction $\mathbf{g} \in H^{-1/2}(\Gamma_N)^N$, find $\mathbf{u}^e \in H_0^1(\Omega)^N$ such that

D. Laishram (✉) · K. Leishangthem · K. Selija · K. Karbia
Department of Civil Engineering, Manipur Technical University, Imphal 795001, India
e-mail: devasis@mtu.ac.in

$$\begin{aligned}
-\frac{\partial}{\partial x_j} \left(a_{ijkh}^\varepsilon \frac{\partial u_k^\varepsilon}{\partial x_h} \right) &= f_i \quad \text{in } \Omega, \\
\mathbf{u}^\varepsilon &= 0 \quad \text{on } \Gamma_D, \\
a_{ijkh}^\varepsilon \frac{\partial u_k^\varepsilon}{\partial x_h} n_j &= g_i \quad \text{on } \Gamma_N,
\end{aligned} \tag{1}$$

for $i = 1, \dots, N$, where $a^\varepsilon(x)$ is a fourth order symmetric tensor and ε represents the parameter characterizing the heterogeneity of the material.

The linear strain tensor e is given by

$$e_{ij}(\varphi) = \frac{1}{2} \left(\frac{\partial \varphi_i}{\partial x_j} + \frac{\partial \varphi_j}{\partial x_i} \right), \quad \forall i, j = 1, \dots, N, \tag{2}$$

or any $\varphi = (\varphi_1, \dots, \varphi_N)$. Then, Hooke's law gives us the stress tensor defined as,

$$\sigma_{ij} = b_{ijkh} e_{kh}(\varphi) = b_{ijkh} \frac{\partial \varphi_k}{\partial x_h}. \tag{3}$$

The variational form of the problem becomes: Find $\mathbf{u}^\varepsilon \in H_0^1(\Omega)^N$ such that

$$\begin{aligned}
B_\varepsilon(\mathbf{u}^\varepsilon, \mathbf{v}) &\stackrel{\text{def}}{=} \int_{\Omega} a^\varepsilon(x) e(\mathbf{u}^\varepsilon) : e(\mathbf{v}) \, dx = \int_{\Omega} \mathbf{f} \cdot \mathbf{v} \, dx + \int_{\Gamma_N} \mathbf{g} \cdot \mathbf{v} \, ds \\
&\stackrel{\text{def}}{=} F(\mathbf{v}), \quad \forall \mathbf{v} \in H_0^1(\Omega)^N.
\end{aligned} \tag{4}$$

Homogenization. A detailed theory of homogenization can be found in [7]. When homogenized, \mathbf{u}^ε converges to \mathbf{u}^0 , the solution to the variational formulation for the homogenized problem given by: Find $\mathbf{u}^\varepsilon \in H_0^1(\Omega)^N$ such that

$$B_0(\mathbf{u}^0, \mathbf{v}) \stackrel{\text{def}}{=} \int_{\Omega} a^0(x) e(\mathbf{u}^0) : e(\mathbf{v}) \, dx = F(\mathbf{v}), \quad \forall \mathbf{v} \in H_0^1(\Omega)^N, \tag{5}$$

where, a^0 is the homogenized coefficient.

2 Finite Element Heterogeneous Multiscale Method

Using the classical (single-scale) FEM to solve (1) becomes computationally untenable if the scale ε is small (as is the case for microscopically heterogenous materials), since the mesh size h is required to be $\ll \varepsilon$. On the other hand, finding an explicit expression for a^0 is a challenge, which makes applying the homogenization procedure to a variety of problems difficult. The strength of multiscale methods lies in

the fact that it eliminates both issues. We apply one such multiscale method, the finite element heterogeneous multiscale method (FE-HMM) to problems of type (1). The FE-HMM gives an approximate solution without the need to find the homogenized tensor a^0 , while at the same time, being much more computationally cheaper compared to the standard FEM.

2.1 The FE-HMM Algorithm

The theoretical formulation of the FE-HMM is available in [1–4]. Here we provide an explicit computer algorithm for implementing the FE-HMM to problems of linear elasticity in two dimensions, and conduct numerical experiments using the algorithm.

Step 1. Define the macro and micro finite element spaces and their basis. The first step of the algorithm can be described in points as follows.

- Define the *macro finite element space*:

$$\mathcal{V}^p(\Omega, \mathcal{T}_H) = \{\mathbf{v}^H \in H_0^1(\Omega)^N; \mathbf{v}^H|_K \in \mathcal{R}^p(K)^N, \forall K \in \mathcal{T}_H\}, \quad (6)$$

with macro elements $K \in \mathcal{T}_H$. $\mathcal{R}^p(K)$ is either of the spaces $\mathcal{P}^p(K)$ or $\mathcal{Q}^p(K)$ of polynomials for simplicial elements and quadrilateral elements respectively, with degree p in each variable.

- Define the *macro basis*:

Let $\{\varphi_i^H\}_{i=1}^{N_{fx}+N_{fy}}$ denote the macro FE basis $\mathcal{V}^p(\Omega, \mathcal{T}_H)$ where,

$$\varphi_i^H = (\varphi_i^H, 0), \varphi_{N_{fx}+j}^H = (0, \varphi_j^H), \quad i = 1, \dots, N_{fx}, \quad j = 1, \dots, N_{fy}. \quad (7)$$

φ_i^H are the usual basis functions for the scalar finite element space and N_{fx} and N_{fy} denote the total number of unconstrained nodes in the x and y dimensions respectively.

- Define the *micro finite element space*:

$$\mathcal{S}^q(K_\delta(x_{\ell,K}), \mathcal{T}_h) = \{\mathbf{z}^h \in \mathbf{W}(K_\delta(x_{\ell,K})); \mathbf{z}^h|_T, \in \mathcal{R}^q(Q)^N, Q \in \mathcal{T}_h\}, \quad (8)$$

where,

- $x_{\ell,K} \in K$ are integration nodes.
- $K_d(x_{\ell,K}) = x_{\ell,K} + \delta I$ are sampling domains around each $x_{\ell,K}$;
- $I = (-\frac{1}{2}, \frac{1}{2})^N$ and $\delta \geq \varepsilon$,
- and, the $\mathbf{W}(K_\delta(x_{\ell,K}))$ determines the macro–micro coupling and boundary conditions, with,
- $\mathbf{W}(K_\delta(x_{\ell,K})) = \mathbf{W}_{per}(K_\delta(x_{\ell,K}))$ for periodic coupling and,
- $\mathbf{W}(K_\delta(x_{\ell,K})) = H_0^1(K_\delta(x_{\ell,K}))^N$ for Dirichlet coupling, where,

$$\mathbf{W}_{per}(Y) = \left\{ \mathbf{v} \in H_{per}^1(Y)^N; \int_Y v_i dy = 0, \quad i = 1, \dots, N \right\}. \quad (9)$$

- Define the *micro basis*:

Let $\{\boldsymbol{\psi}_{k, K_\delta}^h\}_{k=1}^{2n}$ denote the basis of the micro FE space $\mathcal{S}^q(K_\delta(x_{\ell, K}), \mathcal{T}_h)$, where

$$\boldsymbol{\psi}_k^h = (\psi_k^h, 0), \quad \boldsymbol{\psi}_{n+k}^h = (0, \psi_k^h) \quad k = 1, \dots, n. \quad (10)$$

ψ_k^h are the usual basis functions for scalar micro space $S^q(K_\delta(x_{\ell, K}), \mathcal{T}_h)$ and n denotes the number of nodes in the discretized micro-domain.

Step 2. Compute the macrostiffness matrix. The local macrostiffness matrix \mathbf{A}_K is defined for each $K \in \mathcal{T}_H$ as follows:

$$\begin{aligned} \mathbf{A}_K &\stackrel{\text{def}}{=} B_H(\boldsymbol{\varphi}_i^H, \boldsymbol{\varphi}_j^H)_{i,j=1}^{2i_D} \\ &= \left(\sum_{\ell=1}^{\ell} \frac{\omega_{\ell, K}}{|K_\delta(x_{\ell, K})|} \int_{K_\delta(x_{\ell, K})} a^\varepsilon(x) e(\boldsymbol{\varphi}_{\ell, K_\delta}^h) : e(\boldsymbol{\varphi}_{\ell, K_\delta}^h) dx \right)_{i,j=1}^{2i_D}, \end{aligned} \quad (11)$$

where $\boldsymbol{\varphi}_{i_\ell, K_\delta}^h$ and $\boldsymbol{\varphi}_{j_\ell, K_\delta}^h$ are solutions of the micro problem for each $2i_D$ micro nodes, having coefficients $\boldsymbol{\alpha}_\ell^i = (\alpha_{1,\ell}^i, \dots, \alpha_{2n,\ell}^i)^T$. The local macrostiffness matrices are then assembled to compute the global macrostiffness matrix as given in the algorithm below (Table 1).

Step 3. Solve the macro-problem. The variational form for the macro-problem is written as [1]: Find $\mathbf{u}^H \in \mathcal{V}^p(\Omega, \mathcal{T}_H)$ such that

$$B_H(\mathbf{u}^H, \mathbf{v}^H) = F(\mathbf{v}^H), \quad \forall \mathbf{v}^H \in \mathcal{V}^p(\Omega, \mathcal{T}_H), \quad (12)$$

which can be done by any solver package for linear systems [6, 9], now that we have computed \mathbf{A}_K , and thereby, $B_H(\mathbf{u}^H, \mathbf{v}^H)$.

Table 1 Computer algorithm to compute the global macrostiffness matrix**Algorithm** Macrostiffness Assembly

Input: \mathcal{T}_H : The macro finite element discretization
 \mathcal{T}_h : The micro finite element discretization
 $K_\delta(x_{\ell,K})$: The size of the micro domain
 a^ε : The material coefficient
 ε : The size of the micro length scale

Output: **A**: The macrostiffness matrix

- 1 **function** MICROSTIFFNESS($\mathcal{T}_h, a^\varepsilon, \varepsilon$)
- 2 **initialize** the microstiffness matrix $\mathbf{B}_{\ell,K_\delta}$ to the $2n \times 2n$ zero matrix
- 3 **for** all micro elements T in discretization \mathcal{T}_h
- 4 $(B_{\ell,K_\delta})_{ij}^{11} = \sum_{T \in \mathcal{T}_h} \int_T a^\varepsilon(x) e(\boldsymbol{\psi}_i^h) : e(\boldsymbol{\psi}_j^h) dx, i, j = 1, \dots, n.$
- 5 $(B_{\ell,K_\delta})_{ij}^{12} = \sum_{T \in \mathcal{T}_h} \int_T a^\varepsilon(x) e(\boldsymbol{\psi}_i^h) : e(\boldsymbol{\psi}_j^h) dx, i = 1, \dots, n, j = n, \dots, 2n.$
- 6 $(B_{\ell,K_\delta})_{ij}^{21} = \sum_{T \in \mathcal{T}_h} \int_T a^\varepsilon(x) e(\boldsymbol{\psi}_i^h) : e(\boldsymbol{\psi}_j^h) dx, i = n, \dots, 2n, j = 1, \dots, n.$
- 7 $(B_{\ell,K_\delta})_{ij}^{22} = \sum_{T \in \mathcal{T}_h} \int_T a^\varepsilon(x) e(\boldsymbol{\psi}_i^h) : e(\boldsymbol{\psi}_j^h) dx, i, j = n, \dots, 2n.$
- 8 $\mathbf{B}_{\ell,K_\delta} = \mathbf{B}_{\ell,K_\delta} + \begin{bmatrix} B_{\ell,K_\delta}^{11} & B_{\ell,K_\delta}^{12} \\ B_{\ell,K_\delta}^{21} & B_{\ell,K_\delta}^{22} \end{bmatrix}.$
- 9 **end for**
- 10 **return** $\mathbf{B}_{\ell,K_\delta}$
- 11 **end function**
- 12 **function** PERIODIC(\mathcal{T}_h)
- 13 $b = (\int_T \boldsymbol{\psi}_1^h, \dots, \int_T \boldsymbol{\psi}_{2n}^h).$
- 14 $\bar{D}_{kr} = \boldsymbol{\psi}_k^h(p_r) - \boldsymbol{\psi}_k^h(p_{\sigma(r)}), r = 1, \dots, m.$
 $\triangleright p_r, p_{\sigma(r)}$ and m are explained in the comment to line 45.
- 15 $\bar{\mathbf{D}}^T = \begin{bmatrix} [\bar{D}]_{m \times n} & [\text{zeros}]_{m \times n} \\ [\text{zeros}]_{m \times n} & [\bar{D}]_{m \times n} \end{bmatrix}_{2m \times 2n},$
- 16 $\mathbf{D} = \begin{bmatrix} b_1 & \dots & b_{2n} \\ & \bar{\mathbf{D}} & \end{bmatrix}.$
- 17 $\mathbf{D}_{ri}^{\beta 11} = \left(\varphi_i^H(x_{\ell,K}) + \begin{bmatrix} (x - x_{\ell,K}) & \frac{1}{2}(y - y_{\ell,K}) \end{bmatrix} \begin{bmatrix} \varphi_{i,x}^H(x_{\ell,K}) \\ \varphi_{i,y}^H(x_{\ell,K}) \end{bmatrix} \right) (p_r)$
 $- \left(\varphi_i^H(x_{\ell,K}) + \begin{bmatrix} (x - x_{\ell,K}) & \frac{1}{2}(y - y_{\ell,K}) \end{bmatrix} \begin{bmatrix} \varphi_{i,x}^H(x_{\ell,K}) \\ \varphi_{i,y}^H(x_{\ell,K}) \end{bmatrix} \right) (p_{\sigma(r)}),$
 $1 \leq i \leq i_D, \quad 1 \leq r \leq m.$
- 18 $\mathbf{D}_{ri}^{\beta 21} = \left(\frac{1}{2}(x - x_{\ell,K}) \varphi_{i,y}^H(x_{\ell,K}) \right) (p_r)$
 $- \left(\frac{1}{2}(x - x_{\ell,K}) \varphi_{i,y}^H(x_{\ell,K}) \right) (p_{\sigma(r)}), \quad 1 \leq i \leq i_D, 1 \leq r \leq m.$
- 19 $\mathbf{D}_{ri}^{\beta 12} = \left(\frac{1}{2}(y - y_{\ell,K}) \varphi_{i,x}^H(x_{\ell,K}) \right) (p_r)$
 $- \left(\frac{1}{2}(y - y_{\ell,K}) \varphi_{i,x}^H(x_{\ell,K}) \right) (p_{\sigma(r)}), \quad i_D < i \leq 2i_D, 1 \leq r \leq m.$

(continued)

Table 1 (continued)

20

$$\mathbf{D}_{ri}^{\beta 11} = \begin{pmatrix} \varphi_i^H(x_{\ell,K}) + \left[\frac{1}{2}(x - x_{\ell,K}) \quad (y - y_{\ell,K}) \right] \begin{bmatrix} \varphi_{i,x}^H(x_{\ell,K}) \\ \varphi_{i,y}^H(x_{\ell,K}) \end{bmatrix} \\ - \left(\varphi_i^H(x_{\ell,K}) + \left[\frac{1}{2}(x - x_{\ell,K}) \quad (y - y_{\ell,K}) \right] \begin{bmatrix} \varphi_{i,x}^H(x_{\ell,K}) \\ \varphi_{i,y}^H(x_{\ell,K}) \end{bmatrix} \right) \end{pmatrix} (p_r)$$

$i_D < i \leq 2i_D, \quad 1 \leq r \leq m.$

▷ The expressions 17 to 20 are obtained for [1],
▷ $\varphi_{i,lin,\ell,K\delta}^H(x) = \varphi_i^H(x_{\ell,K}) + e \left(\varphi_i^H(x_{\ell,K}) \right) (x - x_{\ell,K}).$

21

$$\mathbf{D}^\beta = \begin{bmatrix} 0 & \dots & \dots & 0 \\ [\mathbf{D}^{\beta 11}]_{m \times i_D} & [\mathbf{D}^{\beta 12}]_{m \times i_D} & & \\ & & & \\ [\mathbf{D}^{\beta 21}]_{m \times i_D} & [\mathbf{D}^{\beta 22}]_{m \times i_D} & & \end{bmatrix}_{(2m+1) \times 2i_D}.$$

22 **return** $\mathbf{D}, \mathbf{D}^\beta$

23 **end function**

24 **function** DIRICHLET(\mathcal{J}_h)

25 $[\mathbf{D}_{kr}] = [\boldsymbol{\psi}_k^h(p_r)], \quad r = 1, \dots, 2m.$

26

$$\mathbf{D}_{ri}^{\beta 11} = \begin{pmatrix} \varphi_i^H(x_{\ell,K}) + \left[(x - x_{\ell,K}) \quad \frac{1}{2}(y - y_{\ell,K}) \right] \begin{bmatrix} \varphi_{i,x}^H(x_{\ell,K}) \\ \varphi_{i,y}^H(x_{\ell,K}) \end{bmatrix} \\ \end{pmatrix} (p_r),$$

$1 \leq i \leq i_D, \quad 1 \leq r \leq m.$

27 $\mathbf{D}_{ri}^{\beta 21} = \left(\frac{1}{2}(x - x_{\ell,K}) \varphi_{i,y}^H(x_{\ell,K}) \right) (p_r), \quad 1 \leq i \leq i_D, \quad 1 \leq r \leq m.$

28 $\mathbf{D}_{ri}^{\beta 12} = \left(\frac{1}{2}(y - y_{\ell,K}) \varphi_{i,x}^H(x_{\ell,K}) \right) (p_r), \quad i_D < i \leq 2i_D, \quad 1 \leq r \leq m.$

29

$$\mathbf{D}_{ri}^{\beta 22} = \begin{pmatrix} \varphi_i^H(x_{\ell,K}) + \left[\frac{1}{2}(x - x_{\ell,K}) \quad (y - y_{\ell,K}) \right] \begin{bmatrix} \varphi_{i,x}^H(x_{\ell,K}) \\ \varphi_{i,y}^H(x_{\ell,K}) \end{bmatrix} \\ \end{pmatrix} (p_r),$$

$i_D < i \leq 2i_D, \quad 1 \leq r \leq m.$

▷ The expressions 26 to 29 are obtained for [1], $\mathbf{D}_{ri}^\beta = \varphi_{i,lin,\ell,K\delta}^H(p_r).$

30

$$\mathbf{D}^\beta = \begin{bmatrix} [\mathbf{D}^{\beta 11}]_{m \times i_D} & [\mathbf{D}^{\beta 12}]_{m \times i_D} \\ [\mathbf{D}^{\beta 21}]_{m \times i_D} & [\mathbf{D}^{\beta 22}]_{m \times i_D} \end{bmatrix}_{2m \times 2i_D}.$$

31 **return** $\mathbf{D}, \mathbf{D}^\beta$

32 **end function**

33 **function** MACROSTIFFNESS($\mathcal{J}_H, \mathcal{J}_h, K_\delta(x_{\ell,K}), a^\varepsilon, \varepsilon$)

34 **initialize** the global macrostiffness matrix \mathbf{A} to the $N \times N$ zero matrix

35 **for** all macro elements T in discretization \mathcal{J}_H

36 **initialize** the local macrostiffness matrix \mathbf{A}_K to the $2i_D \times 2i_D$ zero matrix

37 **for** all quadrature points $x_{\ell,K}$

38 MICROSTIFFNESS($\mathcal{J}_h, a^\varepsilon, \varepsilon$)

39 **start switch**

40 **case** periodic micro boundary condition

(continued)

Table 1 (continued)

41	PERIODIC(\mathcal{T}_h)
42	case Dirichlet micro boundary condition
43	DIRICHLET(\mathcal{T}_h)
44	end switch
45	Solve the micro problem: Find α_ℓ^i such that [5], $\mathbf{B}_{\ell, K_\delta} \alpha_\ell^i + \mathbf{D}^T \lambda = 0,$ $(\mathbf{D} \alpha_\ell^i)_j = \mathbf{D}_{ji}^\beta.$
	$\triangleright \lambda = (\kappa_0, \lambda_1, \dots, \lambda_{2m})^T, \kappa_0 \in \mathbb{R}^N$ are coefficients of $\boldsymbol{\vartheta}_0 = \sum_{s=1}^{4m} \lambda_s \boldsymbol{\vartheta}_s^h$, where $(\boldsymbol{\vartheta}_s^h)_{s=1}^{4m}$ are basis functions of a finite element space defined on the micro boundary ∂K_δ and denoted by $\mathcal{S}^q(\partial K_\delta, \mathcal{T}_{\partial, h})$.
	$\triangleright \boldsymbol{\vartheta}_s^h = (\vartheta_s^h, 0), \boldsymbol{\vartheta}_{n+s}^h = (0, \vartheta_s^h) \quad s = 1, \dots, 2m$ denotes the usual basis functions for the scalar space $S^q(\partial K_\delta(x_{\ell, K}), \mathcal{T}_{\partial, h})$ and are arranged so that the first $2m$ functions belong to the x dimension. They are further ordered so that m consecutive nodes p_r belong to two intersecting edges of ∂K_δ while the remaining opposing nodes are denoted by $p_{\sigma(r)}$. The remaining $2m$ basis are for the y dimension and are ordered similarly.
46	$\mathbf{A}_K = \mathbf{A}_K + \frac{\omega_{\ell, K}}{ \mathcal{K}_\delta(x_{\ell, K}) } \left((\alpha_\ell^i)^T \mathbf{B}_{\ell, K_\delta} \alpha_\ell^j \right).$
47	end for
48	$\mathbf{A} = \mathbf{A} + [\mathbf{A}_K]'$. \triangleright where $[\mathbf{A}_K]'$ is the local macrostiffness matrix in the global coordinate system, obtained from any classical FEM package [6], [9].
49	end for
50	return A
51	end function

3 Numerical Experiments

We apply the multiscale method to two linear elastic plane strain problems. For the first problem, we compare the multiscale solution to a homogenized solution. To achieve this, we first need to compute the coefficients for the homogenized elasticity tensor, which is done as follows [10].

For the problem (1), a^ε is assumed to represent a linear elastic isotropic material in plane strain condition whose coefficients vary along only one direction. Then, the coefficients of the corresponding homogenized tensor a^0 is given by, for $\mathcal{M}_Y = \frac{1}{|\mathcal{Y}|} \int_{\mathcal{Y}} dy$

$$\begin{aligned}
 a_{1111}^0 &= \frac{1}{\mathcal{M}_Y(1/a_{1111})}, & a_{1112} &= a_{1222} = 0, \\
 a_{1122}^0 &= \frac{\mathcal{M}_Y(a_{1122}/a_{1111})}{\mathcal{M}_Y(1/a_{1111})}, & a_{1212}^0 &= \frac{1}{\mathcal{M}_Y(1/a_{1111})}, \\
 a_{2222}^0 &= \mathcal{M}_Y(a_{2222}) - \mathcal{M}_Y\left(\frac{a_{1122}^2}{a_{1111}}\right) + \frac{(\mathcal{M}_Y(a_{1122}/a_{1111}))^2}{\mathcal{M}_Y(1/a_{1111})}, & & (13)
 \end{aligned}$$

where the components of $a(y_2)$ are given by

$$a_{1111} = a_{2222} = \frac{E(1-\nu)}{(1+\nu)(1-2\nu)}, \quad a_{1122} = \frac{E\nu}{(1+\nu)(1-2\nu)},$$

$$a_{1212} = \frac{E}{2(1+\nu)}, \quad a_{1112} = a_{1222} = 0,$$

and $E = E(y_2)$ denotes the Young's modulus of the material while $\nu = \nu(y_2)$ denotes its Poisson's ratio.

Problem 1 Consider the problem (1), where the domain Ω is defined as a 2D region occupied by the points $(0, 0)$, $(4800, 4400)$, $(0, 4400)$, $(4800, 6000)$, where the unit of distance is mm. Dirichlet boundary conditions are imposed at the end $x = 0$, and the body is subjected to a shearing load $\mathbf{g} = (0, 5)$ N/mm² at the end $x = 4800$. The volume force \mathbf{f} is assumed to vanish and the material is taken to be linear elastic and isotropic. Further, a^ε is assumed to vary along only one direction. Finally, the Young's modulus and Poisson's ratio are defined by the functions

$$E(y_2) = 8.35 \left(\frac{1 + (0.2 + 0.1\cos(2\pi y_2))}{(0.2 + 0.15\sin(2\pi y_2))} \right) \text{kN/mm}^2,$$

$$\nu(y_2) = 0.2 + 0.1\cos(2\pi y_2).$$

From (13), the tensor a^0 can be written (in Voigt Notation) as

$$a^0 = \begin{pmatrix} 56.4099 & 14.6599 & 0 \\ 14.6599 & 83.2061 & 0 \\ 0 & 0 & 20.8750 \end{pmatrix}.$$

The error between \mathbf{u}^0 and \mathbf{u}^H for macro order $p = 1$ and micro order $q = 1$ is plotted in Fig. 1, and the convergence rate is verified to be linear in the H^1 -norm and quadratic in the L^2 -norm [1]. The deformed mesh for the homogenized and multiscale solutions is shown in Fig. 2, while Fig. 3 compares the strain energy density for both solutions.

Problem 2 Consider (1), where the domain is defined by $\Omega = (0, 1) \times (1, 0) \setminus \mathbf{B}(0, 0.5)$ where the unit of distance is metres. Dirichlet boundary conditions in the x dimension are imposed at the end $x = 0$, and in the y dimension at $y = 0$. The body is subjected to shearing load $\mathbf{g} = (1E + 5, 0)$ kN/m² at the end $y = 1$ and the volume force \mathbf{f} is assumed to vanish and the material is taken to be linear elastic and isotropic. Further, a^ε is assumed to be non-uniformly periodic with coefficients (Fig. 4)

$$a_{1111} = a_{2222} = (3E + 7) \left(\frac{1.5 + \sin(2\pi x/\varepsilon)}{1.5 + \sin(2\pi y/\varepsilon)} + \frac{1.5 + \sin(2\pi y/\varepsilon)}{1.5 + \cos(2\pi x/\varepsilon)} + \sin(4xy) + 1 \right),$$

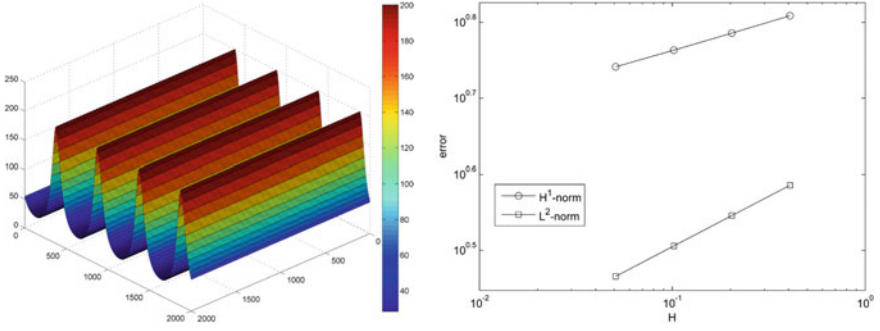


Fig. 1 Plot of Young's modulus $E(y_2)$ (left) and error between \mathbf{u}^0 and \mathbf{u}^H (right)

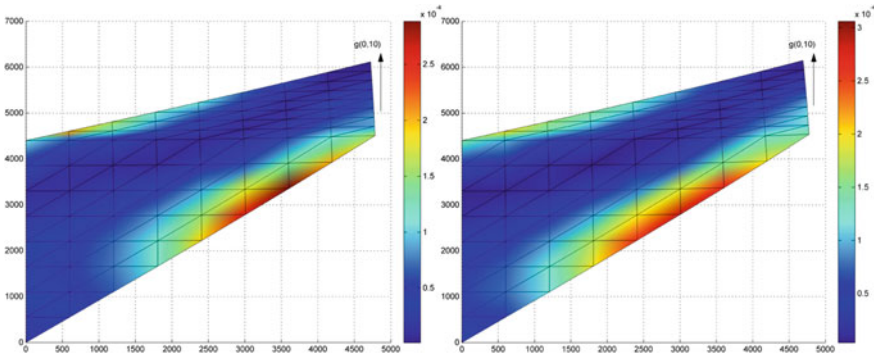


Fig. 2 Deformed mesh for the homogenized solution (left) versus multiscale solution (right)

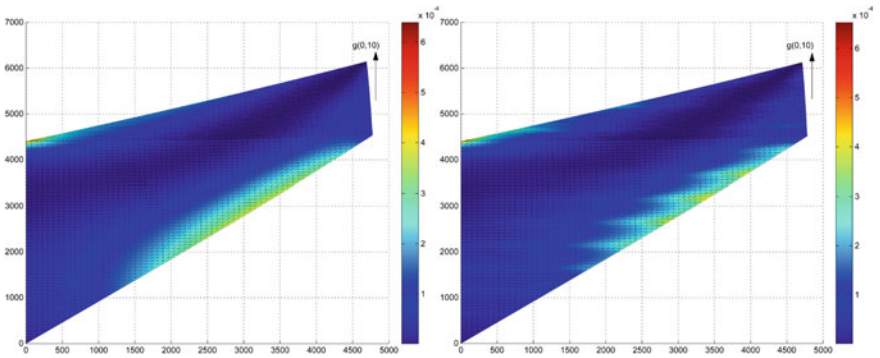


Fig. 3 Strain energy density for the homogenized solution (left) versus multiscale solution (right)

$$a_{1122} = (1E + 7) \left(\frac{1.5 + \sin(2\pi y/\varepsilon)}{1.5 + \cos(2\pi x/\varepsilon)} + \sin(4xy) \right),$$

$$a_{1212} = (1E + 7) \left(2.1 + \frac{2}{1.5 + \cos(2\pi x/\varepsilon)} + \sin(4xy) \right).$$

Problem 2 is solved using a classical finite element algorithm from [9] with a discretization having a degree of freedom of $N = 7.87968E + 5$ and FE space of order $p = 4$. It is also solved using the algorithm presented above with varying macro degree of freedom N and order of macro FE space p and micro degree of freedom n and order of micro FE space q as shown in Tables 2 and 3. The energy and infinity norms of the fine scale solution and multiscale solutions are compared in Table 4.

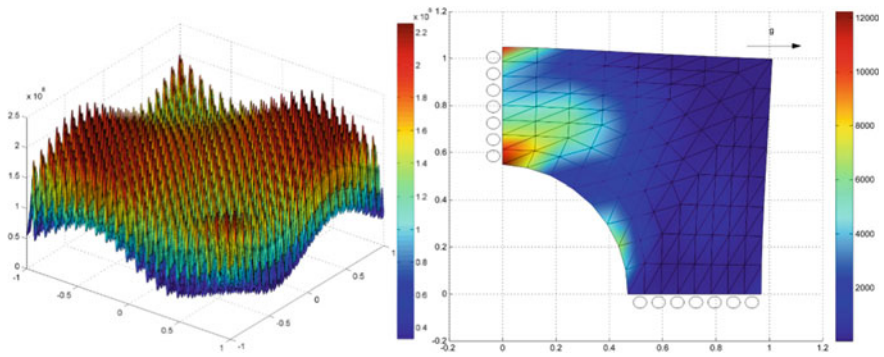


Fig. 4 Plot of material coefficient a_{1111} (left) and deformed mesh for multiscale solution (right)

Table 2 Energy and infinity norms for the multiscale solutions with fixed micro d.o.f. n and varying macro d.o.f. N

Sl. no.	Multiscale solution				
	$n = 9$	$N = 9$	$N = 25$	$N = 81$	$N = 289$
2	$\ \mathbf{u}\ _E$	22.1207	30.5297	36.7621	39.6875
3	$\ \mathbf{u}\ _\infty$	0.0040546	0.0073341	0.010037	0.011269

Table 3 Energy and infinity norms for the multiscale solutions with fixed micro d.o.f. N and varying macro d.o.f. n

Sl. no.	Multiscale solution				
	$N = 25$	$n = 9$	$n = 25$	$n = 81$	$n = 289$
2	$\ \mathbf{u}\ _E$	30.5297	30.8687	30.9272	31.2386
3	$\ \mathbf{u}\ _\infty$	0.0073341	0.0075347	0.0075635	0.0077384

Table 4 Energy and infinity norms for the multiscale solutions versus fine scale solution

Sl. no.	Multiscale solution					Fine scale solution
1	$n = 25$ $N = 25$	$p = 1$ $q = 1$	$p = 2$ $q = 2$	$p = 3$ $q = 3$	$p = 4$ $q = 4$	$N = 7.87968E + 5$ $p = 4$
2	$\ \mathbf{u}\ _E$	30.5297	39.7142	40.642	41.475	42.4995
3	$\ \mathbf{u}\ _\infty$	0.0073341	0.011486	0.01186	0.012032	0.012417

4 Conclusion

We have implemented a multiscale method for plane strain problems in linear elasticity. A computer algorithm to implement the method has also been presented. Two problems have been solved using the algorithm and their results have been compared with the homogenized and fine scale solutions. The results show that the multiscale solution is much more computationally economical in comparison with the standard fine scale finite element solution. We have shown that a fine scale solution with degree of freedom $N = 7.87968E + 5$ and order of FE space $p = 4$ is comparable with the multiscale solution with degrees of freedom $n = 25$, $N = 25$, and order of macro FE space $p = 4$, and micro FE space $q = 4$, which is a striking difference. However, at present, the method is limited to linear problems in elasticity. It may be further developed for multiscale non-linear problems, multiscale phenomena in damage and fracture of materials etc.

References

1. Abdulle A (2006) Analysis of a heterogeneous multiscale FEM for problems in elasticity. *Math Models Methods Appl Sci* 16(4):615–635
2. Abdulle A (2009) The finite element heterogeneous multiscale method: a computational strategy for multiscale PDEs. *GAKUTO Int Ser Math Sci Appl* 31:135–181
3. Abdulle A, Engquist B (2007) Finite element heterogeneous multiscale methods with near optimal computational complexity. *SIAM Multiscale Model Simul* 6(4):1059–1084
4. Abdulle A, Nonnenmacher A (2009) A short and versatile finite element multiscale code for homogenization problems. *Comput Methods Appl Mech Eng* 198(37–40):2839–2859
5. Abdulle A, Schwab C (2005) Heterogeneous multiscale FEM for diffusion problems on rough surfaces. *SIAM Multiscale Mod Simul* 3(1):195–220
6. Albery J, Carstensen C, Funken SA, Klose R (2002) Matlab implementation of the finite element method in elasticity. *Computing* 69(3):239–263
7. Cioranescu D, Donato P (2000) An introduction to homogenization. *Oxford lecture series in mathematics and its applications*. Oxford University Press
8. Efendiev Y, Hou TY (2009) *Multiscale finite element methods: theory and applications*. Springer, Berlin
9. Gockenbach MS (2006) *Understanding and Implementing the finite element method*. SIAM
10. Patrício M, Mattheij R, With G (2008) Homogenisation with application to layered materials. *Math Comp Simul* 79:288–305

Evolution of Four Formulae Derived Over Five Decades to Predict Temporal Scour at Circular Pier



Buddhadev Nandi, Krishanu Sasmal, and Subhasish Das

1 Introduction

The interaction of stream flow and a vertical bridge supporting structure which are creating an obstruction to the flow generates erosion of the sediment bed due to complicated three-dimensional flow separation [1]. The transverse resistivity of the soil supporting the foundation decreases substantially with increasing scour depth, resulting in horizontal deflection of the foundation head. The most significant human aspects are: the insufficiency of hydrological data to base flood magnitude estimations for design purposes; the *absence of reliable techniques for estimating scour at bridge piers*; as well as an inability to predict the impact and accumulation of debris against the bridge structure [2]. In front of such obstructions, the flow velocity is less and on the side of the obstruction, the flow velocity increase which reduces the bed shear stress and the sediment lifted by the action of the horseshoe vortex leads the erosion. Most of the widely used empirical formulas for estimating scour depth under clear water equilibrium (CWE) conditions are derived under conditions of extremely long flow periods. Bridge pier footings designed keeping CWE condition, scour depths can offer significantly higher values than when the flow lasts for a shorter period of time. Smaller scour depths can be attained for a limited time to the peak value of the planned flood hydrograph, thus minimizing the total construction costs. As a result, it is critical to investigate the temporal variation of CWE scour. However, time-dependent studies on the local scouring phenomenon are few.

To determine the maximum depth of scour at bridge piers, several computational and laboratory investigations were conducted. But based on these concepts, bridge pier design may not be cost-effective. Thus, the concept of temporal scour depth (S_{dt}) is established. The S_{dt} is a crucial requirement for safe and cost-effective construction of bridge piers [3]. Due to the gradually increasing scientific interest in evaluating

B. Nandi (✉) · K. Sasmal · S. Das
School of Water Resources Engineering, Jadavpur University, Kolkata, West Bengal, India
e-mail: buddhadevnandi95@gmail.com

S_{dt} , a number of prediction formulae are available [3–9]. Several researchers [10–12] studied the evolution of S_{dt} using well-established computation models.

In the present study, to predict S_{dt} at a circular pier in CWE conditions, four formulae are selected among those that have been derived over five decades. Such four selected formulae are taken from (i) Shen et al. [4], (ii) Melville and Chiew [3], (iii) NCHRP [12] and (iv) Franzetti et al. [9]. These four formulae are compared with well-established S_{dt} experimental data developed by Yanmaz and Altinbilek [13] to verify the accuracy of individual formulae. In addition, several statistical influencing factors are analyzed to achieve the goal.

2 Four Formulae and Experimental Procedure

Several computational and laboratory studies were performed to determine the S_{dt} in CW condition. The reliability of four previously established promising S_{dt} formulae, given below, are tested in this work using 16 literature data from [13] which were conducted in CW conditions with homogeneous bed material.

Shen et al. [4] obtained a formula for scour depth as a function of time by fitting the data from [14] to an exponential function, Eq. 1. The formula was created for circular pier and is predicated on a constrained set of flow and sediment parameters. The same was adopted by NCHRP [12]. Here, P_d is pier diameter, F is Froude number, d_w is depth of flow, V is velocity of the flow, and t is time. Parameters, J and R are dependent upon d_w , P_d , V , t , and F and are determined from the relations given in [12].

Melville and Chiew [3] have collected 84 laboratory sets and developed Eq. 2. This Eq. 2 was used in [8, 11, 12]. Here, V_c is the critical velocity, V_{*c} is critical shear velocity, d_{50} is median sediment diameter, and T is reference time. Now, V_{*c} and T can be determined using other formulae given in [3]. The accuracy of Formula 2 was improved by adjusting the parameters and substituting the maximum scour depth formula with Eq. 2 given in [12], known as S/M formula (Eq. 3). Here, K_1 is arbitrary constant equaling -0.04 . Here, T is determined using other formulae as proposed in [12].

Franzetti et al. [9] proposed a new predictor (Eq. 4) using laboratory data collected from 30 sources and 328 experiments, to evaluate time-dependent and greatest S_{dt} at circular pier in CW conditions. Five dimensionless parameters such as pier slenderness, flow strength, sediment coarseness, and t were considered. Here, $c = 2.57$ (constant), S is sediment relative density, and σ is sediment geometric standard deviation. All related parameter functions are calculated using other formulae given in [9].

$$\frac{S_{dt}}{P_d} = 2.5F^{0.4}\{1 - \exp(JR^2)\} \quad (1)$$

Table 1 Summary of data with necessary experimental range

References	d_w/P_d	V/V_c	P_d/d_{50}	Δ	σ	F
Yanmaz and Altinbilek [13]	1.27–3.51	0.75–0.951	43.93–79.76	1.63–1.64	1.13–1.28	0.28–0.29

$$\frac{S_{dt}}{S_e} = \exp \left\{ -0.03 \left| \frac{V_c}{V} \ln \left(\frac{t}{T} \right) \right|^{1.6} \right\} \quad (2)$$

$$\frac{S_{dt}}{S_e} = \exp \left\{ K_1 \left| \frac{V_c}{V} \ln \left(\frac{t}{T} \right) \right|^{1.6} \right\} \quad (3)$$

$$\frac{S_{dt}}{P_d} = c f_1 \left(\frac{d_w}{P_d} \right) f_2 \left(\frac{P_d}{d_{50}} \right) f_3(\sigma) f_4 \left(\frac{V}{V_c} \right) f_5 \left(\frac{tV}{P_d(S-1)^{0.5}} \right) \quad (4)$$

To determine how the S_{dt} changes, [9] conducted laboratory experiments using single circular bridge pier perspex models with homogeneous bed materials and CW conditions in a 90×67 cm² flume with a 5-m long approach arm. The P_d values of 6.7, 5.7, and 4.7 cm were used for two different uniform bed materials having specific densities of 2691.1 and 2680.9 kg/m³, d_{50} of 1.07 and 0.84 mm. The angle of attack remained constant as V increased. A sketch of 16 selected datasets by [13] is shown in Table 1.

3 Functional Frameworks

Scour depth develops over time and is determined by water flow, sediment properties (σ , ρ_s , d_{50} , V_c), geometry of the obstacle on the bed profile and time. So, the functional relationship can be written as (Eq. 5). Here, the flow parameters are ρ , ν , g , d_w , V ; γ is a correction factor for bed form; α is shape correction factor for obstruction. The functional framework for the selected four literature formulae with their non-dimensional parameters is listed in Table 2.

$$S_{dt} = f^n(\rho_f, \rho_s, \nu, \gamma, g, d_w, V, \sigma, d_{50}, V_c, \alpha, \beta, P_d, t, T) \quad (5)$$

4 Performance of Existing Formulae

In the current study, four previously invented formulae were evaluated for verifying their performance using literature data for CW conditions and the homogeneous bed material. However, due to the homogeneity of the current data, the V/V_c value

Table 2 Parameter for construction of functional framework of four literature formulae

Serial No	Researchers	Functions
1	Shen et al. [4]	$S_{dt}/P_d = f(F, P_d/d_w, d_w, V_t/d_w)$
2	Melville and Chiew [3]	$S_{dt}/S_e = f(V/V_c, \ln(t/T))$
3	NCHRP [12]	$S_{dt}/S_e = f(V/V_c, \ln(t/T))$
4	Franzetti et al. [9]	$S_{dt}/P_d = f(V/V_c, P_d/d_{50}, \sigma, d_w/P_d, \Delta, (tV/P_d \Delta^{0.5}))$

is found smaller than unity, which clearly reflects the CW experimental condition. The accuracy of four formulae dedicatedly created to estimate S_{dt} was graphically validated, as well as the consideration of several statistical influencing parameters. In Figs. 1, 2, 3, 4 the solid lines are the perfect agreement (PA) lines and dashed lines show $\pm 20\%$ deviation from individual PA lines between the observed and predicted normalized S_{dt} .

In Figs. 1 and 4, the X axis represents the observed S_{dt} normalized with P_d and the Y axis represents the computed S_{dt} normalized with P_d . In Figs. 2 and 3, the X axes represent the observed S_{dt} normalized with S_e and Y axes represent the computed S_{dt} normalized with S_e . The numerical formulas for S_{dt} estimation used in [3, 9, 12], and [4] are shown in Figs. 1–4 and collected data from literature [13] are plotted as computed versus measured normalized S_{dt} .

When compared to the observed and computed data by [9], 82% of the literature data falls under the $\pm 20\%$ error line, as seen in Fig. 1. When all 16 datasets were

Fig. 1 Comparison using Eq. 4 [9]

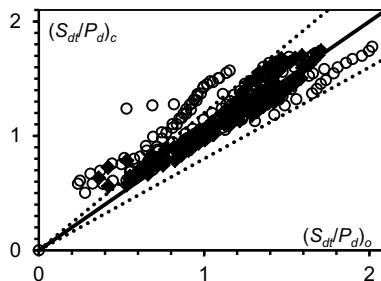


Fig. 2 Comparison using Eq. 2 [3]

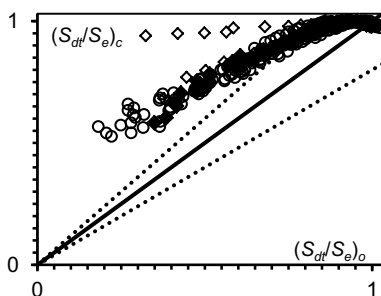


Fig. 3 Comparison using Eq. 3 [12]

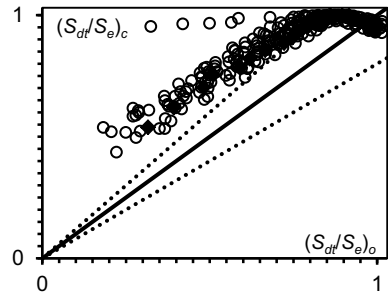
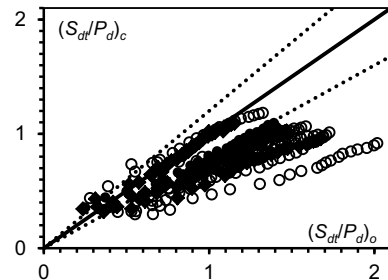


Fig. 4 Comparison using Eq. 1 [4]



compared, three of them fared poorly. The figure shows that no data series is outside the -20% error line, but three hardly few data series points exceed the +20% error band, which is within the maximum bound limit set in [9]. Under prediction of scour depth is conservative and should be avoided in real-world applications; nevertheless, excessive over prediction is equally troublesome for the application engineer when building such bridge piers because it is not economic in engineering terms. However, a higher value for the structural design can be used to produce a higher factor of safety. Both the issue reported in [9], the formula needs to be multiplied by 1.6, i.e., the constant $c = 4.1$ instead of 2.57, for estimating upper-bound scour value.

When computed versus measured normalized scour depth are presented in comparison to each other, 48% of the data from the literature are outside of the $\pm 20\%$ error line. Although all data series initially overestimate the temporal scour depth, at a later stage the computed value is within the error band, as can be seen in Fig. 2, nearly 50% of data points lie outside the 20% error band. As we all know, the upper bound limit is what the field or application engineer works with, however significantly over calculated data results in uneconomical designs for construction. Therefore, calculating the S_e is helpful, but from the temporal perspective, it is rather difficult.

Here, 54% of the data from the literature are outside the $\pm 20\%$ error line when computed versus measured normalized S_{dt} are compared to one another. Even though all data series initially overestimate the temporal scour depth at a later stage, as can be shown in Fig. 3, approximately half of the data points fall below the 20% error

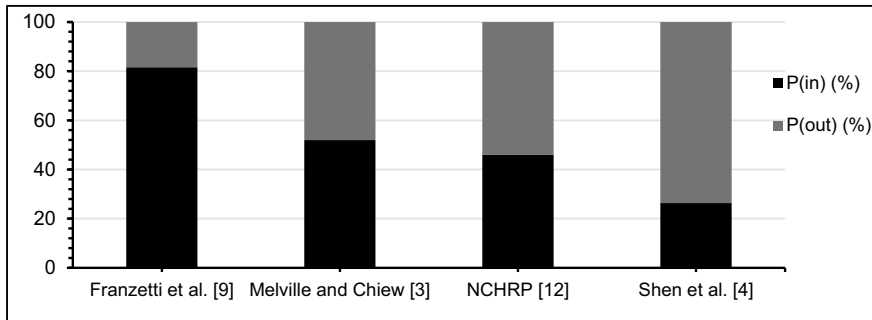


Fig. 5 Percentages in [P(in)] and out [P(out)] considering all 16 datasets

zone. As we all know, the field or application engineer works with the upper bound limit, but drastically over estimated data leads to unsustainable construction designs.

Similar to this, when comparing computed versus measured average scour depth for Shen et al.'s [4] formula presented in Fig. 4., 26% of data from the literature falls within the $\pm 20\%$ error line. About three-fourths of them, are outside the error band and, of those, nearly all of those data points are outside the -20% error band, which makes them useless for designing hydraulic structures like bridges because application engineers occasionally use overestimated values that are within the upper bound limit.

Figure 5 shows the numerical formula for scour depth estimation by [3, 9, 12 and 4] and the data which had been selected from the literature were plotted as computed versus measured normalized scour depth. From the figure, it can be seen that 82% of the literature data falls inside the $\pm 20\%$ error line when compared to the observed and computed data by [9]. Similarly, 52%, 46%, and 26% of data from the literature fall under the $\pm 20\%$ error line when compared with the formulae in [3, 4] and [12].

5 Sensitivity Analysis

A variety of statistical parameters are also used to evaluate the correctness of the literature formulae. Here, 10 statistical parameters are used to indicate the data accuracy namely Correlation Coefficient (CC), RMSE, Coefficient of Determination (R^2), Nash Sutcliffe Efficiency (NSE), Sum of Squared Errors (SSE), MAE, MAPE, NRMSE, Kling-Gupta efficiency (KGE), and Index agreement (IA) shown in Table 3. Compare the predictor performance in this study among four literature formulae in terms of several statistical influencing factors.

The Pearson product-moment CC, sometimes known as Pearson's CC and R^2 equalling the squared value of Pearson's CC, is the most well-known indicator of dependency between two quantities. The highest CC and R^2 are observed for [3] and

Table 3 Sensitivity analysis of selected four literature formulae

Authors	CC	RMSE	R ²	NSE	SSE	MAE	MAPE	NRMSE	KGE	IA	P ^{out} (%)
Franzetti <i>et al.</i> [9]	0.91	0.18	0.82	0.76	9.6	0.14	0.14	0.16	0.81	0.93	18
Melville and Chiew [3]	0.94	0.19	0.88	0.18	10.83	0.16	0.16	0.26	0.53	0.75	48
NCHRP [12]	0.88	0.19	0.78	0.14	11.43	0.17	0.17	0.27	0.55	0.74	54
Shen <i>et al.</i> [4]	0.72	0.41	0.52	-0.32	52.17	0.34	0.34	0.37	0.41	0.66	74

the lowest values are observed in the case of [4], However, [9] has CC and R² values of 0.91 and 0.82 respectively, the second highest among all.

It is simpler to compare models with various scales according to the NRMSE, which links the RMSE to the observed range of the variable. The absolute error is the difference between the computed value and the observed value, represented as an absolute number. The mean absolute error is the average of the absolute differences between computed and real observations, where each difference is given equal weight (MSE). The least squares approach for generating regression coefficients minimizes the SSE, which indicates the error is not eliminated by the regression line. The most popular method of measuring forecasting error is the MAPE, presumably because the units of the variable are scaled to percentages and are therefore simpler to comprehend. In the instance of [9], the non-beneficial criteria such as NRMSE, RMSE, SSE, MAE, and MAPE have lower values, whereas, in the case of [4], they have the highest value.

The IA standardizes the measurement of the model prediction error, which ranges from 0 to 1. The quality of fit measure provides a diagnostically interesting decomposition of the NSE. Taylor skill score links the models’ correlation coefficient and standard deviations. For Franzetti *et al.* [9] formula, the remaining beneficial criteria have the highest value, while Shen *et al.* [4] formula has the lowest value.

To evaluate each formula [3, 4, 9, 12], the beneficial criteria in Table 3 are arranged in decreasing order and the non-benefit criteria are arranged in increasing order. P_{out} values (%) are also arranged in increasing order to evaluate all four formulas. It is noticeable that Eq. (3) [9] performs better than the other formulas as the value of all beneficial criteria is higher and non-beneficial terms are lower in the case of Eq. (3) [9] as shown in Table 3.

6 Conclusions

Several researchers carried out studies to estimate temporal scour depth, S_{dt} . The current study considers four formulas derived over the last six decades. Due to the limited data set collected from the laboratory experiments, this study tries to select the best one for predicting the S_{dt} . Ten different statistical performance metrics, such as CC, RMSE, R^2 , NSE, SSE, MAE, MAPE, NRMSE, KGE, and IA and the proportion of data points outside of the 20% error zone are used to evaluate the performance of the formulae.

The parameters included in this study to measure the computed S_{dt} using four such formulae are flow factors, bed sediment properties, pier geometry and time. The effectiveness of the scour function is quantified as a percentage of the experimental data point for which the normalized computed scour depth differs from the measured one by more than 20% using 16 experimental data from the literature.

Franzetti et al. [9] formula performed better on four-fifths of the data points. Half of the data points outperformed in the case of both Melville and Chiew [3] and NCHRP [12] formulae and for Shen et al. [4] formula, three-fourths of the data set outperformed. It is observed that hardly a few beneficial criteria (CC, R^2) are greater in the case of Melville and Chiew [3] formula, However, Franzetti et al. [9] formula also has good agreement with respect to CC and R^2 . For all other beneficial and non-beneficial criteria such as RMSE, NSE, SSE, MAE, MAPE, NRMSE, KGE, and IA, Franzetti et al. [9] formula performed well in comparison with other formulae.

References

1. Das S, Das R, Mazumdar A (2013) Circulation characteristics of horseshoe vortex in the scour region around circular piers. *Water. Sci. Eng.* 6(1):59–77
2. Zhang G, Liu Y, Liu J, Lan S, Yang J (2022) Causes and statistical characteristics of bridge failures: A review, *J Traffic Transp Eng* (2022)
3. Melville BW, Chiew YM (1999) Time scale for local scour at bridge piers. *J Hydraul Eng* 125(1):59–65
4. Shen HW, Schneider VR, Karaki S (1966) Mechanics of local scour: supplement, methods of reducing scour, Doctoral dissertation. Colorado State University, Libraries
5. Sumer BM, Christiansen N, Fredsøe J (1993) Influence of cross-section on wave scour around piles. *J Waterway Port Coast Ocean Eng.* 119(5):477–495
6. Oliveto G, Hager WH (2002) Temporal evolution of clear-water pier and abutment scour. *J Hydraul Eng* 128(9):811–820
7. Lança RM, Fael CS, Maia RJ, Pêgo JP, Cardoso AH (2013) Clear-water scour at comparatively large cylindrical piers. *J Hydraul Eng* 139(11):1117–1125
8. Choi SU, Choi B (2016) Prediction of time-dependent local scour around bridge piers. *Water Environ J* 30(1–2):14–21
9. Franzetti S, Radice A, Rebai D, Ballio F (2022) Clear water scour at circular Piers: A new formula fitting laboratory data with less than 25% deviation. *J Hydraul Eng* 148(10):1–13
10. Mia MF, Nago H (2003) Design method of time-dependent local scour at circular bridge pier. *J Hydraul Eng* 129(6):420–427
11. Simarro G, Fael CMS, Cardoso AH (2011) Estimating equilibrium scour depth at cylindrical piers in experimental studies. *J Hydraul Eng* 137(9):1089–1093

12. Sheppard DM, Demir H, Melville B (2011) Scour at wide piers and long skewed piers, NCHRP Rep. No. 682. (2011) Washington, DC: Transportation Research Board
13. Yanmaz AM, Altinbilek HDGA (1991) Study of time-dependent local scour around bridge piers. *J Hydraul Eng* 117(10):1247–1268
14. Chabert J, Engeldinger P (1956) Étude des affouillements autour des piles de ponts, Technical Rep. [In French.] Chatou, France: Laboratoire National d'Hydraulique

Improvement in Geometric Design of SH-18: A Case Study



Kundan Meshram and Dhananjay Pandya

1 Introduction

In India moreover as within the whole world transport system plays a vital role in the development of the country as an economic method and within the alternative ways in which additionally like the development of agriculture and industries. It additionally helps us to cut back financial condition by making employment.

The Planning Commission has prepared Model Concession Agreement (MCA) for State Highways. These MCAs follow the Design, Built, Finance and Operate (DBFO) approach that needs the holding in turn the responsibility for comprehensive design. However, the responsibility for providing safe and ultimately rests with the government. Safety on rural highways is of high concern because nearly $2/3$ of road deaths are found on such roads. Geometry is the key factor that affects it like speed of the vehicle which consequently results in crash incidents [1, 5].

Alignment of the road is one amongst the parts of geometry that abrupt into Rural Highways. An elongated tangent or edged curve after a flat curve is an example of inconsistency within the alignment. These alignments induce unwanted and haphazard changes in speed which will cause crashes. So, highway design must be evaluated for compatibility in geometry [2–4]. Several developed countries like The United Kingdom, Australia, Switzerland, Canada, France, and Germany have adopted numerous geometric consistency evaluation techniques for the design process [12].

In the present study, the project area is taken as part of SH-18 which starts at Badnawar and ends in Kardawad village (near Petlawad town) Madhya Pradesh (India).

K. Meshram (✉)

Department of Civil Engineering, Guru Ghasidas Vishwavidyalaya, Bilaspur, Chhattisgarh, India
e-mail: kundan.transpo@gmail.com

D. Pandya

CE-AMD, Shri G. S. Institute of Technology and Science, Indore, M.P, India

1.1 Difficulties in Existing Project Section

- (1) Accidents due to Narrow curves: It is habitual nature of drivers to overtake moving vehicles that are moving on curves which leads to a collision between them, which results in an accident, since once the driver attempts to overtake on an unseeing curve, the overtaking sight distance is nearly negligible, lead to the overturning of the vehicle.
- (2) Slipping of the vehicle in season: The road constructed in hilly and terrain area experience fog in winters and because of fog sight distance for the driver is reduced. During raining season due to precipitation, the road surface becomes slippery which reduces the coefficient of friction between the tyre and the paved surface is greatly reduced. This result is in the slithering of vehicles, particularly 2-wheelers.
- (3) Poor curve negotiation: Due to hilly terrain, driving a vehicle depends purely on the sight distance of the headlight of the vehicle, this is also another reason for accidents because the driver doesn't consider the sharp curves.
- (4) Geometry of road: With the existing condition of road geometry, which has poor stretches. The project section passes through villages and rolling terrain, wherever there are sharp curves. The present vertical curves are typically unsatisfactory except for the Mahi River approach area. Camber provided was found to be flat, for superelevation at most of the curves was inadequate.

There is a primary need to improve the present State Highway(SH)-18, a minimum of 2-Lane standard because the Average Daily Traffic (ADT) and passenger car unit of the project section is 10095 veh/day and 101,056 PC/day respectively in which 8.62% is heavy traffic. The Annual Daily Traffic is increasing by 15% in recent years. Therefore, improving the traffic and travel condition in this section is required by improving the existing geometry of the project section: 1) To confirm balanced road interconnectivity within the state; 2) To reduce specific kinds of accidents; 3) To rupture the period of travelling; 4) To improve the geometrical design of road as per IRC (Indian Roads Congress) and conjointly prep-end all safety measures with high design preciseness; 5) To save time, achieved by using software tool; 6) To subtilized saving in vehicle operation value and less pollution; 7) To uplift economic factor due to quicker higher accessibility.

The aim of the study is to improve geometrical design parameters, horizontal and vertical curves in the existing project section.

2 Study Area

The highways in the state are continuous routes, connecting the headquarters of the district and other important towns inside the state and further joining with major national highways or connecting with other nearby states, Madhya Pradesh, INDIA, the state has a good network of roads.

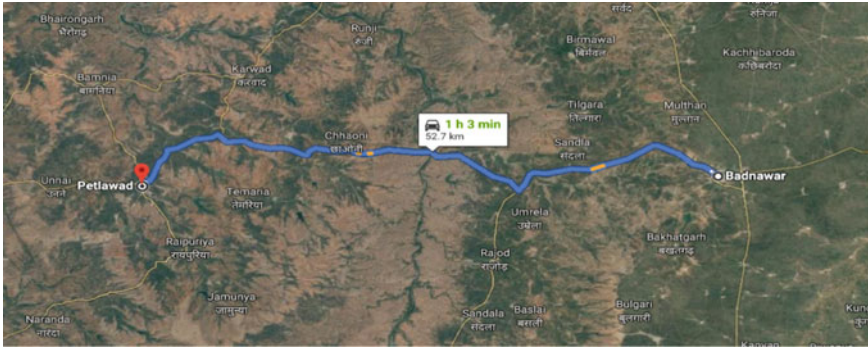


Fig. 1 Study area

The State Highway-18 starts from Bhopal city and ends at Thandala town. The total distance covered by SH-18 is 335 km. in Madhya Pradesh. Major towns covered by SH-18 are “Bhopal—Sehore—Ashta—Dewas—Ujjain—Badnawar—Petlawad—Thandala”, as shown in Fig. 1.

The road section starts from Badnawar town and ends at Kardawad village (near Petlawad) and it covers 44.90 km. length. Town Badnawar is situated in Dhar District and town Petlawad is in Jhabua District. The River Mahi divides the Project Road into Dhar and Jhabua, which lies in the South East of Madhya Pradesh, India.

The aim of this study is to impart road geometrical design into the software system in addition as relate to the planning standards applied to the software system. Bentley MX ROAD (advanced, sting-based modelling tool) software was a system that permits the fast and correct design of all road varieties.

3 Data Collection

3.1 Preliminary Survey

Topographic data was taken by total station and GPS device given in Table 1.

3.2 Volume Count Survey

3.2.1 Average Daily Traffic (ADT) Survey

ADT survey was conducted at chainage no. 17300 and 20,500, as shown in Table 2.

Annual Average Daily Traffic (AADT) was observed by normalizing the ADT at all the locations.

Table 1 Data of total station survey

S.N	Nothing	Easting	Reduce level
1	2,546,315	523,349.9	505.641
2	2,546,349	523,313.0	505.48
3	2,546,382	523,276.1	505.495
4	2,546,416	523,239.1	505.937
5	2,546,450	523,202.1	505.841
6	2,546,482	523,164.1	506.168
7	2,546,510	523,122.7	505.737
8	2,546,538	523,081.2	505.039
9	2,546,565	523,039.5	504.828
10	2,546,593	522,997.9	504.411
11	2,546,863	520,665.0	497.066
12	2,549,275	483,825.9	394.216
13	2,549,277	483,796.0	394.191
14	2,549,279	483,766.0	393.804
15	2,549,277	483,736.3	392.566
16	2,549,273	483,706.6	391.36
17	2,549,268	483,676.9	391.05
18	2,549,264	483,647.3	390.868
19	2,549,259	483,617.6	390.536
20	2,549,256	483,595.1	390.143

3.3 *Hourly Variation and Peak Hour Variation*

The hourly variation and peak hour variation are shown in Table 3.

3.4 *Terrain*

The present road under consideration passes through typically plain/rolling terrain. The following terrain classification has been adopted (Table 4).

3.5 *Design Speed*

The design speed is the guiding criteria for correlating options such as sight distance, curvature and superelevation upon which the safe operation of the vehicles depends.

Table 2 Summary of ADT

Type of vehicle	At km. 17 + 300		At km. 20 + 500	
	Vehicles	PCU	Vehicles	PCU
Fast passenger vehicles				
2-Wheeler	4668	2334	5554	2777
Auto	111	111	71	71
Car/Jeep/Van	3624	3624	5321	5321
Mini Bus	58	87	71	107
2-Axle Bus	42	126	250	750
3-Axle Bus	13	39	151	453
Fast Moving Vehicles				
Mini LCV	344	344	771	771
LCV	312	468	1461	2192
2-Axle Truck	295	885	1259	3777
3-Axle Truck	276	828	1620	4860
MAV (4–6 axle)	190	855	1967	8852
MAV (>6 axles)	0	0	0	0
Tractor	36	54	22	33
Tractor with Trailer	70	315	160	720
JCB, HVM	4	12	2	6
Others	0	0	0	0
Slow Moving Vehicles				
Cycle	11	6	9	5
Cycle Rickshaw	0	0	0	0
Animal Drawn	2	12	0	0
Toll Exempted Vehicles				
Car	5	5	9	9
Bus	0	0	0	0
Truck	0	0	0	0
Total	10,095	10,156	18,716	30,737

Table 3 Peak hour factors observed at traffic count locations

S. No	Survey location	Peak hour volume (PCU)	ADT (PCU)	PHF (%)	Peak hour
1	km. 17 + 300	760	10,156	7.48	9:00 AM – 10:00 AM
2	km. 20 + 500	1976	30,737	6.42	9:00 AM – 10:00 AM

Table 4 Classification of terrain

S. No	Terrain	Cross Slope
1	Plain	< 10%
2	Rolling	10–25%
3	Mountainous	25–60%
4	Steep	> 60%

Table 5 Design speed guidelines

Terrain Nature	IRC: SP: 73–2015		IRC: SP 84–2014	
	Ruling	Minimum	Ruling	Minimum
Plain	100	80	100	80
Rolling	100	80	100	80
Mountainous	60	40	60	40
Steep	60	40	60	40

The design speed for plain and rolling terrain has been proposed as follows (Table 5).

Since, the project road passes through the Plain/Rolling terrain. Hence a design speed of 80 km/hr. has been proposed & IRC: SP: 73–2015 is followed.

3.6 Horizontal Alignment

Software MX Road is used to represent the horizontal alignment. The report is also generated according to the final alignment decided with all the detailing such as IP chainage, tangent, arc length, arc start chainage, arc end chainage, radius hand of arc etc. (Fig. 2).

4 Results and Discussion

With the considerations of IRC specification [6–11] and existing characteristics of the project road, the subsequent design value is taken for carrying out the design of the project work by using the software. The result drawn from the software output is as follows (Table 6).

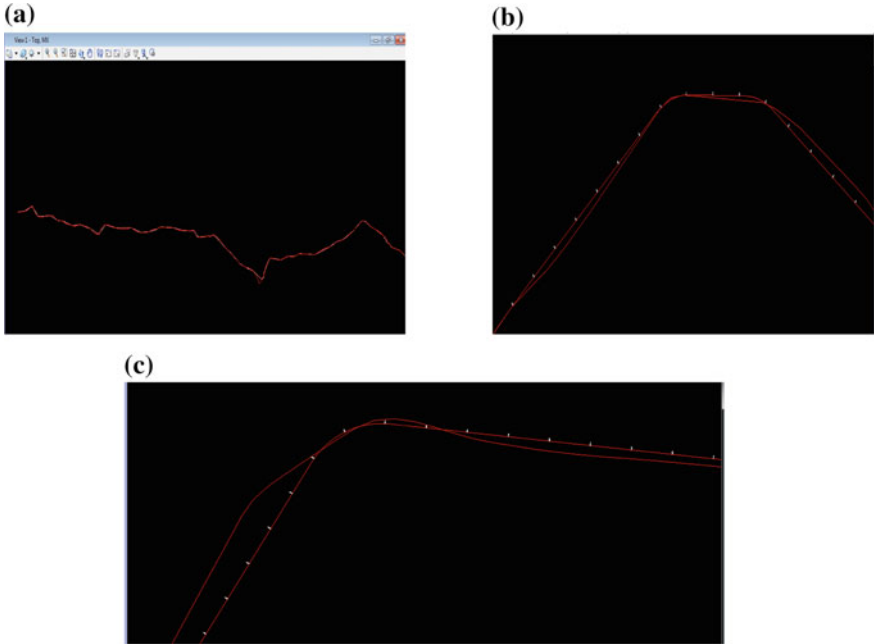


Fig. 2 a New alignment overlapping the existing alignment b Part of Horizontal alignment (Curve-1) c Part of Horizontal alignment (Curve-2).

4.1 Design Standard Proposed

4.2 Horizontal Curve Details

The location of the horizontal curve is given in Table 7.

The results for horizontal curves are shown in Table 8.

Where,

HC = Horizontal Curve, LC = Length of Curve, E = Existing, P = Proposed.

4.3 Vertical Curve Details

The location of the vertical curve is given in Table 9.

The results for horizontal curves are shown in Table 10.

Where,

VC = Vertical Curve, LC = Length of Curve, K = Design Rate of Vertical Curvature, E = Existing, P = Proposed.

Table 6 Design standards adopted

S. No	Items	Existing parameters	Adopted design standards
1)	Design speed	40 kmph	80 kmph
2)	Cross-sectional requirements		
3)	ROW	10 m	12 m
4)	Width of a carriageway on both sides of the median 2-lane carriageway with each lane of 3.5 m width	7.0 m	7.0 m
5)	Shyness	Not available	0.25 m
6)	Paved shoulder width	Not available	2.5 m
7)	Camber/Crossfall		
8)	Carriageway included paved shoulders	2.5%	2.5%
9)	Horizontal alignment		
10)	Ruling radius of horizontal curve	230 m	250 m
11)	Superelevation	5%	7%
12)	Minimum transition length	44.39 m	90 m
13)	Safe stopping sight distance	45 m	180 m
14)	Setback distance at horizontal curve	2.84 m	9 m
15)	Vertical alignment		
16)	Ruling gradient	3.9%	2.5%
17)	Minimum length of vertical curve	30 m	60 m
18)	Gradient		
19)	Maximum	4.5%	3.3%
20)	Minimum	3.4%	0.3%

Table 7 Horizontal curve detail

Horizontal curve (HC)	Chainage No. (Km.)	
	Start	End
HC-1	10 + 690	10 + 750
HC-2	12 + 250	12 + 320
HC-3	25 + 610	25 + 700

Table 8 Results for horizontal curves

HC	LC (Km)	Speed (Kmph)		Radius (m)		Superelevation (%)		Transition length(m)		Setback distance (m)	
		E	P	E	P	E	P	E	P	E	P
HC-1	60	40	80	100	400	4	7	44.39	90	2.11	9.07
HC-2	70	40	808	100	400	4	7	44.39	90	2.12	9.47
HC-3	90	40	80	45	400	8.88	7	53.7	90	2.84	9.48

Table 9 Vertical curve detail

Vertical Curve (VC)	Chainage (Kmph.)	
	Start	End
VC-1	1 + 437	1 + 467
VC-2	2 + 173	2 + 223
VC-3	2 + 607	2 + 697
VC-4	3 + 988	4 + 108
VC-5	5 + 196	5 + 296

Table 10 Results for vertical curve

VC	LC (Km.)		Speed (Kmph)		Radius (m)		Gradient difference (%)		length of VC(m)	K
	E	P	E	P	E	P	E	P		
VC-1	30	159.33	30	80	769.2	7966.5	3.9	2	30	6.544
VC-2	50	132.29	30	80	1471	9992.5	3.4	1.33	50	24.524
VC-3	90	135.75	35	80	2571	16,161	3.5	0.84	90	35.662
VC-4	120	175.23	40	80	3000	13,575	4	-1	120	31.504
VC-5	110	129.29	25	80	2444	19,297	4.5	0.67	100	29.463

The further results are drawn as follows:

- 1 The design speed of alignment is 80 km/h and almost all existing road is utilized.
- 2 Within the proposed Right of Way, all geometrics are planned and farthermost all security measures are viewed.
- 3 Geometrics of the project corridor are designed as per IRC and all safety measures are considered.
- 4 Calculation and application of superelevation with location and link are developed.
- 5 The proposed alignment clashes minimum horizontal curve radius at the junction (minor), where the speeds are finite to a minimum.
- 6 For a few sections, limiting values are adopted where site restriction conquers.

5 Conclusions

The aim of the study is to improve the geometrical design of the existing State Highway. The important parameters of road components like horizontal alignment, vertical profile and side road activities and the combination of these elements were intended as the main influence. A segment that makes risky locations and or road sections and also a necessary factor of each element is considered.

According to the case study following findings were obtained.

- a. Alignment has been designed for 80 Kmph speed in place of 40 kmph and a plan and working cross-sections are developed.
- b. Design of Horizontal and Vertical curves as per the requirement of site condition for removing black spots on the curve.
- c. The proposed superelevation for the horizontal curve is 7% whereas the superelevation for the existing road is less than 7%.
- d. The proposed setback distance for the horizontal curve is 90 whereas the existing setback distance is less than 90.
- e. The length of the vertical curve increases up to four times as compared to the existing length of the curve.
- f. The existing gradient difference of vertical curves is less than the value given in codal provisions as per IRC and the proposed gradient difference of vertical curves is designed as per IRC i.e. 3.3%.

References

1. Vayalamkuzhi P, Amirthalingam V (2016) Influence of geometric design characteristics on safety under heterogeneous traffic flow. *J Traffic Transp Eng* 3(6):559–570
2. Nazimuddin MK, Faheem MI, Aquil MM (2017) Geometric design of a highway using Mx Road, *International J. of Engg. Research and Indu. Appls.*, 10(2017) 25–34
3. Seneviratne PN, Islam MN (1994) Optimum curvature for simple horizontal curves. *J Transp Eng* 120(5):773–786
4. Miaou SP (1994) The relationship between truck accidents and geometric design of road sections: Poisson versus negative binomial regressions. *Accid. Anal. and Prev.* 26:471–482
5. Garber NJ, Ehrhart AA (2000) Effect of speed, flow, and geometric characteristics on crash frequency for two-lane highways. *Transp Res Rec* 1717(1):76–83
6. IRC: 73–1980. Geometrical design of standard for rural (Non-Urban) Highways. The Indian Road Congress, New Delhi
7. IRC: 38–1988. Design of Horizontal Curves for Highway and Design Tables. Indian Road Congress. New Delhi
8. IRC: SP 23–1983. Design of Vertical Curves of Highways. Indian road congress, New Delhi
9. IRC: 64–1990. Capacity of Road in Rural Areas. Indian Road Congress, New Delhi
10. IRC: SP: 73–2015. Manual of Specification & Standards for Two Laning of Highways with Paved Shoulder. Indian Road Congress, New Delhi
11. IRC: SP: 84–2014. Manual of Specification & Standard for Four Laning of Highway through Public Private Partnership. Indian Road Congress, New Delhi
12. Gibreel GM, Easa SM, Hassan Y, Dimeery IE (1999) A state of the art of highway geometric design consistency, *J Transp Eng*, 125 305–313

Comparison of Three Turbulence Models in Predicting the Particle Removal Efficiency of a Sedimentation Tank



Mk Raeesah  and Thiyam Tamphasana Devi 

1 Introduction

Sedimentation is a technique based on gravity which is used to remove suspended particles from water. Every water and wastewater treatment facility uses this technique, which has been around for more than a century. Sedimentation tanks can be either circular, where an up-flow pattern is generated, or rectangular, with a horizontal flow. The turbid water will pass through these tanks at a modest speed, giving the suspended particles time to settle. The properties of the suspended solid particles and the flow field inside the tank affect the process of sedimentation.

To enhance the settling tank design without undergoing time-consuming and expensive studies, Computational Fluid Dynamics (CFD) method can be used. It makes predictions about the concentration distribution and velocity field of suspended particles in sedimentation tanks. Sedimentation tanks have naturally turbulent flow, and the simulation must have the necessary provisions to consider turbulence. The accuracy of projecting a settling tank's hydrodynamics behavior depends heavily on the type of turbulence model used in the CFD analysis of the tank [1]. The most popular turbulence model used in the settling tank simulations is the Standard $k-\varepsilon$. However, this model is observed to predict lesser flow capacity than that of RNG $k-\varepsilon$ and Realizable $k-\varepsilon$ (RKE) models [1] and less accurate results than the SST $k-\omega$ [2]. Moreover, flows with significantly curved streamlines cannot be predicted well by this model, which can only be utilized for flows with high Reynolds numbers [3]. Since RNG $k-\varepsilon$ and RKE models are enhanced versions of this model, they are expected to give more precise results than the standard version. While, the SST $k-\omega$ is a model having good depictions of low Reynolds number flows [4–6], such as the flow through the settling tank. However, the comparison of SST $k-\omega$ with either RNG $k-\varepsilon$ or RKE in predicting the behavior of the sedimentation tank is not found

Mk Raeesah · T. T. Devi (✉)

Department of Civil Engineering, National Institute of Technology Manipur, Imphal 795004, India
e-mail: thiyam85@gmail.com

in the literature. Therefore, the performances of these three models, RNG $k-\varepsilon$, RKE, and SST $k-\omega$, are evaluated in the current research to determine which one gives the most accurate results.

A full-scale 3-D CFD model of a sedimentation tank is utilized to determine the settling efficiencies using the three models. Then, the comparisons are made between the settling efficiency acquired experimentally from a published work and the settling efficiencies obtained from simulations using the three models.

2 Materials and Methods

Both the Euler–Euler and Euler–Lagrange methods can be used to analyze the interaction of solid particles with fluids. The Euler-Euler method takes into account the fluid and particle phases as a continuum. Whereas, the solid phase is assumed as discrete particles and the fluid phase as a continuum in the Euler–Lagrange method. In the present work, we used the Euler–Lagrange technique in Ansys Fluent v18.1[®].

2.1 Governing Equations

The continuity and momentum equations for the flow can be described in Cartesian-tensor form in Eqs. (1) and (2) respectively as

$$\frac{\partial \rho}{\partial t} + \frac{\partial}{\partial x_i}(\rho U_i) = 0 \quad (1)$$

$$\frac{\partial}{\partial t}(\rho U_i) + \frac{\partial}{\partial x_j}(\rho U_i U_j) = -\frac{\partial p}{\partial x_i} + \frac{\partial}{\partial x_j} \left[\mu \left(\frac{\partial U_i}{\partial x_j} + \frac{\partial U_j}{\partial x_i} \right) - \rho \overline{u'_i u'_j} \right] \quad (2)$$

where, U_i and u'_i express the average and fluctuating parts of velocity, ρ means density of fluid, p means the pressure, μ means dynamic viscosity, and x_i expresses the coordinate. The term $-\rho \overline{u'_i u'_j}$ in Eq. (2) is termed as Reynolds stress tensor, which represents the turbulent effects. Using the Discrete Phase Model (DPM), tracking of particles through the water phase is accomplished by accounting for the particle's force balance.

2.2 Turbulence Models

Three turbulence models have to be used to determine and compare their effects in the current research. The three models are RNG $k-\varepsilon$, RKE, and SST $k-\omega$ models. The RNG $k-\varepsilon$ model is improved for simulating swirling and quickly strained flows

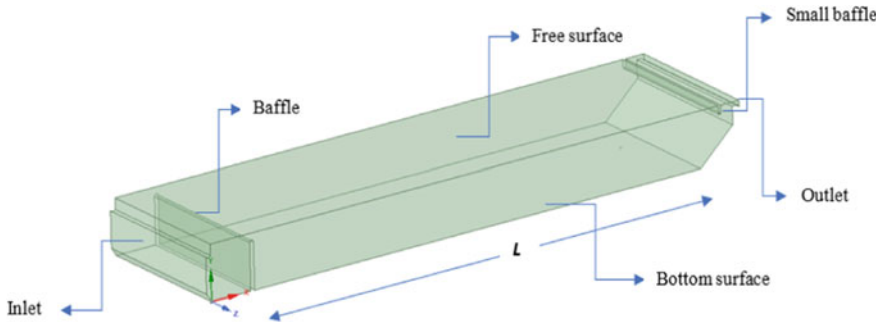


Fig. 1 The configuration of the sedimentation tank adapted from Vahidifar et al. [2]

and the effects of low Reynolds number flows are accounted for in this model [7]. Rostami et al. [8], Tarpagkou & Pantokratoras [9], Kim et al. [10], and Alighardashi & Goodarzi [11] used it in the sedimentation tank studies. Another modified $k-\varepsilon$ model is the RKE model described by Shih et al. [12]. This model gives more precise results than the SKE model for predicting rotating and re-circulating flows [3]. Das et al. [3] used this model in the analysis of settling tanks. The SST $k-\omega$ suggested by Menter [5] is a combination of the $k-\omega$ and $k-\varepsilon$ models. This model combines the $k-\omega$ model's good behavior along the wall with the $k-\varepsilon$ model having good performance in the area of fully formed turbulent flows by using a blending function in a numerically stable way.

3 Sedimentation Tank

The configuration and the flow conditions of the sedimentation tank are adopted from Vahidifar et al. [2] and it has the following dimensions: 42.7 m long, 11.5 m wide, and 4.1 m deep which is shown in Fig. 1. A baffle is placed 3.3 m from the entrance, while a smaller baffle is placed close to the outlet. Wastewater flows into the basin at a rate of 2850 m³/h from the inlet and exits the tank through the outlet. The capacity of the tank is 2007 m³.

4 Simulation

Simulation is performed by creating a full-scale 3-D model in Ansys Workbench. A grid dependency study is done to reduce the error due to the sizes of the meshes and also to find the optimal balance between accuracy, computing time, and convergence. The grid having 5.3 million elements is selected from the three sets of grids 3.5, 5.3 and 6.5 million elements after the analysis of the grid dependency test by comparing

velocity magnitude at different cross sections of the tank. The algorithm for pressure-based solutions is implemented. The Second Order Upwind Discretization methods for the turbulent dissipation rate, the momentum, and the turbulence kinetic energy, the Standard for pressure and the SIMPLE for coupling pressure and velocity are applied for solution methods. The inlet and outlet boundary are respectively subjected to the “Velocity inlet” and “Pressure-outlet” conditions. The inlet has a velocity of 0.0280982 m/s. The turbulence intensity for the inlet and outlet is set at 4.5% and 6% respectively. The free water surface is subjected to a symmetric boundary condition. The other surface boundaries which are in contact with the flow are given the boundary conditions “stationary wall” and “no-slip”.

Additional boundary criteria must first be satisfied to apply the DPM. The condition “Escape” is used for the inlet and outlet, enabling unrestricted passage of the discrete particles through them. The “trap” condition is applied to the tank’s bottom so that when the discrete particles come into touch with them, they end their path, report as “trapped,” and are then treated as settled particles. The condition “reflect” is applied to all other surfaces, allowing particles to bounce off them and continue traveling. The fluid flow was initially resolved without the particles to achieve its constant state. Convergence is attained when all variable residuals are less than 10^{-6} . The mass flow rate and the density of the solid particles are 158.34 gr/s and 5100 kg/m³ respectively. After assigning the particles’ densities and sizes, the particles are then injected from the entrance and their trajectories are tracked.

The particles of 13 classes given in Table 1 are introduced into the water phase separately and are then tracked to determine the sedimentation efficiency of particles. This efficiency indicates the percentage of suspended particles that can be cleared out of the tank. The following formulae are utilized to determine the particle settling efficiency for each class (E_i) as well as the overall settling efficiency (E_{total}).

$$E_i = \left(\frac{n_{i,t}}{n_i} \right) \times 100\% \quad (3)$$

$$E_{total} = \frac{\sum_{i=1}^{13} (m_i \times E_i)}{\sum_{i=1}^{13} m_i} \quad (4)$$

where, $n_{i,t}$, n_i and m_i are the number of particles trapped, number of particles released and mass flow rate of the class i , respectively.

Table 1 Particle size distribution of the 13 particle classes

Particle class	Particle range	Mean particle size	Inlet mass flow rate
1	0–2.464	1.232	7.917
2	2.464–4.743	3.6035	23.751
3	4.743–6.371	5.557	15.834
4	6.371–8.915	7.643	23.751
5	8.915–10.669	9.792	15.834
6	10.669–12.54	11.6045	15.834
7	12.54–14.675	13.6075	15.834
8	14.675–17.288	15.9815	15.834
9	17.288–19.088	18.188	7.917
10	19.088–21.682	20.385	7.917
11	21.682–26.653	24.1675	6.3336
12	26.653–30.4	28.5265	0.7917
13	30.4–34	32.3	0.7917
Total	–	–	158.34

5 Results and Discussion

5.1 Validation

Experimental data on particle settling efficiency from the work of Vahidifar et al. [2] is used for the model validation. The predicted settling efficiencies for each 13 class and total particles from the simulations by the three models and the experimental settling efficiency are presented in Table 2 and also a graph is plotted in Fig. 2.

From Fig. 2, it is found that all the findings obtained from the simulations are close to the value acquired experimentally and hence, have a good match between them.

To compare the accuracy of the settling efficiency predictions for the three models, the error produced by the three models is evaluated and the magnitude of error is calculated in percentage as follows (Eq. 5).

$$\text{Error}(\%) = \left| \frac{\text{Predicted settling efficiency} - \text{Experimental settling efficiency}}{\text{Experimental settling efficiency}} \right| \times 100 \quad (5)$$

The error is calculated for every particle class as well as total particles which are tabulated in Table 3. The model which produces minimum error gives the closest value to the experimental data, which is considered to be the most accurate result.

It is observed from Table 3 that the RNG $k-\varepsilon$ has minimum error for the three particle classes (2, 5, and 11). It means that this model gives the most accurate results

Table 2 The predicted settling efficiencies of the three models and the experimental settling efficiency

Particle class	RNG $k-\epsilon$	RKE	SST $k-\omega$	Expt. data
1	36.69	30.8	28.19	33.16
2	37.45	31.5	29.49	35.07
3	38.59	32.7	31.21	34.1
4	40.45	34.62	33.55	36.5
5	42.64	36.59	37.23	40.65
6	45.26	39.36	39.8	41.93
7	48.23	42.62	44.16	44
8	52.12	47.32	49.34	50.08
9	56.03	52.17	54.39	54.39
10	59.94	56.25	59.06	59.03
11	67.26	64.62	66.58	68.15
12	74.89	74.46	75.27	77.1
13	81.55	81.73	81.87	83.01
Total	45.48	40.10	40.16	42.67

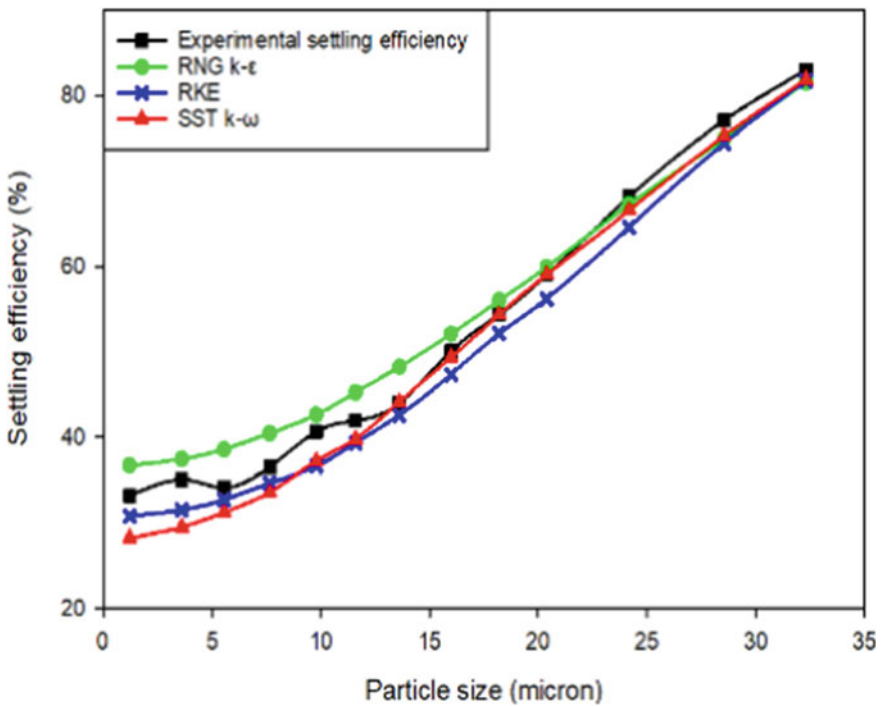


Fig. 2 Experimental settling efficiency and predicted settling efficiencies comparison

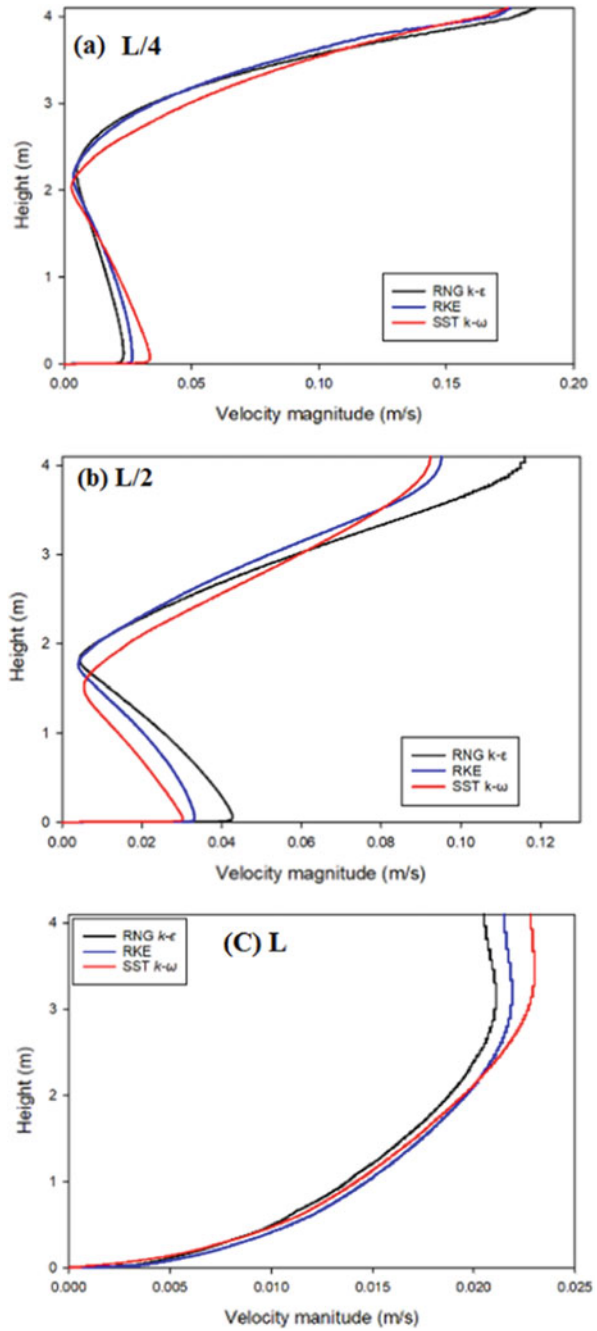
Table 3 Error (%) produced by the three models in the prediction of settling efficiencies

Particle class	RNG $k-\varepsilon$	RKE	SST $k-\omega$
1	10.645	7.11701	14.9879
2	6.7864	10.1796	15.911
3	13.167	4.10557	8.47507
4	10.822	5.15068	8.08219
5	4.8954	9.9877	8.41328
6	7.9418	6.12926	5.0799
7	9.6136	3.13636	0.3636
8	4.0735	5.51118	1.47764
9	3.0153	4.08163	0
10	1.5416	4.70947	0.0508
11	1.30594	5.17975	2.30374
12	2.86641	3.42412	2.37354
13	1.75882	1.54198	1.37333
Total	6.5854	6.02297	5.88235

among the three models for these classes. Similarly, the RKE and the SST $k-\omega$ predict the most accurate results for the three particle classes (1, 3, and 4) and seven particle classes (6, 7, 8, 9, 10, 12, and 13) respectively. The SST $k-\omega$ gives more consistent results than the other two models for the maximum number of classes. Also, the SST $k-\omega$ gives the closest result for the total settling efficiency as it has the minimum error among the three models. As the SST $k-\omega$ has the minimum error for both the highest number of classes and total efficiency, this model yields the most consistent and accurate results among the three models. The distribution of velocity magnitude calculated by the three models for the chosen vertical portions: $L/4$, $L/2$, and L are demonstrated in Fig. 3.

The contour of turbulence kinetic energy for the middle plane of the tank by the three models is presented in Fig. 4. It demonstrates that maximum kinetic energy is found in the model simulated by the RNG $k-\varepsilon$ model while the tank simulated by RKE has the least amount of kinetic energy.

Fig. 3 Comparison of velocity magnitude for RNG $k-\epsilon$, RKE, and SST $k-\omega$ in the middle of the tank at **a** $L/4$, **b** $L/2$ and **c** L



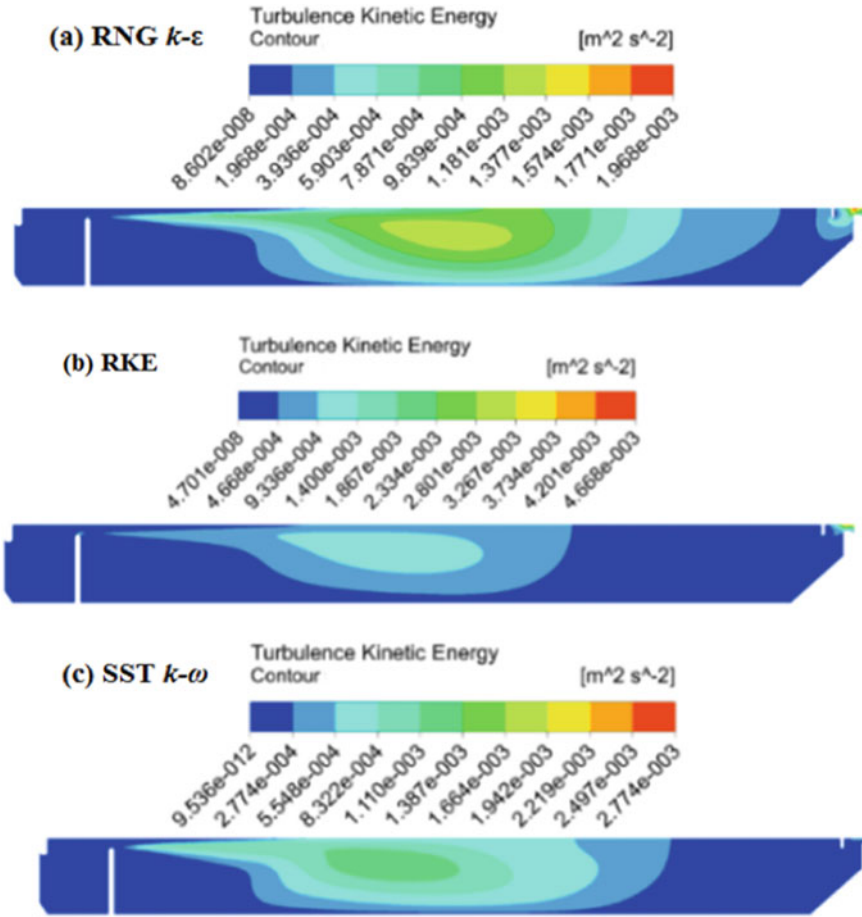


Fig. 4 Comparison of turbulence kinetic energy for a RNG $k-\epsilon$, b RKE c SST $k-\omega$ in the middle plane of the tank

6 Conclusion

The RNG $k-\epsilon$ gives the closest results to the experimental settling efficiency for the three particle classes 2, 5 and 11. Similarly, the RKE model produces the most accurate values for the three particle classes 1, 3, and 4. And, the SST $k-\omega$ gives the most reliable result for the seven particle classes 6, 7, 8, 9, 10, 12, and 13. Therefore, the SST $k-\omega$ gives more precise results than the other two models for the maximum number of particle classes. It is also noted that the overall settling efficiency produced by the SST $k-\omega$ is closest to the overall experimental settling efficiency. Hence, it is concluded that the SST $k-\omega$ model yields the most consistent and accurate results

among the three models. The accuracy of this model can be compared with the other more advanced turbulence model like Large Eddy Simulation in future studies.

Acknowledgements Department of Science and Technology-Science and Engineering Research Board (DST-SERB), New Delhi, Govt. of India, provided full funding for this research project as part of the Core Research Grant Scheme (Grant no. CRG/2020/001341).

References

1. Gao H, Stenstrom MK (2018) Evaluation of three turbulence models in predicting the steady state hydrodynamics of a secondary sedimentation tank. *Water Res* 143:445–456. <https://doi.org/10.1016/j.watres.2018.06.067>
2. Vahidifar S, Saffarian MR, Hajidavalloo E (2019) Numerical simulation of particle-laden flow in an industrial wastewater sedimentation tank. *Meccanica* 54:2367–2383. <https://doi.org/10.1007/s11012-019-01080-6>
3. Das S, Bai H, Wu C, Kao JH, Barney B, Kidd M, Kuethe M (2016) Improving the performance of industrial clarifiers using three-dimensional computational fluid dynamics. *Eng Appl Comput Fluid Mech* 10:130–144. <https://doi.org/10.1080/19942060.2015.1121518>
4. Menter FR (1993) The numerical computation of turbulence. In: 24th fluid dynamics conference, pp 6–9. https://doi.org/10.1142/9789812774071_0006
5. Menter FR (1994) Two-equation eddy-viscosity turbulence models for engineering applications. *AIAA J* 32:1598–1605
6. Fluent A (2013) Ansys fluent theory guide 15.0. In: ANSYS Inc., USA
7. Wilcox DC (1988) Reassessment of the scale-determining equation for advanced turbulence models. *AIAA J* 26:1299–1310. <https://doi.org/10.2514/3.10041>
8. Rostami F, Shahrokhi M, Md Said MA, Abdullah R, Syafalni (2010) Numerical modeling on inlet aperture effects on flow pattern in primary settling tanks. *Appl Math Model* 35:3012–3020 (2010). <https://doi.org/10.1016/j.apm.2010.12.007>
9. Tarpagkou R, Pantokratoras A (2013) CFD methodology for sedimentation tanks: the effect of secondary phase on fluid phase using DPM coupled calculations. *Appl Math Model* 37:3478–3494. <https://doi.org/10.1016/j.apm.2012.08.011>
10. Kim K, Park S, Lee W, Kim J (2020) Simulating the behavior of ballasted flocs in circular lamellar settling tank using computational fluid dynamics (CFD). *Desalin Water Treat* 183:23–29. <https://doi.org/10.5004/dwt.2020.25157>
11. Alighardashi A, Goodarzi D (2019) Simulation of depth and wind effects on the hydraulic efficiency of sedimentation tanks. *Water Environ J* 34:432–440. <https://doi.org/10.1111/wej.12478>
12. Shih TH, Liou WW, Shabbir A, Yang Z, Zhu J (1995) A new $k-\epsilon$ eddy viscosity model for high reynolds number turbulent flows. *Comput Fluids* 24:227–238. [https://doi.org/10.1016/0045-7930\(94\)00032-T](https://doi.org/10.1016/0045-7930(94)00032-T)

Response of Vertically Irregular Buildings to Tsunami



Mrityunjoy Naskar, Rana Roy, and Sunil Singh Mayengbam

1 Introduction

Tsunami is a very disastrous natural event. Such disastrous tsunamis occurred in, the 2004 Indian Ocean tsunami, the 2009 Samoa tsunami, the 2010 Chilean tsunami, the 2011 Great East Japan tsunami, etc. were reported throughout the past two decades [1, 2].

With the evolution of numerical methods, exploring the behaviour of structures due to tsunami is studied with increasing attention [3]. However, the simulation of earthquake-induced tsunamis using a numerical platform may be sensitive to earthquake fault parameters (e.g., [4]). Despite the challenges, researchers are already involved in structural vulnerability assessment using numerical platform to develop a resilient coastal management plan. The structural vulnerability assessment studies in tsunami field mostly conducted nonlinear static pushover analysis (e.g., [5]) on various types of structures viz seaport structures, masonry infill, and reinforced concrete (RC) frames. A limited number of vulnerability assessment studies employ dynamic response history analysis (e.g., [6]). Petrone et al. [6] examined the response of buildings with plane frame assumption and proposed an improved pushover method to estimate structural response which can closely represent that estimated by dynamic time history analysis result. But the estimation of structural response, due to more than one cycle action of tsunami wave using the method is still challenging. Furthermore, tsunami histories may also vary significantly depending on the direction of recording. Consequently, the response of structures to tsunamis

M. Naskar (✉) · S. S. Mayengbam
Department of Civil Engineering, National Institute of Technology Manipur, Imphal 795 004,
India
e-mail: mrityun.jgec@gmail.com

R. Roy
Department of Aerospace Engineering & Applied Mechanics, Indian Institute of Engineering
Science and Technology, Shibpur, Howrah 711 103, India

may vary over the orientation [7]. In view of this, our early study [8] proposed an orientation methodology to estimate proximate response over the orientation by conducting a unidirectional analysis of plane frame regular buildings. But the existing studies never verify the behaviour of vertical geometrically irregular structures under tsunami. A common type of vertical geometric irregularity is the stepped form of buildings, known as ‘stepped building’ after Sarkar et al. [9], is often adopted by the architects for adequate daylight and ventilation in the lower stories.

Against this backdrop, the present study aims to investigate the vulnerability of the vertically irregular buildings under the dynamic action of tsunami waves and estimate an appropriate orientation in which unidirectional analysis of vertical geometrically irregular stepped structures may lead to the worst possible response to provide a safeguard against the uncertainties arises in tsunami analysis.

2 Generation of Tsunami History

The present study used an established numerical model COMCOT (Cornell Multi-Grid Coupled Tsunami) for the simulation of the tsunami [10].

Based on a classical linear elastic theory, following the methodology introduced by Mansinha et al. [11] and modified by Okada [12], the COMCOT model estimates earthquake-induced initial seafloor displacement. COMCOT uses shallow water equations (SWE) in the open ocean and estimates onshore inundation and run-up shortly after tsunami formation [10]. A detailed verification recently made elsewhere by the authors [8] suggests the efficacy of the model.

In the present work, the September 2007 Sumatra earthquake epicentre (latitude: -3.780 , longitude: 100.990) is considered as the source location to estimate tsunami velocity and inundation time histories. Other source parameters are assumed as strike angle (θ) = 30° , rake angle (λ) = 110° , and dip angle (δ) = 75° and magnitude of earthquake (M_w) = 9.1 and focal depth (H) = 25 km for the West Sumatra, Indonesia. Tsunami histories have been recorded at six artificial tide-gauge stations (WS05–WS10) in west Sumatra, Indonesia. However, results of WS09 are presented throughout herein to save space.

3 Tsunami-Induced Loads: Implications of Orientations

Response assessment procedures of structures to tsunamis are relatively simple for plane frames (2-D) (e.g., [5, 6]), which naturally consider one component of tsunami load. For the choice of such 2-D models, structures may be subject to different loads depending on the orientations of the structures and hence the response may also differ. In the present study, 2-D vertically irregular structures are analyzed. As such orientations may bear a significant role.

To study the effects of orientations, velocities pairs in mutually orthogonal directions (say, u_0 and v_0) can be rotated by an arbitrary angle ψ to calculate the velocity components (say, u_ψ and v_ψ) by the following simple transformation.

$$\begin{Bmatrix} u_\psi \\ v_\psi \end{Bmatrix} = \begin{bmatrix} \cos\psi & \sin\psi \\ -\sin\psi & \cos\psi \end{bmatrix} \begin{Bmatrix} u_0 \\ v_0 \end{Bmatrix} \quad (1)$$

For a known value of the velocity component (say u), the tsunami-induced load per unit width (i.e., F/b) may be estimated as under [6].

$$\frac{F}{b} = \text{sgn}(u) \begin{cases} \frac{1}{2} C_D \rho u^2 h & \text{if } F_r < F_{rc} \\ \lambda_F \rho u^{\frac{4}{3}} h^{\frac{4}{3}} g^{\frac{1}{3}} & \text{if } F_r \geq F_{rc} \end{cases} \quad (2)$$

The parameter h denotes the inundation height of the flowing fluid with mass density ρ (taken as 1.2 t/m^3). The force direction is determined by $\text{sgn}(u)$ and g is the acceleration due to gravity. Depending on the increase in flow velocity, the flow regimes change from subcritical to choke and can be characterized by the Froude number (Fr). In Eq. (2), C_D and λ_F is the drag and leading coefficient respectively. To estimate the tsunami load to building frames, a spacing of transverse frames, b has been taken as 5 m. It is thus clear that using (1) and (2), tsunami force per unit width may be computed for different chosen orientations.

Further, we define the tsunami potential as $P_d = \int_0^{T_d} [u^2(t)h^2(t)]^2 dt$, in which t denotes time and T_d represents the duration of the tsunami. The proposed parameter is equivalent to the moment of momentum flux and may indicate structural fragility [13].

Values of the maximum force in the entire history, as denoted by ($F_{u\psi, \max}/b$ and $F_{v\psi, \max}/b$), are noted. Such values are calculated for the velocity components rotated over a range of admissible orientations and are plotted in Fig. 1a. The results indicate that the tsunami-induced loads vary significantly with orientation. Figure 1b depicts the variation of $P_{d,u\psi}$ and $P_{d,v\psi}$. The similarity in variation pattern for P_d with the $F_{u\psi, \max}/b$ and $F_{v\psi, \max}/b$ is apparent. The variation of both the parameters is symmetric and the interchange in component properties would occur after 90° . Hence the tsunami consequences may be estimated over a range of $0-90^\circ$. For the present case, values of P_d and $F_{u, \max}/b$ assume maximum in 75° orientations. Collectively, these patterns in variation appear to indicate that the structural response estimated per unidirectional analysis may be strongly sensitive to the orientations. Hence, in assessing the response of vertically irregular buildings through simple 2-D models, the effect of incidence angles might be of significance and is explicitly considered.

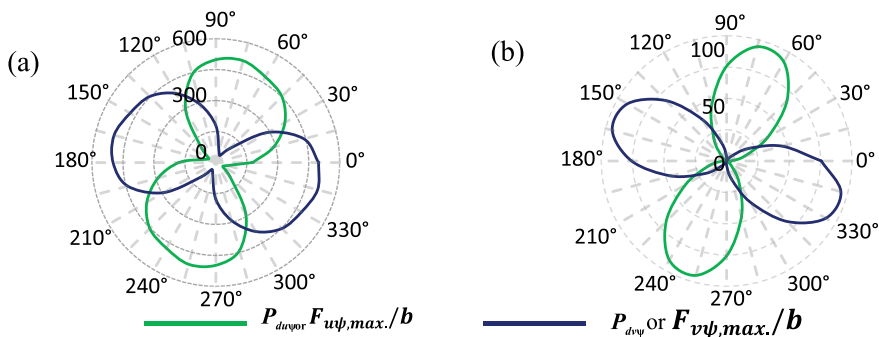


Fig. 1 Variation in (a) $F_{u\psi,max}/b$ and $F_{v\psi,max}/b$. (b) $P_{duv\psi} \times 10^{-6}$ and $P_{dv\psi} \times 10^{-6}$ with change of orientations at West Sumatra, Indonesia

4 Response of Structures

The rigorous analysis has been conducted to study the response of vertically irregular structures. Three regular plane frames (marked as ‘R’) with six-story, eight-story, and ten-story are chosen as representative multi-degree of freedom regular models. Also, six vertical geometrically irregular plane frames (marked as ‘IR’), two with six-story, two with eight-story, and two with ten-story are chosen. The regular building frames are designed to withstand tsunami loads [14]. The frame geometries of the regular buildings are modified in the form of the irregular ones without changing other structural details. The selected six-story, eight-story, and ten-story building frames, each with typical story height and bay length of 3 m and 5 m, respectively, are schematically presented in Fig. 2. The numerical modelling is made using a standard software SeismoStruct, Version 2022 [15]. The members have been discretized into two hundred (200) fibres, each with a uniaxial constitutive relationship, within the framework of forced-based (FB) fibre formulation. By integrating the individual fibres, sectional moment–curvature is simulated. Five (5) Gauss sections are considered to capture the global response through the Gauss–Lobatto quadrature rule. The uniaxial constitutive behaviour of unconfined and confined RC elements is represented by the model originally developed by Mander et al. (1988) and later refined by Martinez-Rueda and Elnashai (1997). On the other hand, a refined model of Filippou et al. (1983), an improved version of Menegotto and Pinto (1973) is used to idealize the behaviour of reinforcing steel considering a bilinear backbone curve and isotropic strain hardening (0.005). The preceding studies have already used similar modelling and noted the detailed idealization (e.g., [8]). The typical story is assumed to have a distributed mass of 8780 kg per unit length and the mass is reduced by 30% for the top story. A stiffness proportional damping of 2% of the tangent stiffness is assumed. The response of the regular and irregular plane frames is computed through unidirectional analysis. The responses for regular and irregular frames are presented in Fig. 3. This shows that the response of irregular frames might exceed that of their regular counterparts. In the unidirectional analysis, several orientations are also

considered to explore the impact of incidence angles explicitly. The responses of six-story, eight-story, and ten-story regular and irregular frames across orientations are presented in Fig. 4. It is evident from Fig. 4 that the response computed through unidirectional analysis may substantially vary with orientations. A careful scrutiny suggests that the maximum response can be obtained by considering the orientations in which F_{\max}/b and P_d are the most intense. Orientations so defined work well for regular and irregular frames. A similar trend is noticed for all regular and irregular frames. Hence, in order to achieve the critical response of vertically irregular buildings, a straightforward unidirectional analysis can be adopted in conjunction with the orientation in which F_{\max}/b or P_d is the most intense. The critical response so obtained may not be the worst possible response; however, a better estimate does not appear possible using 2-D simple framework. Keeping in view that both F_{\max}/b and P_d can be calculated without any reference to a structure, these parameters may be considered as suitable intensity parameters in the context of tsunami hazards. Moreover, the vertically irregular structures are found more vulnerable as compared to the regular structures.

5 Summary and Conclusions

The present study aims to explore the response of earthquake-induced tsunamis to vertically irregular buildings modelled as 2-D finite element model. The study compares the response of regular and irregular frames alongside exploring the sensitivity to incidence angles. In 2-D, unidirectional loading can be applied and hence the effect of incidence angles is studied with a view to identifying the orientation which results in maximum response. A simple definition for such orientation is recognized. The following broad conclusions are drawn.

1. The tsunami load components across the orientations are computed through rotating the pair of the recorded velocity components. The variation pattern of the maximum load per unit width (F_{\max}/b) and the proposed tsunami potential (P_d) of each component shows symmetry of variation over 180° and individual component characteristics are detectably noticed to interchange beyond 90° .
2. The orientation in which the response of vertically regular and irregular structures to unidirectional loading is maximum coincides with the orientation in which F_{\max}/b and P_d is the most intense.
3. The orientation in which the response of vertically regular and irregular structures to unidirectional loading is minimum coincides with the orientation in which F_{\max}/b and P_d is the least intense.
4. The vertically irregular structures are found more vulnerable as compared to the regular structures.

It is thus recommended to (a) rotate a pair of tsunami load histories to the most intense orientation, (b) select the governing load component based on the magnitudes of the F_{\max}/b and P_d of components and (c) carry out a unidirectional analysis. Using

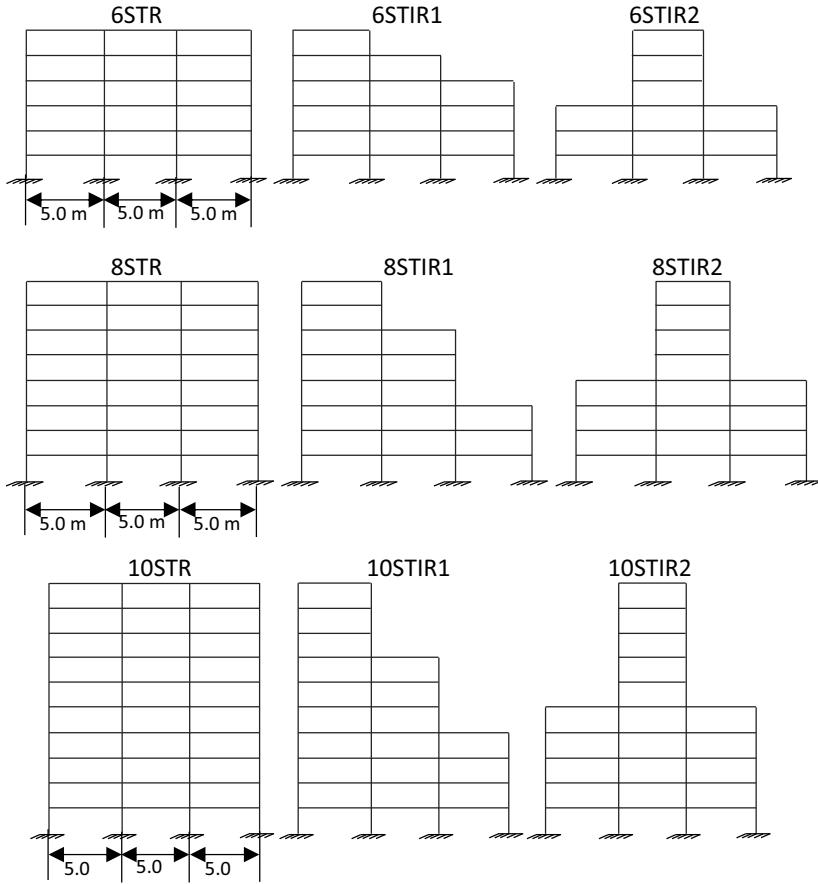


Fig. 2 Configuration of plane frame models selected for the study

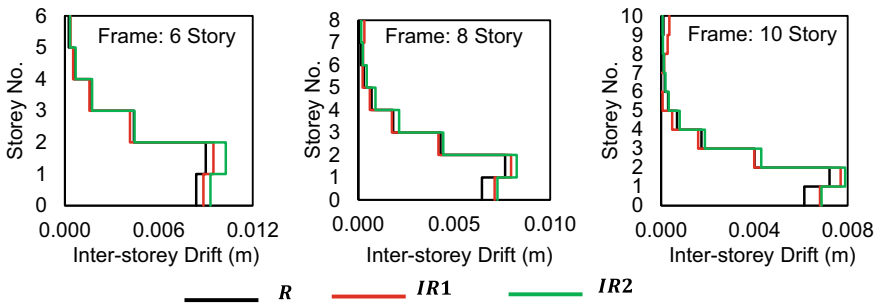


Fig. 3 Variation in response due to vertical irregularity for unidirectional analysis at West Sumatra, Indonesia

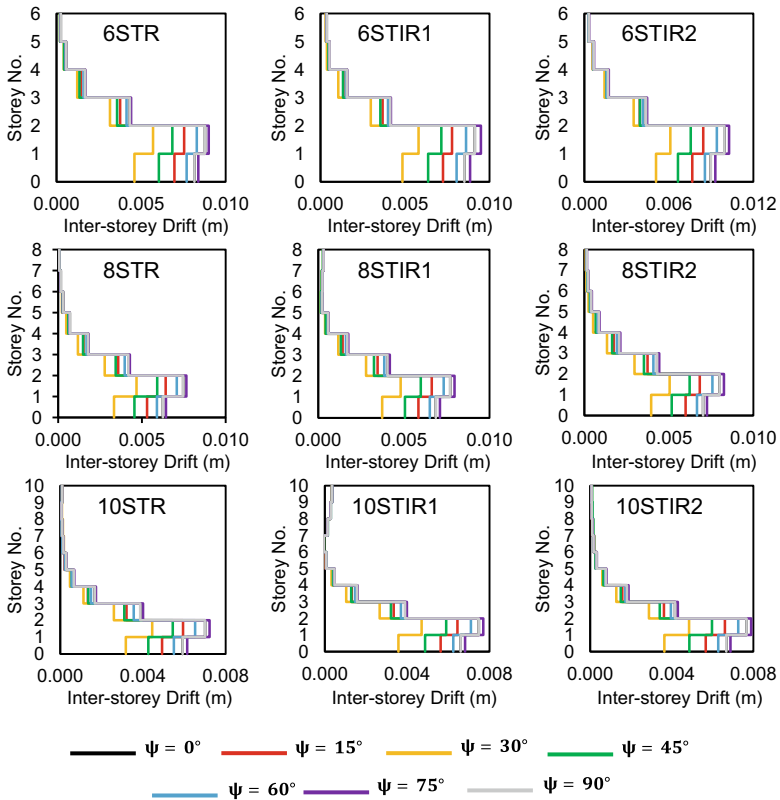


Fig. 4 Variation in response of vertical geometrically regular and irregular frames with change of orientation for unidirectional analysis at West Sumatra, Indonesia

the unidirectional analysis, this methodology may estimate the most critical response under unidirectional loading. However, future studies with other building systems may be pursued to be more conclusive.

References

- Galvan DA, Komjathy A, Hickey MP, Mannucci AJ (2011) The 2009 Samoa and 2010 Chile tsunamis as observed in the ionosphere using GPS total electron content. *J Geophys Res Space Phys* 116(A6):1–21. <https://doi.org/10.1029/2010JA016204>
- Charvet I, Macabuag J, Rossetto T (2017) Estimating tsunami-induced building damage through fragility functions: critical review and research needs. *Front Built Environ* 3(36):1–22. <https://doi.org/10.3389/fbuil.2017.00036>
- Synolakis CE, Bernard EN, Titov VV, K noglu U, Gonz lez FI (2008) Validation and verification of tsunami numerical models. *Pure Appl Geophys* 165:2197–2228. https://doi.org/10.1007/978-3-0346-0057-6_11

4. Gica E, Teng MH, Liu PLF, Titov V, Zhou H (2007) Sensitivity analysis of source parameters for earthquake generated distant tsunamis. *J Waterw Port Coast Ocean Eng* 133(6):429–441. [https://doi.org/10.1061/\(ASCE\)0733-950X\(2007\)133:6\(429\)](https://doi.org/10.1061/(ASCE)0733-950X(2007)133:6(429))
5. Karafagka S, Fotopoulou S, Ptilakis K (2018) Analytical tsunami fragility curves for seaport RC buildings and steel light frame warehouses. *Soil Dyn Earthq Eng* 112:118–137. <https://doi.org/10.1016/j.soildyn.2018.04.037>
6. Petrone C, Rossetto T, Goda K (2017) Fragility assessment of a RC structure under tsunami actions via nonlinear static and dynamic analyses. *Eng Struct* 136:36–53. <https://doi.org/10.1016/j.engstruct.2017.01.013>
7. Pringgana G, Cunningham L, Rogers BD (2021) Influence of orientation and arrangement of structures on tsunami impact forces: numerical investigation with smoothed particle hydrodynamics. *J Waterw Port Coast Ocean Eng* 147(3):04021006:1–16. [https://doi.org/10.1061/\(ASCE\)WW.1943-5460.0000629](https://doi.org/10.1061/(ASCE)WW.1943-5460.0000629)
8. Naskar M, Mayengbam SS, Roy R (Under review) Influence of seismological factors to earthquake-induced tsunami and a simple strategy for tsunami design. *Nat hazards*
9. Sarkar P, Prasad AM, Menon D (2010) Vertical geometric irregularity in stepped building frames. *Eng Struct* 32(8):2175–2182. <https://doi.org/10.1016/j.engstruct.2010.03.020>
10. Wang X (2009) User manual for COMCOT version 1.7 (first draft). Cornell Univ 65:480
11. Mansinha L, Smylie DE (1971) The displacement fields of inclined faults. *Bull Seismol Soc Am* 61(5):1433–1440. <https://doi.org/10.1785/BSSA0610051433>
12. Okada Y (1985) Surface deformation due to shear and tensile faults in a half-space. *Bull Seismol Soc Am* 75(4):1135–1154. <https://doi.org/10.1785/BSSA0750041135>
13. Tanaka N, Onai A, Kondo K (2015) Fragility curve of different damage of wooden building due to tsunami based on tsunami fluid force and its moment. *J Jpn Soc Civ Eng Coast Eng* 71(1):1–11. <https://doi.org/10.2208/kaigan.71.1>
14. American Society of Civil Engineers (ASCE/SEI 7–16) (2017) Minimum design loads and associated criteria for buildings and other structures. *Am Soc Civil Eng*. <https://doi.org/10.1061/9780784414248>
15. SeismoSoft (2022) SeismoStruct—A computer programme for static and dynamic nonlinear analysis of frames structures. Available from <http://www.seismosoft.com>

Integrated Modeling Approach for Developing Sustainable Buildings: A State of the Art



Shubham K. Verma, V. Gupta, S. Thappa, N. Gupta, A. Gupta, V. K. Dogra, Y. Anand, and S. Anand

1 Introduction

The building industry is one of the most energy-intensive sectors globally [1]. It is responsible for nearly 35% of global energy consumption, at the cost of equivalent emissions [2]. These consumptions and emissions are showing annual growth at a very higher rate. In comparison to developed nations, the growth rate of energy consumption is high in developing nations. Urbanization and a growing economy are the possible reasons responsible for this hike. India being a developing nation whose floor area is supposed to double itself in the upcoming two decades is anticipated as having the fastest average annual change in building energy consumption during 2015–2040 [3]. Also, this fast growth in energy consumption makes the nation one of the major contributors to the issues related to climate change. Climate change impacts the atmospheric temperature, relative humidity, rain patterns, etc. which generally influences the indoor environment. Inadequate variations in indoor temperature, relative humidity, and air velocity impact the dwelling conditions, thus enforcing the occupants to utilize mechanical means (like air conditioners and artificial lighting). However, these devices are energy-intensive and are responsible for a large amount of harmful emissions. Also, the utilization of artificial lights generates a huge amount of heat, thus resulting in an increased cooling load. If the structure is properly designed for daylighting, the infiltration of diffused radiations inside the structure can bring adequate lighting without generating much heating effect. Considering this, the analysis of different aspects of buildings becomes necessary.

S. K. Verma · V. Gupta · S. Thappa · N. Gupta · A. Gupta · V. K. Dogra · Y. Anand (✉) · S. Anand (✉)
Shri Mata Vaishno Devi University, Kakryal, Katra, Jammu and Kashmir, India
e-mail: y.anand@smvdu.ac.in

S. Anand
e-mail: sanjeev.anand@smvdu.ac.in

The utilization of engineering tools is one of the most widely adopted solutions. They enable us viability to analyze the design virtually in the pre-construction phase and make necessary alterations if required. Earlier before the advent of computer-based simulation tools, architects mainly rely on calculations for designing the building and their systems. This generally results in the wastage of time and leads to oversized systems. Although, the utilization of simulation tools can bring revolution to the construction industry. Their utilization can be helpful in predicting the comfort level, energy consumption and lifecycle operational cost, thus allowing a designer to take necessary action in the pre-construction phase itself.

Several researchers had utilized different simulation packages for analyzing the dwelling spaces. Among those Magni et al. [4] conducted a detailed cross-comparison study in an office building by utilizing EnergyPlus, TRNSYS, IDA ICE, and MATLAB. While Verma et al. [5] utilized Ansys Workbench for conducting thermal comfort analysis. Further, some studies utilized eQUEST for energy analysis [6]. Subsequently, there are some other tools like COMSOL Multiphysics, OpenStudio, HAP etc. which were utilized for conducting building simulations. So considering the wide range of building simulation packages, the selection of adequate tools becomes extremely important. The selection will be made by considering the benefits and limitations of different tools. Also, conducting whole building simulations demands the collection and compilation of related data. Meanwhile, it has also been observed that software packages that are not in compliance, demand individual design development. Also, most of them are working independently, thus involving higher modeling time while some other packages demand integration and generally result in data loss during data transportation [7]. Considering the limitations of merging architect-dominated design and engineer-dominated simulation tools, it becomes necessary to work towards an integrated performance modeling approach (IPMA) for developing energy-efficient buildings [1]. This will ensure better interoperability among various tools and stakeholders and thus can bring viable solutions. This manuscript is an attempt to review the importance of IPMA in moving towards sustainability. The purpose of this discussion is to highlight the importance of IPMA and showcase how IPMA can bring revolution to the construction industry by extending its support for sustainable buildings.

2 Integrated Performance Modeling Approach (IPMA)

IPMA also known as the integrated design process (IDP) is an approach that is used to build designs for achieving high-performance buildings by considering various social, environmental and budgetary constraints [8]. It depends on a collaborative and multidisciplinary team whose members make the collective decision based on the holistic understanding and shared vision of the project. It follows the design throughout the project life, from pre-construction to the post-construction phase. In general, IPMA [8] is an iterative method (rather than a linear approach), a flexible approach (not a formula) and not a pre-determined approach (different every

time). Generally, in conventional design, “the architect (or designer) and the client” agree on a design concept consisting of a general massing scheme, orientation, and exterior appearance [9]. Then the mechanical, electrical and structural engineers are asked to implement the design and suggest appropriate systems. The problem with conventional practice is that this design process is too quick and simple, often resulting in high operating costs, poor comfort and very few sustainable gestures. However, IPMA provides us with an integrated way to assess the structure in the pre-construction phase. The phases of development in IPMA are similar to the conventional approach; however, the involvement of multiple stakeholders, the feedback system and how the work gets accomplished in each phase differentiate it from the conventional approach as shown in Fig. 1. In the conventional approach, the tasks are performed linearly. All the stakeholders perform their jobs individually. In such cases, extra time is consumed, as all the stakeholders don’t agree on the same design which led to an increment in the overall cost of the project. However, in IPMA, different stakeholders work consecutively. All the stakeholders viz. designer, architect, builder, owner etc. are simultaneously involved in the construction from the starting phases itself. It might be possible, that implementing IPMA involves a slightly higher cost of the structure, however, this cost will be recovered in a short span of time.

Further, it comprises of iterative loops where multiple teams and tools are involved and repeatedly review and refine ideas to resolve problems incurred at each phase as shown in Fig. 2. Meanwhile, it is also important to follow through on the iterations in the IDP process by explicitly identifying subsequent tasks and group meetings, interwoven with the overall project schedule. Further, it proceeds from whole building system strategies, working through increasing levels of specificity, to realize more optimally integrated solutions.

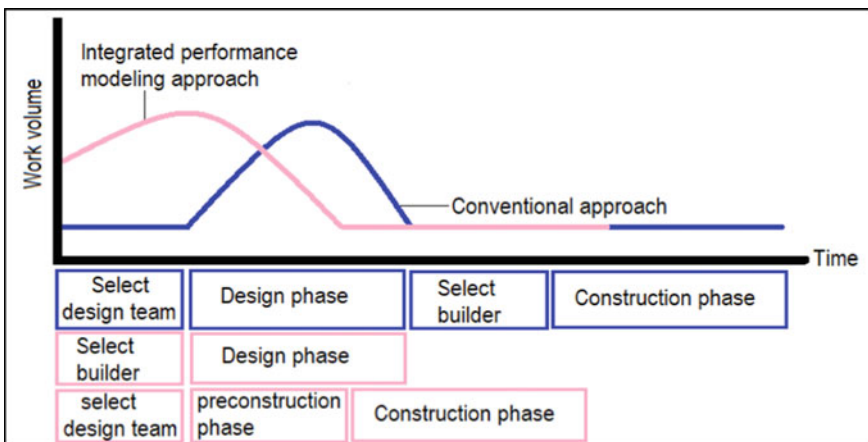


Fig. 1 Conventional versus integrated performance modeling approach [10]

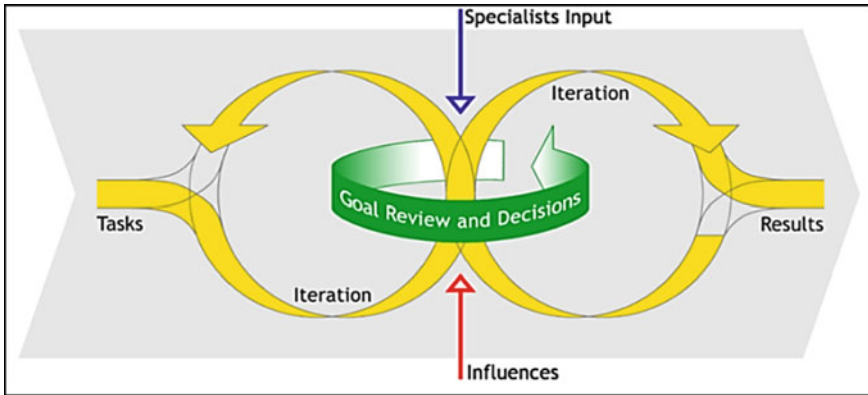


Fig. 2 Iterative loop involved in IPMA implementation [11]

3 Results and Discussions

In this section, the data obtained by reviewing the IPMA is presented and discussed. The results obtained from the literature were broadly divided into three sub-categories viz. Data analysis, IPMA models and benefits and challenges of implementing IPMA. Each of these prospects is elaborated on in subsequent sub-sections.

3.1 Data Analysis

In this section, data regarding the implementation of an IPMA in the building is explored and analyzed. The data has been collected and analyzed from the Scopus database. The keywords searched in the database are defined by (TITLE-ABS-KEY (“integrated design process” OR “IDP” OR “integrative design process”) OR TITLE-ABS-KEY (“Integrated performance modeling” OR “Integrated performance modeling”) AND TITLE-ABS-KEY (building OR buildings)). The search was limited to the title, abstract and keywords section only. As per the Scopus records, a total of 311 manuscripts were found to be published between 2001 and till date. Of the overall publications, around 48% articles are conference papers. Also, there are approximately 43% articles that were published in journals. Meanwhile, there are only 5% review articles available in the literature. Most of these articles presented IPMA/IDP as the approach which can guide the construction sector towards sustainability, thus providing reduced emissions. However, they are not utilized as per their potential.

Further, from the detailed analysis of data, an increasing trend in the average publication rate related to the implementation of the IPMA in buildings is observed as shown in Fig. 3. A total of 311 research papers were found in the database during the said period. Out of the 311 manuscripts, 235 were published in the last decade

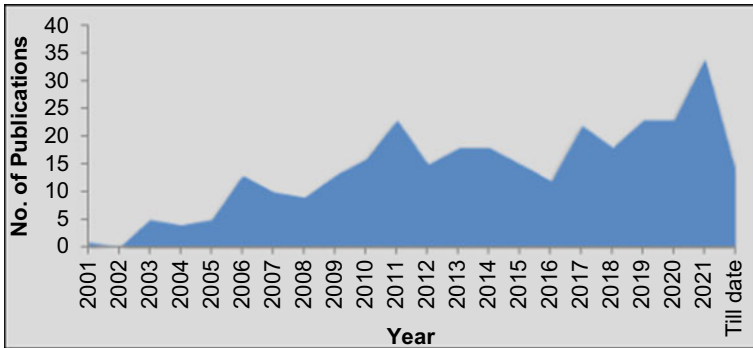


Fig. 3 IPMA publication trend from 2001 to till date (Source Scopus)

i.e. 2011–till date. This clearly indicates that the research interest of the stakeholders in the implementation of IPMA is increasing. Meanwhile, there are some particular years when the publication rate of IPMA shows a sudden hike or fall, thus dictating the slight irregularity in the adoption rate. The main reason for this irregularity is a lack of knowledge and the issues faced by users during the implementation which are further discussed in Sect. 3.3. However, after adopting an integrated approach, a number of studies stated an increment in building performance.

Subsequently, it has been observed that the United States is one of the major contributors in the publications related to the implementation of IPMA. Figure 4 highlights the graphical representation of the seven major contributors to the publications regarding IPMA. In the publication scenario, the United States is having 23.4% of publications. This is followed by Canada, Denmark, Italy, China, Germany, the United Kingdom, and Australia with 11.1, 5.02, 5.02, 4.27, 3.77, 3.77 and 3.27% publications respectively. In this list, India stands at the 17th position with only a 1.51% share of publications. Considering the fact that India is having 2nd most population and almost equivalent rank in the number of buildings, it can play a major role in accomplishing the Sustainable development goals (SDGs). However, to achieve SDGs, it is required to incorporate IPMA strategies effectively. Although, India is not implementing IPMA much in buildings, thus demands attention from policy-makers. Further, the publications are also analyzed for their subject area. Figure 5 showcases the eight major subject areas in which the majority of manuscripts are published. In this list, engineering is one of the most dominant with more than 30% of the manuscripts categorized in the field. This is followed by the social sciences, energy, computer science, environmental science, medicine, and materials science with 11.78, 11, 9.84, 9.46, 3.86, and 3.67% shares respectively. Engineering being a multidisciplinary field is dominating the rate of publication which is obvious. However, the incorporation of other fields like medicine, social science, environment, etc. cannot be denied. Considering this, it is required to bring multiple disciplines together during the design phase. Properly analyzed structures by incorporating IPMA will ensure healthy and sustainable dwellings with minimal utilization

Fig. 4 Publication record of IPMA articles across different nations (*Source Scopus*)

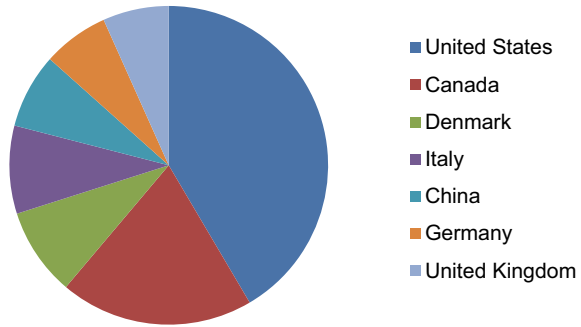
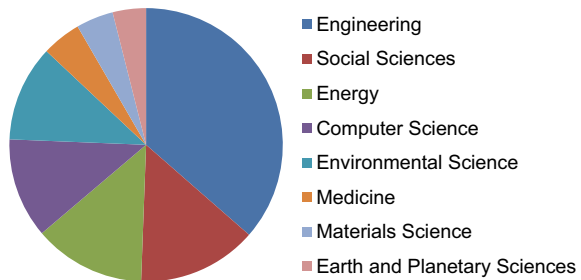


Fig. 5 Publication record of IPMA articles across different areas (*Source Scopus*)



of energy. However, to incorporate IPMA, it is required to check for the existing models in the literature. Various models of IPMA available in the literature were discussed in the subsequent sub-heading.

3.2 Models of Integrated Performance Modeling Approach (IPMA)

IPMA or IDP is a collaborative process/approach which has been used for developing high-performing sustainable buildings. It is not a new concept and has evolved in the construction industry over the last few decades. There exist a number of IDP/IPMA models whose primary aim is to deliver and refine the information as per the requirement. However, due to a lack of knowledge, they have not been utilized as per their potential. Models of IPMA came into existence in the early 90s which gets improvised further. It doesn't represent any pre-determined process, thus a variety of different models gets introduced in the past. Among those, a comparative analysis of a few of the most widely utilized models [11–17] is presented below in Table 1. Based on these models, Ikudayisi et al. [1] recently devised a conceptual model as shown in Fig. 6 which dictates the importance of IDP attributes for developing high-performing buildings. Adopting such models can be beneficial in attaining sustainability by using

the minimum energy. However, apart from these benefits, there exist certain issues/limitations which are elaborated further.

3.3 Benefits and Challenges of Implementing IPMA

IPMA is a collaborative approach/process that offers a flexible system for attaining sustainability in buildings by properly defining the project, design assessment, refinement and documentation. It allows the users with viability to plan analyze and achieve the goals by considering the various social, economic and environmental objectives. Successfully implementing IPMA can avail us with collective and better wisdom and better futuristic associations by ensuring transparency, bringing up open innovative ideas and raising decision-making ability, enhancing long-term and holistic thinking, and can reduce lifecycle cost. Despite these advantages, IPMA is still not adopted as per its potential. Stakeholders generally find it difficult to implement. It has been observed that stakeholders generally find relatedness of work, proper timeline, unclear roles, and modeling and simulation-related issues. These issues/challenges can be reduced by proper implementation; however, lack of knowledge about IPMA put constraints. Also, another important issue is data handling. Stakeholders generally face problems during interpolating the data among different servers. As different simulation engines require distinct file formats, however interpolating one type of file into another consumes time and results in inefficiencies. Meanwhile, most of the discussed issues can be compensated, if the proper methodology of IPMA is adopted. Although IPMA is a flexible approach, thus no standardized set of a process is available. This exaggerates the need to standardize the process. Subsequently, it involves initial investments which generally put constraints on its implications. Other than this, its adoption requires skilled collaborators as a slight discrepancy in implementation can result in an inefficient system. The understanding of workflow, knowledge and information management, skills for integration and collaborative processes are a few other major issues that impact the outcomes. Consequently, high design fees, communication bottlenecks, unfamiliarity with procedures, risk perception, competence, and inadequacy in stakeholder commitments are some of the most critical obstacles which limit the adoption of IPMA.

4 Conclusion

The present study is an attempt to review the implementation of IPMA in buildings. The focus of the study is on analyzing the IPMA literature, reviewing its best available models and discussing various benefits and challenges faced during its implementation. Based on the review, the following conclusions have been drawn:

Table 1 Comparative analysis of different models of IPMA/IDP [1]

Source	Model description	Development	Strength	Limitations
Sanvido and Norton [12]	<ul style="list-style-type: none"> • Presents a way to identify, comprehend, and address professional liability and its effects • Flowcharts and tree nodes are utilized for detailing the activities in the process • Consists of 4 functions and 15 sub-functions 	Based on the literature review	<ul style="list-style-type: none"> • IPMA key activities and roles are covered • Helpful in improving design and techniques 	Sustainability practices are not involved
Lohnert et al. [11]	<ul style="list-style-type: none"> • Presents a generic workflow based on inter-relation of elements and the concept of iterations • Describes activity using flow and Gant chart • Categorizes multidisciplinary activities • Consists of 3 interlocking circles showing the superimposition of different elements viz. actors, activities and goals respectively 	Based on TASK 23 guidelines for IDP	Involves description of all 3 aspects of IDP implementation	Exclusion of performance indicators
Larsson [13]	<ul style="list-style-type: none"> • Presents a model with the integration of existing elements to form a systematic process • 13 activities are used to describe performance benchmarks 	Based on the C-2000 program	Inclusion of key performance indicators	Applicability is constrained to some activities
Larsson [14]	<ul style="list-style-type: none"> • Improvement in existing model • Activities are divided into 16 sections representing activities 	Based on the C-2000 program	Simple and easy to apply in actual practice	Applicability is constrained to some activities
Zimmerman [15]	<ul style="list-style-type: none"> • Presents the process with a linear framework by involving iterative decision-making • Flow chart-based model which is comprised of 10 activities 	IDP guide, Canada	Simple and easy to apply	Limited to some activities

(continued)

Table 1 (continued)

Source	Model description	Development	Strength	Limitations
Riley et al. [16]	<ul style="list-style-type: none"> • Presents a model which elaborates various functions individually, required for designing high-performing buildings • Schematic design, concept development, documentation and developing shop drawings are the four main processes 	Based on the review of different models	Levels of activities are described	Exclusion of performance indicators
Horman et al. [17]	<ul style="list-style-type: none"> • Presents a model with main focus on energy optimization • 8 activities are grouped in 3 sections for reducing the complexity of the system • Processes were executed based on iterative manner 	Based on the literature review	Simple and easy to apply	Limited to the activity pattern

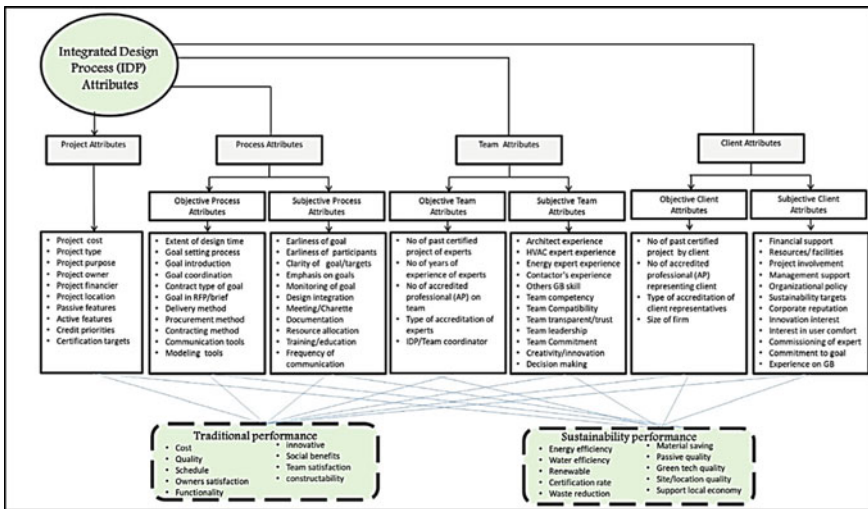


Fig. 6 Conceptual model of IPMA devised by Ikudayisi et al. [1]

- IPMA is an innovative concept whose implementation in buildings ensures the required level of comfort with minimal energy consumption, thus helping the stakeholders in attaining sustainability.
- In comparison with the conventional approach, IPMA is more convenient and efficient, thus providing sustainable solutions.
- From the analysis of IPMA publication data, it has been observed that the incorporation of IPMA is progressively raising the bar globally. Among the various nations, its adoption is dominant in developed countries while developing nations are still slow in adoption. This raises concerns related to sustainability and demands the attention of stakeholders towards the adoption of IPMA in developing nations.
- Talking about India, the adoption rate of IPMA is quite low, however, a conscious effort could have been provided for increasing the implementation of IPMA.
- IPMA is involving interdisciplinary researchers, thus exaggerating the need to involve multidisciplinary stakeholders to build healthy and sustainable buildings.
- There are 7 major models of IPMA as discussed in Sect. 3.2. Their main aim is to deliver and refine the information as per the requirement. However, due to certain limitations discussed in Sect. 3.3, they are not utilized as per the potential.

References

1. Ikudayisi AE, Chan AP, Darko A, Adegun OB (2022) Integrated design process of green building projects: a review towards assessment metrics and conceptual framework. *J Build Eng* 50:104180
2. GABC (2020) Global status report for buildings and construction: towards a zero-emissions, efficient and resilient buildings and construction sector. Global alliance for buildings and construction. https://globalabc.org/sites/default/files/inline-files/2020%20Buildings%20GSR_FULL%20REPORT.pdf
3. International Energy Outlook (IEO) (2017) US energy information administration. [https://www.eia.gov/outlooks/ieo/pdf/0484\(2017\).pdf](https://www.eia.gov/outlooks/ieo/pdf/0484(2017).pdf)
4. Magni M, Ochs F, de Vries S, Maccarini A, Sigg FX (2020) Detailed cross comparison of building energy simulation tools results using a reference office building as a case study. *Energy Build* 250:111260
5. Verma SK, Anand Y, Anand S (2020) Analysis for determining the impact of air quality and thermal comfort in an enclosed cavity. *Mater Today Proc* 28:2205–2211
6. Muhammad A, Karinka S (2022) Comparative energy analysis of a laboratory building with different materials using eQUEST simulation software. *Mater Today Proc* 52:2160–2165
7. Nasyrov V, Stratbücker S, Ritter F, Borrmann A, Hua S, Lindauer M (2014) Building information models as input for building energy performance simulation—the current state of industrial implementations. In: *eWork and eBusiness in architecture, engineering and construction: ECPPM 2014*. CRC Press, Netherlands, pp 479–486
8. B.G.B. Roundtable (2007) Roadmap for the integrated design process-part one: summary guide. BC Green Building Roundtable, Vancouver, BC, Canada
9. Bragança L, Vieira SM, Andrade JB (2014) Early stage design decisions: the way to achieve sustainable buildings at lower costs. *Sci World J* 2014:365364
10. Keeler M, Vaidya P (2016) *Fundamentals of integrated design for sustainable building*. Wiley

11. Löhnert G, Dalkowski A, Sutter W (2003) integrated design process: a guideline for sustainable and solar-optimised building design. IEA Task 23:1–62
12. Sanvido VE, Norton KJ (1994) Integrated design-process model. *J Manag Eng* 10(5):55–62
13. Larsson N (2004) The integrated design process. *Int Initiat Sustain Built Environ (iiSBE)*
14. Larsson N (2009) The integrated design process; history and analysis. *Int Initiat Sustain Built Environ* 514
15. Zimmerman A, Eng P (2006) Integrated design process guide. Canada Mortgage and Housing Corporation, Ottawa, ON
16. Riley D, Magent C, Horman M (2004) Sustainable metrics: a design process model for sustainable buildings. In: *Proceedings of the CIB world building congress*
17. Horman MJ, Riley DR, Lapinski AR, Korkmaz S, Pulaski MH, Magent CS, Luo Y, Harding N, Dahl PK (2006) Delivering green buildings: process improvements for sustainable construction. *J Green Build* 1(1):123–140

Investigation of Local Scour and Flow Field Around Bridge Pier with and Without Collar Through Numerical Simulation



Ningombam Bishwajit Singh and Thiyam Tamphasana Devi 

1 Introduction

Localized scouring in the surrounding areas of a bridge pier has the potential to expose a significant portion of the erodible bed around the bridge pier. The extent of erosion could be such that the anchorage depth of the pier foundation shall not be sufficient enough to keep the structure safe leading to the failure of the bridge. Recent incidents of failure of bridges due to localized scouring have been reported in the literature. These failures suggest the need of finding reliable and effective scour protection countermeasures. Devices for scour protection are broadly classified into bed armoring and flow-altering countermeasures [1]. The flow-altering device of collar plate skirting around the pier has been experimentally studied extensively by several researchers [2–7]. Mashahir et al. [8] drew a comparison with the results of Ettema [9] and stated that a collar plate having a diameter three times the pier diameter has better efficacy than two times the pier diameter in mitigating the scour depth when placed at the level of the sediment bed. Garg et al. [7] stated that a collar having a minimum diameter of three times the collar plate can completely arrest the formation of scour when positioned at bed level. A parametric study on the use of collars by Setia et al. [10] found that a collar plate having a size of 2.5 times that of the pier diameter resulted in the reduction of scour depth by 85% as compared to scour depth around an unprotected pier.

Recent advancement in computational resources has increased the applicability of numerical simulation in the study of hydraulic structures. In previous studies, most of the researchers used the RANS model to simulate the bridge scour model. In the past few years, more advanced turbulence models like Detached Eddy Simulation (DES) and Large Eddy Simulation (LES) have also been employed in the study of localized scouring around the bridge pier. Kirkil et al. [11] investigated turbulence

N. B. Singh · T. T. Devi (✉)

Department of Civil Engineering, National Institute of Technology, Manipur 795004, India
e-mail: thiyam85@gmail.com

at a circular bridge pier using the DES turbulence model and showed the features of large-scale eddies which are responsible for the scour process. Alemi et al. [12] numerically investigated the flow behavior around a cylindrical bridge pier using the LES Smagorinsky model. Tafarojnoruz et al. [13] describe the flow pattern within the scour cavity for a submerged pile using the LES turbulence model. Chen et al. [14] introduced a new model of collar known as a hooked collar and studied both experimentally and numerically the flow field. The result shows that the maximum turbulent kinetic energy has been significantly reduced and the scour protection efficacy has been reduced to 42% when placed at the bed level.

2 Numerical Model Set up

2.1 Characteristics of Flow Domain and the Sediment Bed

The computational domain has a dimension of $2.25 \text{ m} \times 1 \text{ m} \times 0.286 \text{ m}$ ($L \times B \times H$). A cylindrical pier of diameter 90 mm is positioned 1.08 m away from the upstream inlet in the longitudinal direction. Along the lateral direction, it is placed midway between the two lateral walls. A very mild slope of 0.1% i.e. 1 in 1000 is also maintained. The length of the domain is chosen based on the findings of Sarker [15] that the pile can influence its flow field up to a length of 12 times the pier diameter. It is also ensured that the chosen diameter of the cylindrical pier is less than 10% of the channel width to prevent the influence of lateral boundaries on the scour depth as reported in Chiew and Melville [16].

The numerical simulation is prepared for 2 types of models. The first model is for a cylindrical pier that is unprotected. In this model, the cylindrical pier has a diameter of 90 mm. The other model is the cylindrical pier protected with a collar. “Garg et al. [7] found that the use of a single collar which has a minimum diameter of 3 times the pier diameter can completely restrain the formation of scour when positioned at the level of sediment bed”. “Mohammad et al. [8] and Ettema [9] stated that a collar plate whose diameter is three times the pier diameter is more efficient than the collar with twice the pier diameter in preventing the scour formation when both the collars are placed on the channel bed level”. Thus, the width of the collar plate (D) is chosen to be three times the width of the pier (d). Figure 1 represents the schematic diagram of the model of the pier protected by the collar.

2.2 Sediment Scour Model

A single sediment species of diameter 0.418 mm having a density of 2650 kg/m^3 is chosen. Other parameters such as maximum packing fraction, coefficient of entrainment, bed load coefficient, and angle of repose are assumed. The prescribed

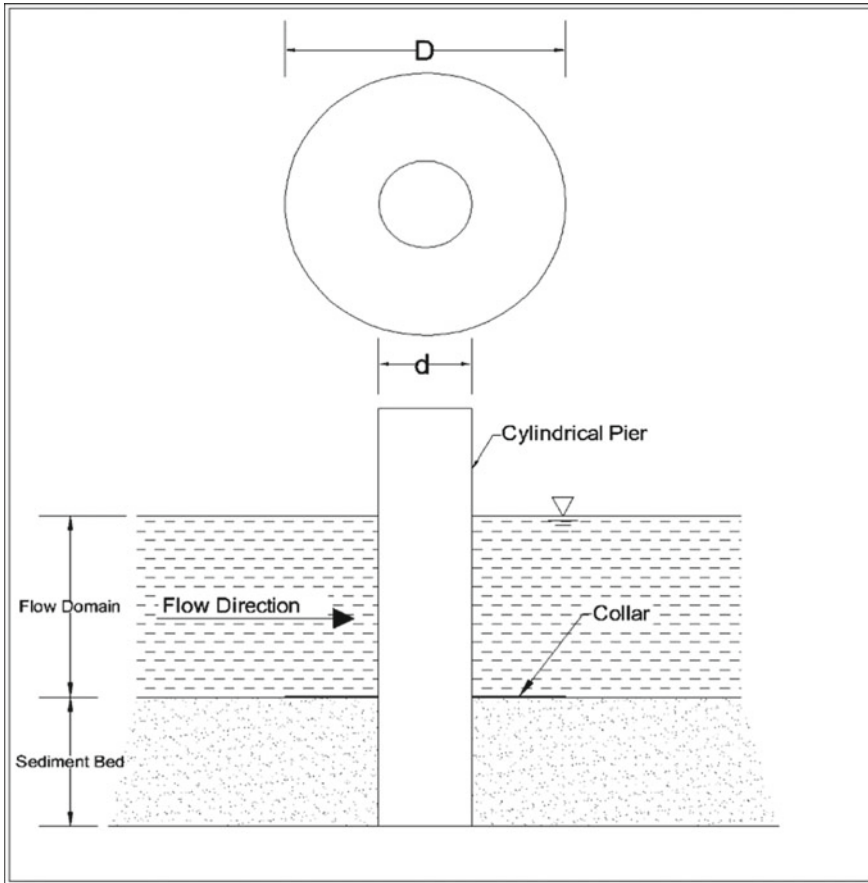


Fig. 1 Schematic diagram of collar round the cylindrical pier placed at bed level

critical Shield's number is calculated based on Soulsby-Whitehouse Equation. The dimensionless parameter d_{*i} is calculated prior to the finding of the critical Shield's parameter (Eq. 1).

$$d_* = d_i \left[\frac{\rho_f (\rho_i - \rho_f) g}{\mu_f} \right]^{1/3} \tag{1}$$

where d_* is the dimensionless diameter of sediment, d_i is the sediment diameter, ρ_f is the density of the fluid, ρ_i stands for a density of sediment species, μ_f and g represent dynamic viscosity and acceleration due to gravity respectively.

Thus, using the Soulsby White House equation provided underneath the dimensionless critical parameter is calculated as (Eq. 2).

$$\theta_{cr,i} = \frac{0.3}{1 + 1.2d_*} + 0.055[1 - \exp(-0.02d_*)] \quad (2)$$

where $\theta_{cr,i}$ represents the dimensionless critical shield parameter. The calculated values of the dimensionless diameter of sediment (d_*) and the prescribed dimensionless critical shield parameters ($\theta_{cr,i}$) are 1.057 and 0.1334.

2.3 Mesh

Mesh plays a vital role in the accurate determination of results. The time of operation of the simulation process is also dependent on the size of the cell. In order to numerically model the flow domain in three dimensions and to make good modeling of the formation of scour hole and vortices, the nested meshing technique is adopted. It is also ensured that the outer mesh cell size and the inner cell size do not differ by large value and hence aspect ratio of 1:2 is maintained. Keeping an aspect ratio of nearly 1:2 will help in minimizing the error empirically. The outer mesh block is assigned a cell size of 2 cm while the inner nested mesh block is assigned a cell size of 1 cm. The total cell count of both the larger and smaller cell size is 302658. The calculations are performed on CPU core 20 with 56 GB RAM. The large domain and the presence of a number of cells consume an enormous time of more than 48 h.

2.4 Boundary Conditions

Assigning appropriate boundary conditions to form an essential part of a numerical simulation. They are chosen in such a manner that they correspond to the physical conditions of the model. The assigned boundary conditions direct the motion of the fluid leading to the formation of a unique solution. At the inlet boundary, the boundary condition of volumetric flow rate (V_{fr}) is applied. The constant flow rate of 0.035 cumecs is set with the elevation of fluid being fixed at 0.284 m. At the outlet, the specified pressure (P) is applied with the same fluid elevation as set earlier. The topmost boundary which is the free surface is assigned as specified pressure (P) with zero fluid fraction. The two lateral sides are specified as symmetric boundaries (S). The bottom floor is set as a wall (W) which acts as a frictionless surface. In order to attain faster convergence, a constant water depth of 11.6 cm is set throughout the computational domain in the initialization stage. The applied boundary conditions are tabulated in Table 1 which is shown below. Further, we assign LES turbulence model which relies more on calculation of eddies larger than mesh cell size rather than modeling of eddies smaller than the cell size.

Table 1 Applied boundary conditions

Inlet	Outlet	Lateral sides	Free surface	Bottom floor
Volumetric flow rate	Specified pressure	Symmetry	Specified pressure	Wall

3 Numerical Results

Figure 2 shows the fully developed scour cavity around the circular pier at the end of the simulation period of 1800 s. The extent of development of scour hole is almost symmetrical about the axis which is longitudinal to the direction of flow. However, the developed scour hole remains unsymmetrical about the axis which is transverse to the direction of flow as observed from the center of the pier. When gauged from the center of the pier the degree of extent of scour hole formation extends for a considerable length at the downstream portion as compared with the upstream length. The greatest extent of scour depth is recorded as high as 8.58 cm. The site of the highest scour depth is not exactly at the center of the upstream of the cylinder but is slightly shifted in the lateral direction. It is so because the scouring on areas adjacent to the pier nose is more intensive. The scour topography is in good agreement with the scour pattern of Zhu [17] which indicates that scouring is predominant beside the pier.

At the upriver of the nose of the pier, one can observe from Fig. 3 that the approaching velocity vectors decelerate to form a vertical stagnation plane. The vectors are then re-directed downwards and made to impinge on the sediment bed

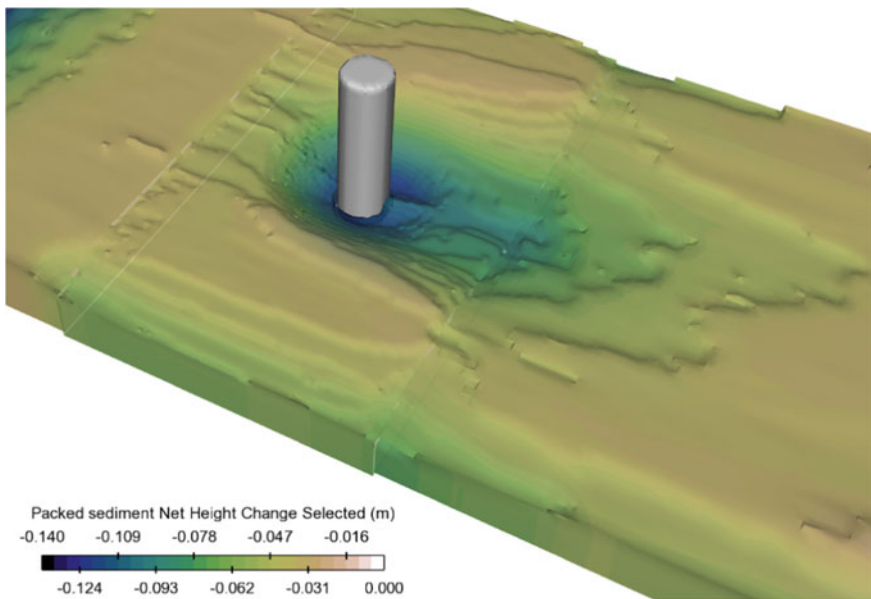


Fig. 2 Isometric view of scour hole formation around the unprotected pier

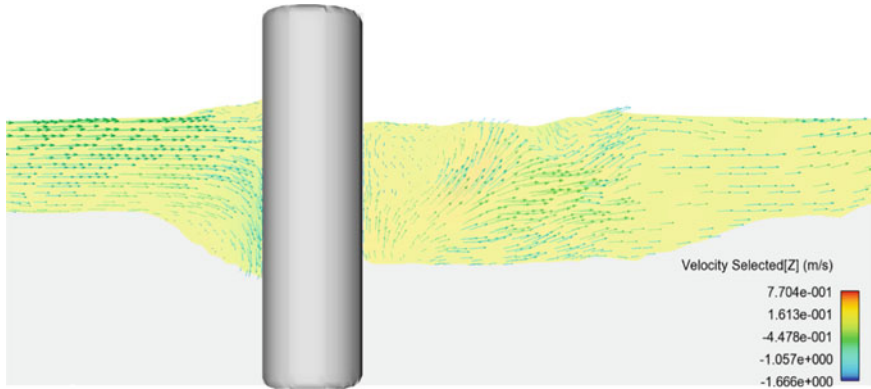


Fig. 3 Velocity vectors along Z direction at the vertical symmetrical plane ($y = 0.5$ m)

which is located underneath. This downflow induces scour development. Within the upstream scour cavity, recirculation of velocity vectors is observed which is an indication that horseshoe vortices are formed. At the downstream of the cylindrical pier, upwelling of velocity vectors is present which suggests the growth of wake vortices responsible for dislodging the eroded sediments away from the base of the pier. The above vector representation clearly indicates the mechanism of formation of the scour hole as explained by various researchers like Graf and Istiarto [18], Kothiyari and Kumar [19] and Melville and Coleman [20].

Figure 4 shows the visualization of velocity vectors of the flow domain around a pier protected by a collar. The presence of the collar plate is able to shield the downward impact of downflow as it acts as an erosion-resistant surface. It is able to arrest the sinking horseshoe vortex and mitigate the growth of scour cavity around the pier. Figure 5 shows the scour cavity developed around the pier protected by collar at the end of the simulation time of 1800 s. One can observe from Fig. 5 that the depression of the scour hole is substantially reduced as weighed against the depth of scour of an unguarded pier. Furthermore, the areal extent of scour cavity developed around the cylindrical pier protected by collar plate has been notably minimized.

Figure 6 shows the plot of the change of scour depth with time. In the case of unprotected pier, the scour depth rises rapidly in the early stage of scouring. However, for the pier protected by collar, the scour depth remains more or less the same from the instant of 600 s till the end of the simulation. It indicates that scour depth has attained equilibrium. The highest recorded scour depth for the collar-protected pier is as high as 1.1 cm. Hence the effectiveness of using a collar plate as scour mitigation remedy is 87.71%. This is in good agreement with the experimental result of Setia and Shubhneet [4] which stated 85% scour protection efficacy of collar plate (2.5D) over the scour penetration of an unguarded pier. However, the obtained scour protection efficacy of 87.71% is lesser as compared to the result of Garg et al. [7] having 100% efficacy of collar (3D) when positioned at the bed level. Figure 7 illustrates the plan view of the scour cavity developed around the pier protected by the collar. The

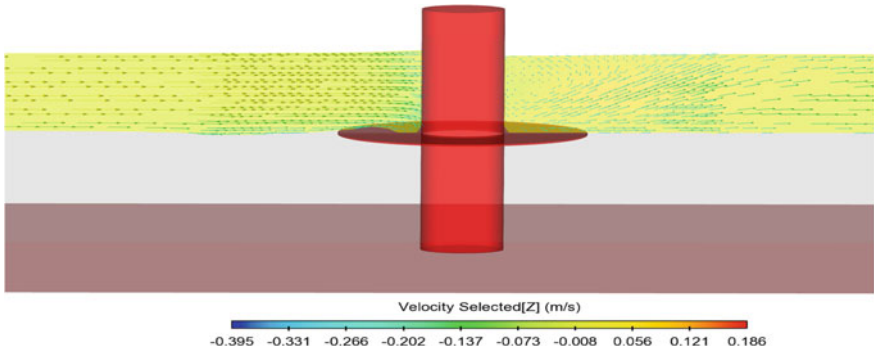


Fig. 4 Velocity vectors along Z direction at the vertical symmetrical plane ($y = 0.5$ m) of pier protected with collar

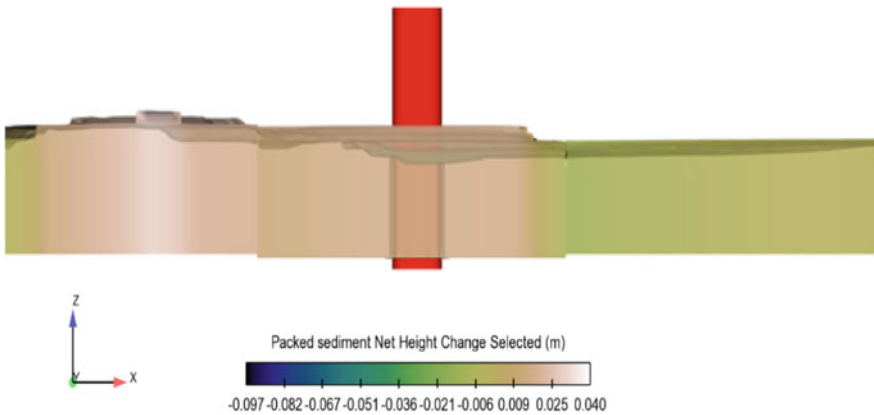


Fig. 5 Side elevation view of scour hole formation around the pier-protected collar plate

scour pattern so developed varies significantly with that of the scour pattern of the unprotected pier. One can observe that the scour is shifted radially outwards from the pier.

No scour is seen to occur at the downstream location of the pier. In the case of unprotected pier scour happens at the close surrounding area of the pier. However, for the collar-protected pier, scour is seen to occur around the periphery of the collar except at the downstream portion.

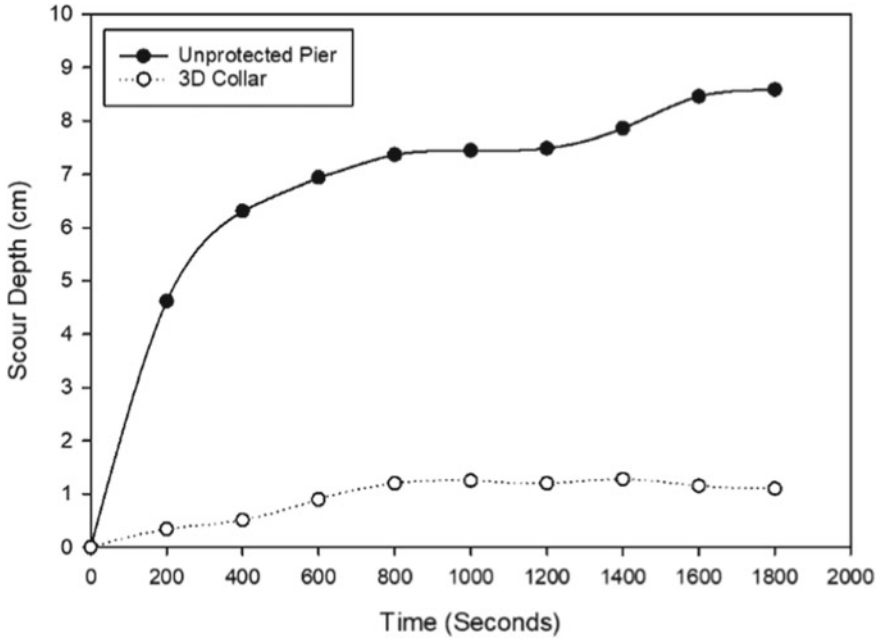
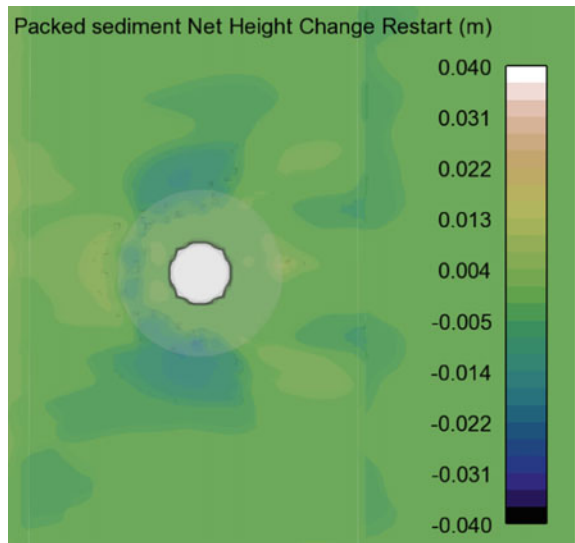


Fig. 6 Temporal change of scour depth

Fig. 7 Plan view of the scour cavity formed around the collar-protected pier



4 Conclusion

A collar plate skirting around the pier of diameter three times the pier diameter is capable of decreasing the scour depth by 87.71%. It can also be inferred that the usage of collar plate is not able to entirely remove scour when positioned at the top of the sediment bed. It is able to impede the growth of the horseshoe vortex and effectively inhibit the development of scour around the cylindrical pier. The efficacy of the collar plate will remain unaltered by variations in the direction of flow as the collar plate is symmetrical about the pier. Hence, collar plate of 3 times the pier size placed at the bed level can be effectively used to mitigate the scour formation.

References

1. Singh NB, Devi TT, Kumar B (2022) The local scour around bridge piers—a review of remedial techniques. *J Hydraul Eng* 28(S1):527–540. <https://doi.org/10.1080/09715010.2020.1752830>
2. Dargahi B (1991) Controlling mechanism of local scouring. *J Hydraul Eng* 116(10):1197–1214. [https://doi.org/10.1061/\(ASCE\)0733-9429\(1990\)116:10\(1197\)](https://doi.org/10.1061/(ASCE)0733-9429(1990)116:10(1197))
3. Chiew Y (1992) Scour protection at bridge piers. *J Hydraul Eng* 118(9):1260–1269. [https://doi.org/10.1061/\(ASCE\)0733-9429\(1992\)118:9\(1260\)](https://doi.org/10.1061/(ASCE)0733-9429(1992)118:9(1260))
4. Setia B (1997) Scour around bridge piers: mechanism and protection. Dissertation, Department of Civil Engineering, Indian Institute of Technology, Kanpur, India
5. Kumar V, Raju KGR, Vittal N (1999) Reduction of local scour around bridge piers using slots and collars. *J Hydraul Eng* 125(12):1302–1305. [https://doi.org/10.1061/\(ASCE\)0733-9429\(1999\)125:12\(1302\)](https://doi.org/10.1061/(ASCE)0733-9429(1999)125:12(1302))
6. Kim UY, Kim JS, Ahn SJ, Hahm CH (2005) Scour countermeasure using additional facility in front of bridge pier. In: 31st IAHR congress 2005: water engineering for the future, choices and challenges. Seoul, pp 5823–5829
7. Garg V, Setia B, Verma DVS (2005) Reduction of scour around a bridge pier by multiple collar plates. *J Hydraul Eng* 11(3):66–80. <https://doi.org/10.1080/09715010.2005.10514802>
8. Mashahir MB, Zarrati AR, Rezayi MJ (2004) Time development of scouring around a bridge pier protected by collar. In: 2nd International conference on scour and erosion, Meritus Mnadarin, Singapore
9. Ettema R (1980) Scour at bridge piers. Dissertation, Department of Civil Engineering, University of Auckland, New Zealand
10. Setia BS (2016) Scour protection by collar plates: a parametric study. In: Proceedings of the international conference on fluvial hydraulics, river flow, pp 486–494
11. Kirkil G, Constantinescu G, Ettema R (2009) Detached Eddy simulation investigation of turbulence at a circular pier with scour hole. *J Hydraul Eng* 135(11):888–901. [https://doi.org/10.1061/\(ASCE\)HY.1943-7900.0000101](https://doi.org/10.1061/(ASCE)HY.1943-7900.0000101)
12. Alemi M, Pêgo JP, Maia R (2017) Numerical investigation of the flow behavior around a single cylinder using large Eddy Simulation model. *Ocean Eng* 145:464–478. <https://doi.org/10.1016/j.oceaneng.2017.09.030>
13. Tafarojnoruz A, Lauria A (2020) Large eddy simulation of the turbulent flow field around a submerged pile within a scour hole under current condition. *Coast Eng J* 62(4):489–503. <https://doi.org/10.1080/21664250.2020.1807453>
14. Chen SC, Tfwala S, Wu TY, Chan HC, Chou HT (2018) A hooked-collar for bridge piers protection: flow fields and scour. *Water* 10(9):1–12. <https://doi.org/10.1080/21664250.2020.1807453>

15. Sarker M (1998) Flow measurement around scoured bridge piers using acoustic-Doppler velocimeter (ADV). *Flow Meas Instrum* 9(4):217–227. [https://doi.org/10.1016/S0955-5986\(98\)00028-4](https://doi.org/10.1016/S0955-5986(98)00028-4)
16. Chiew YM, Melville BW (1987) Local scour around bridge piers. *J Hydraul Res* 25(1):15–26
17. Zhu ZW, Liu ZQ (2012) CFD prediction of local scour hole around bridge piers. *J Cent South Univ Technol* 19(1):273–281. <https://doi.org/10.1007/s11771-012-1001-x>
18. Graf WH, Istiarto I (2002) Flow pattern in the scour hole around a cylinder. *J Hydraul Res* 40(1):13–20. <https://doi.org/10.1080/00221680209499869>
19. Kothyari UC, Kumar A (2010) Temporal variation of scour around circular bridge piers. *ISH J Hydraul Eng* 16:35–48. [https://doi.org/10.1061/\(ASCE\)0733-9429\(1992\)118:8\(1091\)](https://doi.org/10.1061/(ASCE)0733-9429(1992)118:8(1091))
20. Melville BW, Coleman SE (2000) Bridge scour. Water Resources, LLC, CO, USA

Significance of Effective CBR in the Design of Flexible Pavement



**Khwairakpam Sachidanada, Polem Jesiada,
and Naoroibam Bidyamani Chanu**

1 Introduction

Nanotechnology The development of national highways played an important role in the development of a country. The most advanced country, the USA stands in first position while India stands in second position in terms of the length of the road along the national highways. In highways, the subgrade played an important role in the long-lasting of the roads. As the national highways are composed of different pavement layers, the consideration of the effectiveness of these different layers of soil for the design of pavement is important. Improperly planned, designed, constructed & maintained roads can disrupt the social & economic characteristics of any size community. Therefore, for conservative & proficient construction of roads, the correct design of the thickness of pavement is crucial.

The flexible pavements generally consist of one or more layers of soil in which the top layer is made stiffer. The strength of pavement is generally based on the area of load distribution and not on the type of soil. In Manipur, the highways are generally constructed in the form of flexible pavement. Normally, the roads are having cracks, holes, etc. and it does not last long. The condition of the road may be due to the ineffective design of the roads without consideration of the below soil types. The CBR of soil for different types of soil needs to be considered and the product shall be the effective CBR, which is generally the result of the different soil types.

K. Sachidanada (✉) · P. Jesiada · N. B. Chanu
Department of Civil Engineering, National Institute of Technology Manipur, Langol,
Manipur 795004, India
e-mail: khsachidananda@gmail.com

2 Literature

Few kinds of literature have been referred to find the importance of the design of pavements. Some of the literature have been highlighted below:

- (a) Awadhesh et al. [1] studies the durability of the cement concrete pavement as compared to flexible pavements. The study suggested the rigid concrete pavement for the weaker soil types, costly aggregates and the bad drain condition. But the paper also showed that cement concrete pavements are not suitable for expansive soil.
- (b) Nataatmadja et al. [2] highlight the importance of soil subgrade under traffic loading. The paper also discusses the various ways to obtain the effective CBR of the subgrade soil. A new method for the calculation of effective CBR has also been proposed and validated on other pavements also.
- (c) IRC 37 [3] is the design guidelines for flexible pavements. As road traffics are changing and different construction has been done, IRC 37 included both new and older design methods in the current design practices. The IRC mainly gives guidelines to increase the life of road conditions.
- (d) IS 2720 (Part 16) [4] covers the testing procedures for finding the California Bearing Ratio (CBR) of the soil. The CBR of the soil generally determines the strength of the soil.

3 Methodology

For the current study, different soil samples were collected from different locations in the Imphal area. Dry density was calculated using the Modified Procter test. The various steps involved in the correlation include the determination of index properties of the soil like specific gravity, dry density, liquid limit, plastic limit (PL), plasticity index (PI), optimum moisture content, particle size analysis, determination of CBR value of the sample followed by the calculation of effective CBR based on the subgrade soil and the embankment soil. The properties of the soil samples were tested as per IS 2720 and the results are presented in Tables 1, 2 and 3 (Figs. 1, 2 and 3).

4 Procedures

Use Certain procedures have to be followed, to find the CBR of soil and the lists are given below:

- (a) The CBR test is generally in soil sample passing on a 20 mm test sieve. The large-size soils are removed. For performing the test of CBR the optimum moisture content of the soil is very much needed. Once the density of the compacted soil is known the exact amount of soil required for the test can be found out.

Table 1 Properties of soil sample

Index properties	Sample 1(Subgrade)	Sample 2 (Embankment)
Specific gravity	2.56	2.47
Dry density	1.61 g/cc	1.59 g/cc
Plastic limit	23%	26%
Liquid limit	27%	32%
Plasticity index	4	6
Proctor test: OMC	10%	10%
MDD	2.10 g/cc	2.03 g/cc

Table 2 Sieve analysis

Sieve analysis	Sample 1 (subgrade) (%)	Sample 2 (embankment) (%)
100 mm	62.75	100
75 mm	62.75	100
19 mm	44.483	72.15
4.75 mm	27.123	36
2 mm	21.823	28.15
425 μ	9.34	10.25
75 μ	0.68	3.3

Table 3 CBR values of soils

	Sample 1 (subgrade)	Sample 2 (embankment)
CBR	18%	7%

- (b) The cylindrical mould of CBR specimen has to be weight.
- (c) A load hammer of 4.5 kg has been used to compact the soil sample.
- (d) Placed the annular cylindrical plunger into the cylindrical mould.
- (e) A force-measuring device is attached.
- (f) Apply force into the soil at the rate of 1+0.2 mm/min.
- (g) Record reading of the force gauge at the interval of penetration 0.25 mm to total penetration not exceeding 7.5 mm.

These complete the procedures for finding the CBR of the soil samples. The calculated values of the CBR soil sample are listed in Table 3.

Fig. 1 Weighing of the soil sample



Fig. 2 Weighing of the soil sample 2



Fig. 3 CBR testing of soil samples



5 Results and Discussion



Based on the procedures mentioned above, the CBR of the soil samples came out to be 7 and 18% respectively for the embankment and the subgrade soils. The variation of the soil samples is very different as the embankment is the existing soil before the soil layers have been laid to get the required CBR value. Based on the values of these soil samples, the effective CBR of the soil sample has been calculated based on IRC 37:2012. The effective CBR value came out to be around 13%. As the minimum CBR value of 10% is required for the highway design, the result shows that the soil is not too bad but for getting higher loads the pavement needs to be laid thicker, which it means is uneconomical as compared to the higher effective CBR value soils that will require lesser pavement thickness.

References

1. Singh AK, Nigam M, Srivastava RK (2021) Study of durability for cement concrete pavement and flexible pavement in expansive soil region. *J Emerg Technol Innov Res (JETIR)* 8(6):f531–f539
2. Nataatmadja A., Tao SY, Chim K (2012) Design subgrade CBR for flexible pavements: comparison of predictive methods. In: 25th ARRB conference-shaping the future: linking policy, research and outcomes, Perth, Australia
3. IRC:37-2012 (2012) Tentative guidelines for the design of flexible pavements. Published by Indian Roads Congress. Kama Koti Marg, Sector-6, R.K. Puram
4. IS 2720 (Part 16) (1987) Indian Standard Methods of test for soil, Part 16, Laboratory determination of CBR. Published by Bureau of Indian Standards, Manak Bhavan, Bahadur Shah Zafar Marg, New Delhi

Rathong glacier's Line-Of-Sight (LOS) Velocity Measured Using the Modified Four-Pass DInSAR Technique



Devishri Kangjam , Rajkumar Kamaljit Singh ,
Khoisnam Nanaoba Singh, Jayaprasad Pallipad, Maganti Srinivasa Tarun,
Deepak Putrevu, Arundhati Misra, and Mamata Maisnam

1 Introduction

The areas on Earth where water freezes into snow or ice are referred to as the cryosphere. Some of its characteristic features include freshwater ice, sea ice, permafrost, glaciers, ice sheets, etc. Of these, glaciers hold approximately 69% of the world's fresh water [1] and constitute a valuable resource sustaining various lifeforms. Glaciers are very sensitive to change in temperature and climate [2–4]. Monitoring of glacier velocity is important because it gives us insight about the response of glacier flow dynamics to climate change, glacier ice mass variation over a period of time as well as information about glacial hazards [2, 5, 6]. Several factors such as surface slope, gravity, thickness of ice, viscosity of ice, surrounding climate temperatures, etc. influence the movement of glaciers [3, 6]. Glacier movement can be monitored using either field-based surveys or remote sensing techniques. Although field surveys are accurate, they are logistically difficult and time-consuming. So remote sensing techniques come to our rescue and microwave sensors are particularly useful for glacial applications because of their penetration capabilities bypassing cloud cover [6]. We used the Modified four-pass Differential Synthetic Radar Interferometry (DInSAR) technique to estimate the velocity of Rathong glacier.

Synthetic Aperture Radar (SAR) is an active sensor equipped with its own energy source for illuminating the target and hence can image in daylight or at night. It

D. Kangjam (✉) · K. N. Singh · M. Maisnam
Department of Physics, National Institute of Technology, Imphal 795004, Manipur, India
e-mail: kdevishri08@gmail.com

D. Kangjam · R. K. Singh
Department of Basic Sciences, Manipur Technical University, Imphal 795004, Manipur, India

J. Pallipad · M. S. Tarun · D. Putrevu · A. Misra
Space Applications Centre-ISRO, Ahmedabad, Gujarat, India

Table 1 Details of the sentinel-1 SLC data sets used in the study

Sl. no	Date of data acquisition (master/slave)	B_{\perp} (m)	B_{temp} (days)	Pair name
1	<ul style="list-style-type: none"> • 18-6-2019/24-7-2019 • 12-6-2020/18-7-2020 	<ul style="list-style-type: none"> • -115.49 • 16.02 	<ul style="list-style-type: none"> • 36 • 36 	<ul style="list-style-type: none"> • Topo • Defo
2	<ul style="list-style-type: none"> • 9-11-2019/15-12-2019 • 27-11-2020/2-1-2021 	<ul style="list-style-type: none"> • 7.72 • -111.67 	<ul style="list-style-type: none"> • 36 • 36 	<ul style="list-style-type: none"> • Defo • Topo

operates at microwave frequencies and the spectral range is subdivided into frequency bands namely Ka, K, Ku, X, C, S, L, and P in order of decreasing frequencies. Interferometric Synthetic Aperture Radar (InSAR) is a remote sensing technique that analyzes phase differences between two or more SAR acquisitions with the goal of measuring surface topography and/or surface deformation [7]. For the first time, Goldstein et al. [8] used the radar interferometry technique to monitor ice sheet motion. Two-pass and three-pass DInSAR were used by Massonnet et al. [9] and Zebker et al. [10] respectively. DInSAR measures the displacement of a target by using the phase information between two SAR images [6]. SAR Interferometry can detect the surface change of cm to mm level accuracy [11].

2 Study Area and Datasets

The present study has been carried out for Rathong glacier, located in Sikkim, India. The Rathong River originates from its snout. The glacier is south-east facing and is located within a U-shaped valley, separated by lateral moraines on both sides [3]. In 2011, the glacier was 6.3 km long and extended over 3.942 km² in area [12].

For our study, Sentinel-1A data sets are downloaded from the Alaska Satellite Facility maintained by NASA (<https://search.asf.alaska.edu/#/>). Interferometric Wide swath (IW) is Sentinel-1's primary acquisition mode over land [13]. We use the Level-1 Single Look Complex (L1 SLC) in IW mode and vertical-vertical (VV) polarization. The important parameters of the Sentinel-1 C-band datasets used are given in Table 1. 1 arc-sec Shuttle Radar Topography Mission (SRTM) Digital Elevation Model (DEM) is used to remove the topographic phase from the generated interferogram.

3 Methodology

Initially, we search for the suitable Sentinel-1A SLC satellite data through their perpendicular baseline B_{\perp} , temporal baseline B_{temp} , availability of precise orbits, path, and frame. Then we selected four such datasets to estimate the glacier velocity using modified four-pass DInSAR technique. The downloaded datasets are processed using the open-source software Sentinel Applications Platform (SNAP) (version

8.0). Within SNAP, the Sentinel-1 Toolbox (S1TBX) was used for the DInSAR processing. The topographic-pair (topo-pair) is the SLC pair having longer B_{\perp} as compared to the deformation-pair (defo-pair) [14]. Each pair is coregistered to align both images at sub-pixel accuracy. In doing so we select the subswath and bursts of each SLC data corresponding to our area of interest and also update the orbit vectors with their precise orbit files. The black demarcation space between any two neighbouring bursts is removed using the TOPSAR deburst tool. We then generate an interferogram which consists of phase information due to topography, displacement, atmospheric contribution and noise. For estimating velocity, all other components except displacement are to be removed. To lower the phase noise, the phase is filtered using Goldstein phase filtering and then multilooked. Phase due to topography is removed by using 1 arc-sec SRTM DEM.

Next, we perform the phase unwrapping as the interferogram contains wrapped phase values in the range $\pm\pi$. We then coregister the unwrapped topo and defo pairs. The unwrapped phase is converted to *LOS displacement* which is the displacement of the target along the line-of-sight obtained by using [14]

$$LOS\ displacement = -\frac{\lambda'}{4\pi} \left(\varphi^{DP} - \frac{B_{\perp}^{DP} r^{TP} \sin \theta_0^{TP}}{B_{\perp}^{TP} r^{DP} \sin \theta_0^{DP}} \varphi^{TP} \right) \quad (1)$$

$$\text{and } \lambda' = \frac{\lambda}{1 - \frac{B_{\perp}^{DP} r^{TP} \sin \theta_0^{TP} T^{TP}}{B_{\perp}^{TP} r^{DP} \sin \theta_0^{DP} T^{DP}}} \quad (2)$$

where φ^{DP} and φ^{TP} are the unwrapped phases due to the defo-pair and topo-pair respectively; r is the slant range; θ_0 is the look angle and λ' is the nominal wavelength. Finally, *LOS displacement* is converted to LOS velocity by using the temporal baseline between the SAR images.

4 Results and Discussion

Table 1 gives information about the selected master and slave SLC images of each pair along with their perpendicular and temporal baselines. Selection of appropriate image pair is very important for DInSAR applications in order to get accurate results. We have selected two datasets, each dataset consisting of four SLC products in order to apply the modified four-pass DInSAR technique. The first velocity map is generated using data corresponding to summer season, with the topo-pair data having longer perpendicular baseline of summer 2019 and defo-pair data of summer 2020. The second velocity map is generated using data corresponding to winter season, with the defo-pair data having shorter perpendicular baseline of winter 2019 and topo-pair data of winter 2020. All the above combinations of data pairs are selected such that they have the same temporal baseline of 36 days between the acquisition of master and slave data.

Figure 2a shows the variation of slope for the glacier. The slope is maximum in the northernmost part, from where the glacier originates. It gradually decreases and finally is minimum near the snout portion as indicated by the dark green shade. The LOS velocity map for Rathong glacier corresponding to Sl.no. 1 of Table 1 is shown in Fig. 2b. In the starting portion or head of the glacier, the velocity varies from -0.134 to -0.082 cm/day. In the portion of the glacier lying in the latitude range of 27.58°N – 27.6°N , the velocity varies from -0.081 to -0.029 cm/day. Then towards the snout region of the glacier, the velocity ranges from -0.028 to 0.024 cm/day. Thus, the velocity slowly decreases as we move from the head to the snout. For the datasets corresponding to Sl. no. 2 of Table 1, the LOS velocity map is shown in Fig. 2c. The flow rate is roughly the same from the starting zone till about the middle portion of the glacier with values ranging from -0.079 to -0.013 cm/day. And from the portion lying in the latitude of 27.58°N upto the snout region of the glacier, the velocity varies from -0.045 to 0.021 cm/day. Here, the positive and negative signs indicate the direction of glacier movement. The negative sign in the LOS velocities indicates that the glacier is moving away from the satellite and the positive sign indicates the glacier movement towards the satellite [6]. Also, in both the cases the decrease in velocity follows the decrease in slope of the region.

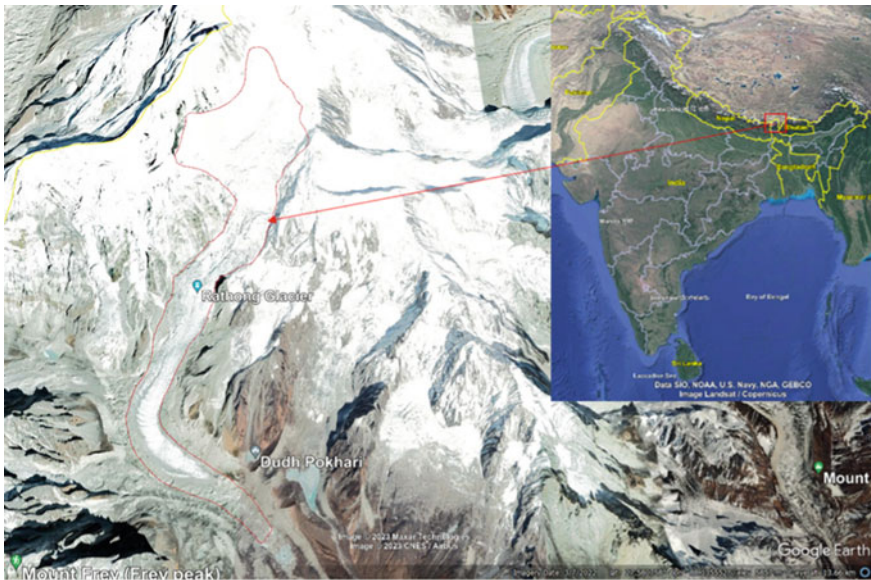


Fig. 1 Location of our study area. Rathong glacier is shown by the red polygon overlaid on Google Earth imagery of 3rd July 2022

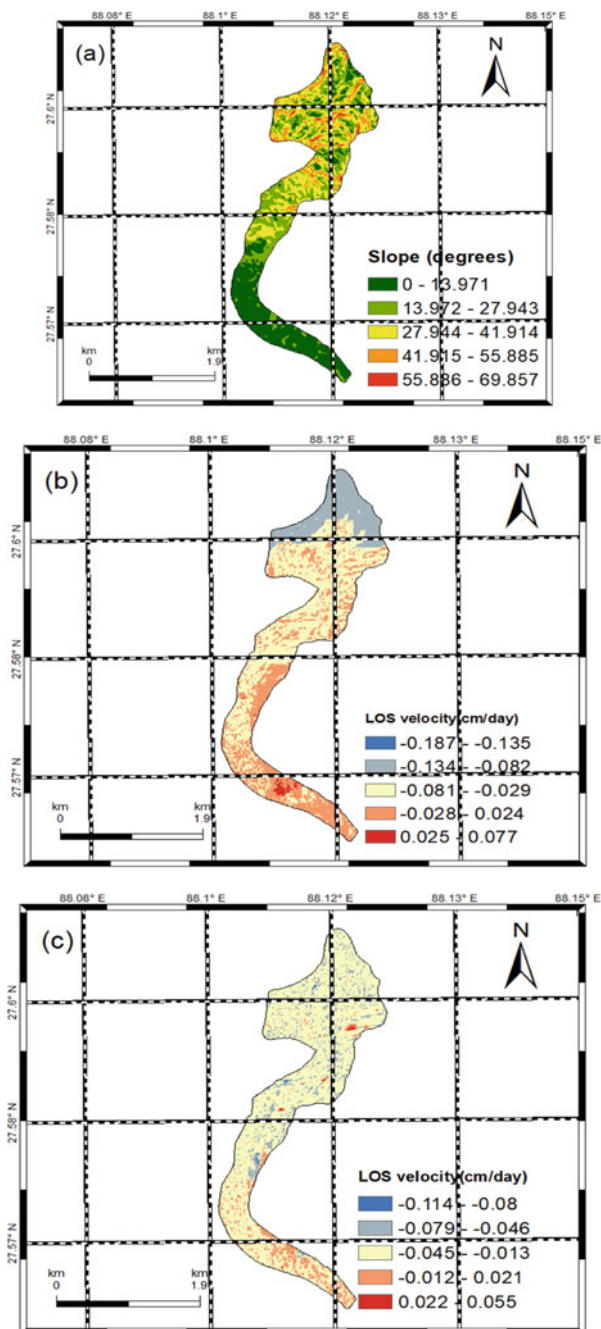


Fig. 2 a Slope of Rathong glacier. b, c Line-of-sight (LOS) velocity for Rathong glacier corresponding to the data sets given in Table 1, Sl. no. (1) and (2) respectively

5 Conclusion

It can be concluded that with the use of Differential SAR Interferometry technique, the phase difference between two or more SAR acquisitions can be related to the displacement or deformation of the target on the Earth's surface. And from this displacement, we can compute the velocity of the target. Phase unwrapping of the generated phase is the most crucial step in InSAR processing [15]. We should ensure that this step produces correct results so that we can relate the interferometric phase to the displacement. As a result of unwrapping, the correct multiple of 2π is added to the interferometric phase for each pixel. In general, the Rathong glacier is found to be a very slowly moving glacier. The LOS velocity is found to vary with change in perpendicular baseline and different combinations of topo and defo pairs corresponding to different seasons of the year. The effect of change in temporal baseline on the velocity can also be studied. The slope of the region also affects the movement of the glacier in its different zones.

Acknowledgements The authors sincerely acknowledge the support and guidance provided by the Space Applications Centre-ISRO, Ahmedabad, under which this study was carried out. Also, the valuable insights and support provided at various stages of the study by the Department of Basic Sciences, Manipur Technical University, Imphal, and the Department of Physics, National Institute of Technology, Imphal, are much appreciated. We also acknowledge the Alaska Satellite Facility Distributed Active Archive Center (<https://search.asf.alaska.edu/#/>) for giving free access to Earth observation data products, thereby enabling us to download our Sentinel-1A SAR SLC data.

References

1. Glacier Quick Facts, National Snow and Ice Data Center. <https://nsidc.org/cryosphere/glaciers/quickfacts.html>. Last accessed 31 May 2022
2. Ke C-Q, Kou C, Ludwig R, Qin X (2013) Glacier velocity measurements in the Eastern Yigong Zangbo Basin, Tibet, China. *J Glaciol* 59(218):1060–1068. <https://doi.org/10.3189/2013JG12J34>
3. Sharma RK, Pradhan P, Chettri D, Sharma NP, Shrestha DG (2013) Ground truthing, snout monitoring and stakes fixation to study glacier ice velocity in East Rathong Glacier, West Sikkim, India. *Int J Recent Sci Res* 4(1):50–54
4. Kumar P, Kotlarski S, Moseley C, Sieck K, Frey H, Stoffel M, Jacob D (2015) Response of Karakoram-Himalayan glaciers to climate variability and climatic change: a regional climate model assessment. *Geophys Res Lett* 42(6):1818–1825. <https://doi.org/10.1002/2015GL063392>
5. Rignot EJ, Mouginot J, Scheuchl B (2011) Ice flow of the Antarctic ice sheet. *Science* 333(6048):1427–1430. <https://doi.org/10.1126/science.1208336>
6. Nela BR, Singh G, Kulkarni AV, Malik K (2018) Optimum conditions for differential SAR interferometry technique to Estimate Himalayan glacier velocity. *ISPRS Ann Photogram, Remote Sens Spat Inf Sci* IV(5):137–40 <https://doi.org/10.5194/isprs-annals-IV-5-137-2018>
7. Flores A, Herndon K, Thapa R, Cherrington E (2019) The SAR handbook: comprehensive methodologies for forest monitoring and biomass estimation. NASA Tech Rep 20190002563 (2019). <https://doi.org/10.25966/ez4f-mg98>

8. Goldstein RM, Engelhardt HE, Kamb B, Frolich RM (1993) Satellite radar interferometry for monitoring ice sheet motion: application to Antarctic ice stream. *Science* 262(5139):1525–1530. <https://doi.org/10.1126/science.262.5139.1525>
9. Massonnet D, Rossi M, Carmona C, Adragna F, Peltzer G, Feigl K, Rabaute T (1993) The displacement field of the Landers earthquake mapped by radar interferometry. *Nature* 364(6433):138–142. <https://doi.org/10.1038/364138a0>
10. Zebker HA, Rosen PA, Goldstein RM, Gabriel A, Werner CL (1994) On the derivation of coseismic displacement fields using differential radar interferometry: the landers earthquake. *J Geophys Res* 99:19617–19634
11. Chunxia Z, Yu Z, Eongchen E, Zemin W, Jiabing S (2011) Estimation of ice flow velocity of calving glaciers using SAR interferometry and feature tracking. In: *Proceedings of fringe 2011*, pp 49. ESA SP-697, Frascati, Italy (2011). ISBN 978-92-9092-261-2
12. Agrawal A, Tayal S (2013) Assessment of volume change in East Rathong glacier, Eastern Himalaya. *Int J Geoinform* 9(1), 73–82 (2013)
13. Braun A, Veci L (2020) Sentinel-1 toolbox TOPS interferometry tutorial
14. Liu G, Guo H, Yue H, Perski Z, Yan S, Song R, Fan J, Ruan Z (2015) Modified four-pass differential SAR interferometry for estimating mountain glacier surface velocity fields. *Remote Sens Lett* 7(1):1–10. <https://doi.org/10.1080/2150704X.2015.1094588>
15. https://www.iirs.gov.in/iirs/sites/default/files/StudentThesis/balaji_p_m.sc_thesis.pdf. Last accessed 14 December 2022